Solutions optimales linéaires et non-linéaires dans une couche limite hypersonique : stabilité et contrôle en boucle ouverte

Arthur Poulain

INSTITUT POLYTECHNIQUE DE PARIS

NNT : 2023IPPAX127

Thèse de doctorat

ÉCOLE POLYTECHNIQUE

IP PARIS

Optimal linear and non-linear solutions in hypersonic boundary layers: stability and open-loop control.

Thèse de doctorat de l'Institut Polytechnique de Paris
préparée à l'École polytechnique

École doctorale n°626 École doctorale de l'Institut Polytechnique de Paris (EDIPP)
Spécialité de doctorat : Mécanique des fluides et des solides, acoustique

Thèse présentée et soutenue à Meudon, le 13/12/2023, par

ARTHUR POULAIN

Composition du Jury :

Jean-Christophe Robinet Professeur, ENSAM Paris (Dynfluid)	Président
David Fabre Maitre de conférences, Université Paul Sabatier (IMFT)	Rapporteur
Markus J. Kloker Research director, University of Stuttgart (IAG)	Rapporteur
Ardeshir Hanifi Docent, KTH (Linné FLOW)	Examinateur
Denis Sipp Directeur de recherche, ONERA (DAAA)	Directeur de thèse
Georgios Rigas Senior Lecturer, Imperial College London (Dept. of Aeronautics)	Encadrant
Cédric Content Ingénieur de recherche, ONERA (DAAA)	Invité
Franck Hervy Ingénieur, Direction Générale de l'Armement (AID)	Invité

Remerciements

Such as these three years spent between France (in the wide forest of Meu-don) and UK (in the wide city of Lon-don), these acknowledgments are an inhomogeneous mixture of French and English. My first thanks are towards the referees Markus Kloker and David Fabre who took the time to read and deliver a fruitful feedback on this concise manuscript. Jean-Christophe Robinet and Ardeshir Hanifi are also thanked for the interesting talks we had before and during the defence. Thanks to S. Esquieu and Y. Hwang for having assessed my work midway through my PhD thesis. Je remercie également l'AID (DGA) d'avoir financé cette thèse et notamment Franck Hervy as well as the FR/UK cooperation with DSTL (thanks for your limitless enthusiasm Jitu Patel) hoping this scheme will last. Je remercie bien entendu les quelques membres concernés de l'école doctorale IPP qui assurent le soutien de leurs élèves.

Un immense merci à toi Denis, notamment pour avoir cru en mes capacités pour mener à bien cette thèse (c'était loin d'être gagné vu l'aventure qu'aura été BROADCAST). Ton enthousiasme très communicateur a été l'une de mes plus grandes sources de motivation car que ce soit après une heure de gribouillage de formules mathématiques dans ton bureau (souvent à propos d'adjoint) ou après nos réunions en groupe sur Jitsi, je repartais toujours avec un surplus d'inspiration (et de travail). À l'avenir, je tacherai de conserver ta façon positive d'analyser un résultat ou un bug informatique. This positive outlook was also shared by you, George, through your encouraging attitude. Despite the distance, you were always available to suggest me how to solve the many issues I was facing. I will not forget the nice restaurants, the city trips in your small convertible car in London, Cadiz beach (just to be clear, it does not seem but we have worked a lot) and all the efforts you made to make me come to Imperial or go to the US. Enfin, Cédric, tu as été tout simplement indispensable, autant techniquement (BROADCAST n'existerait tout simplement pas) qu'humainement (tu m'as bien plus que soutenu en toutes circonstances et je n'aurais pas atteint la fin de cette thèse sans toi). Nous en avons résolu des foutus bugs ensemble ! Overall, I think we were a good team and I hope you three will continue to work together with new students. Mes derniers remerciements pour l'encadrement vont à Eric qui a été contraint de s'éloigner peu à peu avec l'évolution progressive du sujet de thèse, ton aide ponctuelle a néanmoins été précieuse.

Le centre de Meudon de l'ONERA m'a formidablement bien accueilli. Je remercie notamment tous les permanents de l'unité MASH. Entre autres, je remercie Mathieu L., Samir, Colin, Guillaume B. et Julien D. de MASH, Johann, Nicolò, Sébastien B. et Emeric de Châtillon et José de Toulouse pour m'avoir aidé (pour certains grandement) ou simplement donné un conseil sur mes travaux. Un grand merci à Tanya pour son aide logistique et administrative et sa

grande patience pour m'expliquer toutes les procédures nécessaires.

Merci évidemment à tous les doctorants, post-doctorants et stagiaires qui animent le centre de Meudon. La liste est longue. Merci aux plus anciens que je n'ai que rapidement croisés, Julien L., Luis et Markus, à ceux qui ont brillamment quitté l'ONERA (avec un diplôme de thèse ou une indemnité de fin de contrat, les deux se valent), Xavier, Euryale et Alexandre. Pierre N. (l'expert en transition de couche limite hypersonique avec actionneur dans le fluide) et Romain P. (l'expert en Python mais aussi tout ce qui est lié à la programmation), de par votre choix de table pour la pause repas, je vous classe également parmi les doctorants. Cela a été une immense chance pour moi que vous restiez tous deux à Meudon à l'issue de votre thèse, vous avez été deux repères supplémentaires au cours de ces trois ans, vous avez entretenu la bonne ambiance au sein du groupe des doctorants et je vous considère comme mes deux "grands frères de thèse". Clément, avec ou sans ta casquette CEA, ce fut une joie de t'avoir avec nous pendant cette dernière année, tu es la preuve vivante que l'on peut ressortir sain d'esprit et d'humeur joviale d'une thèse passée à implémenter un solveur pour la transition de couches limites hypersoniques. Then, my French-Spanish-German companions, Arthur V., Carmen and Julian, it has been a pleasure to start together this adventure and we can be proud of ourselves to have reached the end, these were nice running in Meudon forest, climbing session, many chats and beers. Enfin les jeunes insouciants qui font preuve d'une courageuse résilience, Mathieu S., Michele et Loïc pour ces intenses parties de ping-pong, Raphaël pour ta bonne humeur sans égale, Aron for your discrete jokes, Kévin pour ta grande sympathie, les braves nouveaux arrivants Hugo et Vianney, mes sporadiques collègues de bureau Thomas et Dimitri, Victor pour ces échanges passionnants de construction de matrices (et autres sujets), Alexis pour ces discussions F1 et bons souvenirs de KTH, les nombreux sympathiques stagiaires dont Aldo (I have no doubt you will succeed in your future career in research).

My thanks to the people at Imperial College who welcomed me like a king during six months. Thanks to Clodagh for her administrative help! Merci à Thibault pour ses conseils en programmation, git et documentation. Huge thanks to the group meeting members, it was a pleasure to see you (even remotely) every week and see how you were progressing in your own thesis. Thanks Tai and Simon! Thanks Yusuf for the nice conversations (I am impatient to read your novels), Chengwei for being such a nice person and the discussions about your incredible numerical and experimental work (I loved helping you a bit at the wind tunnel), Flavio for your keen interest (I really enjoyed working in close collaboration with you) and Priyam, you are doing such an impressive work! Thanks Kazuki as well for your kindness! Thanks Yaxin, Defne, Elise, Dan and Tullio for the nice lunch breaks shared, Filippo and Chi Hin for the chats in the office. Many thanks to Samantha and Gabriel for having warmly welcomed me in the heart of London and their cute/naughty cats Helios and Selene.

Je remercie mes amis qui m'ont aidé à libérer de temps en temps mon esprit de l'obsession de la thèse. Les Chameaux évidemment pour les parties de belote, jeux de société et tennis : Julien, Quentin et Clotilde, Antoine C., Jean, Jean-Loup, Louis et Shubo. Mais aussi mon "voisin" et "ex-collègue" Antoine B. pour les nombreuses sorties ciné et après-midi jeux de société souvent partagés avec plaisir avec Lucas et Viviane entre autres. Merci à Philip et Alice pour les escapades en plein-air hors de Paris, Romain T. pour le petit temps que nous nous sommes recroisés à Londres, à Jules, Colin H., Colin C. et Benoit pour ces chouettes nouvel ans, à Wilfried que je prenais plaisir à retrouver en Dordogne et qui a certainement été un modèle pour cette thèse et mon plus vieil ami Alexandre dont j'ai été l'heureux témoin de tant d'accomplissements durant ces trois dernières années.

Biologiquement parlant, je dois évidemment remercier ma famille mais ma gratitude va bien au-delà de ma simple existence. Je remercie mes grands-parents disparus (que j'ai pu connaître ou non) pour leur soutien afin que je puisse m'accomplir à travers mes études et mes

grands-parents toujours en forme pour leur appui moral sans faille et pour toutes ces joyeuses réunions de famille avec oncles, tantes et cousin·e·s (aussi bien Poulain que Lacourt). Merci par ailleurs à Vincent et Simon d'être quasiment venu par surprise à ma soutenance ! Je remercie mes deux parents pour leur amour et leurs encouragements durant ces trois années et surtout toutes celles qui les ont précédées. Un grand merci à ma sœur qui m'a permis de voyager un peu en choisissant ces dernières années d'excellents lieux de vacances (pardon d'études). Quel que soit tes choix futurs, je t'encouragerai toujours. Sauf si c'est une thèse !

Enfin, je souhaite mentionner ceux qui m'ont transmis leur savoir qui a été utile pendant cette thèse. Une des premières tâches de cette thèse a été la résolution d'un polynôme du second degré, la solution m'ayant été enseignée neuf ans auparavant, je citerai neuf "professeur·e·s" (un·e par année, liste non exhaustive) : Mme et M. Astié, M. Raynaud, Mme Goutelard, M. Lembrez, Mme Ortiz Clerc, David Birch, M. Ringertz et Dimitrios Papadogiannis.

Publications and communications

Publications

- A. Poulain, C. Content, D. Sipp, G. Rigas, E. Garnier. BROADCAST: A high-order compressible CFD toolbox for stability and sensitivity using Algorithmic Differentiation. *Computer Physics Communications*, 2023.
- A. Poulain, C. Content, G. Rigas, E. Garnier, D. Sipp. Adjoint-based linear sensitivity of a supersonic boundary layer to steady wall blowing-suction/heating-cooling. *Journal of Fluid Mechanics*, 2024.
- A. Poulain, G. Rigas, C. Content, A. Schioppa, P. Nibourel, D. Sipp. Space-Time Spectral Method: optimal non-linear solutions in compressible boundary layer flows. *Computer Methods in Applied Mechanics and Engineering*, in preparation for submission.

This PhD thesis manuscript has been written from the three articles above. They respectively correspond to chapters 2, 3 and 4.

Communications

- Linear sensitivity of a hypersonic boundary layer by Algorithmic Differentiation through the toolbox BROADCAST. 14^{th} *ERCOFTAC SIG 33 Workshop, Cadiz (Spain).* June 2022.
- Linear sensitivity of a hypersonic boundary layer to steady wall blowing and heating. 75^{th} *Annual meeting APS DFD, Indianapolis (US).* November 2022.
- Optimal location for steady wall blowing or heating actuators in a hypersonic boundary layer. 57^{th} *3AF International Conference on Applied Aerodynamics AERO2023, Bordeaux (France).* March 2023.

Contents

Introduction

Context and motivation

Hypersonic flow physics understanding is challenging. The high speeds generate shock waves (flow discontinuities), large skin-friction yielding additional viscous drag (larger fuel consumption), high heat-flux which may damage the vehicle integrity (surface ablation) and eventually chemical reactions (not studied in the present work). Then, the high flying altitude environment includes rarefied air (low free-stream density and temperature) and small disturbances (few particles, aerosol, acoustic waves and turbulent spots). Under these conditions, a key parameter for the design of hypersonic vehicles is the flow topology which is, especially for wall-bounded flows, whether it is laminar or turbulent [168] (Figure 1). While the latter produces larger wall-shear stresses and wall-temperature, the former is much more sensitive to the inherent flow detachment over convex geometries. Therefore, it is desirable to maintain a laminar boundary layer to reduce drag and wall heat-flux (thinner thermal protection) to get the largest payload and then to be able to promote transition to the turbulent state in the region where separation occurs resulting from the surface geometry or the interaction with an impinging shock wave. Indeed, for air-breathing vehicles, a separated flow ingested by the scramjet strongly affects the performance and may lead to failure [10].

However, the environmental conditions, large Mach numbers and relatively low Reynolds numbers, prevent a quick natural transition as the one observed at lower speeds [168]. Therefore, it is first necessary to understand the laminar to turbulent transition process and secondly to alter it through a control mechanism.

Transition is produced by the growth of instabilities. Small amplitude free-stream disturbances (vortical or acoustic waves) as well as wall roughness may excite these instabilities, through the receptivity process [161], which are subsequently amplified by various linear mechanisms, such as the Mack modes [106] or non-modal streaks [129]. Laminar flow control may then either modify the mean-flow to promote/damp the instabilities growth [59] or erase them by injecting out-of-phase waves through a closed-loop control [84].

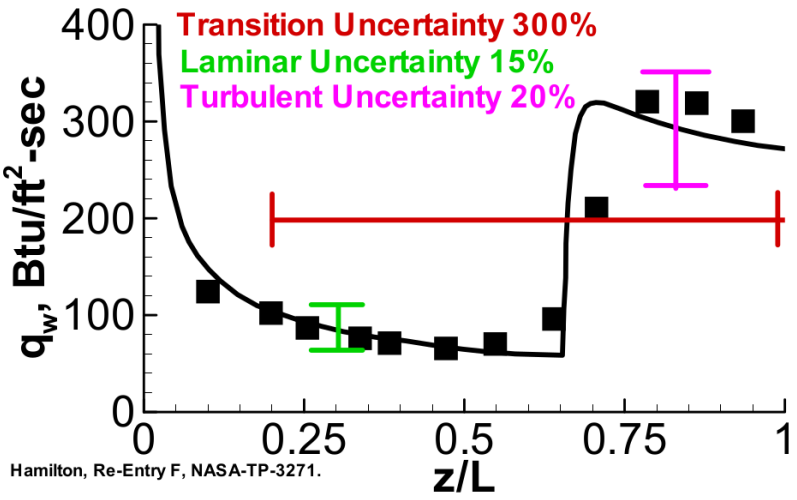

Figure 1: Uncertainty of the surface heating increase induced by the laminar to turbulent transition from Schneider [169].

Objectives

To sum up, the transition to turbulence is caused by the amplification of linear instabilities which are well known for hypersonic boundary layers [20, 106]. Nonetheless, these perturbations are optimal only at linear regime. Optimal non-linear solutions, also called worst-case disturbances, have already been computed at incompressible regime [32, 155] or at hypersonic regime under the constraint of a sum of eigenmodes derived from the linear theory [77]. The novelty of the present work is the identification of the optimal non-linear solutions developing in a hypersonic boundary layer and the characterisation of the optimal open-loop wall actuator to control them.

Then, the objectives are to:

- Develop the numerical framework and tools to study the linear and non-linear optimal solutions (worst-case disturbances) in hypersonic laminar flows.
- Identify the optimal instabilities of the attached hypersonic boundary layer promoting laminar to turbulent transition.
- Compute the optimal open-loop mean-flow wall control to promote or delay the transition.

Outline

The chapter 1 presents the key results from the literature on laminar to turbulent transition at supersonic and hypersonic regimes. The open-loop control of the linear instabilities is also mentioned. The different methods to compute these instabilities and their respective assumptions are as well described.

Figure 2 shows an overview of the present work split into 4 sections. Two chapters (2 and 4) deal with the identification of the instabilities and both others (3 and 5) offer the computation of the optimal open-loop control. From initial linear analyses (chapters 2 and 3), further results are derived in the non-linear framework (4 and 5). The main case explored is the boundary layer developing over an adiabatic flat plate at Mach number 4.5.

The chapter 2 presents a general framework to solve and analyse the large-scale discretised dynamical system defined by the compressible Navier-Stokes equations, through direct and

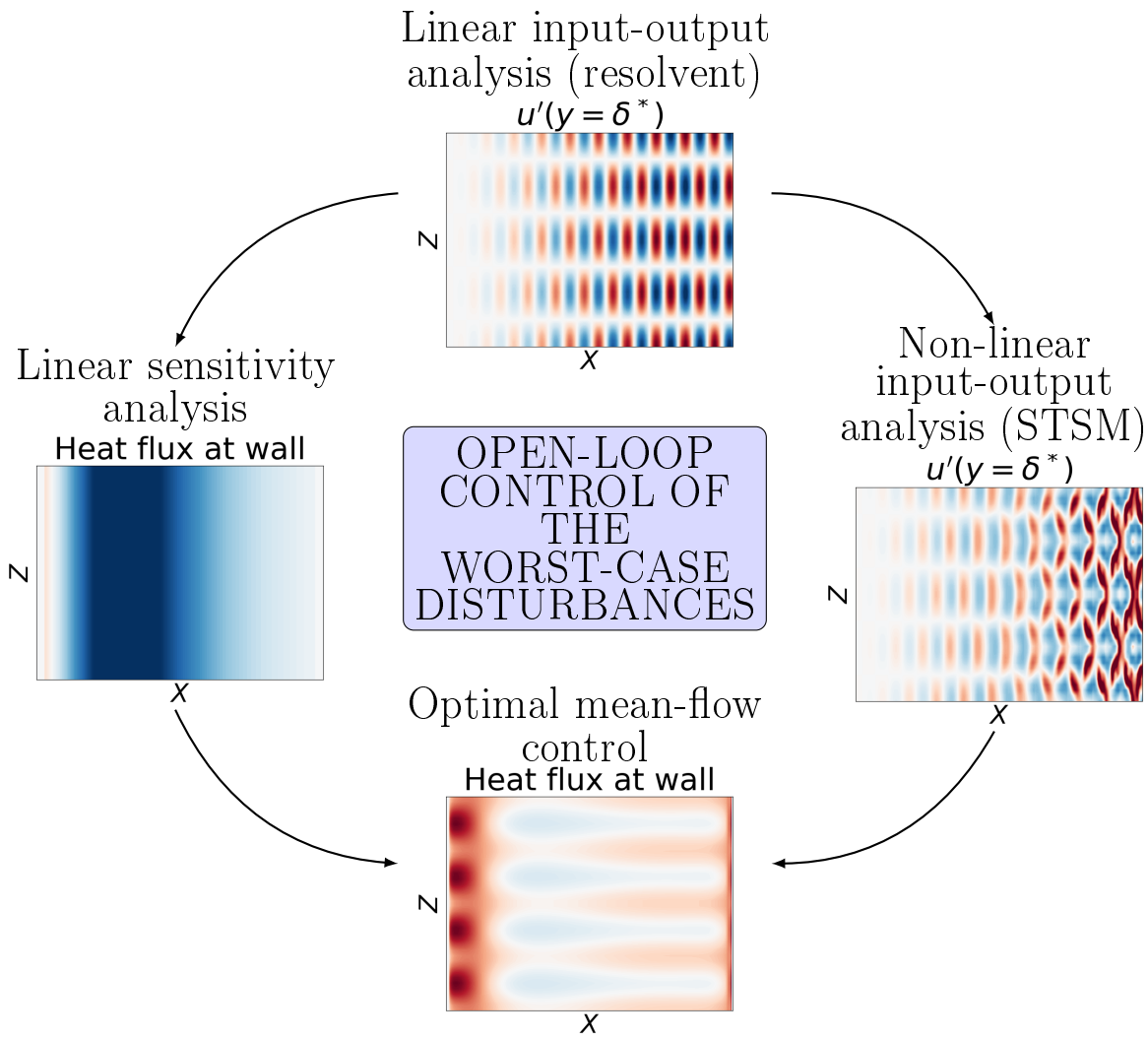

Figure 2: Outline of the PhD thesis: application to the first Mack mode induced transition in a $M_\infty = 4.5$ boundary layer. Top view (x-z plane) of iso-contours (red for positive and blue for negative) of the streamwise velocity fluctuations (u') along the displacement thickness ($y = \delta^*$) and the heat-flux at wall ($y = 0$). Chapter 2 identifies the linear instabilities through linear input-output analysis. Chapter 3 offers the optimal control to damp them through linear sensitivity analysis. Chapter 4 identifies the non-linear interactions promoting laminar to turbulent transition with non-linear input-output analysis. Eventually, Chapter 5 presents the optimal mean-flow control to delay or promote the transition induced by the worst-case disturbances calculated in Chapter 4.

adjoint derivatives computed with Algorithmic Differentiation. This methodology is developed here with high-order numerical schemes to show how to efficiently and accurately find fixed-points as well as to perform linear global stability and resolvent analysis.

The chapter 3 presents the derivation of the linear sensitivity of the optimal gains i.e. the optimal location for small amplitude open-loop control of linear instabilities. The sensitivity to base-flow modifications is first computed. Wall-based control is then explored by computing the optimal location for steady wall blowing/suction or heating/cooling actuators to damp the main instabilities. The design of a realistic wall heat-flux actuator targeting all the instabilities is ultimately attempted.

The chapter 4 presents the weakly non-linear analysis near bifurcation for globally unstable compressible flow. Then, for amplifier flows, the extension of the linear resolvent to non-linear input-output analysis which takes into account the non-linear interactions of a finite number

of time and spanwise harmonics, through a pseudo-spectral method (equivalent to harmonic balanced method), is described thoroughly. The transition of a boundary layer induced by the optimal forcing is studied.

The chapter 5 presents the open-loop control of the non-linear solutions derived in chapter 4. To get an actuator closer to realistic configurations, mean-flow heat-flux control is derived. A comparison is performed with the linear sensitivity derived in chapter 3 and the optimal heat-flux profiles to delay or promote the laminar to turbulent transition of the boundary layer are computed.

Chapter 1

State of the art

Chapter foreword:

This chapter presents the key results from the literature on laminar to turbulent transition at supersonic regime through the different paths to transition (linear and non-linear mechanisms). The open-loop control of the linear instabilities by suction or heating is also mentioned. The various methods to compute these instabilities and their assumptions, from linear to non-linear analysis, are eventually presented.

1.1 Laminar to turbulent transition in boundary layers

Laminar to turbulent transition was early observed by Reynolds [153] through an experiment performed in a pipe. Injecting dye in the flow, he noticed that its trajectory changed when the flow velocity was increased. Initially straight and parallel to the pipe direction (no lateral mixing), at a critical value of the aptly named Reynolds number (proportional to the velocity), the dye adopts a chaotic behaviour involving mixing and vortices. The flow topology has moved from laminar to turbulent. Not only this transition exists for pipe flows but also in boundary layers e.g. the flow along a flat surface.

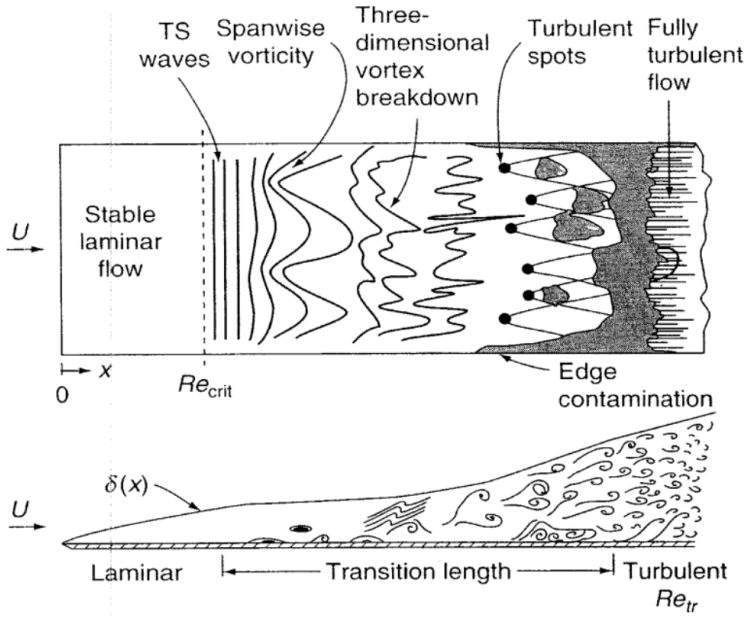

Figure 1.1: Typical transition scenario of an incompressible boundary layer from White [198].

Figure 1.1 describes the natural transition scenario in a quiet environment for an incompressible boundary layer. The initial laminar flow acts as a filter i.e. more or less receptive to some disturbances. These perturbations may come from the external environment as vorticity, acoustic or entropy waves, turbulence, particles, aerosols or from surface disturbances as roughness, waviness, uneven ablation or vibrations [169]. These ingested disturbances are exponentially amplified as Tollmien-Schlichting (TS) waves [165] which are two-dimensional viscous instabilities. They reach a threshold amplitude (streamwise velocity fluctuations of the order of magnitude of 1% of the free-stream velocity) and yield secondary mechanisms. Spanwise periodic waves arises then generating three-dimensional vortices which promote the streaks through the lift-up effect [16, 22, 137]. These structures eventually saturate and break down to turbulence. This is one of the scenario possible depending on the amplitude of the forcing environmental disturbances

Indeed, Morkovin [129] offered a schematic description (Figure 1.2) of the different paths followed by the laminar to turbulent transition. Path A in Figure 1.2 refers to a quiet environment ("natural" transition), such as the transition generated by the TS waves described above. However, the primary modes can be of different nature. Concave geometries generate Görtler vortices [65], compressibility produces inviscid Mack modes [106] or shear-layers amplify Kelvin-Helmholtz instabilities [45]. Other instabilities arise from the entropy-layer [44] or the cross-flow [91, 149]. These linear instabilities compete and later interact to trigger the secondary mechanisms, such as the streaks or Λ-shaped structures, which will break down through turbulent spots [144]. The rises of skin-friction, heat transfer and intermittency

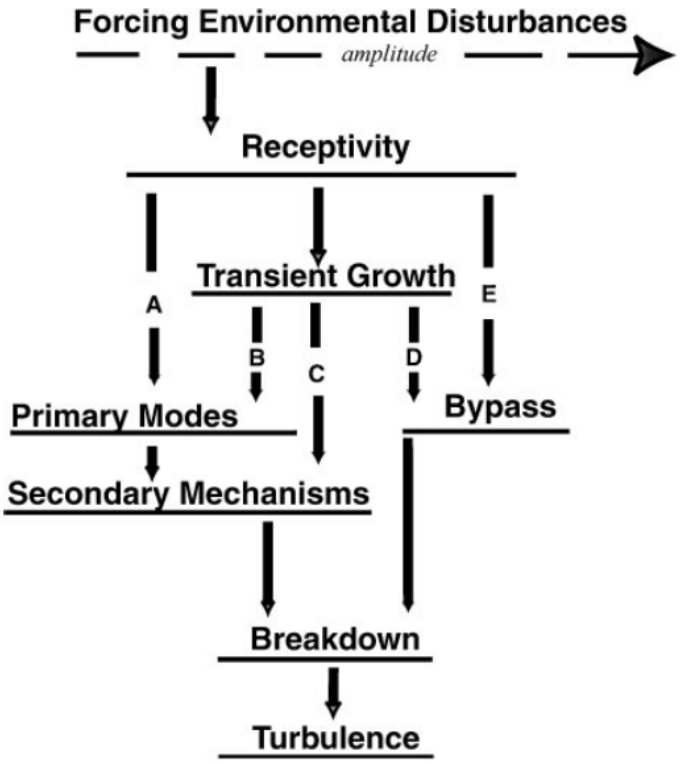

Figure 1.2: Paths of boundary layer transition from Morkovin [129].

precede the fully turbulent flow. Paths B, C and D include another mechanism called the transient growth. The superposition of linearly stable but non-orthogonal (non-normality of the linearised Navier-Stokes operator) eigenmodes may initially lead to the amplification of the disturbances energy before asymptotically decaying [166]. This non-modal transient growth may either feed the linear amplification of the other instabilities (path B) [67], trigger directly the secondary mechanisms (path C) [88] or even bypass them (path D, see for instance the blunt-body paradox [151]). Finally, path E corresponds to the rapid transition scenario where the different mechanisms involved have not yet been clearly identified such as for large roughness.

1.1.1 Linear instabilities

Under environmental disturbances of low amplitude, the linear instabilities play a key role to understand the transition according to Morkovin [129]. Various type of instabilities have already been cited above. Focusing on the zero pressure gradient boundary layer without crossflow, the main instabilities are the two-dimensional viscous Tollmien-Schlichting waves [165] at incompressible regime (visualised in Figure 1.3) and the Mack modes [106] at higher Mach numbers. The first Mack mode is the compressible equivalent of the TS waves.

Increasing the free-stream Mach number M_∞, the necessary condition [147] for the existence of an inviscid instability is satisfied by the emergence of a generalised inflection point in the density-velocity profile. Therefore, the first Mack mode is one of these inviscid instabilities. Furthermore, as the two-dimensional instability grows faster at low Mach numbers, from $M_\infty \gtrsim 2$, oblique waves with a cross-flow angle of around 60° are the most amplified (see Figure 1.4).

At larger Mach numbers, a region of sonic relative Mach number (difference of the Mach numbers based on the local streamwise velocity and based on the phase velocity) appears close to the wall. At $M_\infty \gtrsim 2$, this layer is large enough so that instabilities may grow inside. Mack

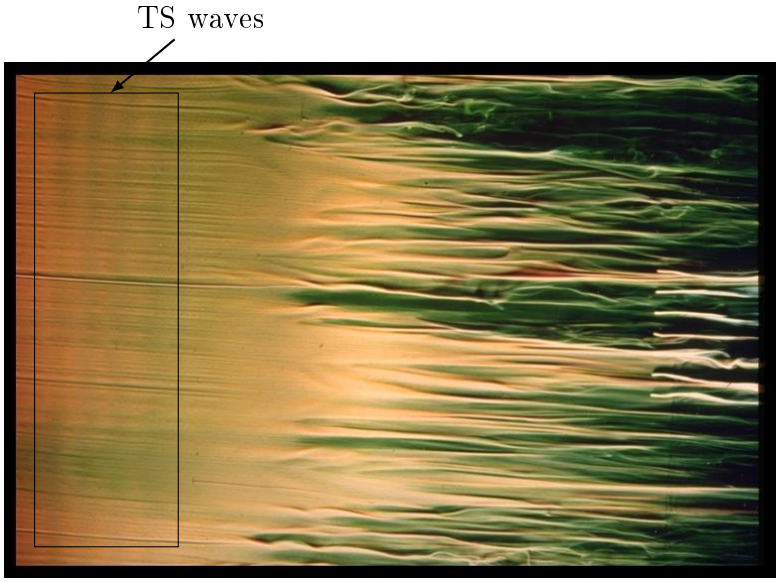

Figure 1.3: Tollmien-Schlichting waves visualised by dye in a hydrodynamic tunnel [197].

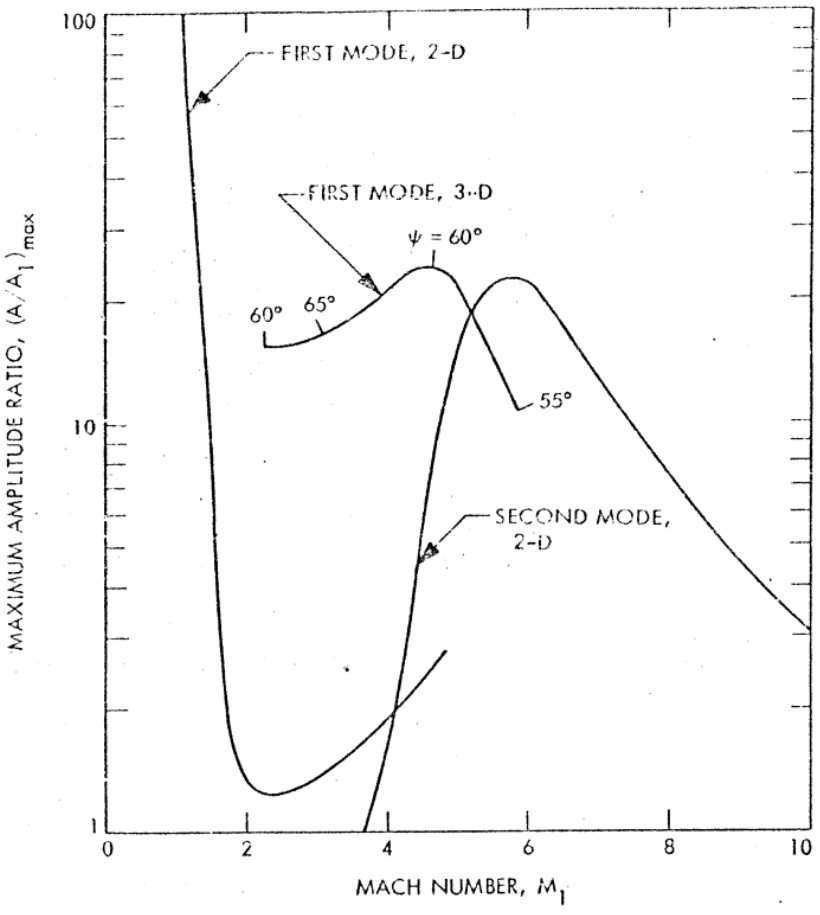

Figure 1.4: Energy amplification of the Mack modes with respect to the Mach number [107].

[106] showed that these supersonic flows display an infinity of unstable modes, called Mack modes. Around $M_\infty \sim 5$, two inviscid Mack modes are predominant: the vortical first Mack mode described above, located close to the generalised inflection point, and the two-dimensional second Mack mode which is an acoustic wave trapped between the wall and the relative sonic

line (rope-like structure from Figure 1.5). The amplification rate of the second Mack mode prevails the first Mack mode from $M_\infty \gtrsim 5$ (Figure 1.4) but as the flow region where the second Mack mode grows is generally shorter, both Mack modes compete [20, 105]. In another terminology, the Mack modes result from the synchronisation of the phase speed of the local Fedorov's modes F and S [50], respectively a fast and a slow acoustic wave, that promotes the instability of the latter. Further analyses are still performed to describe the velocity and thermodynamic components of the Mack modes [172].

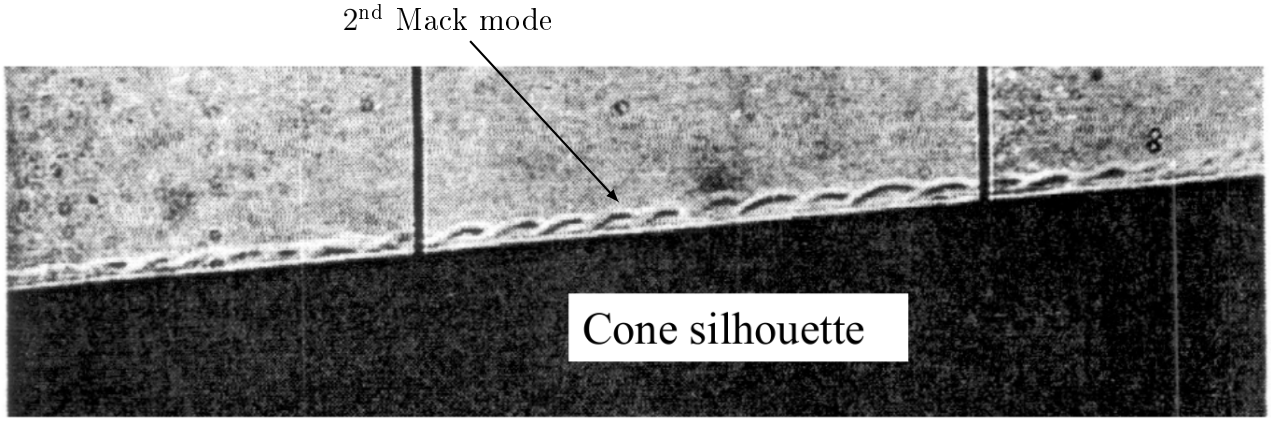

Figure 1.5: Second Mack mode ("rope waves") visualised by shadowgraph on a sharp cone at Mach 8 [43].

1.1.2 Non-linear mechanisms

Following the amplification of the linear instabilities, secondary mechanisms steer the flow towards turbulence. They result from the saturation of the linear instabilities and from the non-linear interactions between different unstable modes.

At incompressible regime, two well-known routes to transition follow the modal amplification of the TS waves. The first is the *K*-type transition [92, 156] where the two-dimensional TS wave interacts with two oblique waves of the same frequency (fundamental resonance), whose non-linear interaction generate aligned Λ-shaped vortices. The second path, which is quite similar, is the *H*-type transition [70, 86]. The two-dimensional TS wave interacts with two oblique waves of the subharmonic (half of the fundamental) frequency, producing staggered Λ-shaped structures. Herbert [70] showed that the subharmonic waves have a faster amplification than the fundamental one through secondary linear analysis of the periodic flow.

At compressible regime, the oblique waves amplify faster (larger linear growth rate) which promote the oblique breakdown transition scenario. They generate unstable streaks of various types depending on the symmetry of the flow (fundamental or subharmonic, sinuous or varicose) [3] which later break down. Chang and Malik [28] described the streaks development as a wave-vortex triad: the non-linear triad interactions of the oblique waves and a streamwise vortex promote the rapid growth of the vortex mode. When the streamwise velocity fluctuations reach an amplitude of the order of magnitude of 4 to 5% of the free-stream velocity, the skin-friction starts to rise (transition onset), higher harmonics are produced and staggered structures appear. Laible and Fasel [95] showed that the oblique mode feeds the streaks and the non-modal effect (transient growth) increases the amplitude of the streaks but do not affect its growth rate.

The first Mack mode oblique breakdown has been thoroughly studied at $M_\infty = 1.6$ [28], $M_\infty = 2$ [160] , $M_\infty = 3$ [121], $M_\infty = 4.5$ [201] and $M_\infty = 6$ [55, 190]. For the same initial energy, the second Mack mode breakdown is slower to promote transition both at $M_\infty =$

4.5 [201] and $M_\infty = 6$ [55]. Conversely to its incompressible equivalent, the fundamental breakdown is faster than the subharmonic resonance for both the first [28] and second Mack mode breakdown [66, 191]. Figure 1.6 illustrates the first Mack mode oblique breakdown process [201]. In 1.6(b), the flow mainly includes the fundamental oblique Mack waves which generate staggered Λ-shaped vortices downstream. In 1.6(c), these vortices are connected by their legs and break down downstream through both the thickening of the boundary layer and the appearance of smaller structures near the wall. Eventually, in 1.6(d), hairpin vortices denote the late stages of the transition towards the turbulent flow observed in 1.6(e).

Eventually, Jahanbakhshi and Zaki [77] derived the optimal worst-disturbances in a data-driven framework. For low disturbances energy, they found that the non-linear interactions of a pair of oblique first Mack mode and two second Mack modes optimally trigger transition at $M_\infty = 4.5$.

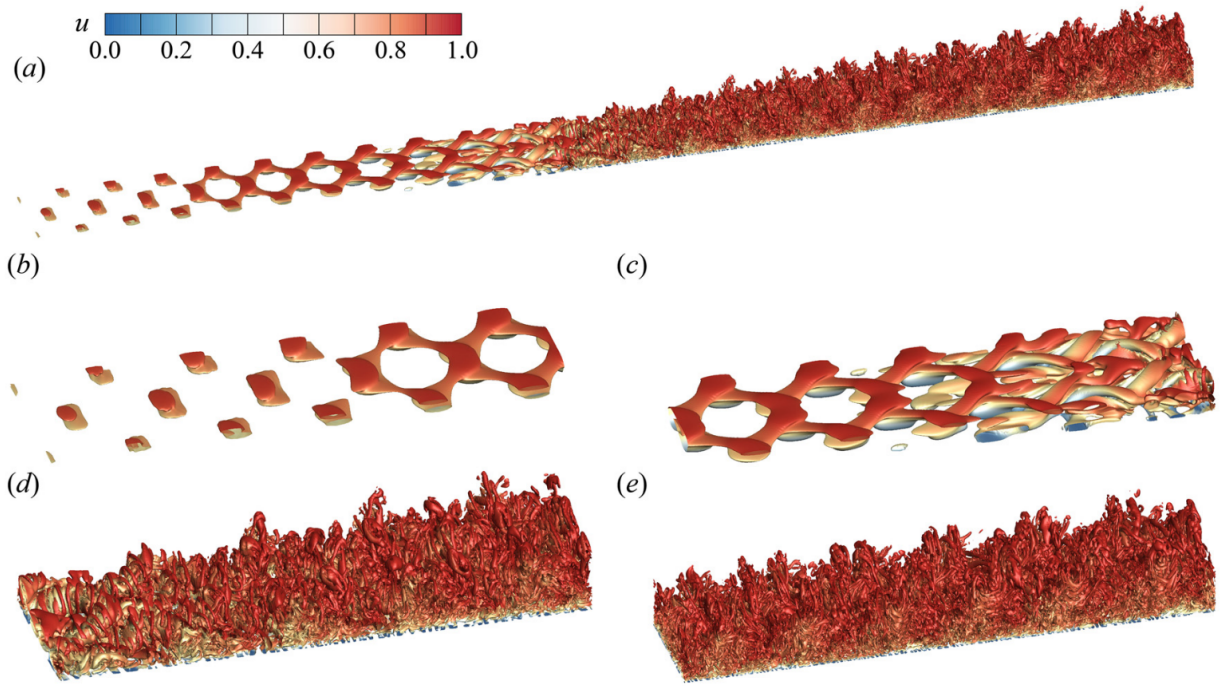

Figure 1.6: Q-criterion for the visualisation of the structures generated by the first Mack mode oblique breakdown from the Direct Numerical Simulation (DNS) of Zhou et al. [201] at $M_\infty = 4.5$. (a) Full view: $0.45 < x < 1.1$ m. (b) Zoomed: $0.45 < x < 0.6$ m. (c) Zoomed: $0.6 < x < 0.75$ m. (d) Zoomed: $0.75 < x < 0.9$ m. (e) Zoomed: $0.9 < x < 1.1$ m.

1.1.3 Mean-flow control of the linear instabilities

As specified in the introduction, it is often desirable to maintain a laminar flow. Therefore, laminar flow control has been an intense subject of research [84]. It includes two main families: wave-cancellation methods, which attenuate the instabilities with out-of-phase waves (closed-loop control) [125, 133] and steady mean-flow manipulations [59], which we will focus on in the present work, with a special interest in blowing/suction and heating/cooling control systems. All these methods are applied upstream the transition onset to damp the growth of the linear instabilities before they reach high amplitude.

1.1.3.1 Suction control

Suction control, when applied to incompressible flows, is optimal to damp the two-dimensional Tollmien-Schlichting waves when the actuator is located near branch I (beginning of the unstable region of the local mode, similar location as the optimal forcing from the resolvent analysis) according to the asymptotic analysis [148], the experimental work [152] and the local scattering approach [73]. For supersonic boundary layers, asymptotic analyses demonstrated that the second Mack mode is also highly receptive to unsteady blowing/suction located near Branch I of mode S [49]. Wang et al. [195] showed that unsteady blowing/suction strongly excites the mode S (slow) if located upstream of the point where mode F (fast) and S phase velocities synchronise (called synchronisation point in the rest of the manuscript) while the effect is much lower when the actuator is downstream. The synchronisation point seems to be linked to the optimal location for local control as Fong et al. [53] noticed an opposite effect on the growth of mode S if a roughness element (similar behaviour to local blowing) is located before or after the synchronisation point in the DNS computation of a hypersonic boundary layer.

1.1.3.2 Heat-flux control

Wall cooling/heating control has been extensively investigated. Mack [108] showed that the growth of the Mack modes are sensitive to the wall temperature: a uniformly cooled wall damps the first Mack mode but destabilises the second Mack mode. Therefore, for Mach numbers much below 4 [108], cooling the wall in order to modify the base-flow represents a control technique to delay the laminar to turbulent transition. Wang and Zhong [194] found that the hypersonic boundary layer is less sensitive to unsteady temperature perturbation than unsteady blowing/suction. For subsonic boundary layers, a heating strip at the leading edge has a stabilising effect [89] while the opposite effect if located further downstream [117]. For supersonic boundary layers, Masad and Abid [118] found by N-factor analysis that a heating strip upstream also stabilises by damping the first Mack mode. The experimental work [175] on a cone at higher Mach number showed that the second Mack mode instability is damped by localised wall cooling. To find the optimal location of a wall heating device, DNS simulations of hypersonic flows were carried out. Fedorov et al. [51] showed that the region upstream of the neutral point is optimal to place a heating device in order to stabilise the second Mack mode but Soudakov et al. [181] underlined that this location depends on the receptivity region for a sharp cone at Mach 6. Recent studies [6, 200] found that cooling upstream of the synchronisation point and heating downstream damp the second Mack mode. Furthermore, localised strips of wall cooling and heating combinations are nearly as effective as controlling the whole boundary [6]. On a Mach 6 cone, Oz et al. [134] showed using local stability analysis that uniform wall cooling over the entire surface destabilises the boundary layer but a local wall cooling strip upstream of the synchronisation point damped the instabilities and conversely if located downstream.

1.1.3.3 Optimal location for control actuators

The previous studies presented in both sections above were based on parametric analyses which cannot span the full range of optimal locations. General approaches using gradient-based optimisation have been proposed thereafter. They rely on the adjoint-based linear sensitivity of the base-flow, i.e. the indicator of the regions where small modifications of the base-flow have the highest impact on the growth of instabilities.

An adjoint method to find the optimum suction distribution on a Blasius boundary layer through the minimisation of N-factor was explored by Balakumar and Hall [4]. Parabolised

stability equations and their adjoint equations were later solved to perform sensitivity analysis of compressible flows [145]. Sensitivity was later exploited to iteratively decrease the energy of the Tollmien-Schlichting (T-S) waves [193] through wall transpiration or to damp the T-S waves, streaks and oblique waves [146] via steady suction. At the same period, Airiau et al. [1] developed a similar framework and extended the analysis to suction panels of finite length. While previous methods computed the optimal suction control to damp a fixed disturbance, Zuccher et al. [203] offered a "robust" control which damps the most disrupting instability for the controlled flow. The extension of the sensitivity analysis of steady blowing to the global analysis framework was later given by Brandt et al. [17] for an incompressible boundary layer. Sensitivity of the global eigenvalue problem has also been computed for shape optimisation. Iterative methods [114, 196] have been employed to optimise the geometry in order to gradually damp the growth rate of the most unstable mode. However, these techniques require to repeat expensive computations of base-flow, stability and sensitivity as they are valid only in the linear regime. Boujo [15] offered a second-order sensitivity method to extend the validity of the linear sensitivity and therefore reduce the total number of iterations to optimise a geometry.

Apart from the adjoint-based methods, Jahanbakhshi and Zaki [78] applied an ensemble-variational approach (data-driven method) to compute the optimal wall heat-flux control to delay transition. Alternation of almost spanwise-homogeneous cooling and heating strips upstream the synchronisation point efficiently damps the first and second Mack modes (Figure 1.7).

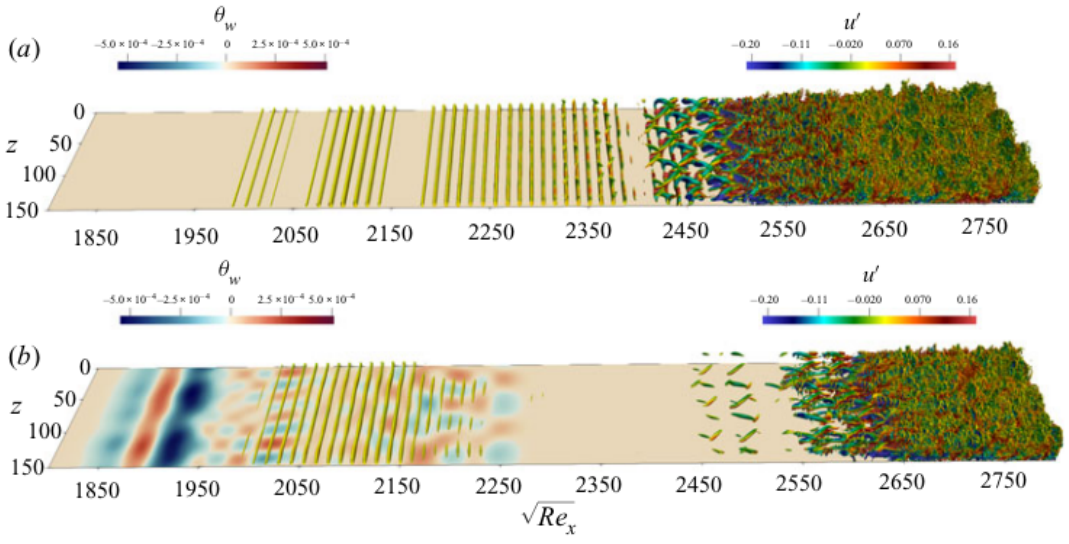

Figure 1.7: Optimal wall heat-flux θ_w from Jahanbakhshi and Zaki [78] to delay the transition induced by the non-linear interactions of first and second Mack modes [77]. (a) Flow structures without control. (b) Flow structures with heat-flux control.

1.2 Methods for dynamical system analysis

Laminar to turbulent transition is a bifurcation from a stable state (laminar flow) to another state (turbulent flow) through unstable transient mechanisms (described in the previous section). Therefore, this problem may be viewed as a dynamical system. The accurate simulation of high-speed aerodynamics requires non-linear discretisation schemes. Hence, once the governing equations are spatially discretised, the flow-state $\mathbf{q}$ is high-dimensional and the residual

$\mathbf{R}(\mathbf{q})$, such that

$$d\mathbf{q}/dt = \mathbf{R}(\mathbf{q}, \boldsymbol{\delta}), \tag{1.1}$$

is strongly non-linear. We have here made explicit the dependence of the dynamics with respect to an external control parameter $\boldsymbol{\delta}$, which can be for example the Reynolds or Mach numbers. Within the framework of dynamical systems, analysing the system consists in determining, as a function of the parameter $\boldsymbol{\delta}$, all fixed-points, periodic orbits, and their respective stability properties to establish bifurcation diagrams. The sensitivity and control of such systems, for example understanding how a weak forcing (uncertainty) or open/closed-loop control affects these bifurcation diagram, are crucial for optimisation. The accurate evaluation of the $N^{th}-$order derivative of the residual $\mathbf{R}(\mathbf{q})$ steps in as a key-enabler to deal with the points mentioned above (see Figure 1.8 for overview). The different dynamical system tools applied to fluid mechanics are described in the subsequent sections.

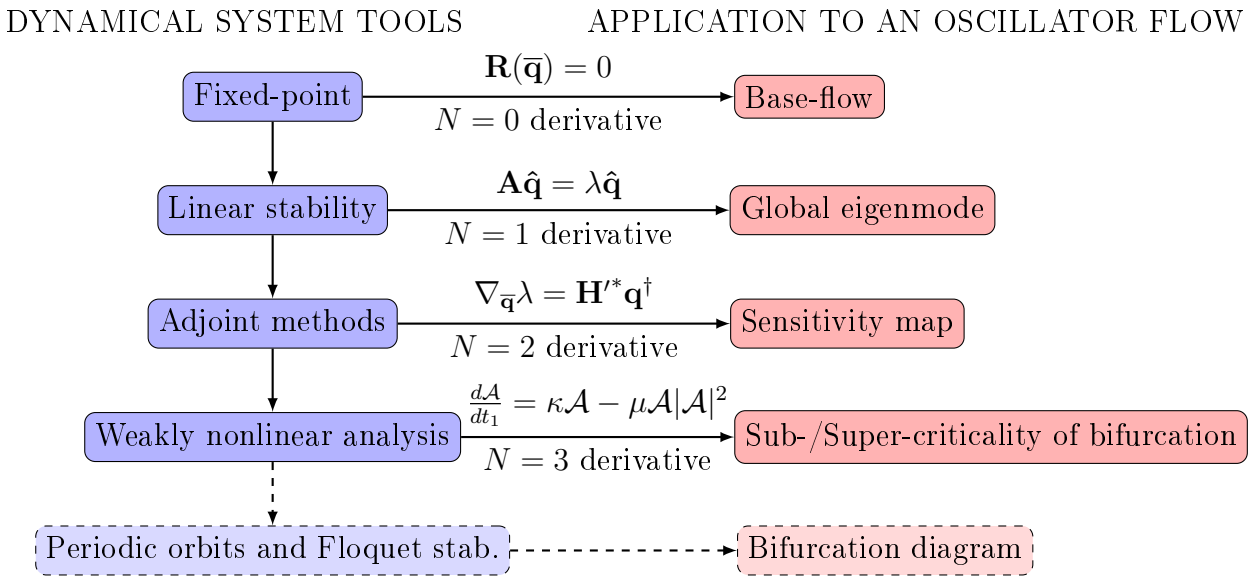

Figure 1.8: Dynamical system analysis and its application to an oscillator flow (flow around a cylinder for instance).

1.2.1 Base-flow

The base-flow, written $\overline{\mathbf{q}}$ for steady simulations or $\mathbf{q_b}$ for unsteady ones, corresponds to a fixed-point of the zeroth order $N = 0$ derivative of the residual:

$$\mathbf{R}(\overline{\mathbf{q}}) = 0. \tag{1.2}$$

Several methods are available to determine such points: global (explicit or implicit) time-stepping methods, local implicit time-stepping methods [80] or Newton-Raphson algorithms [37] are most common. Many of these are based on the solution of a linear system involving the first-order $N = 1$ derivative of the residual, the Jacobian matrix $\mathbf{A} = \partial\mathbf{R}/\partial\mathbf{q}$. Disturbances $\mathbf{q}'$ around the base-flow are computed through (non-)linear stability analysis.

1.2.2 Linear stability

Linear stability theories predict the early stages of the amplification before the non-linear interactions play a leading role resulting in the breakdown towards laminar to turbulent transition. Boundary layer flows can be studied by local stability analysis (LST) [109] and parabolised

stability equations (PSE) [182] for weakly non-parallel flows. For more general configurations, global stability or resolvent analyses, the latter taking into account the non-modal phenomena arising from the non-normality of the Navier-Stokes operator [178], have become computationally affordable in the recent years. They involve the computation of the first-order $N = 1$ derivative of the residual.

1.2.2.1 Linear local stability analysis

Linear local stability theory (LST) is valid only on parallel flows in the streamwise direction. However, it has often been applied with success to boundary layers where the flow is weakly non-parallel (different time/space scales between the disturbances and the base-flow variations in the streamwise direction). Under this assumption, the eigenmode $\hat{\mathbf{q}}$ is independent of x and an ansatz of the fluctuations is made of the form

$$\mathbf{q}' = \hat{\mathbf{q}}(y) e^{i(\alpha x - \omega t + \beta z)}. \tag{1.3}$$

For the spatial LST [167], the frequency ω is set real ($\omega = \omega_r$) and the streamwise wavenumber α is complex ($\alpha = \alpha_r + i\alpha_i$) while β is the spanwise wavenumber. Linearising the Navier-Stokes equations and injecting the ansatz (1.3) leads to a dispersion relation between α, ω, Re_x and M. Fixing the three latter parameters, the dispersion relation gives the complex value of α. Depending on the sign of α_i, the disturbances exponentially decay ($\alpha_i > 0$) or grow ($\alpha_i < 0$) in the streamwise direction. The phase velocity c of the disturbances is defined as

$$c = c_r + ic_i = \frac{\omega}{\alpha} = \frac{\omega_r \alpha_r}{|\alpha|^2} - i\frac{\omega_r \alpha_i}{|\alpha|^2}. \tag{1.4}$$

The LST computations of the streamwise wavenumber α and the eigenmode $\hat{\mathbf{q}}$ are repeated along x for different density/velocity/temperature profiles which may be extracted from self-similar theory, asymptotic analysis or Direct Numerical Simulations (DNS). The LST has been widely applied to the hypersonic boundary layer to reveal its intrinsic instabilities [105, 106, 150] and their dependency to wall temperature [108, 118, 134].

1.2.2.2 Parabolised stability equations

The linear parabolised stability equations (PSE) [29, 71] relax the parallel approximation to slowly varying flows. The dependency of the disturbance in the streamwise direction is split into two parts. It is assumed that the eigenmode $\hat{\mathbf{q}}$ slowly varies in x such that its second derivative in x disappears in the equations while the streamwise modulation and growth are taken into account by the exponential term $\alpha(x)$. The ansatz becomes

$$\mathbf{q}' = \hat{\mathbf{q}}(x, y) e^{i(\int_{x_0}^{x} \alpha(\xi)\, d\xi - \omega t + \beta z)}. \tag{1.5}$$

The PSE are solved by marching procedure, the initial solution at x_0 being computed by LST. Furthermore, an additional condition allows deriving iteratively the complex streamwise wavenumber α. However, Li and Malik [100] pointed out that, without further flow assumptions, the step-size must be larger than the inverse of the real part of α for solver stability, preventing then high spatial resolution. PSE has enabled for instance to study supersonic boundary layers disturbed by roughness elements [42].

1.2.2.3 One-Way Navier-Stokes equations

Towne et al. [187] highlighted that some ill-posed regularisation techniques of the PSE limit the validity of the method as acoustic waves travelling downstream are strongly damped. They

offered another form of parabolisation with the One-Way Navier-Stokes (OWNS) equations [186] which isolate upstream and downstream travelling waves in order to filter out the former. The equations are solved in a characteristic form where an eigenvalue decomposition of the linear operator is performed. An approximate projection operator is then derived to solve only the associated downstream travelling disturbances. For instance, OWNS equations have been applied to study the convective instabilities of the hypersonic boundary layer [87].

1.2.2.4 Linear global stability analysis

To study any two-dimensional flow configuration, global stability analysis removes all assumptions in the streamwise direction. The ansatz becomes

$$\mathbf{q}' = \hat{\mathbf{q}}(x, y)e^{\lambda t + i\beta z}, \tag{1.6}$$

with the complex $\lambda = \sigma + i\omega$. This form means that the streamwise direction must be discretised as well. The rise of the computational resources has made the global stability analysis affordable for academic configurations. The discrete linearised operator i.e. the Jacobian matrix $\mathbf{A}$ is built and its asymptotic stability [74] is evaluated by looking at the most unstable eigenvalues of $\mathbf{A}$ [75]:

$$\mathbf{A}\hat{\mathbf{q}} = \lambda\hat{\mathbf{q}}. \tag{1.7}$$

Globally unstable flows (at least one global mode exhibits $\sigma = \Re(\lambda) > 0$) correspond to oscillator flows while the globally-stable base-flows ($\Re(\lambda) < 0$ for all global modes $\hat{\mathbf{q}}$) exhibiting strong pseudo-resonances are noise-amplifiers, which are studied through resolvent analysis [189] according to Huerre *et al.* [74]. Attached boundary layers are noise-amplifiers while, for instance, flows around bluff bodies (cylinder [48]) or shock-wave / supersonic boundary layer interactions [157] are oscillator flows.

1.2.2.5 Non-modal growth

So far, the linear local and global methods described in the previous sections focused on modal stability i.e. the amplification of instabilities at an asymptotic time horizon. However, transient growth may occur within a finite time [166]. The linear analysis relies on an initial value problem where the maximum amplification $G(t)$ is defined as

$$G(t) = \max_{\hat{\mathbf{q}}(0)} \frac{\|\hat{\mathbf{q}}(t)\|^2}{\|\hat{\mathbf{q}}(0)\|^2} = \|e^{t\mathbf{A}}\|^2. \tag{1.8}$$

As the eigenvectors of the Jacobian are not orthogonal (non-normality of the operator), $G(t)$ cannot be approximated as the growth of the leading eigenvalue of $\mathbf{A}$ for a finite time t. Therefore, the amplification $G(t)$ must be computed through a complete eigenvalue decomposition. Hanifi et al. [67] applied non-modal growth analysis on a compressible boundary layer to highlight the lift-up mechanism generating the streaks. They also showed how the growth of the oblique mode is strengthened by non-modal mechanisms.

1.2.2.6 Resolvent analysis

In the global stability analysis, if the real part of the eigenvalue λ is positive, then the fixed point is unstable at large times. For stable configurations, pseudo-resonance properties [178, 189], including the non-modal effects, associated to $\mathbf{A}$ are assessed by looking, for a given frequency ω, at the largest eigenvalues μ^2, called optimal gains, of the Hermitian matrix:

$$\mathcal{R}\mathcal{R}^*\check{\mathbf{q}} = \mu^2\check{\mathbf{q}}, \tag{1.9}$$

where $\mathcal{R} = (i\omega\mathbf{I} - \mathbf{A})^{-1}$ is the resolvent operator and the matrix $\mathcal{R}^* = (-i\omega\mathbf{I} - \mathbf{A}^*)^{-1}$ may be evaluated either from the adjoint discrete operator or with the conjugate transpose of $\mathcal{R}$. This is equivalent to perform the singular value decomposition (SVD) of the resolvent operator. The right and left singular vectors of the SVD correspond to the optimal forcing $\check{\mathbf{f}}$ (the flow is the most receptive to these disturbances) and response $\check{\mathbf{q}}$ (generated by the optimal forcing). Bugeat et al. [20] performed resolvent analysis to underline both the modal (Mack modes) and non-modal (streaks) instabilities in the hypersonic boundary layer. Towne et al. [188] also offered an alternative efficient resolvent analysis through OWNS. Otherwise, Martini et al. [115] suggested another resolvent approach based on a time-stepping method to compute simultaneously the optimal gains associated with several frequencies. The adjoint matrix $\mathbf{A}^*$ is also a key-ingredient for gradient-based optimisation [63] and sensitivity studies [122].

1.2.3 Linear sensitivity

The sensitivity of the instabilities predicted by any linear stability methods may then be derived. To compute it, higher-order derivatives such as the second order derivative operator $N = 2$ (called Hessian and written $\mathbf{H} = \partial^2\mathbf{R}/\partial\mathbf{q}^2$) and adjoint operators are required. They allow the performance evaluation of open-loop control strategies [59, 112, 124]. These approaches rely on the linear structural sensitivity, i.e. region of the flow the most sensitive, of an unstable eigenvalue λ (oscillator flow [112]) or of an optimal gain μ^2 (noise-amplifier flow [17]) to perturbations of the base-flow, to the introduction of small-amplitude steady forcings [123] or to geometry modifications [114], which may provide qualitative control maps.

1.2.4 Weakly non-linear analysis

Weakly non-linear analyses extend the validity of linear analysis above the critical parameter $\boldsymbol{\delta} > \boldsymbol{\delta_c}$ in order to describe the transient process leading to the secondary mechanisms for instance [48].

According to Sipp and Lebedev [177], for incompressible oscillator flows, the second $N = 2$ derivative ($N = 3$ derivative for compressible flows) allows to evaluate the coefficient of the cubic non-linear term in the Stuart-Landau amplitude equation that governs the behaviour of the instability in the vicinity of the critical parameter $\boldsymbol{\delta} \approx \boldsymbol{\delta_c}$. Hence, it determines whether a bifurcation is sub- or super-critical [34], which is of major importance for the determination of the flight-envelope of an aircraft [38, 130].

For incompressible noise-amplifiers, Ducimetière et al. [46] developed a weakly non-linear analysis for non-normal operators. An amplitude equation is derived for a small parameter based on the inverse of the optimal gain $\epsilon \sim 1/\mu^2$. Within this framework, the response for the given optimal forcing as well as the transient growth are well predicted in comparison with DNS at a much lower computational cost.

1.2.5 Non-linear analysis

Eventually, the subsequent steps of the laminar to turbulent transition have to be studied through non-linear analysis. To reveal the secondary mechanisms, the linear methods were extended such as non-linear PSE (NPSE) [85, 110] and non-linear OWNS [180]. At high forcing amplitude, Time Spectral Methods (TSM) are required to converge the finite amplitude non-linear interactions where non-linear PSE fails [170]. Global stability analysis were also expanded through harmonic-balanced methods (HBM) for oscillator [176] and noise-amplifier [155] flows. The computation of the secondary periodic orbits [61] and the assessment of their stability

can be performed by non-linear HBM or TSM methods [27, 170] and Floquet or Hill-Floquet stability analyses [185]. Time-stepping (or matrix-free) methods [32, 56] are another approach to perform linear and non-linear analysis. Finally, the prediction of the complete breakdown to turbulence, the intermittency and the fully turbulent flow is solved by DNS.

1.2.6 Continuous and discrete frameworks

Most of the stability methods introduced rely on the construction of the linearised operators. First and second-order derivative operators are tractable in a continuous framework in the case of simple governing equations and simple spatial discretisation scheme such as the incompressible Navier-Stokes equations at moderate Reynolds number with Taylor-Hood finite elements without stabilisation [112]. There, all the equations are first derived in a continuous form (direct first-order, adjoint, second-order derivatives) and then discretised. Specific numerical methods and analysis are required at each step to discretise the resulting equations. For instance, FreeFem++ [69] and FEniCS [102] can be used to obtain spatial discretisations of any partial-differential equation from its weak form. However, the continuous framework becomes difficult to implement for systems driven by more complex PDE or more complex spatial discretisations, e.g. high-order discretised finite-volume compressible Navier-Stokes equations for advection dominated flows. For example, the continuous linearised and adjoint operators need special treatment in presence of shock waves [60] and the continuous adjoint only gives an approximation to the continuous gradient for a discrete objective function [140]. Conversely, in a discrete framework, the Jacobian and adjoint matrices are computed from the already discretised (and well-behaved) residual and exhibit the same level of accuracy [41]: the discrete method consists in discretising the governing equations and boundary conditions with a given spatial scheme and then computing the linearised and adjoint operators on these discretised set of equations. For instance, SU2 [136] and elsA [25] codes are built within this framework. The present work is built upon the discrete framework.

1.3 Governing equations of fluid dynamics

We consider the compressible Navier-Stokes equations written in conservative form

$$\frac{\partial \mathbf{q}}{\partial t} + \nabla \cdot \mathbf{F}(\mathbf{q}) = 0, \tag{1.10}$$

with $\mathbf{q} = (\rho, \rho\mathbf{v}, \rho E)$ denoting respectively the density, momentum and total energy of the fluid and $\mathbf{F}(\mathbf{q})$ the associated fluxes. In expanded form, the Navier-Stokes equations read

$$\frac{\partial \rho}{\partial t} + \nabla \cdot (\rho\mathbf{v}) = 0, \tag{1.11}$$

$$\frac{\partial (\rho\mathbf{v})}{\partial t} + \nabla \cdot (\rho\mathbf{v}\mathbf{v} + p\mathbf{I} - \boldsymbol{\tau}) = 0, \tag{1.12}$$

$$\frac{\partial (\rho E)}{\partial t} + \nabla \cdot ((\rho E + p)\mathbf{v} - \boldsymbol{\tau} \cdot \mathbf{v} - \lambda \nabla T) = 0, \tag{1.13}$$

with $E = p/(\rho(\gamma - 1)) + \frac{1}{2}\mathbf{v} \cdot \mathbf{v}$, $\boldsymbol{\tau} = \eta(\nabla\mathbf{v} + (\nabla\mathbf{v})^T) - \frac{2}{3}\eta(\nabla \cdot \mathbf{v})\mathbf{I}$, $\mathbf{I}$ the identity matrix, $\lambda = \eta c_p/Pr$, c_p the isobaric heat capacity and P_r the Prandtl number ($P_r = 0.72$). To close the system, two more equations are required. First, one assumes a homogeneous, thermally and calorically perfect gas. The perfect gas law is

$$p = \rho r T, \tag{1.14}$$

with $r = 287.1$ J.kg^{-1}.K^{-1} the specific gas constant. Then, the Sutherland's law is selected to link the viscosity η to the temperature [183],

$$\eta(T) = \eta_{ref} \left(\frac{T}{T_{ref}} \right)^{3/2} \frac{T_{ref} + S}{T + S}, \tag{1.15}$$

with $S = 110.4$ K the Sutherland's temperature, $\eta_{ref} = 1.716 \times 10^{-5}$ kg.m^{-1}.s^{-1} and $T_{ref} = 273.15$ K.

After spatial discretisation described in §2.1.3, the discrete residual is noted $\mathbf{R}(\mathbf{q}) = -\nabla \cdot \mathbf{F}(\mathbf{q})$.

Chapter outcome summary:

Laminar to turbulent transition in hypersonic boundary layers is generally the consequence of the amplification of linear instabilities (Mack modes) which trigger secondary mechanisms (three-dimensional vortices, streaks,...) that later break down to turbulent spots. In order to control the transition, the consensus has not been reached for the optimal location to apply an open-loop wall heating/cooling actuator despite many studies. The various stability methods and their approximations for fluid mechanics have been presented from linear (local, PSE, OWNS, non-modal, global, resolvent) to non-linear analysis by way of linear sensitivity and weakly non-linear analysis.

Chapter 2

Optimal linear instabilities: numerical methods and applications

Chapter foreword:

This chapter presents a general framework to solve and analyse large-scale discretised dynamical systems, representing conservative boundary value problems, through direct and adjoint derivatives computed with Algorithmic Differentiation. The methodology is developed here for the compressible Navier-Stokes equations discretised with high-order finite volume methods to show how to efficiently and accurately find fixed-points as well as to perform linear global stability and resolvent analysis. It is applied to a low Mach number flow around a circular cylinder and boundary layer flows at various Mach number regime.

2.1 Theory and implementation for linear stability tools

In the following, we will present the program implementation, discretisation schemes and various numerical algorithms implemented in BROADCAST.

2.1.1 BROADCAST

The open-source CFD code BROADCAST, built within the discrete framework, is based on the compressible Navier-Stokes equations. It extracts the exact N-order derivatives by Algorithmic Differentiation (AD) through the TAPENADE [68] software. The spatial discretisation scheme relies on a high-order shock-capturing numerical scheme for compressible flow simulations [171]. As a toolbox oriented towards simple test case applications such as two-dimensional or axi-symmetrical configurations, BROADCAST is currently restricted to 2D curvilinear structured meshes and runs as a sequential code. Nonetheless, after the full state derivative operators have been extracted by BROADCAST, the Newton solver and stability tools, using PETSc [5], may distribute the operators on multi-cores with MPI and OpenMP [23, 96]. Even if the base-flow is assumed two-dimensional, linear 3D perturbations are addressed on the same 2D domain by considering spanwise periodic perturbations of a given period, as done for example in Bugeat et al. [20]. This extends the stability analyses to harmonic 3D linear disturbances at a slightly larger but affordable computational cost. The extension to linear 3D perturbations implemented in BROADCAST follows Bugeat et al. [20], however, the linearisations are here performed by AD and not by a finite difference method.

The BROADCAST code has been developed to complement other open-source CFD codes already used for stability. As the incompressible code Semtex [12], it solves two-dimensional problems with a Fourier expansion in the transverse direction but for compressible flows. As SU2 [136], it generates discrete derivative and adjoint operators through AD but BROADCAST uses Source-Transformation AD (ST-AD) instead of Operator-Overloading AD (OO-AD) for SU2, ST-AD being faster to compute the adjoint [120]. BROADCAST has a high-order finite volume numerical scheme which reaches high accuracy at the cell centre for steady solutions. To obtain high-order accurate unsteady solutions everywhere in the grid, additional flux reconstruction terms [192] or Discontinuous Galerkin methods such as in the spectral solver Nektar++ [26] must be implemented. BROADCAST has not been designed to perform heavy three-dimensional time-stepping Direct Numerical Simulations (DNS) but rather as a self-contained code performing dynamical system analysis of simple compressible fluids, as presented in Figure 1.8.

The code BROADCAST is available at https://github.com/onera/Broadcast.

2.1.2 Program implementation

As a development-oriented tool, one of the objective of BROADCAST is fast and easy modifications to plug different numerical models or methods. This leads the programming language choice to sub-routines written in Fortran (version 90) for computational efficiency called by main programs written in Python for components modularity and to ease new developments. This functional approach, which is at the opposite of a black-box code, has however the drawback not to offer a friendly user-interface. The organisation of the code and a short description of the program files are given in Figure 2.1 and Table 2.1.

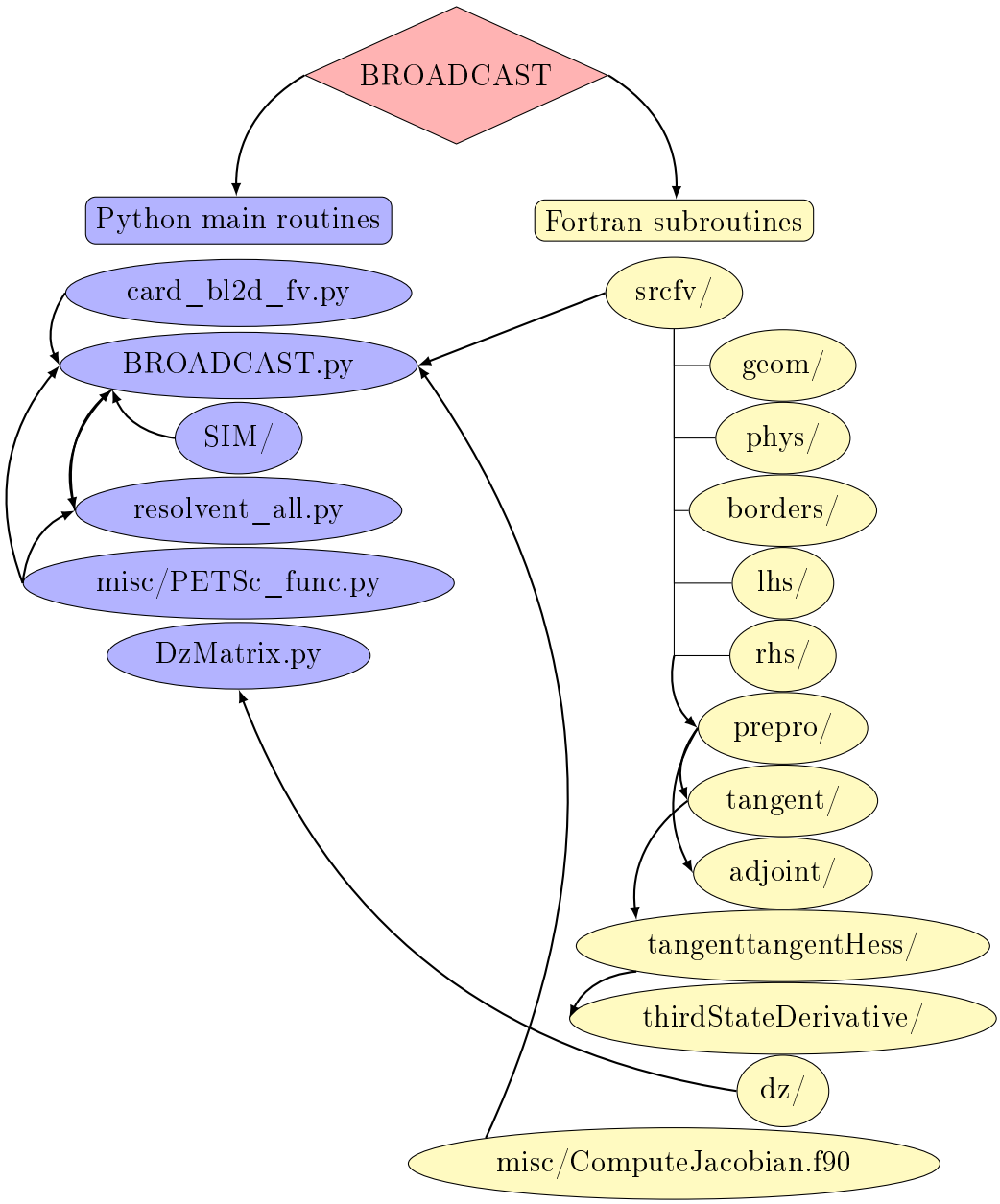

Figure 2.1: Organisation of BROADCAST code. Description of the programs in Table 2.1.

PYTHON PROGRAMS	
card_bl2d_fv.py	Card to run BROADCAST (Num. parameters, options...)
BROADCAST.py	Main program (mesh, init., dim. choice, BC location...)
SIM/	Folder including self-similar profile generator
resolvent_all.py	Main functions to perform 2D resolvent analysis
resolvent_all3D_1block.py	Likewise for 3D resolvent
misc/PETSc_func.py	All the useful PETSc functions
DzMatrix.py	Compute the spanwise contributions of the Jacobian
biglobal_cyl.py	2D/3D global stability analysis for cylinder
Hessian_cyl.py	Compute the Hessian operator applied to a given mode
FORTRAN PROGRAMS	
geom/	Metrics computation
phys/	Primitives and viscosity computations
borders/	Boundary conditions
lhs/	Basic matrix-free inversion for time-stepping method
rhs/	Spatial numerical scheme for residual computation
prepro/	Preprocessed files for AD
tangent/	Linearised files computed by AD
adjoint/	Linearised files computed by AD in backward mode
tangenttangentHess/	Twice linearised files computed by AD
thirdStateDerivative/	Third time linearised files computed by AD
dz/	Spanwise contributions of the Jacobian operator
misc/ComputeJacobian.f90	Functions to construct the Jacobian

Table 2.1: Main program files description (not exhaustive).

2.1.3 Spatial Discretisation

The finite volume framework, the associated convective and viscous flux and the implementation of the boundary conditions are presented below.

2.1.3.1 Finite volumes

In order to work within the finite volume framework, the conservative equation (1.10) is written in its weak formulation:

$$\int_\Omega \frac{\partial \mathbf{q}}{\partial t}\, d\Omega + \int_\Omega \nabla \cdot \mathbf{F}(\mathbf{q})\, d\Omega = 0, \tag{2.1}$$

which becomes using the Green-Ostrogradski theorem

$$\int_\Omega \frac{\partial \mathbf{q}}{\partial t}\, d\Omega + \int_\Gamma \mathbf{F}(\mathbf{q}) \cdot n\, d\Gamma = 0, \tag{2.2}$$

with Ω the domain volume, Γ the boundaries and n the outer normal.

The equation (2.2) is discretised and applied to each cell volume $\Omega_{i,j}$ and its edges $\partial\Omega_{i,j}$ (considering 2D meshes):

$$|\Omega_{i,j}| \frac{\mathrm{d}\mathbf{q}_{i,j}}{\mathrm{d}t} + \sum_{\Gamma \in \partial\Omega_{i,j}} |\Gamma|\, \mathbf{h}_\Gamma(\mathbf{q}, n) = 0, \tag{2.3}$$

with $\mathbf{h}_\Gamma$ the flux through the edge Γ, $|\Omega_{i,j}|$ the cell volume and $|\Gamma|$ the edge area. Here the term $\mathbf{q}_{i,j}$ can represent either the average value in the cell or the cell-centred value. Both values are identical up to a second order accuracy [119],

$$\mathbf{q}_{i,j} = \frac{1}{|\Omega_{i,j}|} \int_{\Omega_{i,j}} \mathbf{q}\, d\Omega_{i,j} = \mathbf{q}(x_{C_{i,j}}) + O(h^2), \tag{2.4}$$

with $x_{C_{i,j}}$ the cell centre. Equation (2.3) is therefore 2nd order accurate. Then the approximation method used to compute Eq. (2.3) in BROADCAST relies on an extension of the finite difference framework. The time-derivative component is approximated by its cell-centred value and the flux is derived from a high order finite difference scheme. As shown in Eq. (2.4), this method is strictly at most of order 2 in the finite volume sense, however, Rezgui et al. [154] showed that a high order accuracy in the finite difference sense is reached on Cartesian and smoothly deformed (curvilinear) meshes. It was further pointed out by van Leer and Nishikawa [192] that such hybrid (Finite Difference/Finite Volume) schemes reach high-order accuracy when volume integration does not appear in the equations which is the case for steady solutions.

Equation (2.3) is finally recast into

$$\frac{\mathrm{d}\mathbf{q}}{\mathrm{d}t} = \mathbf{R}(\mathbf{q}), \tag{2.5}$$

with $\mathbf{R}$ as the nonlinear residual defined as the sum of the fluxes through the edges of a cell divided by its volume. The fluxes $\mathbf{F}$ are split into two components, inviscid and viscous.

2.1.3.2 Convective flux

The space discretisation for the inviscid flux follows the FE-MUSCL (Flux-Extrapolated-MUSCL) scheme [36]. This is a high order accurate upwind scheme resulting from an upwind recursive correction to the leading truncation error term of a centred second order scheme [98,

99]. It is equivalent to a MUSCL scheme constructed with a N-order extrapolation to the fluxes. This high-order convective scheme has been assessed by Sciacovelli et al. [171] showing excellent results in accuracy and shock capturing features in hypersonic flow simulations. Thanks to its definition, the FE-MUSCL scheme can be readily extended to various orders. In BROADCAST, numerical scheme orders from 3rd to 9th are implemented. The order of accuracy of this high-order finite difference scheme applied in finite volume framework has been assessed in Petropoulos et al. [141] (see Figure 6.(a) in the cited paper). A further description of the FE-MUSCL scheme and its implementation are detailed below.

In 1D, from Sciacovelli et al. [171], assuming a regular grid spacing h, from Eq. (2.3), the discrete scheme for inviscid flow is written for the cell index i:

$$\frac{\mathrm{d}\mathbf{q}_i}{\mathrm{d}t} + \frac{(\boldsymbol{\delta}\mathbf{F})_i}{h} = 0, \tag{2.6}$$

with $\boldsymbol{\delta}$ the difference operator between two cells: $\boldsymbol{\delta}(\cdot)_{i+\frac{1}{2}} = (\cdot)_{i+1} - (\cdot)_i$ and $\mathbf{F}_{i+\frac{1}{2}}$ the inviscid numerical flux at cell interface $i+\frac{1}{2}$. For a ninth-order scheme, this flux is written

$$\mathbf{F}_{i+\frac{1}{2}} = \left(\left(\mathbf{I} - \frac{1}{6}\boldsymbol{\delta}^2 + \frac{1}{30}\boldsymbol{\delta}^4 - \frac{1}{140}\boldsymbol{\delta}^6 + \frac{1}{630}\boldsymbol{\delta}^8\right)\boldsymbol{\mu}\mathbf{f} - \mathbf{D}\right)_{i+\frac{1}{2}}, \tag{2.7}$$

with $\mathbf{f}$ the physical flux, $\boldsymbol{\mu}$ the cell average operator: $\boldsymbol{\mu}(\cdot)_{i+\frac{1}{2}} = \frac{1}{2}\left((\cdot)_{i+1} + (\cdot)_i\right)$ and $\mathbf{D}$ the numerical dissipation term.

The third order scheme is for instance constructed keeping only the first two terms in the brackets. As flow discontinuities are inherent in compressible flows, dissipation is required and written as a non-linear artificial viscosity term associated with the spectral radius of the inviscid flux $\lambda_{i+\frac{1}{2}}$. Then, the dissipation coefficient $D_{i+\frac{1}{2}}$ is written

$$\mathbf{D}_{i+\frac{1}{2}} = \lambda_{i+\frac{1}{2}}\left(\epsilon_2\boldsymbol{\delta}\mathbf{q} + \epsilon_4\boldsymbol{\delta}^9\mathbf{q}\right)_{i+\frac{1}{2}}, \tag{2.8}$$

with $\epsilon_{2_{i+\frac{1}{2}}} = \kappa_2 \max\left(\phi_i, \phi_{i+1}\right)$ and $\epsilon_{4_{i+\frac{1}{2}}} = \max\left(0, \kappa_4 - \epsilon_{2_{i+\frac{1}{2}}}\right)$. The dissipation coefficients range respectively $0 \leq \kappa_2 \leq 1$ and $\kappa_4 = \frac{1}{1260}$ as the next leading coefficient in the Taylor expansion (Eq. (2.7)). A shock sensor ϕ_i is used and its expression is

$$\phi_i = \frac{1}{2}\left(1 - \tanh\left(2.5 + 10\frac{\delta x}{c}\nabla\cdot\mathbf{v}\right)\right) \times \frac{(\nabla\cdot\mathbf{v})^2}{(\nabla\cdot\mathbf{v})^2 + |\nabla\times\mathbf{v}|^2 + \epsilon} \times \left|\frac{p_{i+1} - 2p_i + p_{i-1}}{p_{i+1} + 2p_i + p_{i-1}}\right|, \tag{2.9}$$

with c the local sound velocity, δx the local horizontal cell size, ϵ a small fixed parameter to avoid a division by zero and p_i the local pressure. In Eq. (2.9), the last term is the pressure based shock sensor of Jameson [81] and the second term is the discrete form of Ducros' vortex sensor which measures the ratio between the local divergence of velocity and the velocity rotational [47]. The first term is the sensor modification offered by Bhagatwala and Lele [11] which is switched on only in region of negative dilatation. These three sensors are put in series so that they bypass each other in order to reduce the magnitude of the low-order dissipation. The sensor ϕ is then activated in region of strong divergence of velocity typically around shocks so that the flow discontinuities are well-captured by locally decreasing the scheme accuracy to 2nd order. In vortex regions, the sensor tends to zero and the dissipation is driven by the high-order term associated with κ_4 which damps high-frequency oscillations while minimising the level of numerical dissipation.

The stencil of this scheme needs (order+1)/2 cells in each direction to compute the inviscid flux. For instance, in 1D, the ninth order scheme requires 5 cells at the left and 5 cells at

the right of the current cell. Close to the computational domain boundaries, the appropriate number of ghost cells is added to the mesh. This treatment is applied for the porous boundary conditions such as inflow, outflow and extrapolation. However, for wall boundaries, another strategy is followed as offered in Cinnella and Content [36]. The physical flux is imposed at the first mesh interface (first cell layer) and high-order off-centred schemes are used to compute the flux in the next cell layers (from the second to the fifth cell layer for a ninth order scheme). The same order of accuracy is thus preserved everywhere, whether the flux is computed fully inside the domain, using ghost cells or close to a wall boundary condition.

2.1.3.3 Viscous flux

The viscous fluxes are computed on a five-point compact stencil inside the domain (fourth order accurate) and on a three-point compact scheme near the solid boundaries (second order accurate) in order to get only one layer of ghost cells at a wall interface. The five-point compact scheme was first suggested by Zingg et al. [202] but this conservative scheme was not fourth-order accurate for all the second order derivative viscous terms. The viscous flux discretisation implemented in BROADCAST is the one offered by Shen et al. [174] which computed new coefficients to reach fourth order accuracy for all derivative terms. These coefficients are modified to move from a cell-centred definition to a face location one.

2.1.3.4 Boundary conditions and ghost cells

Boundary conditions are enforced with layers of ghost cells around the domain. The number of layers depends on the order of the numerical scheme and is equal to (order+1)/2. The residual $\mathbf{R}$ is therefore computed from the "augmented" state vector $\mathbf{q}_{large} = \mathbf{q} + \mathbf{q}_{\text{ghost}}$ and returns a vector $\mathbf{R}(\mathbf{q}_{large})$ of the size of the initial state vector $\mathbf{q}$.

Solid boundary conditions such as walls fill ghost cells from the information inside the domain to force zero velocity or no flux exchange at the boundary for instance. The detailed implementation of the wall boundary conditions is given in appendix A. Permeable boundary conditions fill ghost cells with information either from inside the domain or the external user-fixed state depending on the direction given by the characteristic relations [143]. For example, Dirichlet boundary condition is prescribed when all characteristics are ingoing (supersonic inlet). Conversely, an extrapolation is made when all characteristics are outgoing (supersonic outlet).

2.1.4 Time-stepping

BROADCAST includes time-stepping methods to compute base-flow. An explicit low-storage Runge-Kutta [13] and an implicit LU-SGS in which we use an approximated Jacobian [199] are available. However, in this work, any base-flow is computed by a Newton algorithm described in the following section. The time-steppers can then be used to get an initial guess.

2.1.5 Base-flow

To find a fixed-point $\overline{\mathbf{q}}$ satisfying Eq. (1.2), different algorithms are possible, whose among them the Newton method. It consists of an iterative method, where from a state $\mathbf{q}^n$, we build $\mathbf{q}^{n+1} = \mathbf{q}^n + \delta\mathbf{q}^n$, with

$$\mathbf{A}(\mathbf{q}^n)\,\delta\mathbf{q}^n = -\mathbf{R}(\mathbf{q}^n), \tag{2.10}$$

where $\mathbf{A}(\mathbf{q}^n) = \left.\frac{\partial \mathbf{R}}{\partial \mathbf{q}}\right|_{\mathbf{q}^n}$ is the Jacobian operator evaluated at $\mathbf{q} = \mathbf{q}^n$. The Newton algorithm must be initialised by a guess. A constant reference state may perform well for simple flows. If it fails, it is better to initialise the algorithm with approximate solutions that have been generated by other numerical simulations or with a time-stepping method. A way to speed up the algorithm consists in keeping the same Jacobian for different Newton iterations (pseudo-Newton method). A criterion is thus required to decide when the Jacobian must be computed again. However, as it requires a further user-parameter to be tuned, we decided not to follow this path and recompute the Jacobian at each iteration.

To ensure convergence regardless of the initial state, a pseudo-transient continuation method (or relaxation method) has been implemented following Crivellini and Bassi [37]:

$$\left(\frac{\mathbf{I}}{\Delta t} + \mathbf{A}(\mathbf{q}^n)\right) \delta\mathbf{q}^n = -\mathbf{R}(\mathbf{q}^n), \tag{2.11}$$

with Δt a pseudo time-step derived from an adaptive CFL number, $CFL = (||\mathbf{v}|| + \sqrt{\gamma p/\rho})\Delta t/\Delta x$, Δx being the local mesh size:

$$CFL_n = \frac{CFL_0}{r_n}, \tag{2.12}$$

$$r_n = \max\left(\frac{\|\mathbf{R}(\mathbf{q}^n)\|_{L^2}}{\|\mathbf{R}(\mathbf{q}^0)\|_{L^2}}, \frac{\|\mathbf{R}(\mathbf{q}^n)\|_{L^\infty}}{\|\mathbf{R}(\mathbf{q}^0)\|_{L^\infty}}\right), \tag{2.13}$$

with $\|\cdot\|_{L^2}$ and $\|\cdot\|_{L^\infty}$ being respectively the L^2 and L^∞ norms [37]. During the first iterations, the term $\mathbf{I}/\Delta t$ in Eq. (2.11) penalizes the norm of $\delta\mathbf{q}$ in the transient phase. Then, from an initial CFL_0, the CFL number increases with the decrease of the residual norm and the additional term disappears so as to recover the Newton algorithm and quadratic convergence properties.

Algorithme 1 Base-flow pseudo-algorithm

Initialisation:
  Geometry and boundaries
  Mesh
  Reference parameters
  State normalisation
Solution initialisation (self-similar or uniform flow)
for $1 \rightarrow M$ **do**
    Update ghost cells with boundary conditions (BC)
    Compute residual $\mathbf{R}(\mathbf{q})$
    Compute residual norm & relaxation coefficient
    Construct Jacobian $\mathbf{A}$ (see Algo. 2)
    Solve linear system $\mathbf{A}\,\delta\mathbf{q} = -\mathbf{R}$ with LU algorithm
    Update state vector $\mathbf{q}$ and check residual convergence
end for
Write state vector & Jacobian.

The pseudo-algorithm to compute the base-flow is described in Algo. 1. Typically, starting from a self-similar solution for a boundary layer, Newton algorithm requires ≈ 10 iterations to converge.

2.1.6 Construction of Jacobian matrix and linear solver

The Jacobian operator construction method is similar to the one offered by Benbaba [8] and Mettot [123], except that the evaluation of the derivative is performed through AD instead of finite-difference. The Jacobian matrix corresponds to the linearised discrete residual and is extracted by successive matrix-vector products and stored in a sparse format.

For the explicit construction of the matrix of dimension n, by choosing the vector $\mathbf{v}$ as a canonical vector, n different matrix-vector products $\mathbf{Av}$ would be required to fill in all the entries $\mathbf{A}_{ij}$ of the Jacobian $\mathbf{A}$. Nevertheless, with a finite-volume discretisation, the Jacobian is sparse and exhibits a block-diagonal shape: the vector $\mathbf{v}$ can be therefore chosen such that different entries of the Jacobian are computed in a single matrix-vector product. This strategy significantly reduces the number of operations. The choice of the vector $\mathbf{v}$ depends only on the stencil of the discretisation scheme, a high-order scheme requiring more matrix-vector products to be performed as its stencil is wider.

Within a discrete framework, the linearisation of the residual can be performed by finite difference methods [124] but the derived operators are approximated up to an ϵ error (ϵ^2 for a second-order finite difference). A finite difference method exploiting a complex-step approximation [18] may also be used to considerably improve the accuracy. However, ϵ is a user-input parameter depending on the normalisation [93] and N further ϵ parameters would be required to compute the N-derivative operators. An alternative method to compute the derivative operators is Algorithmic Differentiation (AD) [62]. A Source-Transformation AD code reads the script lines of the governing equations and generates a new script with the algorithmically computed analytic differentiation of the discretised equations. The Algorithmic Differentiation retains the same approximation error as the residual. Once compiled, the computation time of AD is of the same order of magnitude as a finite difference method while it reaches machine-precision accuracy. Furthermore, it does not depend on any user-input parameter ϵ. The useful feature of the AD method is that successive derivatives can be computed quickly without further parameters so that N-order derivative operators are extracted easily.

In BROADCAST, instead of computing $\mathbf{Av}$ by a finite difference, the linearised residual is computed by Algorithmic Differentiation (AD) [62] through the Source-Transformation AD code *TAPENADE* [68]. This results in faster computation than a high-order finite difference method (which requires the computation of several residuals) while keeping the analytical accuracy. Also, successive derivatives can be computed robustly and accurately (finite differences method would require to adapt several case-dependent ϵ parameters). Another advantage of Algorithmic Differentiation is that it can also run in backward mode, enabling the calculation of the adjoint derivative $\mathbf{A}^*\mathbf{v}$ for any $\mathbf{v}$, while finite difference methods are limited to the calculation of $\mathbf{Av}$.

Algorithme 2 Jacobian extraction pseudo-algorithm

1: **for** $1 \rightarrow p$ **do**
2: Compute a test-vector $\mathbf{v}$
3: Update ghost cells of $\mathbf{v}$ with the linearised BC by AD
4: Compute $\mathbf{Av}$ with the linearised residual by AD
5: Convert $\mathbf{Av}$ to Jacobian entry $\mathbf{A}_{ij}$
6: **end for**
7: **Remove the zero entries computed**
8: **Construct Jacobian A in CSR format.**

The pseudo-algorithm to extract the Jacobian operator is described in Algo. 2. It requires p Matrix-vector products. The scalar p depends on the number of equations (5 for

the compressible Navier-Stokes equations) and the stencil of the discretisation scheme. Here, $p = 5 \times (\text{stencil width})^2$. For the 7th order scheme, $p = 5 \times (9)^2 = 405$. However as the inviscid scheme is not compact, some matrix-vector products computed contain zero entries. Step 7 of the algorithm is then necessary to remove the Jacobian zero entries computed so that the Jacobian in CSR (Compressed Sparse Row) format stores only non-zero entries. The non-zero values of a sparse Jacobian are plotted in Figure 2.2 as an example.

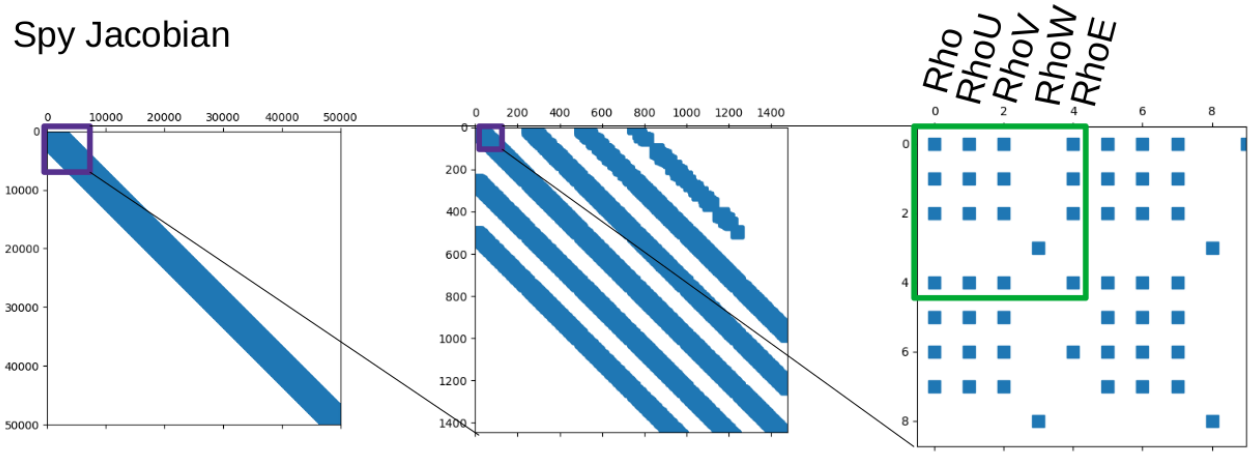

Figure 2.2: Non-zero values of the sparse Jacobian for the 3rd order convective scheme with 50 cells in X and 200 cells in Y. One may notice the off-centred scheme for the first 500 rows corresponding to the two first layers of cells above the wall as described in §2.1.3.2.

All linear systems involving sparse matrices are then solved using the PETSc software interface [5] which includes the direct sparse LU solver from MUMPS [2]. With the BROADCAST code being written in Python language, the petsc4py version is used [39].

2.1.7 Oscillator flows

In the following, the global stability analysis is described for oscillator flows such as cylinder flow.

2.1.7.1 Global modes

The linear global stability of the 2D base-flow $\overline{\mathbf{q}}(x, y)$, which is a solution of the steady compressible Navier-Stokes equations, is assessed by the calculation of the global modes.

Small amplitude perturbations represented by the vector $\mathbf{q}'(t) = e^{\lambda t}\hat{\mathbf{q}}$ are added to the base-flow $\overline{\mathbf{q}}$. Linearising Eq. (1.1), we obtain the eigen-problem in Eq. (1.7). If there exists one eigenvalue λ whose real part is positive, then the base-flow is linearly unstable and either the system should be time-stepped or a weakly non-linear analysis should be performed to determine the final saturated non-linear state.

Here, the largest magnitude eigenvalues and corresponding eigenvectors are calculated with an Arnoldi algorithm. For this, we rewrite eigen-problem (1.7) as

$$(\mathbf{A} - s\mathbf{I})^{-1}\hat{\mathbf{q}} = \frac{1}{\lambda - s}\hat{\mathbf{q}}, \tag{2.14}$$

where s is a shift-parameter to indicate where the eigenvalues should be looked for. Hence, the eigenvalues of $\mathbf{A}$ close to s are also the largest magnitude eigenvalues of $\mathbf{C} = (\mathbf{A} - s\mathbf{I})^{-1}$.

Arnoldi methods rely on the construction of Krylov subspaces, which are obtained by computing recursively matrix-vector products $(\mathbf{Cv}, \mathbf{C^2v}, \ldots, \mathbf{C^pv}, \ldots)$ with $\mathbf{v}$ a Krylov vector.

We use the SLEPc library [158] which implements various Krylov-Schur methods [72] whose Arnoldi algorithm. Computation of the global modes is performed with the steps described in Algo. 3.

Algorithme 3 Global mode pseudo-algorithm

Initialisation:
  Read geometry and state vector
  Read shift s
  Construct Jacobian $\mathbf{A}$ (see Algo. 2)
Definition of the shift-inverted matrix C:
  Construct matrix $s\mathbf{I} - \mathbf{A}$
  Define matrix-vector product $\mathbf{Cv}$ ($\mathbf{C} = (s\mathbf{I} - \mathbf{A})^{-1}$ is never computed)
Solve largest magnitude eigenvalue of Eq. (2.14):
  Arnoldi method
  Store the largest magnitude eigenvalue λ' and its eigenvector $\hat{\mathbf{q}}$
Write eigenvalue $\lambda = \lambda'^{-1} + s$ and global mode $\hat{\mathbf{q}}$.

2.1.7.2 Adjoint global modes

The adjoint operator $\mathbf{A}^*$ gives access to the adjoint modes through Eq. (2.15),

$$\mathbf{A}^*\tilde{\mathbf{q}} = \lambda^*\tilde{\mathbf{q}}. \tag{2.15}$$

As the Jacobian $\mathbf{A}$ is real, the discrete adjoint operator is directly computed by transposition of $\mathbf{A}$. The adjoint mode corresponding to its direct global mode is targeted with the same shift-and-invert method written in Eq. (2.14) replacing $\mathbf{A}$ by $\mathbf{A}^*$ and λ by λ^*.

Furthermore, to associate an adjoint mode $\tilde{\mathbf{q}}$ with its direct mode $\hat{\mathbf{q}}$, a scalar product must be chosen for normalisation. A first choice leads to the L^2 inner product $\langle \mathbf{u}, \mathbf{v} \rangle = \mathbf{u}^*\mathbf{v} = \sum_i u_i v_i$ and then $\langle \tilde{\mathbf{q}}, \hat{\mathbf{q}} \rangle = 1$. However as the direct and adjoint modes generally have a different spatial support (direct mode is located downstream while adjoint mode is upstream), the local mesh size should be taken into account in the inner product. This gives the discrete inner product defined by the matrix $\mathbf{Q}$ in Eq. (2.16).

$$\langle \mathbf{u}, \mathbf{v} \rangle\big|_{\mathbf{Q}} = \mathbf{u}^*\mathbf{Q}\mathbf{v} = \int_\Omega \mathbf{u}^*\mathbf{v}\, d\Omega. \tag{2.16}$$

The adjoint mode $\mathbf{q}^\dagger$ normalised with the discrete inner product given by Eq. (2.16) ($\langle \mathbf{q}^\dagger, \hat{\mathbf{q}} \rangle\big|_{\mathbf{Q}} = 1$) is then $\mathbf{q}^\dagger = \mathbf{Q}^{-1}\tilde{\mathbf{q}}$.

2.1.8 Amplifier flows

Amplifier flows [74] are globally stable but may exhibit local convective instabilities. Instead of considering the eigenvalues of the Jacobian, we focus on the input/output properties of the resolvent operator. Indeed, if all of the eigenvalues λ are stable i.e. all small-amplitude perturbations are exponentially stable in time (globally stable but convectively unstable), then it is relevant to perform a resolvent analysis to study the linear dynamics of the flow and identify its pseudo-resonances.

For this, we transform to frequency-space and consider a small-amplitude forcing field $\mathbf{f}'(t) = e^{i\omega t}\check{\mathbf{f}}$ that is applied to the right-hand-side of Eq. (1.10) and which may be restricted, through a prolongation matrix $\mathbf{P}$, to specific regions of the flow or specific components of the state. $\mathbf{P}$ is a rectangular matrix, containing only zeros and ones, and of size equal to the dimension of the state $\mathbf{q}$ times the dimension of the forcing $\mathbf{f}$. The linear response of the flow $\mathbf{q}'(t) = e^{i\omega t}\check{\mathbf{q}}$ is then governed by $\check{\mathbf{q}} = \mathcal{R}\mathbf{P}\check{\mathbf{f}}$, with $\mathcal{R} = (i\omega\mathbf{I} - \mathbf{A})^{-1}$ denoting the resolvent operator, $\mathbf{A} = \partial\mathbf{R}/\partial\mathbf{q}$ the Jacobian and $\mathbf{I}$ the identity matrix. The resolvent operator corresponds to a transfer function between the input (forcing) and the response (perturbations). The resolvent analysis is often called input-output analysis for this reason. The optimal forcings / responses are then computed by optimising the input-output gain μ^2 between the energy of the response and the energy of the forcing,

$$\mu^2 = \sup_{\check{\mathbf{f}}} \frac{\|\check{\mathbf{q}}\|_q^2}{\|\check{\mathbf{f}}\|_f^2}, \tag{2.17}$$

with $\|\cdot\|_q$ and $\|\cdot\|_f$ the user-selected norms to evaluate the amplitude of the fluctuations and the forcing. These measures are defined with their associated discrete positive Hermitian matrices $\mathbf{Q}_q$ and $\mathbf{Q}_f$,

$$\|\check{\mathbf{q}}\|_q^2 = \check{\mathbf{q}}^*\mathbf{Q}_q\check{\mathbf{q}} \quad , \quad \|\check{\mathbf{f}}\|_f^2 = \check{\mathbf{f}}^*\mathbf{Q}_f\check{\mathbf{f}}, \tag{2.18}$$

where only $\mathbf{Q}_f$ is required to be definite. For compressible flows, a common choice for $\mathbf{Q}_q$ and $\mathbf{Q}_f$ consists in Chu's energy [35] in order to take into account the pressure ($\check{p}$) and entropy ($\check{s}$) disturbances, which writes for dimensionless fluctuations:

$$E_{\text{Chu}} = \check{\mathbf{q}}^*\mathbf{Q}_{\text{Chu}}\check{\mathbf{q}} = \frac{1}{2}\int_\Omega \left(\overline{\rho}\|\check{\mathbf{v}}\|^2 + \frac{1}{\gamma}\frac{\check{p}^2}{\overline{p}} + \gamma(\gamma-1)M^4\,\overline{p}\,\check{s}^2\right) d\Omega. \tag{2.19}$$

Chu's energy is the sum of the kinetic energy of the perturbation and a thermodynamic component (potential energy from compression and from heat exchange) with appropriate coefficients to exclude the conservative compression work [67] in order to obtain a norm which does not increase in time in the absence of sources of energy [58]. Matrix $\mathbf{Q}_q = \mathbf{Q}_{\text{Chu}}$ for Chu's energy norm is block-diagonal whose writing form with conservative variables is detailed in appendix B.

Similarly to Bugeat et al. [20] and Sartor et al. [162], we choose here to apply the forcing only on the momentum equations and measure $\mathbf{Q}_f$ as the discrete inner product ($\mathbf{Q}_f = \mathbf{Q}$ in Eq. (2.16)).

$$\|\check{\mathbf{f}}\|_f^2 = \int_\Omega \check{\mathbf{f}}^*\check{\mathbf{f}}\, d\Omega. \tag{2.20}$$

Matrix $\mathbf{Q}_f$ is positive-definite.

Solving for μ_i^2 over a range of frequencies ω provides the most receptive frequency (where $\mu_i(\omega)^2$ is the largest) and the associated optimal forcing mode $\check{\mathbf{f}}_i$.

From an algorithmic point of view, we solve for the optimal gain in Eq. (2.17) by rewriting

$$\mu^2 = \sup_{\check{\mathbf{f}}} \frac{\check{\mathbf{q}}^*\mathbf{Q}_q\check{\mathbf{q}}}{\check{\mathbf{f}}^*\mathbf{Q}_f\check{\mathbf{f}}} = \sup_{\check{\mathbf{f}}} \frac{(\mathcal{R}\mathbf{P}\check{\mathbf{f}})^*\mathbf{Q}_q(\mathcal{R}\mathbf{P}\check{\mathbf{f}})}{(\mathbf{P}\check{\mathbf{f}})^*\mathbf{Q}_f(\mathbf{P}\check{\mathbf{f}})} = \sup_{\check{\mathbf{f}}} \frac{\check{\mathbf{f}}^*\mathbf{P}^*\mathcal{R}^*\mathbf{Q}_q\mathcal{R}\mathbf{P}\check{\mathbf{f}}}{\check{\mathbf{f}}^*\mathbf{Q}_f\check{\mathbf{f}}}. \tag{2.21}$$

The optimisation problem defined by Eq. (2.21) is the Rayleigh quotient. It is equivalent to the generalised Hermitian eigenvalue problem

$$\underbrace{\mathbf{P}^*\mathcal{R}^*\mathbf{Q}_q\mathcal{R}\mathbf{P}}_{=\mathbf{C}}\check{\mathbf{f}}_i = \mu_i^2\mathbf{Q}_f\check{\mathbf{f}}_i. \tag{2.22}$$

Its eigenvalues are ranked such that $\mu_i^2 \geq \mu_{i+1}^2$ and the associated eigenvectors are $\check{\mathbf{f}}_i$, which we normalise to $\check{\mathbf{f}}_i^* \mathbf{Q}_f \check{\mathbf{f}}_i = 1$. The normalised responses ($\check{\mathbf{q}}_i^* \mathbf{Q}_q \check{\mathbf{q}}_i = 1$) are then obtained through

$$\check{\mathbf{q}}_i = \mu_i^{-1} \mathcal{R} \mathbf{P} \check{\mathbf{f}}_i. \tag{2.23}$$

The bases $\check{\mathbf{f}}_i$ and $\check{\mathbf{q}}_i$ are orthonormal bases of the input and output spaces.

From the definition of the Hermitian matrix $\mathbf{C} = \mathbf{P}^* \mathcal{R}^* \mathbf{Q}_q \mathcal{R} \mathbf{P}$, the different steps to compute $\mathbf{Cv}$ are detailed in Algo. 4.

Algorithme 4 Matrix-free pseudo-algorithm

1: **Compute Cv:**
2: Compute $\mathbf{v}_1 = \mathbf{P}\,\mathbf{v}$
3: Solve linear system $\mathbf{v}_2 = \mathcal{R}\mathbf{v}_1$ with sparse LU algorithm
4: Compute $\mathbf{v}_3 = \mathbf{Q}_E\,\mathbf{v}_2$
5: Solve linear system $\mathbf{v}_4 = \mathcal{R}^*\mathbf{v}_3$ (LU decomposition of $\mathcal{R}$ done at step 3)
6: Compute $\mathbf{v}_5 = \mathbf{P}^*\,\mathbf{v}_4$
7: Update $\mathbf{v} = \mathbf{v}_5$.

Computation of the resolvent modes is performed following the steps described in Algo. 5. As one may notice, the frequency ω appears in matrix $\mathcal{R} = (i\omega\mathbf{I} - \mathbf{A})^{-1}$. So, to compute the optimal gain and its associated forcing and response over a range of n frequencies, the steps from 6 to 13 have to be reproduced n times in Algo. 5. To overcome this, Martini et al. [115] offered an alternative resolvent approach based on a time-stepping method to compute simultaneously the optimal gains associated with several frequencies.

Algorithme 5 Resolvent mode pseudo-algorithm

1: **Initialisation:**
2: Read geometry and state vector
3: Compute norm matrices $\mathbf{Q}_q$ & $\mathbf{Q}_f$
4: Compute prolongation/restriction matrix $\mathbf{P}$
5: Construct Jacobian $\mathbf{A}$ (see Algo. 2)
6: **Definition of Hermitian matrix C:**
7: Construct matrix $i\omega\mathbf{I} - \mathbf{A}$
8: Define matrix-vector product $\mathbf{Cv}$ (see Algo. 4)
9: **Solve generalised eigenvalue problem (Eq. (2.22)):**
10: Arnoldi method
11: Store the largest eigenvalue μ^2 and its eigenvector $\check{\mathbf{f}}$
12: **Solve linear system $\check{\mathbf{q}} = \mathcal{R}\mathbf{P}\check{\mathbf{f}}$**
13: **Write optimal gain μ, forcing $\check{\mathbf{f}}$ and response $\check{\mathbf{q}}$.**

2.1.9 Three-dimensional perturbations

The extension of global stability analysis to linear 3D perturbations follows Bugeat et al. [20]. The fluctuations being periodic in the z-direction, the perturbation field can be searched under the form

$$\mathbf{q}'(x, y, z, t) = \check{\mathbf{q}}(x, y) e^{i(\omega t + \beta z)} + c.c. \tag{2.24}$$

where β is the real wavenumber in the z-direction. A similar form is assumed for the optimal forcing, global direct and adjoint modes. These perturbations can therefore be studied on the

same 2D mesh without discretisation of the z-direction. The z-dependency of the forcing and response are taken into account analytically. One can split the 3D residual $\mathbf{R}$ as the sum of the 2D discretised residual $\mathbf{R}_{2D}$ and its z-derivative components $\mathbf{R}_z$,

$$\mathbf{R}(\mathbf{q}) = \mathbf{R}_{2D}(\mathbf{q}) + \mathbf{R}_z(\mathbf{q}). \tag{2.25}$$

For the compressible Navier-Stokes equations, the $\mathbf{R}_z$ residual in conservative form can be written as the sum of four functions:

$$\mathbf{R}_z(\mathbf{q}) = \mathbf{B}(\mathbf{q})\frac{\partial \mathbf{q}}{\partial z} + \mathbf{C}_1(\mathbf{q})\frac{\partial^2 \mathbf{q}}{\partial z^2} + \frac{\partial \mathbf{C}_2}{\partial \mathbf{q}}\frac{\partial \mathbf{q}}{\partial z}\frac{\partial \mathbf{q}}{\partial z} + \mathbf{D}_1(\mathbf{q})\frac{\partial \mathbf{q}}{\partial z} \odot \mathbf{D}_2(\mathbf{q})\frac{\partial \mathbf{q}}{\partial z}. \tag{2.26}$$

Notation $\odot$ refers to the Hadamard product (element-wise product of two matrices or vectors).

The matrices for the z-derivatives in the short expression Eq. (2.26) are derived as

$$\mathbf{B}(\mathbf{q})\frac{\partial \mathbf{q}}{\partial z} = \left(\sum_k \boldsymbol{\alpha}_k(\mathbf{q})\frac{\partial \mathbf{a}_k(\mathbf{q})}{\partial \mathbf{q}}\right)\frac{\partial \mathbf{q}}{\partial z}, \tag{2.27}$$

$$\mathbf{C}_1(\mathbf{q})\frac{\partial^2 \mathbf{q}}{\partial z^2} = \left(\sum_l \boldsymbol{\lambda}_l(\mathbf{q})\frac{\partial \mathbf{b}_l(\mathbf{q})}{\partial \mathbf{q}}\right)\frac{\partial^2 \mathbf{q}}{\partial z^2}, \tag{2.28}$$

$$\frac{\partial \mathbf{C}_2}{\partial \mathbf{q}}\frac{\partial \mathbf{q}}{\partial z}\frac{\partial \mathbf{q}}{\partial z} = \left(\sum_l \boldsymbol{\lambda}_l(\mathbf{q})\frac{\partial^2 \mathbf{b}_l(\mathbf{q})}{\partial \mathbf{q}^2}\right)\frac{\partial \mathbf{q}}{\partial z}\frac{\partial \mathbf{q}}{\partial z}, \tag{2.29}$$

$$\mathbf{D}_1(\mathbf{q})\frac{\partial \mathbf{q}}{\partial z} \odot \mathbf{D}_2(\mathbf{q})\frac{\partial \mathbf{q}}{\partial z} = \sum_m \boldsymbol{\gamma}_m(\mathbf{q})\frac{\partial \mathbf{c}_m(\mathbf{q})}{\partial \mathbf{q}}\frac{\partial \mathbf{q}}{\partial z} \odot \frac{\partial \mathbf{d}_m(\mathbf{q})}{\partial \mathbf{q}}\frac{\partial \mathbf{q}}{\partial z}, \tag{2.30}$$

with the expressions of $\boldsymbol{\alpha}_k, \mathbf{a}_k, \boldsymbol{\lambda}_l, \mathbf{b}_l, \boldsymbol{\gamma}_m, \mathbf{c}_m$ and $\mathbf{d}_m$ listed in Table 2.2.

Then, the spanwise contributions of the Jacobian operator are derived. Given a general flow $\mathbf{q}$ and keeping only the first-order terms for small fluctuations $\mathbf{q}'$, the linearisation of Eq. (2.25) around $\mathbf{q}$ yields

$$\mathbf{A}(\mathbf{q})\mathbf{q}' = \left(\mathbf{A}_{2D}(\mathbf{q}) + \mathbf{A}_z(\mathbf{q})\right)\mathbf{q}',$$

with

$$\begin{aligned}\mathbf{A}_z(\mathbf{q})\mathbf{q}' = &\overbrace{\left[\frac{\partial \mathbf{B}}{\partial \mathbf{q}}\frac{\partial \mathbf{q}}{\partial z} + \frac{\partial \mathbf{C}_1}{\partial \mathbf{q}}\frac{\partial^2 \mathbf{q}}{\partial z^2} + \frac{\partial^2 \mathbf{C}_2}{\partial \mathbf{q}^2}\frac{\partial \mathbf{q}}{\partial z}\frac{\partial \mathbf{q}}{\partial z} + \mathbf{D}_1(\mathbf{q})\frac{\partial \mathbf{q}}{\partial z} \odot \frac{\partial \mathbf{D}_2}{\partial \mathbf{q}}\frac{\partial \mathbf{q}}{\partial z} + \mathbf{D}_2(\mathbf{q})\frac{\partial \mathbf{q}}{\partial z} \odot \frac{\partial \mathbf{D}_1}{\partial \mathbf{q}}\frac{\partial \mathbf{q}}{\partial z}\right]}^{=\mathbf{A}_z^q(\mathbf{q})}\mathbf{q}' \\ &+ \underbrace{\left[\mathbf{B}(\mathbf{q}) + 2\frac{\partial \mathbf{C}_2}{\partial \mathbf{q}}\frac{\partial \mathbf{q}}{\partial z} + \mathbf{D}_1(\mathbf{q})\frac{\partial \mathbf{q}}{\partial z} \odot \mathbf{D}_2(\mathbf{q}) + \mathbf{D}_2(\mathbf{q})\frac{\partial \mathbf{q}}{\partial z} \odot \mathbf{D}_1(\mathbf{q})\right]}_{=\mathbf{A}_z^z(\mathbf{q})}\frac{\partial \mathbf{q}'}{\partial z} + \underbrace{\mathbf{C}_1(\mathbf{q})}_{=\mathbf{A}_z^{z^2}(\mathbf{q})}\frac{\partial^2 \mathbf{q}'}{\partial z^2}.\end{aligned} \tag{2.31}$$

For linear input-output analysis i.e. through the ansatz Eq. (2.24) and under the assumption of the linearisation around a homogeneous base-flow $\mathbf{q_b}$ in the z-direction, Eq. (2.31) reduces to

$$\mathbf{A}_z(\mathbf{q_b})\mathbf{q}' = \left(i\beta\mathbf{B}(\mathbf{q_b}) - \beta^2\mathbf{C}_1(\mathbf{q_b})\right)\mathbf{q}'. \tag{2.32}$$

For non-linear input-output analysis i.e. for a general state $\mathbf{q}$ and to take into account the non-linear interactions between the different spanwise wavenumbers (β, 2β, 3β...), the general expression Eq. (2.31) is used.

Continuity equation									
k	α_k	a_k	l	λ_l	b_l	m	γ_m	c_m	d_m
1	1	ρw							
Momentum equation in x-direction									
k	α_k	a_k	l	λ_l	b_l	m	γ_m	c_m	d_m
1	1	$\rho uw - \mu\frac{\partial w}{\partial x}$	1	$-\mu$	u	1	-1	μ	u
2	$\frac{2}{3}\frac{\partial \mu}{\partial x}$	w							
3	$\frac{2}{3}\ \mu$	$\frac{\partial w}{\partial x}$							
Momentum equation in y-direction									
k	α_k	a_k	l	λ_l	b_l	m	γ_m	c_m	d_m
1	1	$\rho vw - \mu\frac{\partial w}{\partial y}$	1	$-\mu$	v	1	-1	μ	v
2	$\frac{2}{3}\frac{\partial \mu}{\partial y}$	w							
3	$\frac{2}{3}\mu$	$\frac{\partial w}{\partial y}$							
Momentum equation in z-direction									
k	α_k	a_k	l	λ_l	b_l	m	γ_m	c_m	d_m
1	1	$\rho w^2 + p + \frac{2}{3}\mu\left(\frac{\partial u}{\partial x} + \frac{\partial v}{\partial y}\right)$	1	$-\frac{4}{3}\mu$	w	1	$-\frac{4}{3}$	μ	w
2	$-\frac{\partial \mu}{\partial x}$	u							
3	$-\frac{\partial \mu}{\partial y}$	v							
4	$-\mu$	$\frac{\partial u}{\partial x} + \frac{\partial v}{\partial y}$							
Energy equation									
k	α_k	a_k	l	λ_l	b_l	m	γ_m	c_m	d_m
1	1	$(\rho E + p)w$	1	$-\lambda$	T	1	-1	λ	T
2	$\frac{2}{3}\frac{\partial(\mu u)}{\partial x}$	w	2	$-\mu u$	u	2	$-\mu$	u	u
3	$\frac{2}{3}\mu u$	$\frac{\partial w}{\partial x}$	3	$-\mu v$	v	3	$-u$	μ	u
4	$-\frac{\partial(\mu w)}{\partial x}$	u	4	$-\frac{4}{3}\mu w$	w	4	$-\mu$	v	v
5	$-\mu w$	$\frac{\partial u}{\partial x}$				5	$-v$	μ	v
6	$\frac{2}{3}\frac{\partial(\mu v)}{\partial y}$	w				6	$-\frac{4}{3}\mu$	w	w
7	$\frac{2}{3}\mu v$	$\frac{\partial w}{\partial y}$				7	$-\frac{4}{3}w$	μ	w
8	$-\frac{\partial(\mu w)}{\partial y}$	v							
9	$-\mu w$	$\frac{\partial v}{\partial y}$							
10	$-\mu\frac{\partial w}{\partial x}$	u							
11	$-u$	$\mu\frac{\partial w}{\partial x}$							
12	$-\mu\frac{\partial w}{\partial y}$	v							
13	$-v$	$\mu\frac{\partial w}{\partial y}$							
14	$\frac{2}{3}\mu\left(\frac{\partial u}{\partial x} + \frac{\partial v}{\partial y}\right)$	w							
15	$\frac{2}{3}w\left(\frac{\partial u}{\partial x} + \frac{\partial v}{\partial y}\right)$	μ							
16	$\frac{2}{3}\mu w$	$\frac{\partial u}{\partial x} + \frac{\partial v}{\partial y}$							

Table 2.2: Spanwise contributions of the Cartesian Navier-Stokes equations.

2.2 Stability analysis

The BROADCAST code and its stability tools are validated on a circular cylinder at low Mach number [48, 177] and on a hypersonic boundary layer developing on an adiabatic flat plate [20]. These cases allow to validate the solver on both Cartesian and curvilinear grids as well as for both hypersonic and incompressible regimes. The stability analysis is then repeated on different boundary layers as a preliminary work for the next chapters on linear sensitivity and non-linear input-output analysis. Computations of this chapter are performed on HPC with the following features: 128 GB RAM & 2 sockets of 12 cores (Broadwell Intel Xeon CPU E5-2650 v4 at 2.2 GHz). The code has been optimised and tested within an Intel (version 2017) compilation environment.

2.2.1 Cylinder flow

In the following, the global stability analysis around a circular cylinder at low Mach number is performed for validation purpose.

2.2.1.1 Geometry, mesh, boundary conditions and base-flow

The circular cylinder is studied for low-Mach number flow to allow validation with incompressible results. The Navier-Stokes equations are non-dimensionalised by the triplet (ρ_∞, U_∞, T_∞). The freestream Mach number is $M_\infty = 0.1$ and the freestream temperature is $T_\infty = 288$ K and several Reynolds numbers are computed between $Re = 40$ and $Re = 100$ with the Reynolds number defined as $Re = \rho_\infty U_\infty D/\mu_\infty$ with D the diameter of the cylinder.

The computational domain is circular with an outer radius of $100D$. The O-mesh is curvilinear (deformed Cartesian grid) with a stretching in the wall-normal direction and a refinement in the wake downstream. The mesh is fine enough in the wall-tangent direction to get a smooth curvilinear grid where the high-order numerical scheme remains valid [54, 154]. The reference mesh size is 630 points in the wall-tangent direction and 300 points in the wall-normal direction. An adiabatic no-slip wall condition is prescribed at the surface of the cylinder. This is a Dirichlet condition for velocity and a boundary layer assumption resulting in a zero wall-normal pressure gradient at the interface (gradient computed at second order under the assumption of a Cartesian regular grid at the interface). A non-reflecting condition is imposed at the outer radius with the free-stream conditions taken as reference. It is based on the characteristic relations and it determines pressure, density and velocity depending on the directions of the ingoing/outgoing characteristics [143]. Connectivity conditions are added (through additional ghost cells) to close the mesh in the upstream part.

We choose the fifth order numerical spatial scheme and the base-flow (Figure 2.3a) was converged up to a decrease of 12 orders of magnitude of the L^2 norm of the residual in 6 Newton iterations starting from a constant reference state for several Reynolds numbers around the first bifurcation. Maximum RAM memory used is 40 GB and elapsed time is 190 seconds per Newton iteration.

2.2.1.2 Global modes

The eigenvalue problem (1.7) for global stability is solved at different Reynolds numbers to find the most unstable global mode. The spectrum at $Re = 46.8$ is plotted in Figure 2.4, which corresponds to criticality: $\lambda = \sigma + i\omega$, with $\sigma = 0$. The eigenvalues λ are normalised by U_∞/D. The most unstable mode and its associated adjoint mode at criticality are plotted in Figure

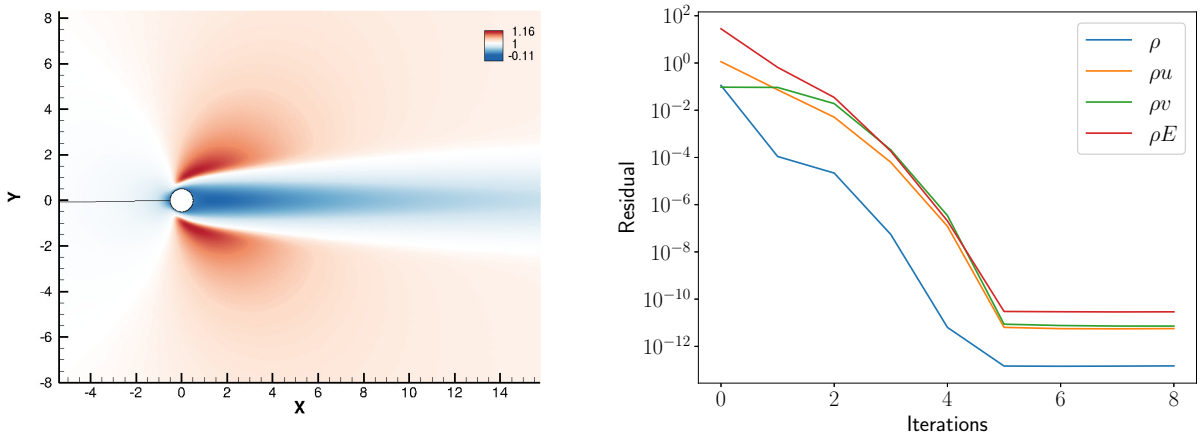

(a) (b)

Figure 2.3: Base-flow and residual convergence at $Re = 46.8$ and $M_\infty = 0.1$. (a) Streamwise velocity of the base-flow. (b) Evolution of the L^2 norm of the residual with respect to the number of Newton iterations to converge the base-flow.

2.5. RAM memory used is 40 GB and elapsed time is 160 seconds per iteration of the Arnoldi algorithm.

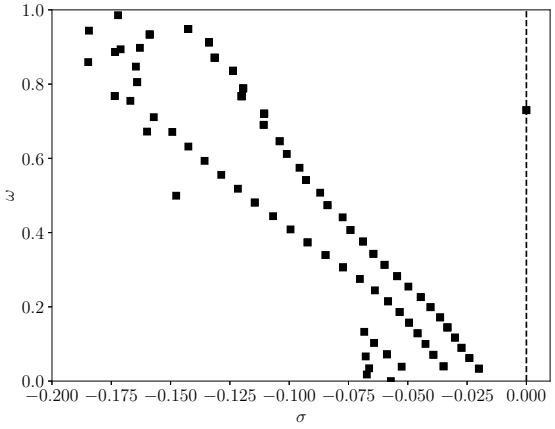

Figure 2.4: Discretised spectrum (partial view) of the eigenvalues at $Re = 46.8$ and $M_\infty = 0.1$.

Evolution of the growth rate of the most unstable eigenvalue with Reynolds number is plotted in Figure 2.6a and compared with the calculations of Fabre [48], which was obtained with an incompressible solver. Overall, good agreement is achieved. Furthermore, 3D instabilities computed with the 3D Jacobian $\mathbf{A}_{3D}$ at $Re = 100$ show the same evolution of the growth rate with the spanwise wavenumber β (Figure 2.6b) normalised by the diameter D as the one provided by incompressible Navier-Stokes equations discretised with FreeFEM software [69, 111] (mesh of 138708 triangles with P2 and P1 elements).

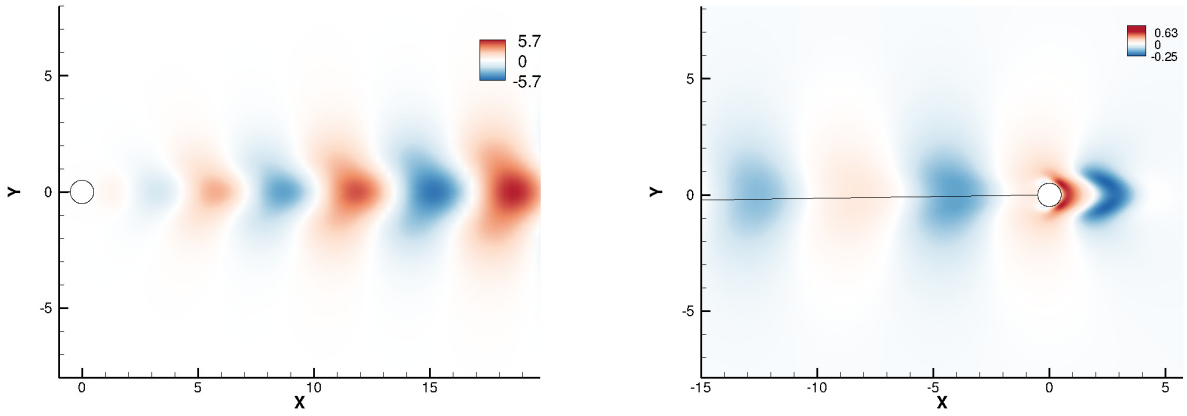

(a) **(b)**

Figure 2.5: Direct and adjoint modes at $Re = 46.8$ and $M_\infty = 0.1$. Same normalisation as in Sipp and Lebedev [177]. (a) Real part of the normal velocity of the direct mode $\hat{\mathbf{q}}_1$. (b) Real part of the normal velocity of the adjoint mode $\mathbf{q}_1^\dagger = \mathbf{Q}^{-1}\tilde{\mathbf{q}}_1$. The black line upstream the cylinder denotes the connectivity line to enclose the mesh.

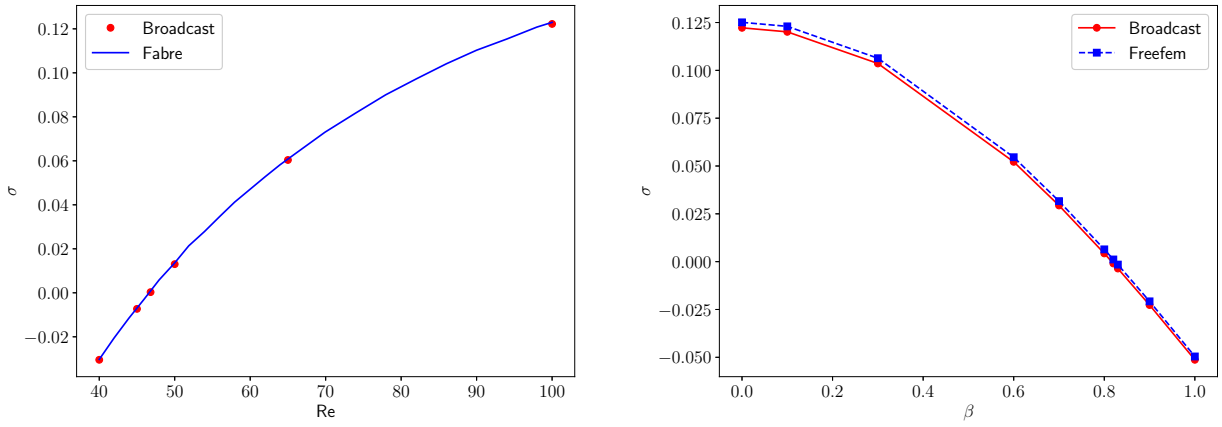

(a) **(b)**

Figure 2.6: Growth rate as a function of Reynolds number and spanwise wavenumber for cylinder flow at $M_\infty = 0.1$. (a) Evolution of the growth rate with Reynolds number for $\beta = 0$ and $M_\infty = 0.1$. Comparison with the incompressible results obtained by Fabre et al. [48]. (b) Evolution of the growth rate with the wavenumber β at $Re = 100$ and $M_\infty = 0.1$. Comparisons done with incompressible results obtained with FreeFEM software [69, 111].

2.2.2 Boundary layer flow

In the following, the base-flow computation and the resolvent analysis of several boundary layers over an adiabatic flat plate are performed.

2.2.2.1 Geometry, mesh and boundary conditions

The adiabatic flat plate is studied at low Mach number and at hypersonic regime. The Navier-Stokes equations are non-dimensionalised by the triplet (ρ_∞, U_∞, T_∞). The freestream Mach number is M_∞, the freestream temperature is $T_\infty = 288$ K and the unit Reynolds number

defined as $Re_{\text{unit}} = U_\infty/\nu_\infty$. Reference length is chosen as $1/Re_{\text{unit}}$ such that the spatial coordinates (x, y, z) then correspond to (Re_x, Re_y, Re_z), where for example $Re_x = U_\infty x/\nu_\infty$.

The flat plate geometry is studied in a rectangular computational domain. The domain starts with a thin boundary layer profile at $Re_{x,\text{in}}$ and ends at $Re_{x,\text{out}}$. The height of the domain is high enough in order not to affect the development of the boundary-layer or the stability analysis. In practice, the domain height is about $9\,\delta^*_{\text{out}}$ with δ^*_{out} the compressible displacement thickness at the outlet. The Cartesian mesh is equispaced in the x-direction and stretched in the wall-normal direction (y-direction). The stretching has the following properties: maximum $y^+ \leq 1$, cell height geometric growth rate of 2% from $y = 0$ till $y = 3\delta^*_{\text{out}}$ and then a growth rate increase from 2% till 10% from $y = 3\delta^*_{\text{out}}$ till $y = L_y$. The reference mesh has the size $(N_x, N_y) = (N_x, 150)$ with N_x given in Table 2.3.

Four different boundary conditions are applied around the rectangular domain. First, at the inlet, a Dirichlet boundary condition is applied for supersonic flow and a non-reflecting boundary condition for subsonic flow. The imposed flow profile corresponds to a compressible self-similar solution for u, v, ρ and T. A self-similar solver for compressible boundary layer flow without pressure gradient is implemented in BROADCAST. It uses the Levy-Lee transformation, the Chapman-Rubesin [31] linear law for viscosity and a shooting method to solve the self-similar equations [7, 33]. One should note that the wall-normal velocity v computed from self-similar equations is small but not zero in the free-stream. This velocity is imposed at the inlet without any further treatment. At the outlet, a zeroth-order extrapolation boundary condition is applied for supersonic flow while a non-reflecting condition with free-stream pressure taken as reference (zero pressure gradient assumed) is used for subsonic flows. Then, an adiabatic no-slip wall is prescribed at the bottom and a non-reflecting condition is employed at the top boundary.

Various cases are considered for this work depending on the analysis performed: low Mach number for validation purpose, hypersonic regime, shorter domain for non-linear input-output analysis or Chu's energy as the forcing norm for sensitivity analysis. All cases are described in Table 2.3.

Name	Analysis	M_∞	$Re_{x,in}$	$Re_{x,out}$	$\mathbf{Q}_f$	$\mathbf{Q}_q$	$Re_{x,opt}$	N_x
B40	Base-flow	4	8160	2×10^6	-	-	-	1000
L45	Lin.	4.5	8160	2×10^6	L^2	Chu	1.75×10^6	1000
S01	Sens.	0.1	4300	7.5×10^5	L^2	Kinetic	6×10^5	1000
S45	Lin./Sens.	4.5	8160	2×10^6	Chu	Chu	1.75×10^6	1000
N01	Lin./Non-lin.	0.1	0.3×10^5	3.6×10^5	L^2	Kinetic	3.6×10^5	300
N45	Lin./Non-lin.	4.5	0.3×10^5	3.6×10^5	L^2	Chu	3.6×10^5	300

Table 2.3: Boundary layer test cases. Specific analyses are performed depending on the case studied. Lin. means resolvent (linear input-output) analysis, Sens. means linear sensitivity and Non-lin. is for non-linear input-output analysis.

2.2.2.2 Base-flow

Case B40

The compressible self-similar solution is taken as initial state for the Newton method. On the reference mesh, at $M_\infty = 4$, with the seventh-order numerical scheme, the Newton algorithm converges in 7 iterations (high initial CFL as the self-similar solution is close to the base-flow solution) and decreases the residual L^2 norms by 12 orders of magnitude.

Boundary layer profiles at Mach number $M_\infty = 4$ are extracted at different streamwise locations and plotted with respect to the self-similar variable $\frac{y}{x}\sqrt{\frac{Re_x}{2}}$ in Figure 2.7. The base-flow computed remains self-similar and the different profiles overlap. Furthermore, streamwise velocity and temperature profiles are validated against Özgen and Kırcalı [135]. Both show good agreement with a maximum difference of 1% of the wall temperature prediction.

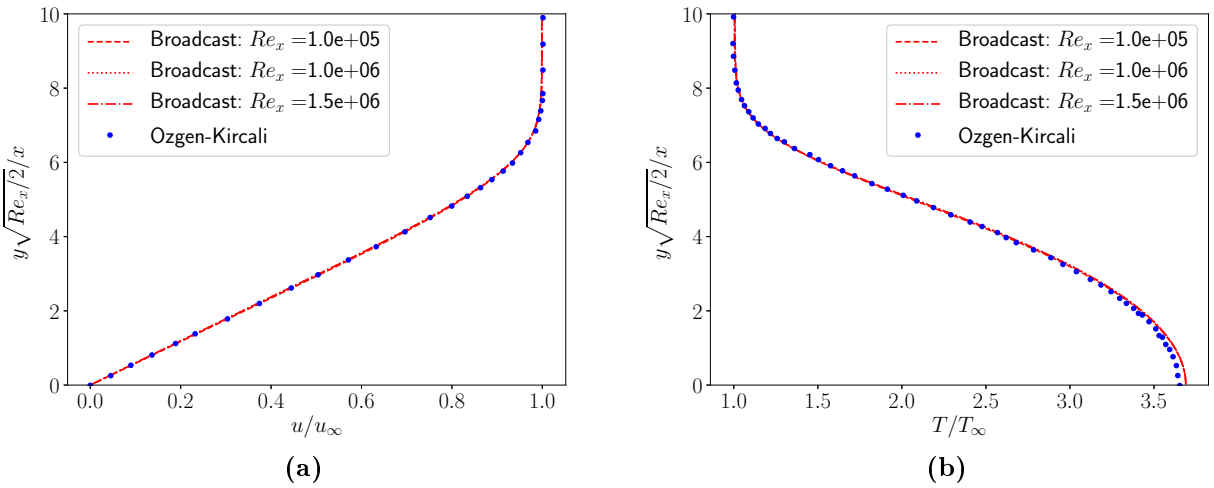

Figure 2.7: Boundary layer profiles at $M_\infty = 4$ plotted with respect to the self-similar variable at different streamwise locations. Comparison with Özgen and Kırcalı [135]. (a) Streamwise velocity profile. (b) Temperature profile.

Case L45

Then, a base-flow solution is computed at $M_\infty = 4.5$ (Figure 2.8). The slope of the ratio of the Reynolds number based on the displacement thickness on the square root of the Reynolds number $Re_{\delta^*}/\sqrt{Re_x}$ is computed to compare the base-flow with Bugeat et al. [20]. BROADCAST code gives a ratio of 8.29 while Bugeat has 8.32 meaning that both boundary layer base-flows follow a similar evolution.

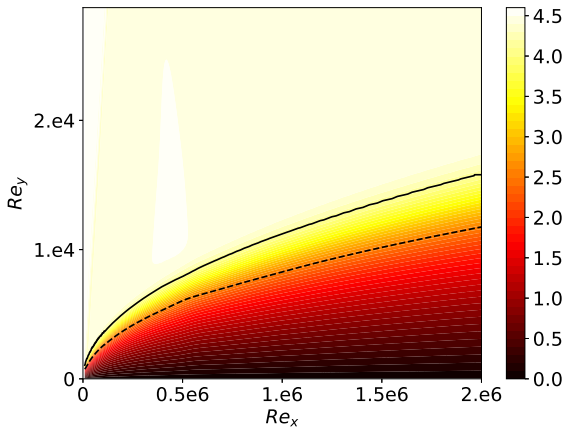

Figure 2.8: Mach number field of the base-flow. Solid line indicates the boundary layer thickness δ_{99}. Dashed line indicates the displacement thickness δ^*.

2.2.2.3 Resolvent modes

The frequency is normalised as $F = (\omega L_{\text{ref}})/U_\infty$ with $L_{\text{ref}} = Re_{\text{unit}}^{-1}$. The wavenumber β is also normalised with the reference length scale L_{ref}. The energies given in Table 2.3 restricted to $Re_x \leq Re_{x,opt}$ and $Re_y \leq Re_{L_y}/2$ are chosen for $\mathbf{Q}_q$ and $\mathbf{Q}_f$ through the restriction / prolongation matrix P.

Case L45

Forcing is applied only on momentum equations. Optimal gains μ_0 for 2D perturbations ($\beta = 0$) are plotted in Figure 2.9 at different frequencies. At $M_\infty = 4.5$, the second Mack mode corresponds to the frequency with the highest peak in Figure 2.9. Because the second Mack mode appears at high frequency, a fine mesh is necessary to converge well the peak value of the optimal gain. One may notice in Bugeat et al. [20] that a twice finer mesh (from $N_x = 1600$ to $N_x = 3200$) improved the optimal gain by 50 %. The suboptimal gain μ_1 is also plotted in Figure 2.9 and appears 4 times smaller than the optimal gain at the frequency of the second Mack mode ($F = 2.3 \times 10^{-4}$).

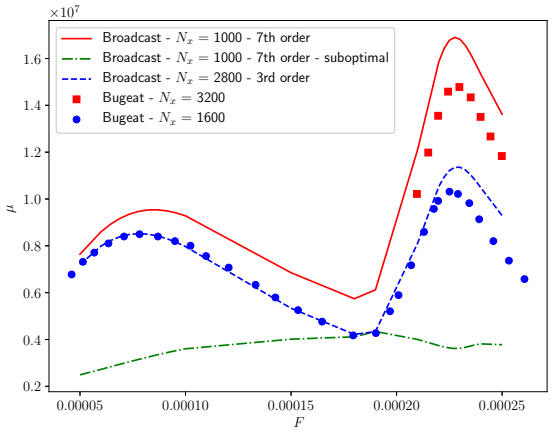

Figure 2.9: Optimal gains μ_i for 2D instabilities ($\beta = 0$) as a function of normalised frequency F. Comparison with Bugeat et al. [20].

The optimal gain convergence is assessed at the second Mack mode frequency F in Table 2.4. The computational performance (RAM and elapsed time) are compared for different mesh refinements and scheme orders. The number of cells per wavelength ξ in x-direction N_c/ξ is also shown for mesh convergence. According to the optimal forcing and response shapes plotted in Figure 2.10, the streamwise direction is the critical one as the wave is mainly oriented in the x-direction. The mesh convergence in y-direction has also been assessed and $N_y = 150$ appears to be sufficient. The seventh order scheme with 225000 points ($N_x = 1500$) is enough to reach the peak gain while a coarser mesh with $N_x = 1000$ at the same scheme order gives a gain smaller by only 1%. Taking the latter as the reference, a comparison of the performance of the different scheme orders is presented in Table 2.5. All computations are run at the same memory cost (38 GB RAM) by a mesh adjustment in the streamwise direction and the performance criterion is again the optimal gain at the second Mack mode frequency $F = 2.3 \times 10^{-4}$. Results from this iso-memory cost analysis underlines two elements. First, at this frequency, increasing the numerical scheme order from a low order (third order) to a fifth or a seventh order is heavily beneficial as the 3rd order scheme ends up at a smaller gain than all the other schemes (see Table 2.4 and Figure 2.9). Secondly, increasing to a high order (ninth order) is not always the

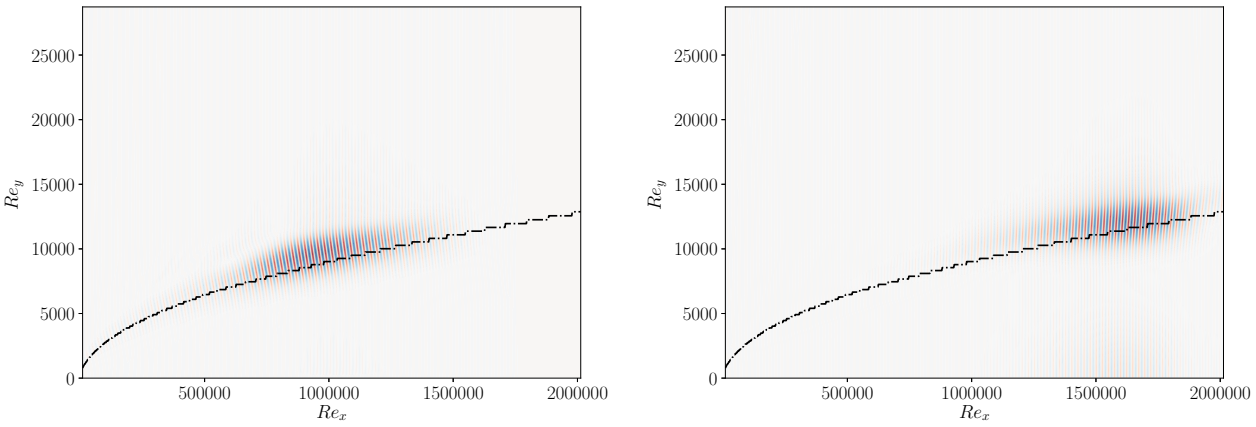

Figure 2.10: Optimal forcing and response for the second Mack mode at $F = 2.3 \times 10^{-4}$ ($\beta = 0$). Red (resp. blue) colour is negative (resp. positive) value. The black dash-dotted line denotes the generalised inflection point. (a) Streamwise momentum component of the optimal forcing $\check{\mathbf{f}}$. (b) Density component of the optimal response $\check{\mathbf{q}}$.

best solution. Indeed to keep the same memory cost, a high order scheme must be applied on a coarser mesh. However, a minimum number of cells per wavelength is always required, approximately here around 12 to capture the second Mack mode gain. It means that depending on the considered frequency, it exists an optimal scheme order in terms of memory that the user may have to choose. The seventh order scheme is then kept for all the computations performed in this work.

Optimal gain μ_0	Scheme order	N_x	N_c/ξ	RAM (GB)	Elapsed time (s)
1.70×10^7	9th	2000	24	113	1530
1.70×10^7	7th	1500	18	56	480
1.69×10^7	7th	1000	12	38	300
1.23×10^7	3rd	20000	240	285	10800
1.22×10^7	3rd	6000	72	99	1821

Table 2.4: Mesh convergence: optimal gain convergence at the second Mack mode frequency $F = 2.3 \times 10^{-4}$. N_c/ξ is the number of cells per wavelength in the streamwise x-direction. $N_y = 150$. Tolerance for Arnoldi algorithm is set to 10^{-4}.

Optimal gain is then computed with $\beta \neq 0$. The three-dimensional gains (Figure 2.11) compare well with those of Bugeat et al. [20], highlighting streaks around $\beta = 2.2 \times 10^{-4}$ at zero frequency and the first oblique Mack mode strongest for $\beta = 1.2 \times 10^{-4}$ and $F = 2.9 \times 10^{-5}$.

Then the eigenvectors for the three predominant modes (streak, first and second Mack modes) are compared through their streamwise energy growth. An energy density is defined as the integral of the local energy in the wall-normal direction. For example, $d_{\mathrm{Chu}}(x) = \int_0^{y_{\max}} \check{\mathbf{q}}(x,y)^* \mathbf{Q}_{\mathrm{Chu}}(x,y) \check{\mathbf{q}}(x,y)\, dy$ for the optimal response. Eventually, a forcing density is defined as $d_{\mathrm{F}}(x) = \int_0^{y_{\max}} |\check{\mathbf{f}}|^2\, dy$. Forcing and Chu's energy densities are plotted in Figures 2.12. They have similar trends to the ones predicted by Bugeat et al. [20].

Optimal gain μ_0	Scheme order	N_x	N_c/ξ	nnz in Jacobian	RAM (GB)	Elapsed time (s)
1.66×10^7	9th	700	8.4	59×10^6	38	290
1.69×10^7	7th	1000	12	72×10^6	38	300
1.68×10^7	5th	1500	18	85×10^6	38	360
1.13×10^7	3rd	2800	33.6	93×10^6	38	440

Table 2.5: Iso-computation cost at 38 GB RAM: optimal gain at the second Mack mode frequency $F = 2.3 \times 10^{-4}$. nnz in Jacobian represents the total number of non-zero entries in the Jacobian matrix. $N_y = 150$. Tolerance for Arnoldi algorithm is set to 10^{-4}.

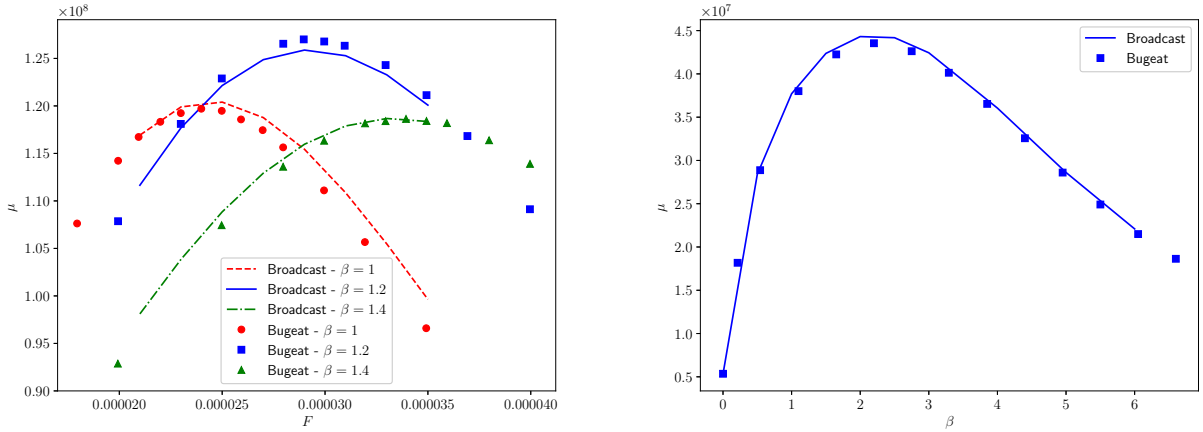

(a) **(b)**

Figure 2.11: Optimal gain: 3D linear instabilities. (a) Optimal gain with respect to the normalised frequency at the normalised wavenumbers $\beta = 1 \times 10^{-4}$, $\beta = 1.2 \times 10^{-4}$ and $\beta = 1.4 \times 10^{-4}$. Peaks refer to the first Mack mode. (b) Optimal gain with respect to the normalised wavenumber multiplied by 10^4 at zero frequency. The peak is related to streaks. Comparison with Bugeat et al. [20].

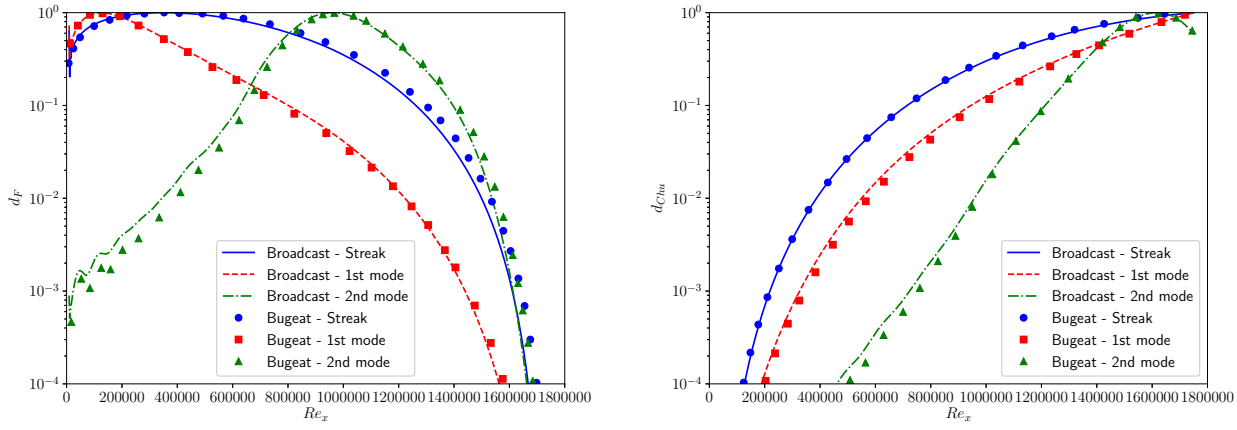

(a) **(b)**

Figure 2.12: Energy density of the streaks, first and second Mack modes normalised by their maximum value with respect to the Reynolds number based on x. (a) Forcing density. (b) Chu's energy density. Comparison with Bugeat et al. [20].

Case S45

The results from case S45 are very similar to those of case L45 as the resolvent analysis is performed on the same boundary layer but the forcing is here applied on all five components requiring then to use Chu's energy for the forcing norm $\mathbf{Q}_f$.

At $M_\infty = 4.5$, the second Mack mode exhibits a large gain, $\mu_0 = 1.80 \times 10^7$ which is obtained for $\beta = 0$ and $F = 2.3 \times 10^{-4}$. The optimal gains are also computed with $\beta \neq 0$ (Figure 2.13a). The three-dimensional gains highlight streaks ($\mu_0 = 4.66 \times 10^7$) around $\beta = 2 \times 10^{-4}$ at zero frequency and the first oblique Mack mode is the strongest instability ($\mu_0 = 1.16 \times 10^8$) for around $\beta = 1.2 \times 10^{-4}$ and $F = 3 \times 10^{-5}$. Therefore, we observe that a forcing acting on all the equations yields similar results (optimal frequency, spanwise wavenumber and gain ratio) as a forcing restricted to momentum equations.

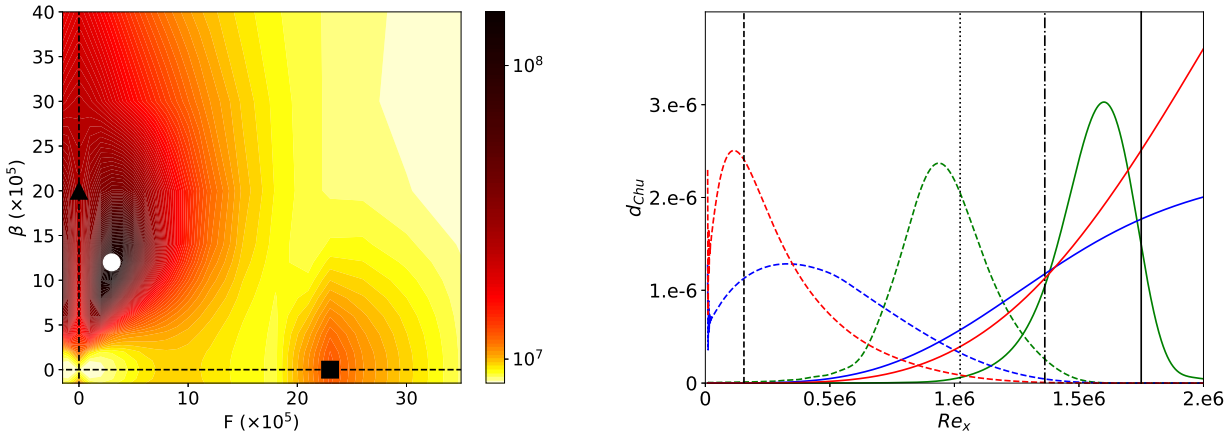

(a) **(b)**

Figure 2.13: Resolvent analysis. (a) Optimal gain μ_0 with respect to the frequency F and the spanwise wavenumber β. White circle denotes the first Mack mode, black triangle the streaks and black square the second Mack mode. (b) Energy density d_{Chu} of the optimal forcing (dashed lines) and response (solid lines) of the streaks (blue), the first (red) and second (green) Mack modes. Black vertical lines indicate branch I of first Mack mode (dashed line), branch I of mode S (dotted line), branch II of mode S (dashed-dotted line) and the end of the optimisation domain for resolvent analysis (solid line).

The streamwise evolution of the resolvent modes is again illustrated through their streamwise energy growth (same evolution than in the logarithmic Figures 2.12). Chu's energy densities of the forcing and response for the streaks, first and second Mack modes are plotted in Figure 2.13b and compared with spatial local stability analysis (LST). The LST numerical method performed here relies on a Chebyshev collocation method for the wall-normal direction and the dispersion relation is solved through LAPACK library. An isothermal boundary condition is prescribed for the linearised disturbances ($T' = 0$ at wall). The code has been developed by Chanteux et al. [30] following Saint-James [159] framework and validated on a supersonic boundary layer by Nibourel et al. [133]. The LST analysis has been performed at the same frequency (ω) and spanwise wavenumber (β) of the first and second Mack modes (see symbols in Figure 2.13a). The streamwise locations of branch I (resp. II) which is the beginning (resp. end) of the unstable region in the x-direction of the local modes are also plotted in Figure 2.13b. The maximal optimal forcing location for the first and second Mack modes agree well with branch I location of their respective local modes. Branch II of the first Mack mode is downstream of the domain end while branch II of the local mode S (linked to

the second Mack mode) is slightly upstream of the maximal optimal response location of the second Mack mode. As suggested by Sipp and Marquet [178], the discrepancies between local branches and maxima of the resolvent analysis are explained both by non-parallel effects [57] and Orr mechanism, the non-modal non-parallel unstable region being therefore larger than the local modal one. Furthermore, in comparison with the first Mack mode, larger differences between local and resolvent analyses are noticed for the second (higher frequency) where the Orr mechanism is stronger [178].

Case N01

To reproduce incompressible results, we consider the case of a low Mach number boundary layer developing over an adiabatic flat plate [155] which is about 6 times shorter in the streamwise direction than the cases L45 and S45. Forcing is applied only on momentum equations.

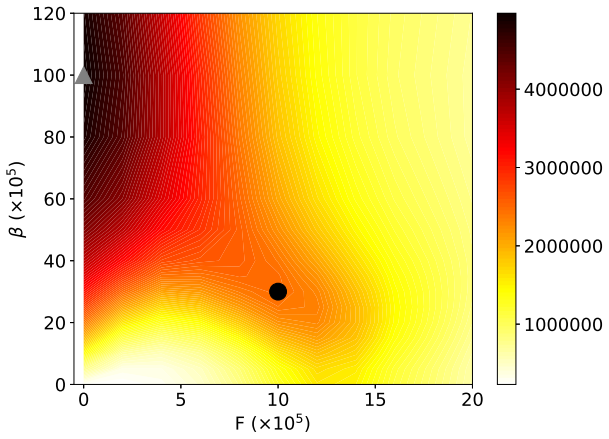

Figure 2.14: Optimal gain μ_0 of the linear resolvent analysis at Mach number 0.1 with respect to the frequency F and the spanwise wavenumber β. Grey triangle denotes the streaks ($F = 0$, $\beta = 100 \times 10^{-5}$) and black circle the oblique TS waves ($F = 10 \times 10^{-5}$, $\beta = 30 \times 10^{-5}$).

At Mach number 0.1, as for Rigas et al. [155], the optimal gain (Figure 2.14) highlights streaks around $\beta = 100 \times 10^{-5}$ at zero frequency as the global maximum and oblique Tollmien-Schlichting (TS) waves around $F = 10 \times 10^{-5}$ and $\beta = 30 \times 10^{-5}$ as a local maximum.

Case N45

The same short adiabatic flat plate configuration than Case N01 is considered but with a hypersonic boundary layer at Mach number 4.5. Forcing is again applied only on momentum equations.

At Mach number 4.5, in Figure 2.15a, the optimal gains highlight different mechanisms than for incompressible regime. The strongest instability is now the equivalent of the oblique TS waves for compressible flows which is the first Mack mode at similar frequency $F = 8 \times 10^{-5}$ and spanwise wavenumber $\beta = 30 \times 10^{-5}$. The streaks are less dominant and maximal at $\beta = 50 \times 10^{-5}$, half of the spanwise wavenumber of the incompressible boundary layer. Eventually, an additional planar mode appears at high frequency $F = 52 \times 10^{-5}$: the second Mack mode. In comparison with the long flat plate, cases L45 and S45, the same instabilities are highlighted by the resolvent analysis, however, they have larger frequency and spanwise wavenumber as the boundary layer is thinner in the short domain. For this case, the domain is about 6 times shorter which means that the outlet boundary layer thickness is about $\sqrt{6} \approx 2.5$ smaller. This

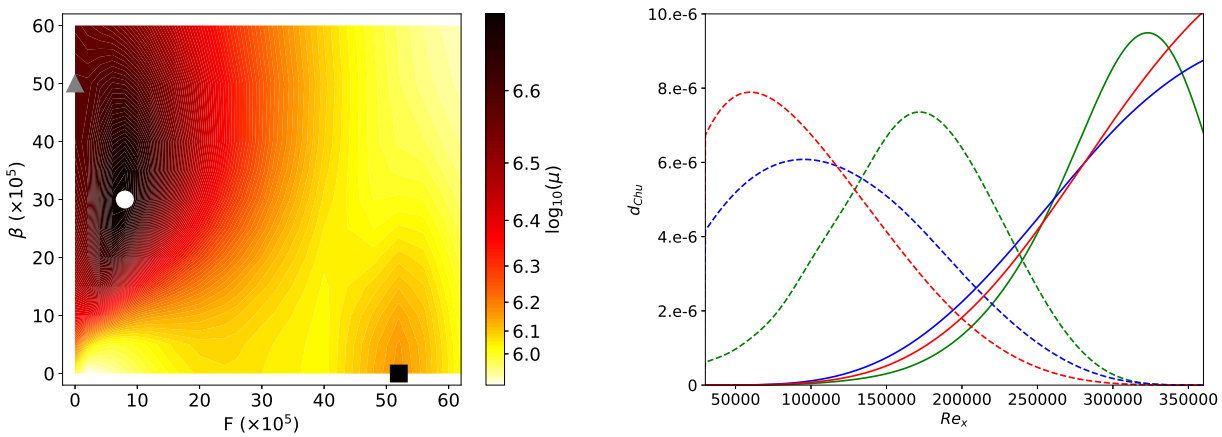

(a) **(b)**

Figure 2.15: Linear resolvent analysis at Mach number 4.5. (a) Optimal gain μ_0 with respect to the frequency F and the spanwise wavenumber β. White circle denotes the first Mack mode ($F = 8 \times 10^{-5}$, $\beta = 30 \times 10^{-5}$), grey triangle the streaks ($F = 0$, $\beta = 50 \times 10^{-5}$) and black square the second Mack mode ($F = 52 \times 10^{-5}$, $\beta = 0$). (b) Energy density of the optimal forcing (dashed lines) and response (solid lines) of the streaks (blue), the first (red) and second (green) Mack modes.

approximated factor 2.5 is present in the optimal frequency and spanwise wavenumber between S45 and N45 for the three instabilities.

Energy densities of the forcing and response for the streaks, first and second Mack modes are plotted in Figure 2.15b and show similar evolution than for the long flat plate (Figure 2.13b).

Chapter outcome summary:

The BROADCAST code and the methods implemented for fixed-point computation, stability and resolvent analysis have been presented and assessed. They rely on a two-dimensional discretisation where the spanwise-periodic three-dimensional perturbations are solved with Fourier expansion. They have been validated on the flow around a cylinder and then applied to a hypersonic ($M_\infty = 4.5$) boundary layer where the resolvent analysis identified the three main global mechanisms: the steady streaks, the first oblique Mack mode and the two-dimensional high-frequency second Mack mode.
The high-order scheme associated with low dissipation has showed accurate results in agreement with literature at a low computational cost for resolvent gains computations at high frequencies. Furthermore, this scheme may be used to Mach numbers as low as $M_\infty \approx 0.1$ to explore the incompressible regime both on Cartesian and curvilinear meshes. Finally the Algorithmic Differentiation tool allowed accurate and straightforward evaluations of the various residual derivatives that are necessary for stability analyses.

Chapter 3

Open-loop control of the linear instabilities

Chapter foreword:

This chapter presents the derivation of the linear sensitivity of the optimal gains i.e. the optimal location for small amplitude open-loop control of the linear instabilities calculated in the previous chapter. The sensitivity to base-flow modifications is validated on the flow around a cylinder and for boundary layer flow at low Mach number. It is then computed at higher Mach number. Wall-based control is explored by computing the optimal location for steady wall blowing/suction or heating/cooling actuators to damp the main instabilities in the $M_\infty = 4.5$ boundary layer. The design of a realistic wall heat-flux actuator targeting all the instabilities is ultimately attempted.

3.1 Linear sensitivity analysis theory

3.1.1 Sensitivity of eigenvalues

Linear sensitivity of an unstable eigenvalue λ (globally unstable flow) provides knowledge on the evolution of an eigenvalue with a small variation of the base-flow. It is studied following the method described by Mettot et al. [124]. The eigenvalue λ is assumed to depend on the base-flow $\overline{\mathbf{q}}$ [14] so that a base-flow modification $\delta\overline{\mathbf{q}}$ produces a variation of the eigenvalue $\delta\lambda$, that is

$$\delta\lambda = \langle \nabla_{\overline{\mathbf{q}}}\lambda, \delta\overline{\mathbf{q}} \rangle. \tag{3.1}$$

The sensitivity of the eigenvalue with respect to base-flow variations written $\nabla_{\overline{\mathbf{q}}}\lambda$ above is a complex vector whose real part represents the sensitivity of the amplification rate (real part of the eigenvalue λ) while the imaginary part represents the angular frequency (imaginary part of the eigenvalue λ). The inner product $\langle \cdot, \cdot \rangle$ is the one associated with the L^2 norm. From Sipp et al. [179], any variation of the Jacobian $\delta\mathbf{A}$ generates the variation $\delta\lambda$:

$$\delta\lambda = \langle \tilde{\mathbf{q}}, \delta\mathbf{A}\hat{\mathbf{q}} \rangle, \tag{3.2}$$

where $\tilde{\mathbf{q}}$ is the adjoint mode.

For a given global mode $\hat{\mathbf{q}}$, the variation of the Jacobian $\delta\mathbf{A}$ is assumed to be induced by the variation of the base-flow $\delta\overline{\mathbf{q}}$,

$$\delta\mathbf{A}\hat{\mathbf{q}} = \left.\frac{\partial(\mathbf{A}\hat{\mathbf{q}})}{\partial\mathbf{q}}\right|_{\overline{\mathbf{q}}} \delta\overline{\mathbf{q}}. \tag{3.3}$$

Then the sparse Hessian operator $\mathbf{H}$ is

$$H_{ijk} = \left.\frac{\partial^2 R_i}{\partial q_j \partial q_k}\right|_{\overline{\mathbf{q}}}. \tag{3.4}$$

Noticing that the Hessian is the second derivative of the residual around the base-flow, it can be computed easily applying a second time the Algorithmic Differentiation (AD) tool to the linearised residual. Introducing the Hessian $\mathbf{H}$ into the equation (3.3), it can be recast as

$$\delta\mathbf{A}\hat{\mathbf{q}} = \mathbf{H}(\hat{\mathbf{q}}, \delta\overline{\mathbf{q}}), \tag{3.5}$$

with $\mathbf{H}(\hat{\mathbf{q}}, \delta\overline{\mathbf{q}}) = \mathbf{H}'\delta\overline{\mathbf{q}}$ and $\mathbf{H}'$ defined as

$$H'_{ik} = \sum_j H_{ijk}\hat{q}_j. \tag{3.6}$$

This leads to $\delta\mathbf{A}\hat{\mathbf{q}} = \mathbf{H}'\delta\overline{\mathbf{q}}$ which can be substituted into the equation (3.2) and results in

$$\delta\lambda = \langle \tilde{q}, \mathbf{H}'\delta\overline{\mathbf{q}} \rangle = \langle \mathbf{H}'^*\tilde{\mathbf{q}}, \delta\overline{\mathbf{q}} \rangle. \tag{3.7}$$

By comparing equations (3.1) and (3.7), the gradient of the eigenvalue is

$$\nabla_{\overline{\mathbf{q}}}\lambda = \mathbf{H}'^*\tilde{\mathbf{q}}. \tag{3.8}$$

Linear sensitivity to other parameters with additional constraints (momentum-divergence-free modifications, steady source term...) can also be investigated. The sensitivity to a steady

source term in the Navier-Stokes equation is here studied by considering a small amplitude force term $\delta\mathbf{f}$. Writing $\mathbf{R}(\overline{\mathbf{q}}+\delta\overline{\mathbf{q}})+\delta\mathbf{f}=0$, one gets at the first order:

$$\delta\overline{\mathbf{q}} = -\mathbf{A}^{-1}\delta\mathbf{f}. \tag{3.9}$$

Then introducing equation (3.9) into equation (3.7) yields

$$\delta\lambda = \langle \mathbf{H}'^{*}\tilde{\mathbf{q}}, -\mathbf{A}^{-1}\delta\mathbf{f}\rangle = \langle -\mathbf{A}^{*-1}\mathbf{H}'\tilde{\mathbf{q}}, \delta\mathbf{f}\rangle. \tag{3.10}$$

By comparing with $\delta\lambda = \langle \nabla_{\mathbf{f}}\lambda, \delta\mathbf{f}\rangle$, the sensitivity with respect to a steady source term is

$$\nabla_{\mathbf{f}}\lambda = -\mathbf{A}^{*-1}\mathbf{H}'^{*}\tilde{\mathbf{q}}. \tag{3.11}$$

Then, continuous and discrete approaches can be linked. The inner product associated with the L^2 norm is replaced by the discrete inner product defined with the Hermitian matrix $\mathbf{Q}$ (Equation (2.16)). The sensitivity becomes $\delta\lambda = \langle \nabla_{\mathbf{f}}\,\lambda|_{\mathbf{Q}}\,, \delta\mathbf{f}\rangle\Big|_{\mathbf{Q}}$ and then:

$$\nabla_{\mathbf{f}}\,\lambda|_{\mathbf{Q}} = -\mathbf{Q}^{-1}\mathbf{A}^{*-1}\mathbf{H}'^{*}\mathbf{q}^{\dagger}, \tag{3.12}$$

with the associated adjoint mode $\mathbf{q}^{\dagger} = \mathbf{Q}^{-1}\tilde{\mathbf{q}}$.

To compute the sensitivity of an eigenvalue with respect to base-flow variations or to a steady source term in Navier-Stokes equations, one requires to have the direct and corresponding adjoint mode, the Jacobian and the Hessian operators. The operators are derived through the AD method.

3.1.2 Sensitivity of optimal gains to base-flow variations, steady forcing and parameter variations

Linear sensitivity of eigenvalues to any general flow parameter has been addressed by Martínez-Cava [113]. Here we focus on optimal gains, as in Brandt et al. [17]. Following the discrete framework introduced in Mettot et al. [124] for eigenvalues and recalled in §3.1.1, we extend the work of Martínez-Cava [113] to optimal gains and emphasize on the link with the concepts of linear sensitivity of the optimal gain to base-flow modifications $\delta\overline{\mathbf{q}}$ and steady forcing $\delta\overline{\mathbf{f}}$, that were initially described in detail in Marquet et al. [112]. We consider the general case of the sensitivity of the optimal gain μ_i^2 to any flow parameter written $\mathbf{p}$, such that

$$\delta\mu_i^2 = (\nabla_{\mathbf{p}}\mu_i^2)^{*}\mathbf{Q}_p\delta\mathbf{p}, \tag{3.13}$$

where $\mathbf{Q}_p$ is a given scalar-product. The parameter $\mathbf{p}$ can be either a scalar number as Re, M_∞, T_∞,... or a large-dimensional vector as the prescribed inlet profile or control vectors (wall-normal velocity or wall-temperature profiles). The latter will be considered for application in the next section. The only restriction in the following is that the control parameter $\mathbf{p}$ has to be invariant in time and in the z-direction, as the base-flow is assumed to remain steady and two-dimensional when varying the control parameter. We consider that the residual depends on the parameter $\mathbf{p}$, $\mathbf{R}(\mathbf{q}) = \mathbf{R}(\mathbf{q},\mathbf{p})$, and consequently also the Jacobian $\mathbf{A}(\mathbf{q},\mathbf{p}) = \partial\mathbf{R}(\mathbf{q},\mathbf{p})/\partial\mathbf{q}$.

The objective of the optimisation is maximising the optimal gain μ_i^2 under the constraint given by the eigenvalue problem written in Eq. (2.22) and that the base-flow is a solution of $\mathbf{R}(\overline{\mathbf{q}},\mathbf{p}) = 0$. Because of the space or component restriction ($\mathbf{P}$ may be degenerate), it is necessary to split the generalised eigenvalue problem (2.22) into three equations in order to handle only matrices without inverses:

$$\mathbf{P}\check{\mathbf{f}}_i = \mu_i(i\omega\mathbf{I}-\mathbf{A})\check{\mathbf{q}}_i, \qquad \mu_i\mathbf{Q}_q\check{\mathbf{q}}_i = (-i\omega\mathbf{I}-\mathbf{A}^{*})\check{\mathbf{a}}, \qquad \mathbf{P}^{*}\check{\mathbf{a}} = \mu_i^2\mathbf{Q}_f\check{\mathbf{f}}_i. \tag{3.14}$$

This system involves an additional component $\check{\mathbf{a}}$ within the eigenproblem. We therefore define the Lagrangian function $\mathcal{L}$ as a function of the state (the optimal gain μ_i^2, the optimal forcing $\check{\mathbf{f}}_i$ and response $\check{\mathbf{q}}_i$, the additional variable $\check{\mathbf{a}}$, the base-flow $\overline{\mathbf{q}}$), the four Lagrangian multipliers $\boldsymbol{\lambda}_1$, $\boldsymbol{\lambda}_2$, $\boldsymbol{\lambda}_3$ and $\boldsymbol{\lambda}_4$, and the control vector $\mathbf{p}$:

$$\begin{aligned}\mathcal{L}([\mu_i^2,\check{\mathbf{f}}_i,\check{\mathbf{q}}_i,\check{\mathbf{a}},\overline{\mathbf{q}}],\boldsymbol{\lambda}_{1\cdots4},\mathbf{p}) &= \mu_i^2+\langle\boldsymbol{\lambda}_1,\mathbf{P}\check{\mathbf{f}}_i-\mu_i(i\omega\mathbf{I}-\mathbf{A}(\overline{\mathbf{q}},\mathbf{p}))\check{\mathbf{q}}_i\rangle\\ &+ \langle\boldsymbol{\lambda}_2,\mu_i\mathbf{Q}_q(\overline{\mathbf{q}})\check{\mathbf{q}}_i+(i\omega\mathbf{I}+\mathbf{A}(\overline{\mathbf{q}},\mathbf{p})^*)\check{\mathbf{a}}\rangle\\ &+ \langle\boldsymbol{\lambda}_3,\mathbf{P}^*\check{\mathbf{a}}-\mu_i^2\mathbf{Q}_f(\overline{\mathbf{q}})\check{\mathbf{f}}_i\rangle+\langle\boldsymbol{\lambda}_4,\mathbf{R}(\overline{\mathbf{q}},\mathbf{p})\rangle. \end{aligned} \tag{3.15}$$

Here $\langle\mathbf{a},\mathbf{b}\rangle=\mathbf{a}^*\mathbf{b}$ is the Hermitian scalar product. By zeroing the variation of $\mathcal{L}$ with the state, taking into account that $\langle\check{\mathbf{f}}_i,\mathbf{Q}_f\check{\mathbf{f}}_i\rangle=1$, we obtain that

$$\boldsymbol{\lambda}_1=\check{\mathbf{a}},\quad \boldsymbol{\lambda}_2=\mu_i\check{\mathbf{q}}_i,\quad \boldsymbol{\lambda}_3=\check{\mathbf{f}}_i,\quad \boldsymbol{\lambda}_4=\mathbf{Q}_f\nabla_{\overline{\mathbf{f}}}\mu_i^2, \tag{3.16}$$

where

$$\frac{\nabla_{\overline{\mathbf{f}}}\mu_i^2}{\mu_i^2} = -\mathbf{Q}_f^{-1}\mathbf{A}^{-1*}\mathbf{Q}_q\frac{\nabla_{\overline{\mathbf{q}}}\mu_i^2}{\mu_i^2}, \tag{3.17}$$

$$\frac{\nabla_{\overline{\mathbf{q}}}\mu_i^2}{\mu_i^2} = \mathbf{Q}_q^{-1}\left[2\,\mathrm{Re}\left(\mathbf{H}'^*\mathcal{R}^*\mathbf{Q}_q\check{\mathbf{q}}_i\right)+\left(\frac{\partial(\mathbf{Q}_q\check{\mathbf{q}}_i)}{\partial\mathbf{q}}\right)^*\check{\mathbf{q}}_i-\left(\frac{\partial(\mathbf{Q}_f\check{\mathbf{f}}_i)}{\partial\mathbf{q}}\right)^*\check{\mathbf{f}}_i\right], \tag{3.18}$$

are two vectors called sensitivity to steady volume forcing and sensitivity to base-flow variations [17, 112, 124] that satisfy

$$\delta\mu_i^2=(\nabla_{\overline{\mathbf{f}}}\mu_i^2)^*\mathbf{Q}_f\delta\overline{\mathbf{f}}=(\nabla_{\overline{\mathbf{q}}}\mu_i^2)^*\mathbf{Q}_q\delta\overline{\mathbf{q}}. \tag{3.19}$$

Matrix $\mathbf{H}'$ is defined as $\mathbf{H}'\delta\overline{\mathbf{q}}=\mathbf{H}(\check{\mathbf{q}}_i,\delta\overline{\mathbf{q}})$ for all $\delta\overline{\mathbf{q}}$, where $\mathbf{H}=\partial\mathbf{A}/\partial\mathbf{q}=\partial^2\mathbf{R}/\partial\mathbf{q}^2$ is the Hessian rank-3 tensor.

In expression (3.18), the components $\partial\mathbf{Q}_{q,f}/\partial\mathbf{q}$ are non-zero in the case of Chu's energy norm. As an aside, Brandt et al. [17] has introduced an additional physical constraint (the time-invariant continuity equation (1.11)) to study the sensitivity to physically relevant base-flow modifications. Details of the computation of the sensitivity to momentum-divergence-free base-flow modifications is given below in §3.1.3.

Finally, the variation of $\mathcal{L}$ with the control vector $\mathbf{p}$ provides the gradient of interest:

$$\frac{\nabla_{\mathbf{p}}\mu_i^2}{\mu_i^2}=\mathbf{Q}_p^{-1}\left[\left(\frac{\partial\mathbf{R}}{\partial\mathbf{p}}\right)^*\mathbf{Q}_f\frac{\nabla_{\overline{\mathbf{f}}}\mu_i^2}{\mu_i^2}+2\,\mathrm{Re}\left(\tilde{\mathbf{H}}'^*\mathcal{R}^*\mathbf{Q}_q\check{\mathbf{q}}\right)\right], \tag{3.20}$$

with $\tilde{\mathbf{H}}'$ defined as $\tilde{\mathbf{H}}'\delta\mathbf{p}=\tilde{\mathbf{H}}(\check{\mathbf{q}}_i,\delta\mathbf{p})$ for all $\delta\mathbf{p}$, $\tilde{\mathbf{H}}=\partial\mathbf{A}/\partial\mathbf{p}=\partial^2\mathbf{R}/\partial\mathbf{q}\partial\mathbf{p}$ being another rank-3 tensor.

In expression (3.20), the first term is interpreted as the variation of the optimal gain induced by the modification of the Jacobian due to the change of the base-flow $\mathbf{A}(\mathbf{q})$ while the second term is the variation of the Jacobian due to the variation of the control parameter $\mathbf{A}(\mathbf{p})$, keeping the base-flow constant. It has been described in a similar context in Guo et al. [64] for eigenvalue sensitivity: Route I is the distortion of the base-flow which induces a modification of the eigenvalue problem, Route II is the direct distortion of the linear operator. Depending on the parameter $\mathbf{p}$ chosen to compute the sensitivity, one route or another is favoured.

The gradients do not depend on the domain height, given that the full forcing/response support is included in the domain, and have been validated by comparing the results with a finite difference method:

$$\lim_{\epsilon\to0}\frac{\mu_i^2(\mathbf{p}+\epsilon\nabla_{\mathbf{p}}\mu_i^2)-\mu_i^2(\mathbf{p})}{\epsilon}\to\|\nabla_{\mathbf{p}}\mu_i^2\|^2. \tag{3.21}$$

3.1.3 Sensitivity to momentum-divergence-free base-flow modifications

From the sensitivity to base-flow modifications $\nabla_{\overline{\mathbf{q}}}\mu_i^2$ given by Eq. (3.18), a restriction to momentum-divergence-free base-flow variations can be performed. Denoting $\nabla^{df}_{\overline{\boldsymbol{\rho u}}}\mu_i^2$ and $\nabla^{df}_{\overline{\boldsymbol{\rho v}}}\mu_i^2$ the sensitivities to momentum-divergence-free modifications of the base-flow momentum, any momentum-divergence-free base-flow modifications $\delta^{df}\overline{\boldsymbol{\rho u}}$ and $\delta^{df}\overline{\boldsymbol{\rho v}}$ yields

$$\delta\mu_i^2 = \langle\nabla^{df}_{\overline{\boldsymbol{\rho u}}}\mu_i^2, \delta^{df}\overline{\boldsymbol{\rho u}}\rangle + \langle\nabla^{df}_{\overline{\boldsymbol{\rho v}}}\mu_i^2, \delta^{df}\overline{\boldsymbol{\rho v}}\rangle = \langle\nabla_{\overline{\boldsymbol{\rho u}}}\mu_i^2, \delta^{df}\overline{\boldsymbol{\rho u}}\rangle + \langle\nabla_{\overline{\boldsymbol{\rho v}}}\mu_i^2, \delta^{df}\overline{\boldsymbol{\rho v}}\rangle. \tag{3.22}$$

As the sensitivity and the momentum base-flow modifications are both momentum-divergence-free, they can be written as functions of scalars:

$$\nabla^{df}_{\overline{\boldsymbol{\rho u}}}\mu_i^2 = \frac{\partial\psi}{\partial y}, \quad \nabla^{df}_{\overline{\boldsymbol{\rho v}}}\mu_i^2 = -\frac{\partial\psi}{\partial x}, \quad \delta^{df}\overline{\boldsymbol{\rho u}} = \frac{\partial\phi}{\partial y}, \quad \delta^{df}\overline{\boldsymbol{\rho v}} = -\frac{\partial\phi}{\partial x}. \tag{3.23}$$

Injecting Eq. (3.23) into Eq. (3.22) and assuming that the equation should be valid for any scalar ϕ, an integration by parts leads to the Poisson equation:

$$-\Delta\psi = \frac{\partial\nabla_{\overline{\boldsymbol{\rho v}}}\mu_i^2}{\partial x} - \frac{\partial\nabla_{\overline{\boldsymbol{\rho u}}}\mu_i^2}{\partial y}, \tag{3.24}$$

with the boundary conditions $\nabla\psi\cdot\mathbf{n} = n_y\nabla_{\overline{\boldsymbol{\rho u}}}\mu_i^2 - n_x\nabla_{\overline{\boldsymbol{\rho v}}}\mu_i^2$ and $\mathbf{n} = (n_x, n_y)$ the boundary normal.

3.1.4 Interpretation of $\nabla_{\mathbf{p}}\mu_i^2$ and $\nabla_{\overline{\mathbf{q}}}\mu_i^2$

We consider the following optimisation problem:

$$\delta\mathbf{p}^m = \underset{\|\delta\mathbf{p}\|_p=1}{\operatorname{argmax}}\,\delta\mu_i^2(\delta\mathbf{p}), \tag{3.25}$$

where $\delta\mu_i^2$ and $\delta\mathbf{p}$ are related through eq. (3.13). It is straightforward to show that

$$\delta\mathbf{p}^m = \frac{\nabla_{\mathbf{p}}\mu_i^2}{\|\nabla_{\mathbf{p}}\mu_i^2\|_p}. \tag{3.26}$$

The gradient is therefore the best profile (of given small amplitude measured with $\|\cdot\|_p$) that optimally increases the gain and therefore optimally strengthens the instability. Conversely, because of linearity, $-\delta\mathbf{p}^m$ is the optimal open-loop control to damp the optimal gain.

For interpretation, $\delta\mu_i^2|^m := \delta\mu_i^2(\delta\mathbf{p}^m)$ may be rewritten as

$$\frac{\delta\mu_i^2|^m}{\mu_i^2} = \underbrace{\left[2\mathbf{Q}_p^{-1}\,\mathrm{Re}\left(\tilde{\mathbf{H}}'^*\mathcal{R}^*\mathbf{Q}_q\check{\mathbf{q}}\right)\right]^*\mathbf{Q}_p\delta\mathbf{p}^m}_{\delta E^m_{\mathbf{A}}} + \underbrace{\left(\frac{\nabla_{\overline{\mathbf{q}}}\mu_i^2}{\mu_i^2}\right)^*\mathbf{Q}_q\delta\overline{\mathbf{q}}^m}_{\delta E^m_{\overline{\mathbf{q}}}}, \tag{3.27}$$

where the first term on the rhs, $\delta E^m_{\mathbf{A}}$, is the variation of the gain due to the induced modification of the Jacobian, and the second part, $\delta E^m_{\mathbf{q}}$, is the variation due to the induced change in base-flow,

$$\delta\overline{\mathbf{q}}^m = -\mathbf{A}^{-1}\left(\frac{\partial\mathbf{R}}{\partial\mathbf{p}}\right)\delta\mathbf{p}^m. \tag{3.28}$$

Finally, the optimal gain variation due to the induced base-flow modification may be broken down into three pieces:

$$\delta E^m_{\overline{\mathbf{q}}} = \delta E^m_c + \delta E^m_p + \delta E^m_s, \tag{3.29}$$

where

$$\delta E_c^m = \int_\Omega \frac{\overline{\rho}\delta\overline{\mathbf{v}}^b \cdot \delta\overline{\mathbf{v}}^m}{2} d\Omega,\ \delta E_p^m = \int_\Omega \frac{\delta\overline{p}^b \delta\overline{p}^m}{2\gamma\overline{p}} d\Omega,\ \delta E_s^m = \frac{\gamma(\gamma-1)M^4}{2} \int_\Omega \overline{p}\delta\overline{s}^b \delta\overline{s}^m d\Omega. \quad (3.30)$$

Here, the notation $(\delta\overline{\mathbf{v}}^b, \delta\overline{p}^b, \delta\overline{s}^b)$ corresponds to the velocity-pressure-entropy variations associated to $\delta\overline{\mathbf{q}}^b := \frac{\nabla_{\overline{\mathbf{q}}}\mu_i^2}{\mu_i^2}$ and $(\delta\overline{\mathbf{v}}^m, \delta\overline{p}^m, \delta\overline{s}^m)$ to $\delta\overline{\mathbf{q}}^m$. In the following, we will represent the contributions $\delta E_{\mathbf{A}}^m$, δE_c^m, δE_p^m and δE_s^m to assess the importance of Jacobian, base-flow kinetic energy, pressure and entropy modifications in the gain variation associated to the optimal control $\delta\mathbf{p}^m$.

Finally, it is also straightforward to show that the above $\delta\overline{\mathbf{q}}^b$ is also the solution to the following optimisation problem:

$$\delta\overline{\mathbf{q}}^b = \underset{\|\delta\overline{\mathbf{q}}\|_q = \|\mu_i^{-2}\nabla_{\overline{q}}\mu_i^2\|_q}{\operatorname{argmax}} \delta\mu_i^2(\delta\overline{\mathbf{q}}), \quad (3.31)$$

where $\delta\mu_i^2$ and $\delta\overline{\mathbf{q}}$ are related through eq. (3.19). Hence, the maximum $\delta\mu_i^2|^b := \delta\mu_i^2(\delta\overline{\mathbf{q}}^b)$, can be rewritten and decomposed as

$$\frac{\delta\mu_i^2|^b}{\mu_i^2} = \left\| \frac{\nabla_{\overline{q}}\mu_i^2}{\mu_i^2} \right\|_q^2 = \delta E_c^b + \delta E_p^b + \delta E_s^b \quad (3.32)$$

where

$$\delta E_c^b = \int_\Omega \frac{\overline{\rho}\|\delta\overline{\mathbf{v}}^b\|^2}{2} d\Omega,\ \delta E_p^b = \int_\Omega \frac{\left(\delta\overline{p}^b\right)^2}{2\gamma\overline{p}} d\Omega,\ \delta E_s^b = \frac{\gamma(\gamma-1)M^4}{2} \int_\Omega \overline{p}\left(\delta\overline{s}^b\right)^2 d\Omega. \quad (3.33)$$

In the following, we will represent the contributions δE_c^b, δE_p^b and δE_s^b to assess the importance of base-flow kinetic energy, pressure and entropy modifications in the gain variation associated to the base-flow modification $\delta\overline{\mathbf{q}}^b$.

3.1.5 Three-dimensional perturbations

As for linear stability with the spanwise contributions of the Jacobian, the additional contributions of the second-order derivative (Hessian) operator can be computed to extend the linear sensitivity to 3D perturbations. However, the following expansions are correct only for 2D sensitivity (homogeneous gradient in z-direction) of eigenvalue/optimal gain of 3D modes. Similarly to the equation (2.32), the 3D Hessian operator can be written as $\mathbf{H}_{3\mathrm{D}}(\check{\mathbf{q}}, \overline{\mathbf{q}}) = \mathbf{H}(\check{\mathbf{q}}, \overline{\mathbf{q}}) + \mathbf{H}_z(\check{\mathbf{q}}, \overline{\mathbf{q}})$. One should notice that the base-flow $\overline{\mathbf{q}}$ remains 2D and only the response $\check{\mathbf{q}}$ brings a new 3D contribution. The three dimensional Hessian is defined as

$$\mathbf{H}_{3\mathrm{D}}(\check{\mathbf{q}}, \overline{\mathbf{q}}) = \left.\frac{\partial\left(\mathbf{A}_{3\mathrm{D}}\check{\mathbf{q}}\right)}{\partial\mathbf{q}}\right|_{\overline{\mathbf{q}}}. \quad (3.34)$$

From equation (2.32), the following expression may be derived,

$$\mathbf{H}'_{3\mathrm{D}} = \mathbf{H}' + i\beta\frac{\partial\mathbf{B}}{\partial\mathbf{q}}\check{\mathbf{q}} - \beta^2\frac{\partial\mathbf{C}_1}{\partial\mathbf{q}}\check{\mathbf{q}}. \quad (3.35)$$

Therefore, the 2D sensitivity of a 3D mode is given by the same equations as the one of a 2D mode but by replacing the 2D Hessian by the 3D Hessian written in equation (3.35).

3.2 Sensitivity analysis

In the following, the linear sensitivity analysis around a circular cylinder at low Mach number is performed for validation purpose.

3.2.1 Cylinder flow

In Figure 3.1, we show the sensitivity of the critical growth rate to a steady source term $\nabla_{\mathbf{f}}\sigma|_{\mathbf{Q}}$ (see Eq. (3.12)). We recover the same sensitivity regions and bounds as found in Figure 15(a) by Mettot et al. [124] while conversely to the finite difference approach, not any further user-input parameters is here required to compute this passive control map.

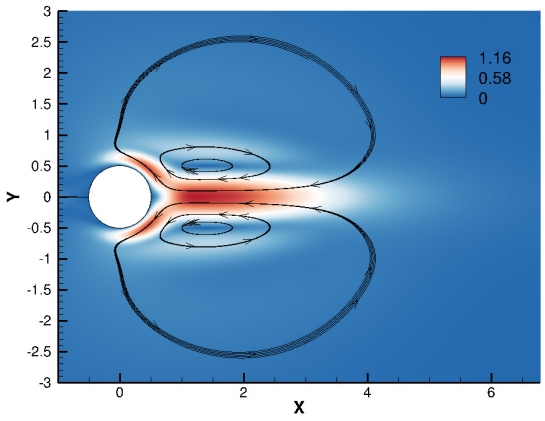

Figure 3.1: Intensity and direction of the momentum component of the growth rate sensitivity to a steady source term $\nabla_{\mathbf{f}}\sigma|_{\mathbf{Q}}$ computed with BROADCAST code. Similar to the Figure 15(a) in Mettot et al. [124].

3.2.2 Boundary layer flow

In the following, the linear stability analysis of a boundary layer over an adiabatic flat plate is performed first at low Mach number regime for validation and then at Mach number 4.5 for the rest of the chapter.

3.2.2.1 Sensitivity of optimal gain at low Mach number

Linear sensitivity of the optimal gain is first computed on an adiabatic flat plate at $M_\infty = 0.1$ (case S01). We compare with Brandt et al. [17] test case where the sensitivity analysis had been derived in a continuous and incompressible framework.

In Brandt et al. [17], the largest optimal gain at zero frequency is obtained for the streaks at $\beta\delta = 0.94$. We compare the sensitivity of this 3D mode to base-flow modifications and to forcing (Eq. 3.18) obtained by BROADCAST with the one from Brandt et al. [17] (Figure 3.2). The wall-normal profile of the streamwise component of the sensitivity to base-flow modifications is plotted at $Re_{\delta^*} = 400$ with δ^* the displacement thickness (Figure 3.2b). They show good agreement.

Then, the discrete linear sensitivity of the streaks to steady wall blowing is plotted in Figure 3.3. They show good agreement while we compare two different frameworks: discrete linearisation in a low Mach compressible framework in our work while Brandt et al. [17] used

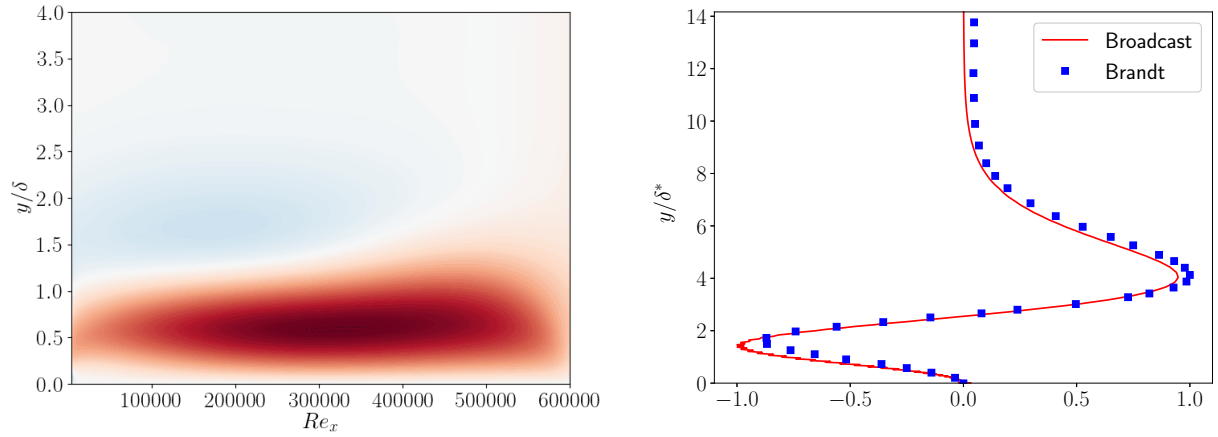

(a) **(b)**

Figure 3.2: Sensitivity of the optimal gain for the streaks ($\beta\delta = 0.94$). Comparison with Brandt et al. [17]. (a) Streamwise component of the sensitivity to steady forcing $\nabla_{\mathbf{f}}\, \mu^2\big|_{\mathbf{Q}}$. Red (resp. blue) colour is negative (resp. positive) gradient. Similar to the Figure 19(a) in Brandt et al. [17]. (b) Wall-normal profile of the streamwise component of the sensitivity to base-flow modifications $\nabla_{\overline{\mathbf{q}}}\, \mu^2\big|_{\mathbf{Q}}$ at $Re_{\delta^*} = 400$ normalised by its maximum value.

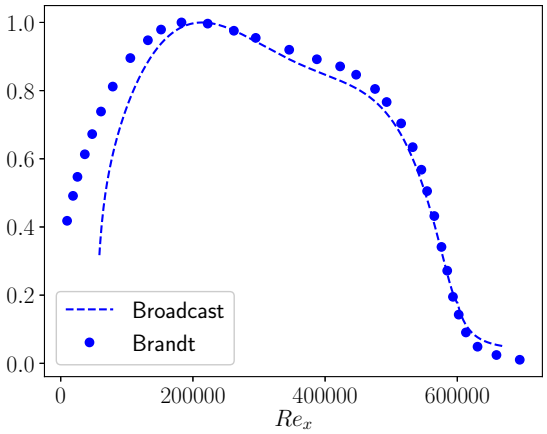

Figure 3.3: Normalised sensitivity of the optimal gain of the streaks ($\beta\delta = 0.94$) to wall blowing $\nabla_{\mathbf{v}_w}\mu^2$. Comparison with Brandt et al. [17].

a continuous linearisation in the incompressible framework. However, slight discrepancies are noticed in the leading edge part which can be explained by the fact that the leading edge was included inside the computational domain used in Brandt et al. [17] while we start at $Re_{x,\text{in}} = 4300$.

3.2.2.2 Sensitivity to base-flow modifications and steady forcing

We consider from now on and until the end of this chapter the hypersonic boundary layer case at $M_\infty = 4.5$ (case S45).

The sensitivities of the optimal gain of the first and second Mack modes to base-flow modifications $\nabla_{\overline{\mathbf{q}}}\mu_0^2$ are computed. To highlight the most predominant contributions in the sensitivity, the total optimal gain variation has been split (Eq. (3.32)) into base-flow variation components of streamwise kinetic energy $\delta E^b_{c_x}$, wall-normal kinetic energy $\delta E^b_{c_y}$, pressure δE^b_p and entropy

δE_s^b. These quantities have been reported in Figure 3.4. The largest component for both Mack modes seems to be the wall-normal kinetic energy. However, as noticed in previous studies [17, 138], a strong wall-normal base-flow velocity modification is not physical since base-flow momentum fields are divergence-free ($\partial_x \delta\overline{\boldsymbol{\rho u}} + \partial_y \delta\overline{\boldsymbol{\rho v}} = 0$). The addition of this constraint strongly damps the wall-normal velocity component of the sensitivity. Therefore, the largest component of the sensitivity becomes the streamwise velocity for both Mack modes followed by the entropy δE_s^b and pressure δE_p^b components, which are one order of magnitude lower for both Mack modes. Overall, the second Mack mode is more sensitive than the first Mack mode. The same conclusions are drawn for the streaks with a sensitivity much below the first Mack mode.

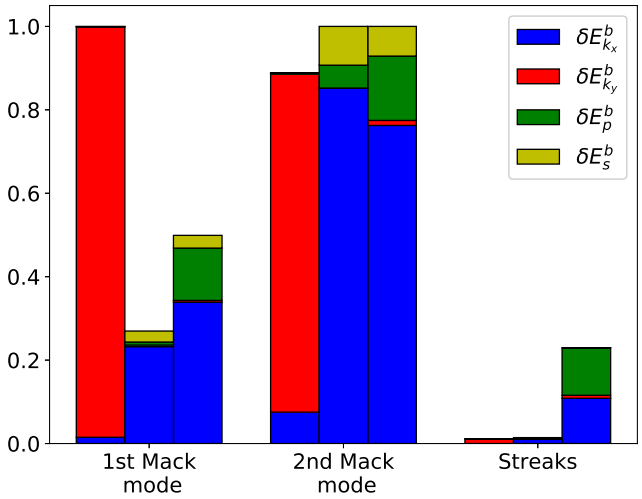

Figure 3.4: Normalised Chu's energy norm components of the sensitivity to base-flow modifications $\nabla_{\overline{\mathbf{q}}}\mu_0^2/\mu_0^2$ (first bar), to momentum-divergence-free base-flow modifications $\nabla_{\overline{\mathbf{q}}}^{df}\mu_0^2/\mu_0^2$ (second bar) and to steady forcing $\nabla_{\overline{\mathbf{f}}}\mu_0^2/\mu_0^2$ (third bar).

In Figure 3.5(a,c), the sensitivity to local modifications of the streamwise base-flow momentum $\nabla_{\overline{\boldsymbol{\rho u}}}\mu_0^2$ is plotted for both Mack modes. The sensitivity of the first Mack mode extends longer in the streamwise direction than the second Mack mode as expected from the wavemaker support (overlap of optimal forcing and response from the resolvent analysis). These sensitivities are strongest in the region between the displacement thickness δ^* and the boundary layer thickness δ_{99} ($u(y=\delta_{99}) = 0.99U_\infty$). This reminds the local results found for Fedorov's mode S [138] or for the incompressible Tollmien-Schlichting waves [17], the sensitivities $\nabla_{\overline{\boldsymbol{\rho u}}}\mu_0^2$ of the first and second Mack modes being negative at the critical layer y_c ($u(y_c) = c_r$ with $c_r = Re(\omega/\alpha)$ the phase velocity of the mode) and positive in the vicinity above and below. Park and Zaki [138] and Guo et al. [64] showed that the mean shear modification contributes the most to the sensitivity resulting in a receptive region around the critical layer. Besides, from Figure 3.5(c), it is seen that, for the second Mack mode, the generalised inflection line y_{GIP} ($\partial[\rho\partial u/\partial y]/\partial y(y_{GIP}) = 0$) of the base-flow, where the optimal forcing and optimal entropy response are maximal, is close to the critical layer y_c of the optimal response.

In Figure 3.5(b,d), the sensitivity to local modifications of the base-flow temperature $\nabla_{\overline{\mathbf{T}}}\mu_0^2$ is plotted for both Mack modes. The gradient $\nabla_{\overline{\mathbf{T}}}\mu_0^2$ is computed from the components of $\nabla_{\overline{\mathbf{q}}}\mu_0^2$ through the linearisation of the definition of the total energy E (chain rule):

$$\nabla_{\overline{\mathbf{T}}}\mu_0^2 = \frac{(\gamma-1)\gamma M^2}{\overline{\rho}}\left(\left(\frac{1}{2}(\overline{u}^2+\overline{v}^2)-\overline{e}\right)\nabla_{\overline{\rho}}\mu_0^2 - \overline{u}\nabla_{\overline{\boldsymbol{\rho u}}}\mu_0^2 - \overline{v}\nabla_{\overline{\boldsymbol{\rho v}}}\mu_0^2 + \nabla_{\overline{\boldsymbol{\rho E}}}\mu_0^2\right). \tag{3.36}$$

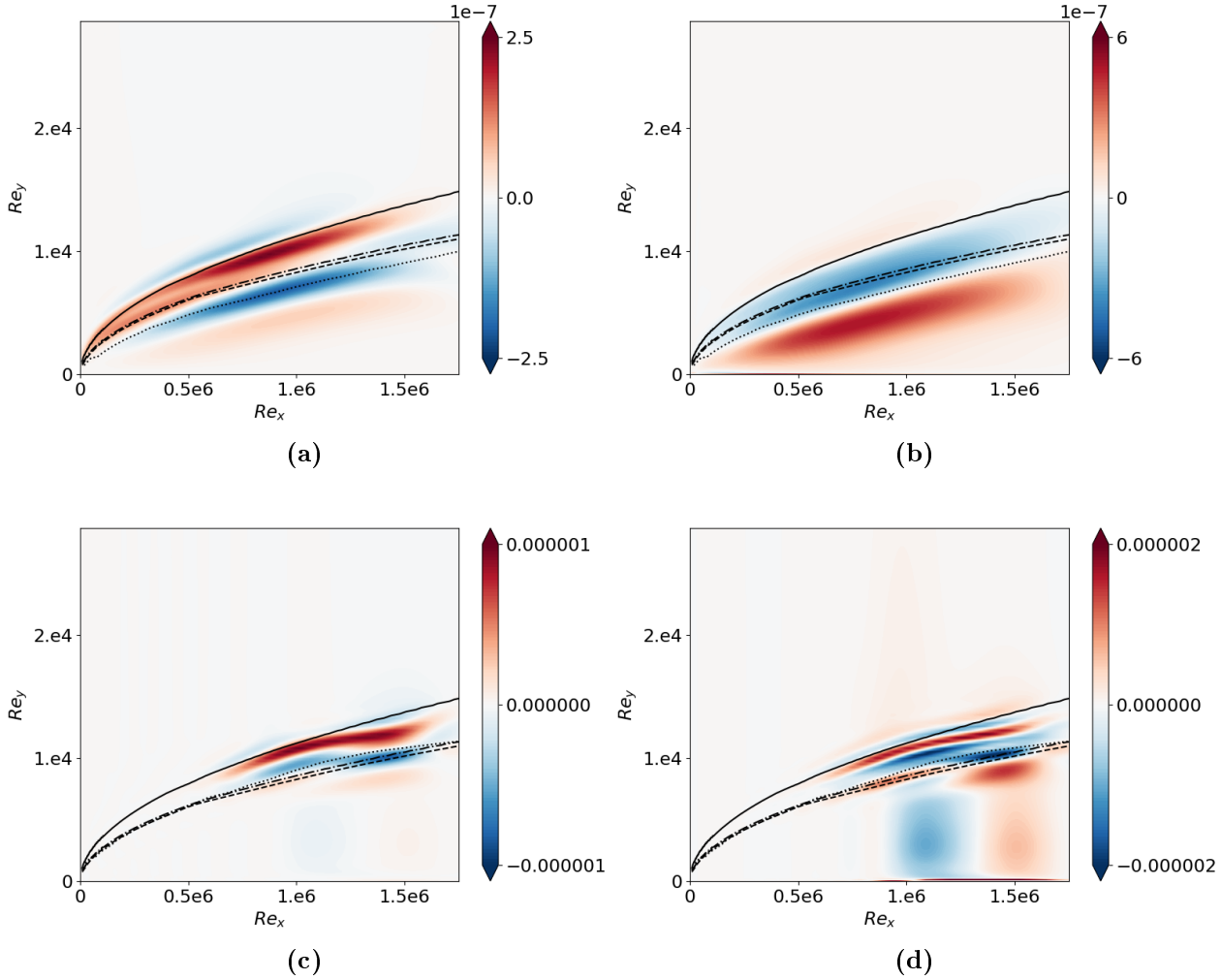

Figure 3.5: Linear sensitivity of the optimal gain to base-flow modifications $\nabla_{\overline{\mathbf{q}}}\mu_0^2/\mu_0^2$. Solid line represents the boundary layer thickness, dash-dotted line indicates the generalised inflection point, dashed line is the displacement thickness and dotted line is the critical layer. (a-b) Sensitivity of the first Mack mode. (c-d) Sensitivity of the second Mack mode. (a,c) Streamwise component of the momentum $\nabla_{\overline{\boldsymbol{\rho u}}}\mu_0^2/\mu_0^2$ (similar to the momentum-divergence-free component). (b,d) Temperature component $\nabla_{\overline{\mathbf{T}}}\mu_0^2/\mu_0^2$.

The gradient $\nabla_{\overline{\mathbf{T}}}\mu_0^2$ is not only located between y_c and δ_{99} anymore. A strong region of the gradient also exists closer to the wall for both Mack modes. In the case of the first Mack mode, the critical layer y_c line separates a positive ($y < y_c$) and a negative ($y > y_c$)) region of the gradient, likely resulting once again from the mean shear distortion. For the second Mack mode, although the sensitivity $\nabla_{\overline{\mathbf{T}}}\mu_0^2$ is similar to $\nabla_{\overline{\boldsymbol{\rho u}}}\mu_0^2$, there is an additional region of large sensitivity to changes of the base-flow temperature close to the wall from $Re_x = 10^6$ until the end of the domain.

From the sensitivity to base-flow modifications $\nabla_{\overline{\mathbf{q}}}\mu_0^2$, the sensitivity of the optimal gain to a steady volume forcing term $\nabla_{\overline{\mathbf{f}}}\mu_0^2$ is deduced. The Chu's energy norm of the sensitivity $\nabla_{\overline{\mathbf{f}}}\mu_0^2$, as well as its decomposition into different components, is reported in Figure 3.4. The different contributions reflect those of the momentum-divergence-free base-flow gradient $\nabla_{\overline{\mathbf{q}}}^{df}\mu_0^2$ for both Mack modes, however the components induced by base-flow pressure variations is larger than those induced by entropy variations and their sum $\delta E_p^b + \delta E_s^b$ exhibit a magnitude similar to the streamwise kinetic energy component $\delta E_{c_x}^b$. For the streaks, the pressure component δE_p^b is

equivalent to the streamwise kinetic energy component $\delta E^b_{c_x}$ while its entropy component δE^b_s is much smaller. The three instabilities display a sensitivity of similar magnitude.

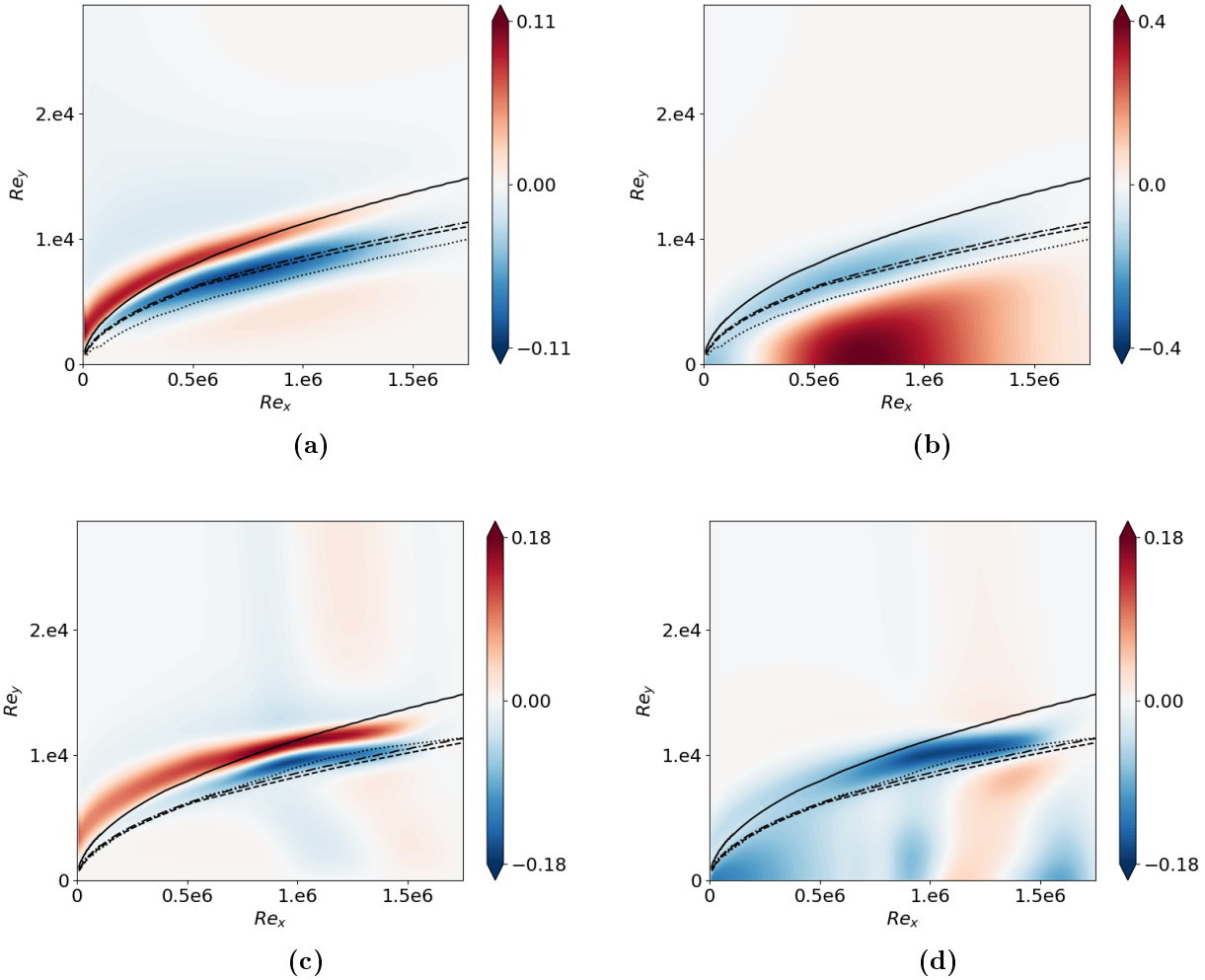

Figure 3.6: Linear sensitivity of the optimal gain to steady forcing $\nabla_{\overline{\mathbf{f}}}\mu_0^2/\mu_0^2$. Solid line represents the boundary layer thickness, dash-dotted line indicates the generalised inflection point, dashed line is the displacement thickness and dotted line is the critical layer. (a-b) Sensitivity of the first Mack mode. (c-d) Sensitivity of the second Mack mode. (a,c) Streamwise component of the momentum $\nabla_{\overline{\boldsymbol{f}_{\boldsymbol{\rho u}}}}\mu_0^2/\mu_0^2$. (b,d) Temperature component $\nabla_{\overline{\mathbf{f}_\mathbf{T}}}\mu_0^2/\mu_0^2$.

In Figure 3.6(a,c), the sensitivity to a steady streamwise momentum source term $\nabla_{\overline{\boldsymbol{f}_{\boldsymbol{\rho u}}}}\mu_0^2$ is plotted for both Mack modes. The gradients for both Mack modes are very similar with a positive region around the boundary layer thickness δ_{99} and a negative region around the displacement thickness δ^*. The mechanism below this gradient might be the local thickening of the boundary layer by the increase of the streamwise mean velocity above the edge and its decrease below.

Then, the sensitivity to a steady heating source term $\nabla_{\overline{\mathbf{f}_\mathbf{T}}}\mu_0^2$, computed with Eq. (3.36) by replacing the components of $\nabla_{\overline{\mathbf{q}}}\mu_0^2$ by $\nabla_{\overline{\mathbf{f}}}\mu_0^2$, is plotted in Figure 3.6(b,d) for both Mack modes. As for $\nabla_{\overline{\mathbf{T}}}\mu_0^2$, the sensitivity $\nabla_{\overline{\mathbf{f}_\mathbf{T}}}\mu_0^2$ has strong distortions inside the boundary layer. For the first Mack mode, the gradient is mainly positive from the wall up to the critical layer ($y < y_c$) except in the region close to the leading edge. However, in the case of the second Mack mode, the largest region of sensitivity (negative gradient) is between the displacement thickness and the boundary layer thickness. Inside the boundary layer, closer to the wall, the gradient varies

a lot in the streamwise direction for the second Mack mode. From an overall perspective, a steady heating source term has an opposite effect inside the boundary layer between the first and the second Mack modes. This recalls the well-known effect of stabilisation by cooling for the first Mack mode and by heating for the second Mack mode [108].

3.2.2.3 Sensitivity to wall boundary control

After the computation of the sensitivity to base-flow modifications and steady forcing in §3.2.2.2, the sensitivity of the streaks, first and second Mack modes to two types of modifications of the wall boundary condition are analysed:

- Small amplitude wall-normal blowing/suction $\delta v_w(x)$ at the surface of the flat plate,
- Small amplitude heat flux $\delta\phi_w(x)$ at the surface of the flat plate.

In both cases, the identity $\mathbf{Q}_p = \mathbf{I}$ is chosen for the norm associated to the parameter spaces $\mathbf{p} = v_w$ and $\mathbf{p} = \phi_w$ as the discretisation along the x-direction is uniform.

In the following, we discuss the opposite of the sensitivity $-\delta\mathbf{p}^m$ (see (3.26)), which corresponds to the optimal wall profile to be prescribed at the surface in order to mitigate the instability. This profile is plotted for blowing/suction control in Figure 3.7a and for heat flux control in Figure 3.7b. In Figure 3.7, the marker "max. Forc." refers to the maximal optimal forcing location of the first Mack mode, "branch I" to the streamwise location of branch I of the local mode linked to the first Mack mode and "max. ampli." to the location of the maximal amplification rate ($\max(-\alpha_i)$) of the local mode.

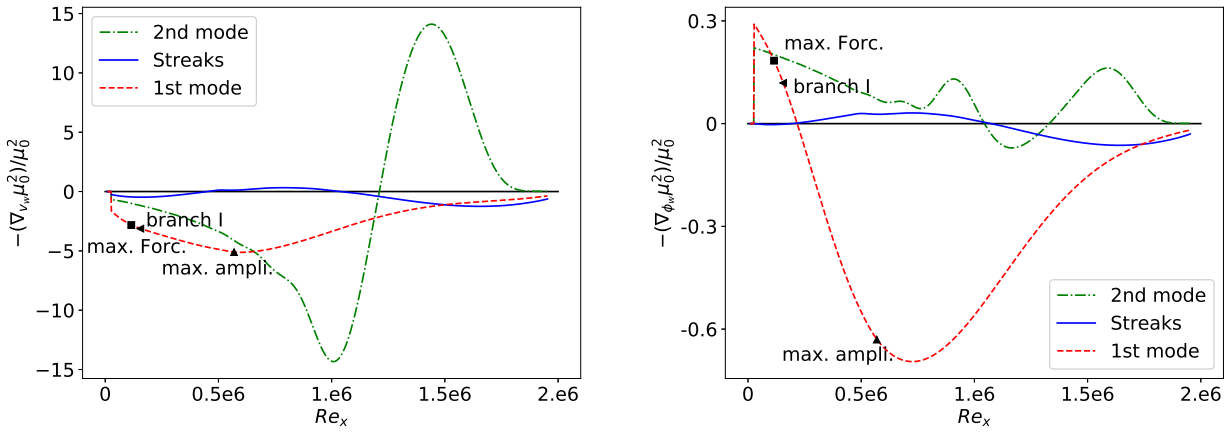

Figure 3.7: Optimal wall control profiles to damp the different instabilities i.e. opposite of the sensitivity of the optimal gain for each instability: $-\delta\mathbf{p}^m$. (a) Optimal wall-velocity profile $-\delta\mathbf{v}_w$. (b) Optimal wall heat flux profile $-\delta\boldsymbol{\phi}_w$.

Both wall velocity and heat flux control gradients highlight that the streaks are not sensitive to boundary control in comparison with the Mack modes. Furthermore, the profile to damp the streaks has a similar behaviour for both types of wall-control i.e negative in the downstream part of the domain where the optimal response of the streaks lies. In Figure 3.7a, the second Mack mode is confirmed to be the most sensitive instability to wall velocity control. Furthermore, it is the only instability among the three which is stabilised by steady wall-blowing (downstream $Re_x = 1.2\times10^6$). The gradient for the second Mack mode is studied in detail in the next section. Optimal suction actuator locations to stabilise each instability are different: $Re_x = 0.6 \times 10^6$

for the first Mack mode (close to the location of the maximal amplification rate of the local mode), $Re_x = 1 \times 10^6$ for the second Mack mode and $Re_x = 1.7 \times 10^6$ for the streaks. However, a suction actuator located anywhere upstream $Re_x = 1.2 \times 10^6$ would damp both Mack modes without affecting much the streaks. The effect of applying the second Mack mode gradient on the stability of the other instabilities is investigated in §3.2.2.4, where the design of an optimal wall-control actuator is attempted.

In figure 3.7b, it is seen that the first Mack mode is the most sensitive to wall heat flux control. The profile to damp the optimal gain of the first Mack mode has one heating zone upstream until $Re_x = 0.21 \times 10^6$ (located slightly downstream of branch I) and one cooling region downstream with the largest sensitivity close to the location of the maximal amplification rate of the local mode. The variations of the optimal wall heat flux profile to damp the second Mack mode are more complex and are studied in detail in another section. By comparing both Mack modes' wall heat flux profiles, they overall display an opposite behaviour with respect to wall heat flux changes [108], however, in some streamwise regions, they follow similar trends. First, at the leading edge, upstream $Re_x = 0.21 \times 10^6$, heating the wall would damp both Mack modes and secondly, downstream, between $Re_x = 1.045 \times 10^6$ and $Re_x = 1.33 \times 10^6$, cooling would produce the same effect. The effect of the application of the first Mack mode gradient on the stability of the other instabilities is investigated in §3.2.2.4. Furthermore, based on the zones where the gradients' sign matches between the first and second Mack modes, a control that damps both instabilities will also be discussed in this section.

One may remark that the optimal wall control profiles given by Figure 3.7 may have been partially predicted from the sensitivity $\nabla_{\mathbf{f}}\mu_0^2/\mu_0^2$ in Figure 3.6. Indeed, by looking at the sign of the gradient close to the wall, one may see that the gradients $\nabla_{\overline{\mathbf{f_T}}}\mu_0^2/\mu_0^2$ for both Mack modes have similar trends for the wall gradient $\nabla_{\phi_w}\mu_0^2$. To a factor, they predict the same streamwise variations, however, the exact derivation of the sensitivity to wall boundary control is necessary as the optimal wall control profiles will be injected at the wall boundary condition to compute new controlled base-flows and perform further resolvent analysis. Therefore, for optimisation, it is required to compute this gradient but to get general information about the sensitivity, the sensitivity to steady forcing seems sufficient for quantities slowly varying close to the boundary condition as the temperature (adiabatic condition).

From the optimal wall control profile $\delta\mathbf{p}^m$, one may compute the linear base-flow variations $\delta\overline{\mathbf{q}}^m$ induced by $\delta\mathbf{p}^m$ using Eq. (3.28). This informs us on the base-flow variations induced by the wall-control, which in turn then change the optimal gain of the instability.

First, the optimal wall-normal velocity control $\delta\mathbf{v}_w$ (which consists in blowing) of the first Mack mode induces a decrease of streamwise momentum (Figure 3.8a) between the boundary layer thickness δ_{99} and the displacement thickness δ^* and a temperature increase (Figure 3.8b) close to the displacement thickness leading to the thickening of the boundary layer. The patterns are quite constant in the streamwise direction, which reflects the quasi-uniform blowing profile $\delta\mathbf{v}_w$ of the first Mack mode. The variations of temperature (positive here) are opposite to those of streamwise momentum, showing that a deceleration of the flow in the boundary layer is accompanied to an increase of its temperature. Second, as the wall-normal velocity control $\delta\mathbf{v}_w$ of the second Mack mode involves blowing and suction along Re_x, the base-flow variations in streamwise momentum (Figure 3.8c) and temperature (Figure 3.8d) exhibit similar streamwise wavy patterns, since these fields are affected both by the induced advection linked to the blowing/suction profile. By comparing the variations $\delta\overline{\mathbf{q}}^m$ induced by wall-normal velocity control $\delta\mathbf{v}_w$ (Figure 3.8) with the gradient $\nabla_{\overline{\mathbf{q}}}\mu_0^2/\mu_0^2$ (Figure 3.5), which is the optimal base-flow variation $\delta\overline{\mathbf{q}}^b$, one may notice how wall control efficiently acts in the sensitive regions. The wall-normal velocity control $\delta\mathbf{v}_w$ indeed manages to act in the most sensitive region of the momentum component of the base-flow, it however fails to induce a shear, which is optimal to

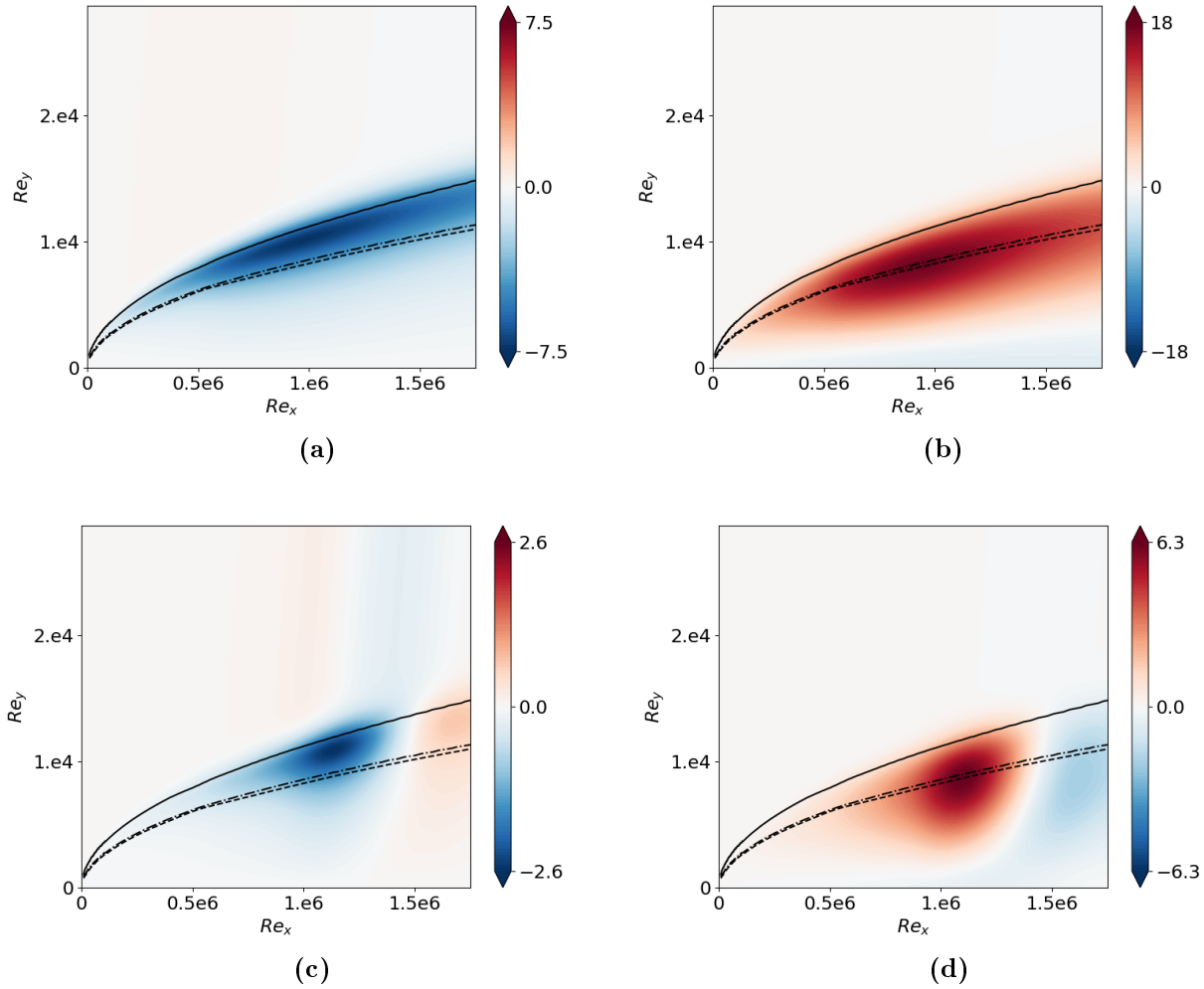

Figure 3.8: Linear base-flow variations $\delta\overline{\mathbf{q}}^m$ induced by the optimal wall-velocity control $\delta\mathbf{p}^m = \delta\mathbf{v}_w$. Solid line represents the boundary layer thickness, dash-dotted line indicates the generalised inflection point and dashed line is the displacement thickness. (a-b) First Mack mode ($\delta\mathbf{v}_w$ corresponds to blowing B). (c-d) Second Mack mode ($\delta\mathbf{v}_w$ corresponds to blowing/suction BS). (a,c) Streamwise component of the momentum $\delta\overline{\boldsymbol{\rho u}}^m$. (b,d) Temperature component $\delta\overline{\mathbf{T}}^m$.

control the Mack modes.

Secondly, the wall heat flux control $\delta\boldsymbol{\phi}_w$ of both Mack modes induces a variation of streamwise momentum (Figures 3.9a and 3.9c) between the boundary layer thickness δ_{99} and the displacement thickness δ^*, acting in the same region as the wall-normal velocity control $\delta\mathbf{v}_w$. The variations of temperature induced by the wall heat flux control $\delta\boldsymbol{\phi}_w$ of both Mack modes reproduce the optimal base-flow variations $\delta\overline{\mathbf{q}}^b$ within the boundary layer (Figures 3.9b and 3.9d compared with 3.6b and 3.6d). Because of its application at the wall, the control is maximal there, which favours the first Mack mode where the largest sensitivity region is at the wall, while the largest sensitivity region of the second Mack mode is above the critical layer. This may explain why the wall heat flux control has a larger effect on the first Mack mode (a factor 3 in terms of magnitude with respect to the second Mack mode).

Finally, the components of the linear gain variation induced by wall boundary control are computed for both Mack modes and reported in Figure 3.10. As it will be confirmed in the next section for the second Mack mode, the variation of gain induced by the modification of the Jacobian is small in comparison with the one induced by base-flow modification for both Mack

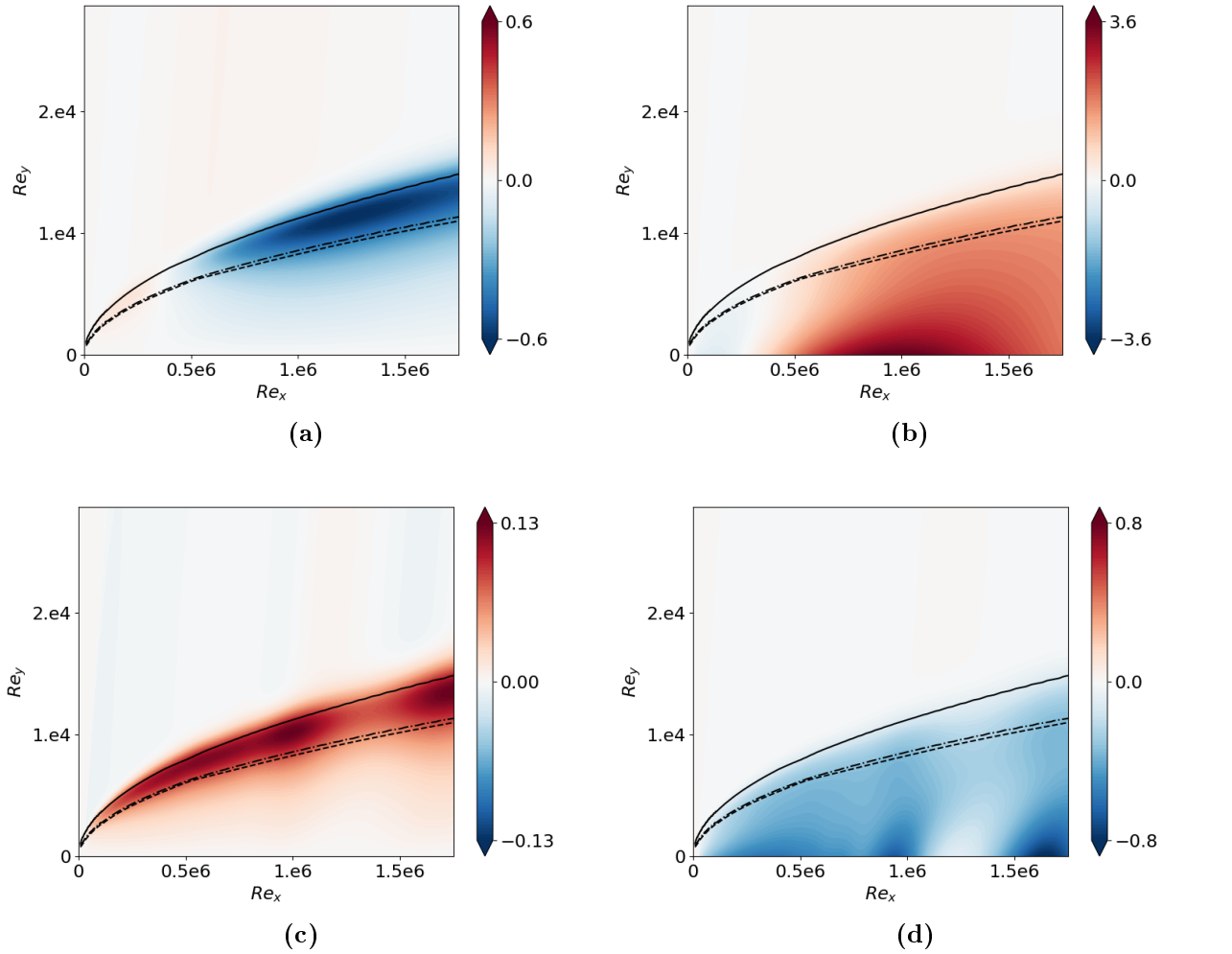

Figure 3.9: Linear base-flow variations $\delta\overline{\mathbf{q}}^m$ induced by the optimal wall heat flux control $\delta\mathbf{p}^m = \delta\boldsymbol{\phi}_w$. Solid line represents the boundary layer thickness, dash-dotted line indicates the generalised inflection point and dashed line is the displacement thickness. (a-b) First Mack mode ($\delta\phi_w$ corresponds to cooling/heating cH). (c-d) Second Mack mode ($\delta\phi_w$ corresponds to cooling/heating/cooling ChC). (a,c) Streamwise component of the momentum $\delta\overline{\boldsymbol{\rho u}}^m$. (b,d) Temperature component $\delta\overline{\mathbf{T}}^m$.

modes. By analysing the contributions driven by the base-flow modification, the pressure component is always the smallest. The streamwise momentum and entropy components represent most of the energy, except for the gain variation of the first Mack mode induced by the optimal heat flux profile and the streaks where the wall-normal component contributes as much as the entropy in the energy. The streamwise momentum energy change always exhibits an effect opposite to the one of the entropy for both Mack modes. Finally, in nearly all cases, the linear gain variation is driven by the streamwise momentum base-flow change, except for the second Mack mode with heat flux control where it is the entropy modification of the base-flow. This raises the possibility of simultaneous control of both Mack modes if a heat flux actuator is designed to trigger variations of same sign in the streamwise momentum and entropy components (the optimal profiles discussed here trigger opposite effects in these two components).

Sensitivity of the second Mack mode to steady wall blowing

The variations of the optimal wall-normal velocity profile to damp the second Mack mode are analysed in further details. Then, linear predictions are compared to non-linear computations

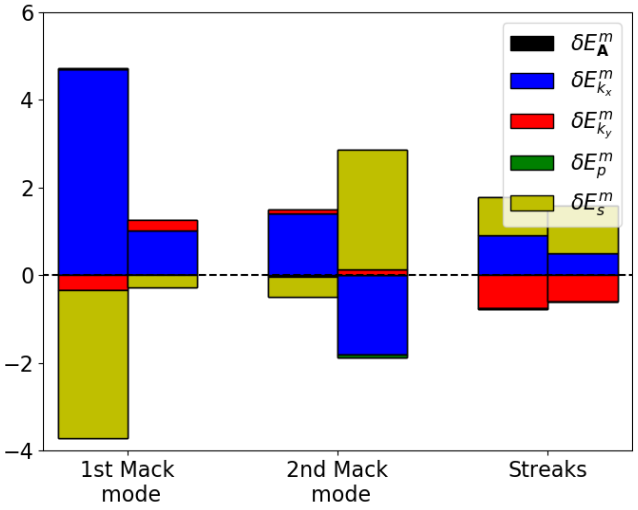

Figure 3.10: Chu's energy norm components of the linear gain variation induced by the wall boundary control normalised for each instability. The first bar refers to the optimal wall-velocity control $\delta\mathbf{v}_w$: blowing for the first Mack mode, blowing/suction for the second Mack mode and blowing/suction/blowing for the streaks. The second bar refers to the optimal wall heat flux control $\delta\boldsymbol{\phi}_w$: cooling/heating for the first Mack mode, cooling/heating/cooling for the second Mack mode and heating/cooling/heating for the streaks. The Jacobian and pressure components are not apparent as they are more than one order of magnitude below the other components.

for increasing blowing amplitudes to assess the predicting capabilities of linear gradients.

First, the optimal steady wall-normal velocity profile to damp the second Mack mode and its decomposition into various components are plotted in Figure 3.11. As seen from the integral energy in Figure 3.10, the gradient $\nabla_{\mathbf{v}_w}\mu_0^2$ is mainly produced from the sensitivity term due to the base-flow variation as the term due to the Jacobian variation is of smaller amplitude. The low impact of the Jacobian modifications on the gradient is due to the fact that the wall-normal velocity prescribed at the wall only appears in the energy equation in the linearised wall boundary condition.

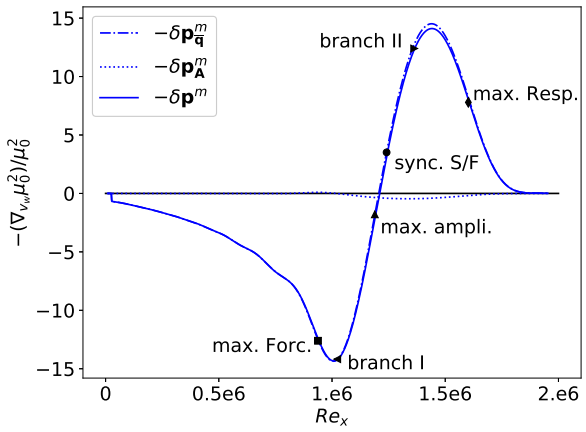

Figure 3.11: Optimal wall-velocity profile to damp the second Mack mode i.e. opposite of the sensitivity of the optimal gain of the second Mack mode to wall blowing $-\delta\mathbf{p}^m = -\delta\mathbf{v}_w$. Base-flow component $-\delta\mathbf{p}_{\mathbf{q}}^m$ and Jacobian component $-\delta\mathbf{p}_{\mathbf{A}}^m$ are also indicated, the latter being almost zero.

The total gradient may be split into two main parts: suction in the upstream region up to $Re_x \approx 1.2 \times 10^6$ and blowing downstream. In Figure 3.11, the markers "max. Forc" and "max. Resp" indicate respectively the locations of maximal optimal forcing and response for the second Mack modes (peak values from Figure 2.13b). The markers "branch I" and "branch II" refer respectively to the beginning and end in the downstream direction of the unstable region of the local mode S. The marker "max. ampli." denotes the location of the largest negative amplification rate of the local mode S. The marker "sync. S/F" indicates the synchronisation point which is the streamwise location where the phase velocities of mode S and F are equal. Furthermore, we give evidence in appendix C that the location of the above points within the gradients (for both types of wall-control) remain relatively constant for different frequencies.

In the following, to fix the control amplitude, we introduce the momentum coefficient C_θ as the ratio between the momentum injected at the wall and the free-stream momentum deficit,

$$C_\theta = \frac{\int_{y=0} |(\rho v^2)'| \, dx}{\int_{x=x_{out}} (\rho_\infty U_\infty^2 - \rho u^2) \, dy}, \tag{3.37}$$

with $(\rho v^2)'$ the difference of wall-normal momentum ρv^2 between controlled and uncontrolled base-flow. To understand the effect of the control profile shown in Figure 3.11, we compare local stability (spatial LST) analysis results applied on the uncontrolled base-flow and on the controlled base-flow with the full stabilising gradient at $C_\theta = 3.2 \times 10^{-6}$. Fong et al. [53] indeed showed that the location of a roughness element upstream or downstream the synchronisation point results in opposite stabilisation effects. We find similar trends as the intersection of the phase velocity of Fedorov's mode F and S is close to the point where the gradient is null in Figure 3.11. We also highlight that the locations of branch I and branch II of mode S are respectively close to the maxima for suction and for blowing.

Phase velocities and amplification rates of modes S and F are shown in Figure 3.12 with and without the application of the stabilising wall profile. The phase velocity of mode S remains quite similar in both cases while the phase velocity of mode F of the controlled base-flow slightly deviates from the original in the control region. This results in a shorter synchronisation region between mode F and S leading to a shorter unstable region for the amplification rate of mode S induced by the modification of branch I location. Zhao et al. [200] noticed the same behaviour for the phase velocity in the case of heating and cooling strips control.

In the following, we compare the prediction obtained by the gradient approach and the exact results obtained by computing the modified base-flow and the associated resolvent gains.

We plot in Figure 3.13a the optimal gain variations for $\beta = 0$ as a function of frequency F (around the first and second Mack modes' frequencies). The exact "nonlinear" optimal gain variations are given with lines and the linear predictions with stars of same colour. The linear predictions are evaluated by writing Eq. (3.21) as $\mu_0^2(\mathbf{p} - \epsilon \nabla_{\mathbf{p}} \mu_0^2) = \mu_0^2(\mathbf{p}) - \epsilon \|\nabla_{\mathbf{p}} \mu_0^2\|^2$ with ϵ a function of C_θ. The maximal optimal gain reduction for different values of C_θ is reported in Table 3.1. At $C_\theta = 3.2 \times 10^{-8}$, the linear prediction remains accurate while from $C_\theta = 3.2 \times 10^{-6}$, the nonlinear (0.811) and linear (0.686) predicted optimal gain ratios of the second Mack mode deviate from each other (the two-dimensional first Mack mode being well predicted by the linear sensitivity according to Figure 3.13a). Increasing further the blowing momentum coefficient C_θ allows reaching an optimal gain ratio of 0.62 at $C_\theta = 1.2 \times 10^{-4}$. However, we observe from the curve $\mu_0(F)$ in Figure 3.13a that the control damps efficiently the optimal gain at the frequency where it was computed but not for lower or higher frequencies resulting in a split of the second Mack mode into two peak regions: a first peak at $F = 2 \times 10^{-4}$ and a second for higher frequencies above $F = 3 \times 10^{-4}$. This effect was also noticed by Miró Miró and Pinna [126] on the growth rate. The optimisation procedure could in principle be pursued by computing a new descend direction to eventually reach a local/global minimum.

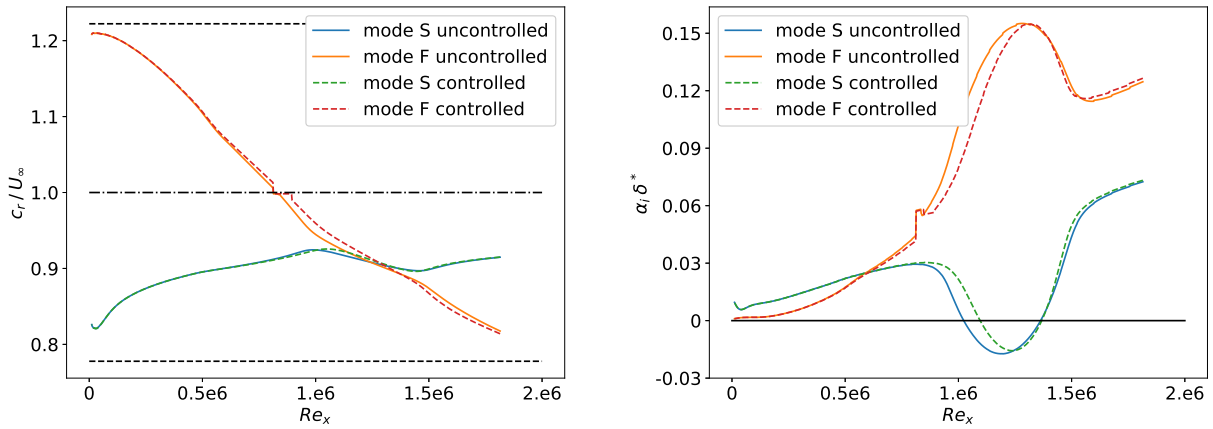

Figure 3.12: Local stability analysis of an uncontrolled base-flow (solid lines) and a controlled base-flow (dashed lines) with the optimal wall-velocity profile $-\nabla_{\mathbf{v}_w}\mu_0^2/\mu_0^2$ at $C_\theta = 3.2\times10^{-6}$. (a) Phase velocity c_r/U_∞. Dashed lines denote respectively from top to bottom the phase velocities $1+1/M_\infty$, 1 and $1-1/M_\infty$. (b) Amplification rate $\alpha_i\delta^*$.

Figure 3.13a overall shows that the control applied on the base-flow strongly reduces the optimal gain μ_0 for the initial frequency of the second Mack mode without modifying the gains of the sub-optimal gain μ_1. While the optimal gain is effectively damped with an increased wall-normal velocity control, the sub-optimal gain remains of similar magnitude compared to the no-control case and does not increase. This results in a low-rank loss of the system (ratio of approximately 4 between optimal and suboptimal gains which decreases to 2 for $C_\theta = 1.2\times10^{-4}$). Therefore, for larger control intensity, the optimal gain alone is not sufficient anymore to characterise the linear dynamics of the boundary layer.

The Chu's energy densities of the optimal forcing and response with blowing/suction control at $C_\theta = 3.2\times10^{-6}$ are plotted in Figure 3.13b and compared to the results without control. The optimal forcing has been shifted slightly downstream while the optimal response exhibits a slightly smaller support (we recall that the response energy is normalised by $\langle\check{\mathbf{q}},\mathbf{Q}_q\check{\mathbf{q}}\rangle = 1$ so that the integral under the curve is 1). The downstream shift of the optimal forcing is expected as the boundary layer thickness has been locally reduced because of the suction at the wall until $Re_x = 1.2\times10^6$. The response is not shifted downstream as the wall-blowing control increases again the boundary layer thickness to almost recover its value without control (an example of boundary layer thicknesses with and without control is shown in Figure 3.17a). This can be understood from spatial LST results, where Branch I is shifted downstream while Branch II does not move.

Sensitivity of the second Mack mode to steady wall heating

The sensitivity analysis and all the subsequent steps performed for the steady wall-blowing control are repeated in the case of the steady wall heat flux control. The optimal wall heat flux profile to damp the second Mack mode is plotted in Figure 3.14. As the gradient with respect to wall-blowing, the contribution from the Jacobian variation in the gradient $\nabla_{\phi_w}\mu_0^2$ is negligible.

The gradient shows two heating and one cooling zones. First, the largest sensitivity is close to the leading edge. This large sensitivity upstream of the forcing was already highlighted by Fedorov et al. [51] through the analysis of the effect of a local volume energy source term. Then,

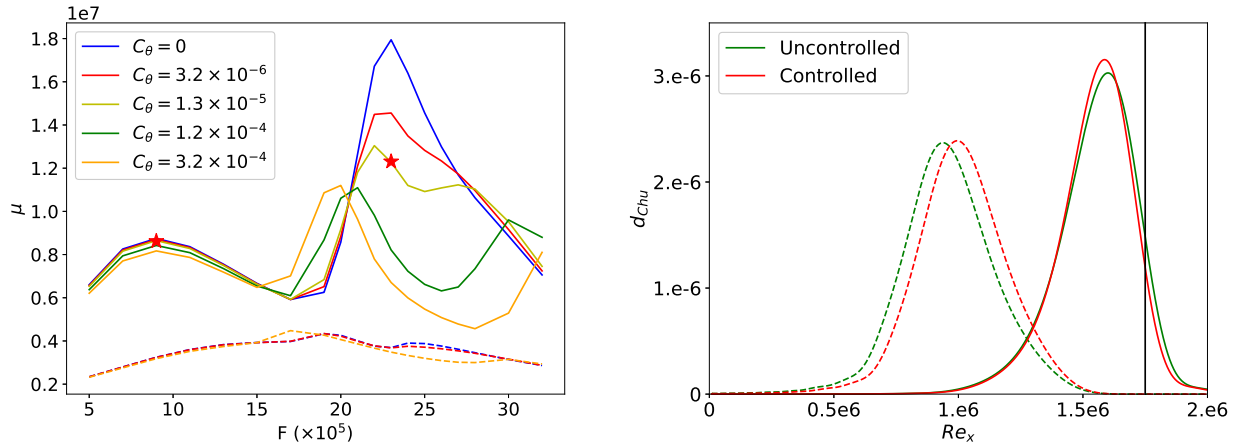

(a) **(b)**

Figure 3.13: Resolvent analysis for different base-flows controlled with the optimal wall-velocity profile $-\nabla_{\mathbf{v}_w}\mu_0^2/\mu_0^2$. (a) Optimal gain μ for $\beta = 0$ with respect to the frequency F for $C_\theta = 0$ (blue), $C_\theta = 3.2\times10^{-6}$ (red), $C_\theta = 1.3\times10^{-5}$ (yellow), $C_\theta = 1.2\times10^{-4}$ (green) and $C_\theta = 3.2\times10^{-4}$ (orange). Solid lines indicate the optimal gain μ_0 while dashed lines indicate the first suboptimal gain μ_1. The stars indicate the linear gain predicted from the gradient. (b) Energy density d_{Chu} of the optimal forcing (dashed lines) and response (solid lines) of the second Mack mode without control (green) and for the controlled base-flow at $C_\theta = 3.2 \times 10^{-6}$ (red). Black vertical line indicates the end of the optimisation domain for resolvent analysis.

C_θ	Gain μ_0	Gain ratio	Linear gain ratio
3.2×10^{-8}	1.755×10^7	0.978	0.973
3.2×10^{-6}	1.456×10^7	0.811	0.686
1.3×10^{-5}	1.304×10^7	0.727	X
1.2×10^{-4}	1.110×10^7	0.618	X
3.2×10^{-4}	1.120×10^7	0.624	X

Table 3.1: Optimal gain evolution of the second Mack mode with respect to the optimal wall-velocity profile $-\nabla_{\mathbf{v}_w}\mu_0^2/\mu_0^2$ at various momentum coefficient C_θ intensity. Gain ratio is computed by $\mu_0(C_\theta \neq 0)/\mu_0(C_\theta = 0)$. The expected linear gain ratio is computed by $\sqrt{\mu_0^2 - \epsilon\|\nabla_{\mathbf{p}}\mu_0^2\|^2}/\mu_0$ with ϵ being a function of C_θ. The cross X indicates that the linear gain ratio would predict an unphysical negative value.

local maxima of the gradient in the heating zone seems to correspond to the maximal forcing and response zones. The same behaviour is noticed at a different frequency (see appendix C). Then, the cooling sensitivity region is located in the wavemaker region where forcing and response overlap, more precisely between branch I and branch II of mode S. Previous studies [6, 200] have found that cooling upstream of the synchronisation point and heating downstream damp the second Mack mode. In the present result, the shift between cooling and heating regions of sensitivity is not located at the synchronisation point (but close to branch II of mode S). This discrepancy may be explained by the fact that, contrary to previous studies where the forcing structure was kept fixed when control was applied, we let the forcing adapt and be optimised as the control is applied (see Figure 3.16b).

We now prescribe the heat flux profile given by $-\nabla_{\phi_w}\mu_0^2$ at the wall, compute a new base-flow and repeat the resolvent analysis. To quantify the wall heat flux control applied to the base-flow, similarly to the blowing momentum coefficient C_θ, we define an energy coefficient C'_θ

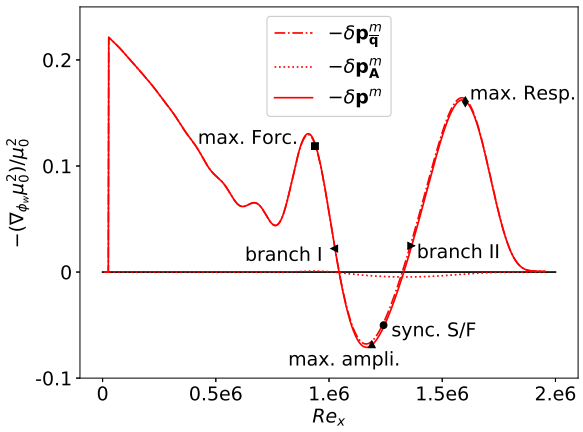

Figure 3.14: Optimal wall heat flux profile to damp the second Mack mode i.e. opposite of the sensitivity of the optimal gain of the second Mack mode to wall heat flux $-\delta\mathbf{p}^m = -\delta\boldsymbol{\phi}_w$. Base-flow component $-\delta\mathbf{p}^m_{\mathbf{q}}$ and Jacobian component $-\delta\mathbf{p}^m_{\mathbf{A}}$ are also indicated, the latter being almost zero.

based on the ratio of energy injected at the wall over the free-stream energy deficit:

$$C'_\theta = \frac{\int_{y=0} \lambda |\frac{\partial T}{\partial y}|\, dx}{\int_{x=x_{out}} (\rho_\infty E_\infty U_\infty - \rho E u)\, dy}, \tag{3.38}$$

with $\lambda \frac{\partial T}{\partial y}$ the heat flux injected (the uncontrolled case being adiabatic) where $\lambda = \eta c_p / Pr$ and η the dynamic viscosity. To understand the effect of the control profile shown in Figure (3.14), we compare local stability (spatial LST) analysis results applied on the uncontrolled base-flow and on the controlled base-flow with the full stabilising gradient at $C'_\theta = 1.0 \times 10^{-2}$.

Phase velocities and amplification rates of modes S and F are shown in Figure 3.15 with and without the application of the stabilising wall profile. Unlike the blowing/suction case, the phase velocity of both modes F and S of the controlled base-flow now slightly deviate from the original ones in the control region. This results in a shorter synchronisation region between mode F and S leading to a shorter unstable region for the amplification rate of mode S induced by both the modification of branch I and II locations. Zhao et al. [200] noticed the same behaviour for the phase velocity in the case of heating and cooling strips control with a stronger increase of the phase velocity of mode F.

In the following, we compare the predictions obtained by the gradient approach and the exact results obtained by computing the modified base-flow and the resolvent analysis.

We plot in Figure 3.16a the optimal gain for $\beta = 0$ as a function of frequency F computed for the controlled base-flow with different values of C'_θ. The maximal optimal gain reduction for different values of C'_θ is reported in the Table 3.2. At $C'_\theta = 1.9 \times 10^{-4}$, the linear prediction remains accurate while above $C'_\theta = 1.0 \times 10^{-2}$, the nonlinear (0.809) and linear (0.658) predicted optimal gain ratios of the second Mack mode start to significantly deviate from each other. The linear predictions for the two-dimensional first Mack mode remain accurate for larger C'_θ. The control applied on the base-flow reduces the optimal gain for the frequencies around the second Mack mode but strongly increases it for the lower frequencies corresponding to the two-dimensional first Mack mode up to the point where this mode becomes the dominant one at $C'_\theta = 2.1 \times 10^{-2}$. Furthermore, the first suboptimal gain μ_1 for the different energy coefficients are also plotted in Figure 3.16a. While the optimal gain μ_0 is effectively damped with an increased wall-temperature control, the suboptimal gain μ_1 increases. As for blowing/suction control, it appears that the optimal response alone will not be sufficient to describe the dynamics of the boundary layer for a large amplitude wall-temperature control.

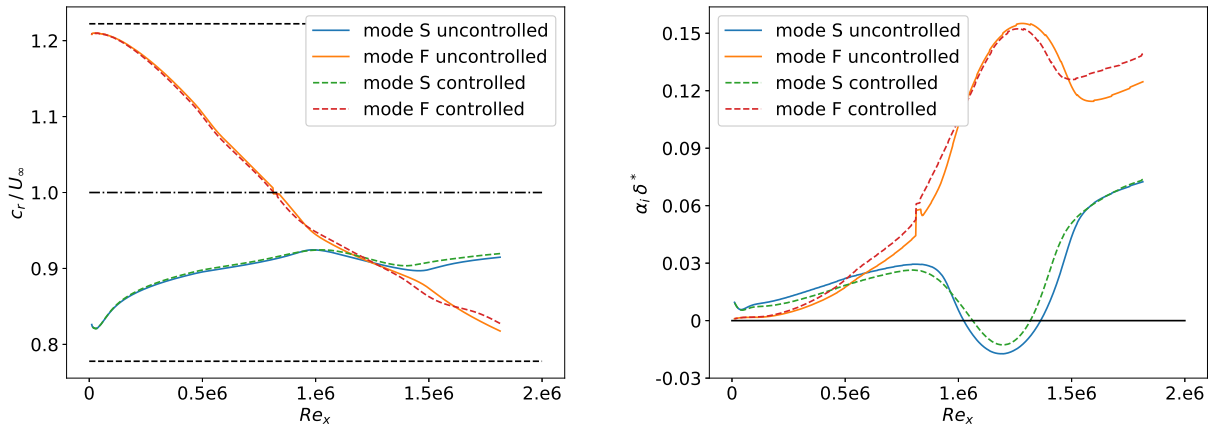

(a) **(b)**

Figure 3.15: Local stability analysis of the uncontrolled base-flow (solid lines) and the controlled base-flow (dashed lines) with the optimal wall heat flux profile $-\nabla_{\phi_w}\mu_0^2/\mu_0^2$ for $C'_\theta = 1.0 \times 10^{-2}$. (a) Phase velocity c_r/U_∞. Dashed lines denote respectively from top to bottom the phase velocities $1 + 1/M_\infty$, 1 and $1 - 1/M_\infty$. (b) Amplification rate $\alpha_i\delta^*$.

The Chu's energy densities of the optimal forcing and response with heating/cooling control at $C'_\theta = 1.66\times10^{-2}$ are plotted in Figure 3.16b and compared without control. Both the optimal forcing and response densities exhibit a larger support with control than without. Comparing with the blowing/suction case, there is both a downstream shift of the optimal forcing and an upstream shift of the optimal response. This can be understood from spatial LST results, where Branch I is seen to be shifted downstream and Branch II upstream.

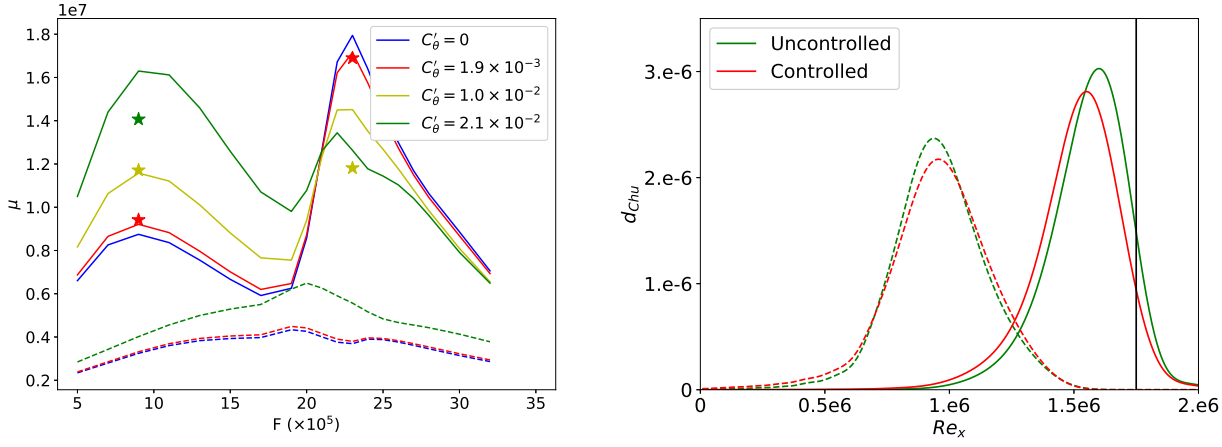

(a) **(b)**

Figure 3.16: Resolvent analysis for different base-flows controlled with the optimal wall heat flux profile $-\nabla_{\phi_w}\mu_0^2/\mu_0^2$. (a) Optimal gain μ for $\beta = 0$ as a function of frequency F for $C'_\theta = 0$ (blue), $C'_\theta = 1.9 \times 10^{-3}$ (red), $C'_\theta = 1.0 \times 10^{-2}$ (yellow) and $C'_\theta = 2.1 \times 10^{-2}$ (green). Solid lines indicate the optimal gain μ_0 while dashed lines indicate the first suboptimal gain μ_1. The stars indicate the linear gain predicted from the gradient. (b) Energy density d_{Chu} of the optimal forcing (dashed lines) and response (solid lines) of the second Mack mode without control (green) and for the controlled base-flow at $C'_\theta = 1.0\times10^{-2}$ (red). Black vertical line indicates the end of the optimisation domain for resolvent analysis.

C'_θ	Gain μ_0	Gain ratio	Linear gain ratio
1.9×10^{-4}	1.789×10^7	0.997	0.994
1.9×10^{-3}	1.716×10^7	0.956	0.942
1.0×10^{-2}	1.451×10^7	0.809	0.658

Table 3.2: Optimal gain evolution of the second Mack mode with respect to the optimal wall heat flux profile $-\nabla_{\phi_w}\mu_0^2/\mu_0^2$ at various energy coefficient C'_θ intensity. Gain ratio is computed by $\mu_0(C'_\theta \neq 0)/\mu_0(C'_\theta = 0)$. The expected linear gain ratio is computed by $\sqrt{\mu_0^2 - \epsilon\|\nabla_{\mathbf{p}}\mu_0^2\|^2}/\mu_0$ with ϵ a function of C'_θ.

3.2.2.4 Design of a wall actuator targeting all instabilities

Once the sensitivity regions of the three instabilities to wall control have been identified (§3.2.2.3), the initial steps for the design of an optimal wall-control actuator can be performed. We first consider the full stabilising profiles given by the gradients $-\nabla_{\mathbf{p}}\mu_0^2/\mu_0^2$ (Figure 3.7) of largest magnitude for blowing/suction and cooling/heating:

- The wall-normal blowing/suction profile $-\nabla_{\mathbf{v}_w}\mu_0^2/\mu_0^2$ of the second Mack mode.
- The wall heat flux profile $-\nabla_{\phi_w}\mu_0^2/\mu_0^2$ of the first Mack mode.

We apply these profiles at the wall, compute a new base-flow and repeat the resolvent analysis over the whole range of spanwise wavenumbers and frequencies, to assess the overall performance of each control strategy. We perform these computations at the finite control amplitude $C_\theta = 3.2 \times 10^{-4}$ for blowing/suction control, at $C'_\theta = 6.4 \times 10^{-3}$ and $C'_\theta = 4.0 \times 10^{-2}$ for heat flux control. Mach number and temperature of the controlled base-flows are plotted in Figure 3.17, resolvent gain maps in Figure 3.18. Table 3.3 summarises the optimal gain reduction for all the actuators considered.

Type of wall control	Intensity	1st mode gain ratio	2nd mode gain ratio	Streaks gain ratio	Global peak ratio
$-\nabla_{\mathbf{v}_w}\mu_0^2$ (2nd Mack mode)	$C_\theta = 3.2 \times 10^{-4}$	0.80	**0.53**	1.07	0.80
$-\nabla_{\phi_w}\mu_0^2$ (1st Mack mode)	$C'_\theta = 6.4 \times 10^{-3}$	**0.69**	1.06	0.99	0.69
$-\nabla_{\phi_w}\mu_0^2$ (1st Mack mode)	$C'_\theta = 4.0 \times 10^{-2}$	–	1.27	1.06	0.42
Heating strip	$C'_\theta = 0.9 \times 10^{-2}$	0.83	**0.72**	0.98	0.83
Cooling strip	$C'_\theta = 0.9 \times 10^{-2}$	**0.75**	1.03	0.93	0.75
Heating & Cooling strips	$C'_\theta = 6.4 \times 10^{-3}$	**0.83**	0.85	0.97	0.83
Heating & Cooling strips	$C'_\theta = 0.9 \times 10^{-2}$	0.81	**0.73**	0.92	0.81

Table 3.3: Optimal gains evolution with respect to different wall control profiles. Gain ratio is computed by $\mu_0(C_\theta \neq 0)/\mu_0(C_\theta = 0)$. Note that 1st (resp. 2nd and Streaks) gain ratio refers to the maximum gain over (F, β) in the region of the 1st Mack (resp. 2nd Mack and Streaks) mode. The last column, global peak ratio, represents the global maximum over the whole domain (F, β): $\max \mu_0(C_\theta \neq 0)/\max \mu_0(C_\theta = 0)$.

For blowing/suction control, we observe in Figure 3.18a that the first Mack mode has also been reduced (optimal gain ratio of 0.80) because of the suction upstream. For two-dimensional disturbances, as seen in §3.2.2.3, the second Mack mode is damped around the frequency where the gradient has been computed but increased at lower and higher frequencies resulting in a shift of the second Mack mode to lower frequencies. Therefore, the overall optimal gain peak

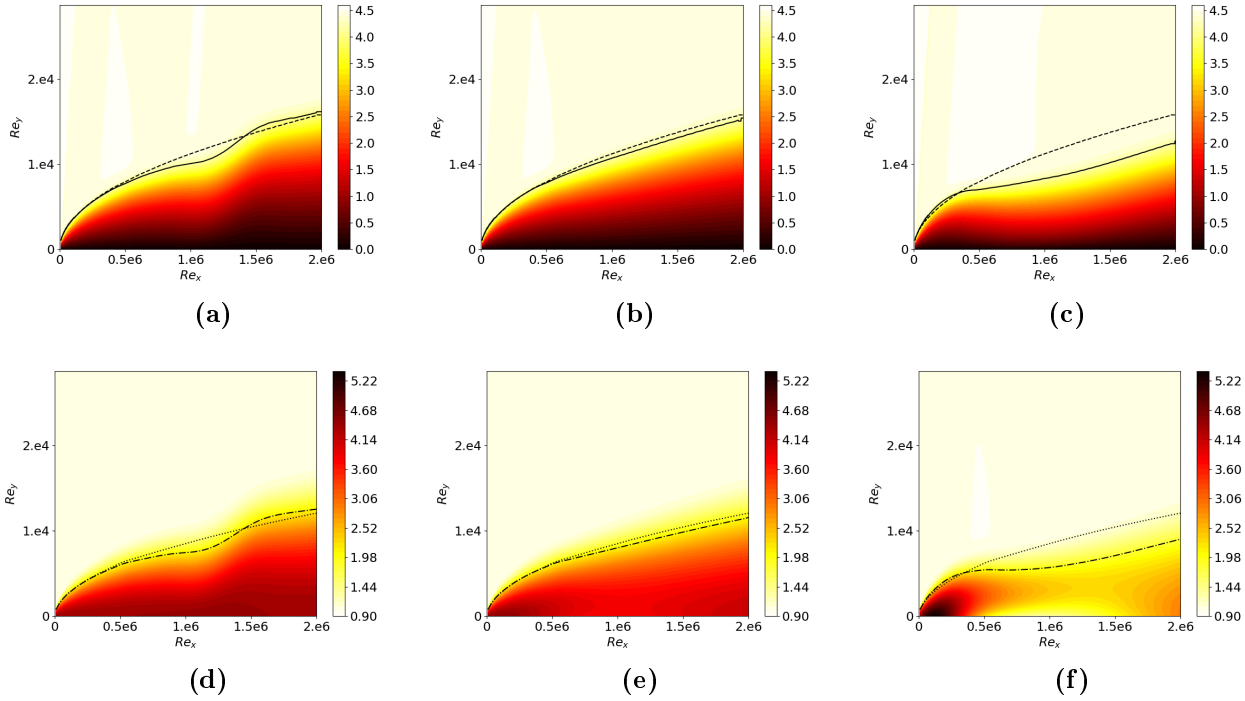

Figure 3.17: Mach number (a-c) and temperature (d-f) of the controlled base-flows. (a,d) Blowing control given by the wall-velocity profile $-\nabla_{\mathbf{v}_w}\mu_0^2/\mu_0^2$ for the second Mack mode at $C_\theta = 3.2 \times 10^{-4}$. (b,e) Heat flux control given by the wall heat flux profile $-\nabla_{\phi_w}\mu_0^2/\mu_0^2$ for the first Mack mode at $C'_\theta = 6.4 \times 10^{-3}$. (c,f) Heat flux control given by the wall heat flux profile $-\nabla_{\phi_w}\mu_0^2/\mu_0^2$ for the first Mack mode at $C'_\theta = 4.0 \times 10^{-2}$. In (a-c), solid line indicates the boundary layer thickness with control and dashed line indicates the boundary layer thickness of the uncontrolled base-flow (see Figure 2.8). In (d-f), dash-dotted line indicates the total energy deficit thickness $\delta_E = \int_{y=0}^{+\infty} \left(1 - \frac{\rho E u}{\rho_\infty E_\infty U_\infty}\right) dy$ and dotted line indicates δ_E of the uncontrolled base-flow.

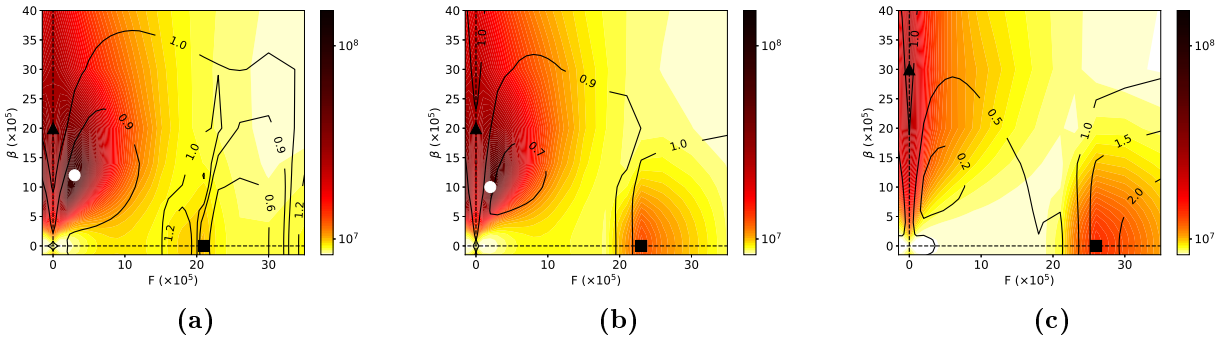

Figure 3.18: Optimal gain μ_0 of controlled boundary layers. White circle denotes the first Mack mode, black triangle denotes the streaks and black square denotes the second Mack mode. Contour lines denote the ratio of the optimal gain with control over the optimal gain without control $\mu_0(C'_\theta \neq 0)/\mu_0(C'_\theta = 0)$ given by Figure 2.13a. (a) Blowing / suction control with wall-velocity profile $-\nabla_{\mathbf{v}_w}\mu_0^2/\mu_0^2$ for the second Mack mode at $C_\theta = 3.2 \times 10^{-4}$. (b) Heat flux control with wall heat flux profile $-\nabla_{\phi_w}\mu_0^2/\mu_0^2$ for the first Mack mode at $C'_\theta = 6.4 \times 10^{-3}$. (c) Heat flux control given with wall heat flux profile $-\nabla_{\phi_w}\mu_0^2/\mu_0^2$ for the first Mack mode at $C'_\theta = 4.0 \times 10^{-2}$.

ratio of the second Mack mode is decreased to 0.53, however, the blowing/suction mechanism is difficult to apply to realistic configurations.

Considering heat flux control, in Figure 3.18b, the frequencies around the first Mack mode

have been reduced leading to an optimal gain ratio of 0.69. Nonetheless, as expected from the heat flux gradients in Figure 3.7b, the second Mack mode is promoted by wall cooling, frequencies higher than $F = 2.2 \times 10^{-4}$ being amplified. Increasing the intensity of the control (Figure 3.18c) leads to the same results exhibiting a larger optimal gain for the second Mack mode while the first Mack mode is damped such that the local peak of this instability vanishes making the streaks the most dominant mechanism (highest optimal gain).

In order to design a wall control actuator which damps all instabilities, two avenues are revealed from the computations above (combining blowing and heating is not considered in this work). The first would be a series of suction actuators in the upstream part of the flat plate which would damp both Mack modes but this option is not selected because of practical implementation challenges in realistic configurations. The second is a series of constant heating and cooling strips with an appropriate location so that they would damp both Mack modes. By inspecting the heat flux gradients in Figure 3.7b, the gradients for both Mack modes have the same direction in two locations: heating from the leading edge until $Re_x = 0.21 \times 10^6$ and cooling between $Re_x = 1.045 \times 10^6$ and $Re_x = 1.33 \times 10^6$. Therefore, we apply a constant heating strip at the first location and a constant cooling strip at the second location, the relative intensity of the heating/cooling strips being computed from the integrals (within each strip location) of the sum of the heat flux gradients of both Mack modes, such that any of the mode is favoured. This yields to a similar amplitude for heating and cooling, the cooling being stronger by 1.175 than the heating.

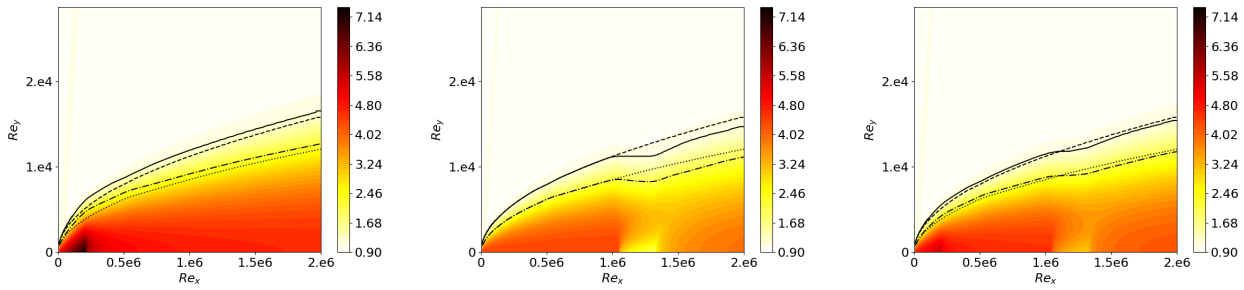

(a) **(b)** **(c)**

Figure 3.19: Temperature of the controlled base-flows. Solid line (resp. dashed) indicates the boundary layer thickness of the uncontrolled (resp. controlled) base-flow. Dotted line (resp. dash-dotted) indicates the total energy deficit thickness δ_E of the uncontrolled (resp. controlled) base-flow. (a) Heating strip upstream with $C'_\theta = 0.9 \times 10^{-2}$. (b) Cooling strip downstream with $C'_\theta = 0.9 \times 10^{-2}$. (c) Heating strip upstream and cooling strip downstream with $C'_\theta = 0.9 \times 10^{-2}$.

We first study the effect of both strips independently and then together, at the same level of C'_θ. The temperature fields of the base-flows are plotted in Figure 3.19 and the resolvent gain maps in Figure 3.20. First, for a single heating strip (Figure 3.20a), two specific $F - \beta$ regions are damped: the first Mack mode / Streaks region and the second Mack mode region. There is also a region in the $F - \beta$ plane, where the instabilities are strengthened by the control, but the instabilities were weak initially in that region, so this actuator indeed attenuates all instabilities. Then, for a single cooling strip (Figure 3.20b), instabilities for all wavenumbers and frequencies below $F = 2.4 \times 10^{-4}$ are damped. Similarly to the cases where the full heat flux gradient profile was prescribed at the wall, the second Mack mode is shifted to higher frequencies and amplified. Therefore, this actuator is very efficient to damp the first Mack mode but it is not robust to mitigate all the instabilities as a second Mack mode appearing at a larger frequency might be promoted by the cooling strip. Eventually, the control through a heating strip upstream and a cooling strip downstream (Figure 3.20c) leads to a similar

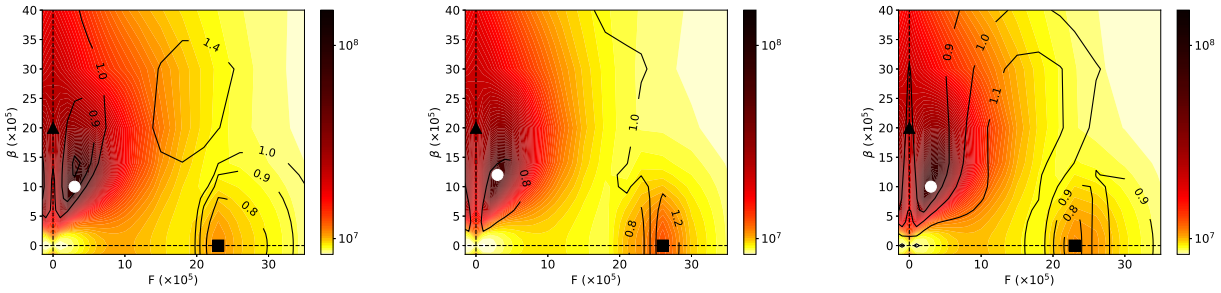

(a) **(b)** **(c)**

Figure 3.20: Optimal gain μ_0 of controlled boundary layers. White circle denotes the first Mack mode, black triangle denotes the streak mode and black square denotes the second Mack mode. Contour lines denote the ratio of the optimal gain with control over the optimal gain without control $\mu_0(C'_\theta \neq 0)/\mu_0(C'_\theta = 0)$ given by Figure 2.13a. (a) Heating strip upstream with $C'_\theta = 0.9 \times 10^{-2}$. (b) Cooling strip downstream with $C'_\theta = 0.9 \times 10^{-2}$. (c) Heating strip upstream and cooling strip downstream with $C'_\theta = 0.9 \times 10^{-2}$.

resolvent map and reduces by the same amount the optimal gains of both Mack modes than with a single heating strip. Moreover, the streaks are more damped with the additional cooling strip. Therefore, for the same energy spent, depending on the context, two strips may represent a better actuator as each strip requires to produce a smaller heat flux than a single heating strip but the mechanism would involve both a heating and a cooling strip.

To conclude, a relevant preliminary design for a wall actuator would be a thin steady heating strip located close to the leading edge (and possibly a second cooling strip downstream) which would modify the base-flow so that the boundary layer is less receptive to streaks, first and second Mack modes. However, only linear computations were performed in this work. To properly design an optimal finite amplitude actuator, one must perform a full iterative nonlinear evaluation (base-flow/stability/sensitivity analyses).

Chapter outcome summary:

Linear sensitivity analysis has revealed the optimal steady wall-blowing and wall-heating actuator locations for a Mach 4.5 boundary layer over an adiabatic flat plate. An adjoint-based optimisation technique allowed to identify the optimal steady wall-actuators to mitigate/strengthen the following instabilities: the streaks, first and second Mack modes. Wall blowing/suction control induces streamwise momentum modifications in the corresponding sensitive region of the flow i.e. between the critical layer and the boundary layer thickness for both Mack modes. Wall heating/cooling control acts in the region of the flow sensitive to temperature variations for the first Mack mode i.e. within the boundary layer close to the wall but fails to induce temperature modifications above the critical layer where it is more optimal for the second Mack mode. For both Mack modes, the variations of optimal gain are mainly driven by the streamwise momentum modifications.
For steady wall-blowing control, several conclusions are drawn. First, the second Mack mode is the most sensitive to blowing/suction control. Suction control is optimal to damp the mode if located upstream of the synchronisation point and conversely for blowing control. Secondly, the second Mack mode is optimally damped by a local suction device located in the region of branch I of the local mode S while the optimal region for the first Mack mode is around the maximum amplification rate of the local first mode. A steady blowing can damp the second Mack mode only if it is applied in the region of branch II of mode S. The application of the optimal wall suction and blowing control, computed for the second Mack mode, in the non-linear regime (finite amplitude control) yields a reduction of the optimal gain of the second Mack mode but shifts its peak to lower or higher frequencies, triggers a small decrease of the first Mack mode gains and lets the streaks unaffected. Therefore, only a local suction actuator would efficiently damp all instabilities.
For heating/cooling control, the first Mack mode appears as the most sensitive instability. In agreement with previous findings [108], the first and second Mack modes have an opposite sensitivity with respect to wall temperature changes, however, wall heating located close to the leading edge damps both Mack modes. In the downstream region, a large cooling region damps the first Mack mode while only a local cooling strip located in the unstable region of mode S damps the second Mack mode but this is suboptimal in comparison with the leading edge region. The application of the optimal wall heating and cooling control, computed for the first Mack mode, at a non-linear regime yields a strong reduction of the first Mack mode gains but strongly amplifies the second Mack mode. The application of a single local steady heating strip close to the leading edge (and possibly a cooling strip downstream in the unstable region of mode S) manages to damp all the instabilities and might be considered as an actuator to delay transition towards turbulence for a various range of frequencies and spanwise wavenumbers.

Chapter 4

Optimal non-linear solutions: numerical methods and application

Chapter foreword:

This chapter initially presents the weakly non-linear analysis near bifurcation for globally unstable compressible flow. It is tested on a low Mach number flow around a circular cylinder. Then, for amplifier flows, the extension of the linear resolvent to non-linear input-output analysis which takes into account the non-linear interactions of a finite number of time and spanwise harmonics is described thoroughly. The latter draws on a pseudo-spectral form through the Space-Time Spectral Method for both time and spanwise dimensions. It is validated on the transition of a boundary layer at low Mach number and then studied at $M_\infty = 4.5$.

4.1 Weakly non-linear analysis

As a step aside, a weakly non-linear analysis is developed for compressible oscillator flows to demonstrate the capabilities of linear tools to predict the stability in the vicinity of bifurcations. However, an equivalent of the weakly non-linear analysis for amplifier flows is described in §4.3.2.3 in link to the non-linear input-output analysis for boundary layer applications.

4.1.1 Weakly non-linear analysis for oscillator flow

The weakly non-linear analysis for cylinder bifurcation was described by Sipp and Lebedev [177] for incompressible flow. The same method is here extended to compressible flows, see details of the derivation of the equations in 4.1.2. In the vicinity of the critical Reynolds number Re_c (value of Reynolds number where the real part of the least stable eigenvalue is zero), introducing a small parameter ϵ defined as $\epsilon^2 = Re_c^{-1} - Re^{-1}$ with $0 < \epsilon \ll 1$, one may predict whether a bifurcation is sub-critical or super-critical by computing the sign of the sum of the coefficients $\mu + \nu + \xi$ of the Stuart-Landau amplitude $\mathcal{A}$ equation (4.1).

$$\frac{d\mathcal{A}}{dt} = \epsilon^2 \kappa \mathcal{A} - \epsilon^2 (\mu + \nu + \xi) \mathcal{A} |\mathcal{A}|^2. \tag{4.1}$$

These coefficients rely on five different modes computed at the critical frequency ω: the first direct mode $\hat{\mathbf{q}}_1$, the corresponding adjoint mode $\tilde{\mathbf{q}}_1$, the zeroth (mean flow) harmonic $\hat{\mathbf{q}}_{20}$, the second harmonic $\hat{\mathbf{q}}_{22}$ and the base-flow modification due to an ϵ Reynolds increase $\hat{\mathbf{q}}_{21}$ (Equations (4.2)-(4.6)).

$$\begin{aligned}
i\omega\hat{\mathbf{q}}_1 - \mathbf{A}\hat{\mathbf{q}}_1 &= 0, && (4.2)\\
-i\omega\tilde{\mathbf{q}}_1 - \mathbf{A}^*\tilde{\mathbf{q}}_1 &= 0, && (4.3)\\
2i\omega\hat{\mathbf{q}}_{22} - \mathbf{A}\hat{\mathbf{q}}_{22} &= \frac{1}{2}\mathbf{H}(\hat{\mathbf{q}}_1, \hat{\mathbf{q}}_1), && (4.4)\\
-\mathbf{A}\hat{\mathbf{q}}_{20} &= \mathbf{H}(\hat{\mathbf{q}}_1, \overline{\hat{\mathbf{q}}_1}), && (4.5)\\
-\mathbf{A}\hat{\mathbf{q}}_{21} &= \partial_{\epsilon^2}\mathbf{R}(\mathbf{q}_0, 0). && (4.6)
\end{aligned}$$

Following the same method described in Sipp and Lebedev [177] in the incompressible framework, by developing the Taylor expansion of the residual $\mathbf{R} = \mathbf{R}(\mathbf{q}, \epsilon^2)$ up to the third order, analytical expressions of the coefficients μ, ν and ξ are found for the compressible framework (Equations (4.8)-(4.10)). They depend on the discrete Hessian $\mathbf{H}$ defined previously and the discrete third-order derivative $\mathbf{T}$ operators. These derivative operators are computed by Algorithmic Differentiation (AD) returning directly the vectors $\mathbf{H}(\mathbf{q}, \mathbf{q})$ or $\mathbf{T}(\mathbf{q}, \mathbf{q}, \mathbf{q})$, preventing then any explicit storage of these operators.

$$\begin{aligned}
\kappa &= \frac{\langle \tilde{\mathbf{q}}_1, \mathbf{H}(\hat{\mathbf{q}}_1, \hat{\mathbf{q}}_{21}) \rangle}{\langle \tilde{\mathbf{q}}_1, \hat{\mathbf{q}}_1 \rangle} + \frac{\langle \tilde{\mathbf{q}}_1, \partial_{\mathbf{q}\epsilon^2}\mathbf{R}(\mathbf{q}_0, 0)\hat{\mathbf{q}}_1 \rangle}{\langle \tilde{\mathbf{q}}_1, \hat{\mathbf{q}}_1 \rangle}, && (4.7)\\
\mu &= -\frac{\langle \tilde{\mathbf{q}}_1, \mathbf{H}(\hat{\mathbf{q}}_1, \hat{\mathbf{q}}_{20}) \rangle}{\langle \tilde{\mathbf{q}}_1, \hat{\mathbf{q}}_1 \rangle}, && (4.8)\\
\nu &= -\frac{\langle \tilde{\mathbf{q}}_1, \mathbf{H}(\overline{\hat{\mathbf{q}}_1}, \hat{\mathbf{q}}_{22}) \rangle}{\langle \tilde{\mathbf{q}}_1, \hat{\mathbf{q}}_1 \rangle}, && (4.9)\\
\xi &= -\frac{1}{2}\frac{\langle \tilde{\mathbf{q}}_1, \mathbf{T}(\hat{\mathbf{q}}_1, \hat{\mathbf{q}}_1, \overline{\hat{\mathbf{q}}_1}) \rangle}{\langle \tilde{\mathbf{q}}_1, \hat{\mathbf{q}}_1 \rangle}, && (4.10)
\end{aligned}$$

where $\langle \mathbf{a}, \mathbf{b} \rangle = \mathbf{a}^* \mathbf{Q} \mathbf{b}$ is the discrete inner product (Eq. (2.16)).

The coefficient μ consists of the response arising from the interaction of the first harmonic with the zeroth harmonic. The coefficient ν consists of the response arising from the interaction of the complex conjugate part of the first harmonic with the second harmonic. The coefficient ξ consists of the response arising from the interaction of the complex conjugate part of the first harmonic twice with the first harmonic (itself). This last coefficient exists only at compressible regime due to the triadic form of the equations.

4.1.2 Equations for weakly non-linear analysis

The method described in Sipp and Lebedev [177] for incompressible flow, developing the Taylor expansion of the residual up to the third order, is applied here on the general form given by the discretised equation (2.5). First, one assumes that the analysis is performed in the vicinity of the critical Reynolds number so that a small parameter ϵ can be defined as $\epsilon^2 = Re_c^{-1} - Re^{-1}$ with $0 < \epsilon \ll 1$. As it is dependent on the Reynolds number, the state vector $\mathbf{q}$ can be written as a Taylor expansion of the parameter ϵ,

$$\mathbf{q}(t, \epsilon) = \mathbf{q}_0 + \epsilon \mathbf{q}_1(t) + \epsilon^2 \mathbf{q}_2(t) + \epsilon^3 \mathbf{q}_3(t) = \mathbf{q}_0 + \epsilon \mathbf{q}, \tag{4.11}$$

with $\mathbf{q} = \mathbf{q}_1(t) + \epsilon \mathbf{q}_2(t) + \epsilon^2 \mathbf{q}_3(t)$.

The discretised residual $\mathbf{R} = \mathbf{R}(\mathbf{q}(t), \epsilon^2)$ is a function of the state vector $\mathbf{q}(t)$ and the parameter ϵ^2. It is expanded up to the third order for these two variables in equation (4.12). Some notations and definitions are introduced for clarity. The Jacobian operator around the base-flow, written $\mathbf{A}$, is equal to $\partial_{\mathbf{q}} \mathbf{R}(\overline{\mathbf{q}}, 0)$ where $\partial_{\mathbf{q}}(\cdot) = \partial(\cdot)/\partial \mathbf{q}$. Then, the Hessian operator appears too as $\mathbf{H}(\mathbf{q}, \mathbf{q}) = [\partial_{\mathbf{qq}} \mathbf{R}(\overline{\mathbf{q}}, 0)\mathbf{q}]\,\mathbf{q}$. In discrete form, it can be expressed as $H_i(\mathbf{q}, \mathbf{q}) = \sum_k \sum_j (\partial_{q_j q_k} R_i(\overline{q}, 0)) q_j q_k$. As this is a symmetric operator, one gets $\mathbf{H}(\mathbf{q}_1, \mathbf{q}_2) = \mathbf{H}(\mathbf{q}_2, \mathbf{q}_1)$. Similarly the third-order derivative operator, written $\mathbf{T}(\mathbf{q}, \mathbf{q}, \mathbf{q}) = [[\partial_{\mathbf{qqq}} \mathbf{R}(\overline{\mathbf{q}}, 0)\mathbf{q}]\,\mathbf{q}]\,\mathbf{q}$, has the same symmetrical properties and is written in discrete form as $T_i(\mathbf{q}, \mathbf{q}, \mathbf{q}) = \sum_l \sum_k \sum_j (\partial_{q_j q_k q_l} R_i(\overline{q}, 0)) q_j q_k q_l$.

$$\mathbf{R}(\mathbf{q}(t), \epsilon^2) = \mathbf{R}(\mathbf{q}_0 + \epsilon \mathbf{q}, \epsilon^2) = \mathbf{R}(\mathbf{q}_0) + \epsilon \mathbf{A}\mathbf{q} + \frac{\epsilon^2}{2}\mathbf{H}(\mathbf{q}, \mathbf{q}) + \frac{\epsilon^3}{6}\mathbf{T}(\mathbf{q}, \mathbf{q}, \mathbf{q}) + \epsilon^2 \partial_{\epsilon^2} \mathbf{R}(\mathbf{q}_0, 0) + \epsilon^3 \partial_{\mathbf{q}\epsilon^2} \mathbf{R}(\mathbf{q}_0, 0)\mathbf{q}. \tag{4.12}$$

By introducing the equations (4.11) and (4.12) into the equation (2.5), written as $\mathrm{d}\mathbf{q}(t)/\mathrm{d}t = \mathbf{R}(\mathbf{q}(t), \epsilon^2)$, one gets the equation (4.13) below which will be studied at the different orders of ϵ.

$$\frac{\mathrm{d}\mathbf{q}_0}{\mathrm{d}t} + \epsilon \frac{\mathrm{d}\mathbf{q}_1}{\mathrm{d}t} + \epsilon^2 \frac{\mathrm{d}\mathbf{q}_2}{\mathrm{d}t} + \epsilon^3 \frac{\mathrm{d}\mathbf{q}_3}{\mathrm{d}t} = \mathbf{R}(\mathbf{q}_0) + \epsilon \mathbf{A}\mathbf{q}_1 + \epsilon^2 \left[\mathbf{A}\mathbf{q}_2 + \frac{1}{2}\mathbf{H}(\mathbf{q}_1, \mathbf{q}_1) + \partial_{\epsilon^2} \mathbf{R}(\mathbf{q}_0, 0) \right] + \epsilon^3 \left[\mathbf{A}\mathbf{q}_3 + \mathbf{H}(\mathbf{q}_1, \mathbf{q}_2) + \frac{1}{6}\mathbf{T}(\mathbf{q}_1, \mathbf{q}_1, \mathbf{q}_1) + \partial_{\mathbf{q}\epsilon^2} \mathbf{R}(\mathbf{q}_0, 0)\mathbf{q}_1 \right]. \tag{4.13}$$

First, at order ϵ^0, the base-flow equation $\mathrm{d}\mathbf{q}_0/\mathrm{d}t = 0 = \mathbf{R}(\mathbf{q}_0, 0)$ is recovered and then $\mathbf{q}_0$ is the base-flow solution. Secondly, at order ϵ^1, one gets the eigenvalue problem (4.14):

$$\frac{\mathrm{d}\mathbf{q}_1}{\mathrm{d}t} - \mathbf{A}\mathbf{q}_1 = 0. \tag{4.14}$$

The general solution is of the following form,

$$\mathbf{q}_1(t) = \mathcal{A}e^{i\omega t}\hat{\mathbf{q}}_1 + \overline{\mathcal{A}}e^{-i\omega t}\overline{\hat{\mathbf{q}}_1}, \tag{4.15}$$

with $\mathcal{A}$ a complex scalar which represents the amplitude and depends on the slow time scale $t_1 = \epsilon^2 t$ according to the Stuart-Landau amplitude equation (4.1), ω the critical frequency and $\hat{\mathbf{q}}_1$ the first eigenmode solution of the equation (4.16).

$$(i\omega\mathbf{I} - \mathbf{A})\,\hat{\mathbf{q}}_1 = 0. \tag{4.16}$$

Thirdly, at order ϵ^2, the equation becomes

$$\frac{\mathrm{d}\mathbf{q}_2}{\mathrm{d}t} - \mathbf{A}\mathbf{q}_2 = \frac{1}{2}\mathbf{H}(\mathbf{q}_1,\mathbf{q}_1) + \partial_{\epsilon^2}\mathbf{R}(\mathbf{q}_0,0) = \frac{1}{2}\mathcal{A}^2 e^{2i\omega t}\mathbf{H}(\hat{\mathbf{q}}_1,\hat{\mathbf{q}}_1) + \frac{1}{2}\overline{\mathcal{A}}^2 e^{-2i\omega t}\mathbf{H}(\overline{\hat{\mathbf{q}}_1},\overline{\hat{\mathbf{q}}_1}) + |\mathcal{A}|^2\mathbf{H}(\hat{\mathbf{q}}_1,\overline{\hat{\mathbf{q}}_1}) + \partial_{\epsilon^2}\mathbf{R}(\mathbf{q}_0,0). \tag{4.17}$$

From the form of the equation (4.17), the solution is sought as

$$\mathbf{q}_2(t) = \mathcal{A}^2 e^{2i\omega t}\hat{\mathbf{q}}_{22} + \overline{\mathcal{A}}^2 e^{-2i\omega t}\overline{\hat{\mathbf{q}}_{22}} + |\mathcal{A}|^2\hat{\mathbf{q}}_{20} + \hat{\mathbf{q}}_{21}, \tag{4.18}$$

with $\hat{\mathbf{q}}_{22}$ the second harmonic, $\hat{\mathbf{q}}_{20}$ the zeroth (mean flow) harmonic and $\hat{\mathbf{q}}_{21}$ the base flow modification due to a ϵ Reynolds increase, respectively solutions of the equations (4.19), (4.20) and (4.21).

$$2i\omega\hat{\mathbf{q}}_{22} - \mathbf{A}\hat{\mathbf{q}}_{22} = \frac{1}{2}\mathbf{H}(\hat{\mathbf{q}}_1,\hat{\mathbf{q}}_1), \tag{4.19}$$

$$-\mathbf{A}\hat{\mathbf{q}}_{20} = \mathbf{H}(\hat{\mathbf{q}}_1,\overline{\hat{\mathbf{q}}_1}), \tag{4.20}$$

$$-\mathbf{A}\hat{\mathbf{q}}_{21} = \partial_{\epsilon^2}\mathbf{R}(\mathbf{q}_0,0). \tag{4.21}$$

Fourthly, at order ϵ^3, the remaining terms in the equation (4.13) give the equation (4.22).

$$\frac{\mathrm{d}\mathbf{q}_3}{\mathrm{d}t} - \mathbf{A}\mathbf{q}_3 = \mathbf{H}(\mathbf{q}_1,\mathbf{q}_2) + \frac{1}{6}\mathbf{T}(\mathbf{q}_1,\mathbf{q}_1,\mathbf{q}_1) + \partial_{\mathbf{q}\epsilon^2}\mathbf{R}(\mathbf{q}_0,0)\mathbf{q}_1. \tag{4.22}$$

In the equation (4.22), by computing only the terms proportional to $e^{i\omega t}$, it reduces to the equation (4.23).

$$i\omega\mathbf{q}_3 - \mathbf{A}\mathbf{q}_3 = -\frac{\mathrm{d}\mathcal{A}}{\mathrm{d}t_1}\hat{\mathbf{q}}_1 + \mathcal{A}\mathbf{H}(\hat{\mathbf{q}}_1,\hat{\mathbf{q}}_{21}) + \mathcal{A}\partial_{\mathbf{q}\epsilon^2}\mathbf{R}(\mathbf{q}_0,0)\hat{\mathbf{q}}_1 + \mathcal{A}|\mathcal{A}|^2\left[\mathbf{H}(\hat{\mathbf{q}}_1,\hat{\mathbf{q}}_{20}) + \mathbf{H}(\overline{\hat{\mathbf{q}}_1},\hat{\mathbf{q}}_{22}) + \frac{3}{6}\mathbf{T}(\hat{\mathbf{q}}_1,\hat{\mathbf{q}}_1,\overline{\hat{\mathbf{q}}_1})\right]. \tag{4.23}$$

Let's introduce the adjoint mode $\tilde{\mathbf{q}}_1$ solution of the adjoint eigenvalue problem (4.24).

$$(-i\omega\mathbf{I} - \mathbf{A}^*)\,\tilde{\mathbf{q}}_1 = 0. \tag{4.24}$$

Then, the goal is to recover the Stuart-Landau amplitude equation from the equation (4.23). As the latter is a "vector" equation and the amplitude equation a "scalar" equation, we compute the dot product of the equation (4.23) with the adjoint mode. The left hand-side of the new equation becomes zero as described in the equation (4.25).

$$i\omega\langle\tilde{\mathbf{q}}_1,\mathbf{q}_3\rangle - \langle\tilde{\mathbf{q}}_1,\mathbf{A}\mathbf{q}_3\rangle = i\omega\langle\tilde{\mathbf{q}}_1,\mathbf{q}_3\rangle - \langle\mathbf{A}^*\tilde{\mathbf{q}}_1,\mathbf{q}_3\rangle = i\omega\langle\tilde{\mathbf{q}}_1,\mathbf{q}_3\rangle - \langle -i\omega\tilde{\mathbf{q}}_1,\mathbf{q}_3\rangle$$
$$= i\omega\langle\tilde{\mathbf{q}}_1,\mathbf{q}_3\rangle - i\omega\langle\tilde{\mathbf{q}}_1,\mathbf{q}_3\rangle = 0. \quad (4.25)$$

And the right hand-side gives the amplitude equation.

$$0 = -\frac{\mathrm{d}\mathcal{A}}{\mathrm{d}t_1}\langle\tilde{\mathbf{q}}_1,\hat{\mathbf{q}}_1\rangle + \mathcal{A}\left(\langle\tilde{\mathbf{q}}_1,\mathbf{H}(\hat{\mathbf{q}}_1,\hat{\mathbf{q}}_{21})\rangle + \langle\tilde{\mathbf{q}}_1,\partial_{\mathbf{q}\epsilon}\mathbf{R}(\mathbf{q}_0,0)\hat{\mathbf{q}}_1\rangle\right) +$$
$$\mathcal{A}|\mathcal{A}|^2\left[\langle\tilde{\mathbf{q}}_1,\mathbf{H}(\hat{\mathbf{q}}_1,\hat{\mathbf{q}}_{20})\rangle + \langle\tilde{\mathbf{q}}_1,\mathbf{H}(\overline{\hat{\mathbf{q}}_1},\hat{\mathbf{q}}_{22})\rangle + \frac{1}{2}\langle\tilde{\mathbf{q}}_1,\mathbf{T}(\hat{\mathbf{q}}_1,\hat{\mathbf{q}}_1,\overline{\hat{\mathbf{q}}_1})\rangle\right] \quad (4.26)$$

$$\Rightarrow \frac{\mathrm{d}\mathcal{A}}{\mathrm{d}t_1} = \mathcal{A}\left(\frac{\langle\tilde{\mathbf{q}}_1,\mathbf{H}(\hat{\mathbf{q}}_1,\hat{\mathbf{q}}_{21})\rangle}{\langle\tilde{\mathbf{q}}_1,\hat{\mathbf{q}}_1\rangle} + \frac{\langle\tilde{\mathbf{q}}_1,\partial_{\mathbf{q}\epsilon}\mathbf{R}(\mathbf{q}_0,0)\hat{\mathbf{q}}_1\rangle}{\langle\tilde{\mathbf{q}}_1,\hat{\mathbf{q}}_1\rangle}\right) +$$
$$\mathcal{A}|\mathcal{A}|^2\left[\frac{\langle\tilde{\mathbf{q}}_1,\mathbf{H}(\hat{\mathbf{q}}_1,\hat{\mathbf{q}}_{20})\rangle}{\langle\tilde{\mathbf{q}}_1,\hat{\mathbf{q}}_1\rangle} + \frac{\langle\tilde{\mathbf{q}}_1,\mathbf{H}(\overline{\hat{\mathbf{q}}_1},\hat{\mathbf{q}}_{22})\rangle}{\langle\tilde{\mathbf{q}}_1,\hat{\mathbf{q}}_1\rangle} + \frac{1}{2}\frac{\langle\tilde{\mathbf{q}}_1,\mathbf{T}(\hat{\mathbf{q}}_1,\hat{\mathbf{q}}_1,\overline{\hat{\mathbf{q}}_1})\rangle}{\langle\tilde{\mathbf{q}}_1,\hat{\mathbf{q}}_1\rangle}\right]. \quad (4.27)$$

By comparison with the Stuart-Landau amplitude equation (4.1), one gets the expression of the coefficients κ, μ, ν and ξ given in the equations (4.7)-(4.10).

4.1.3 Application to cylinder flow

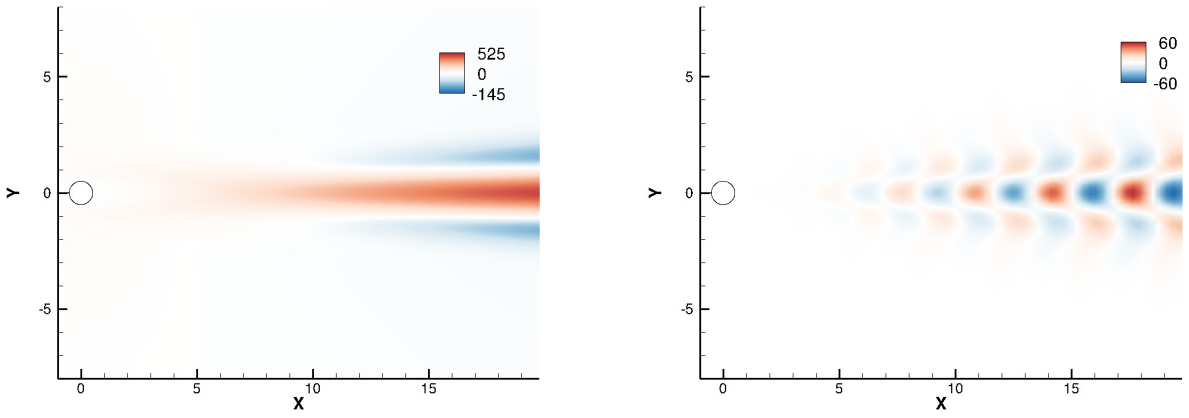

(a) **(b)**

Figure 4.1: Higher harmonics required to compute the Stuart-Landau coefficients μ and ν at $Re = 46.8$ and $M_\infty = 0.1$. Same normalisation as in Sipp and Lebedev [177]. (a) Streamwise velocity of the zeroth harmonic $\hat{\mathbf{q}}_{20}$. (b) Real part of the streamwise velocity of the second harmonic $\hat{\mathbf{q}}_{22}$.

The weakly non-linear analysis is compared to the results given in Sipp and Lebedev [177]. We focus on the coefficients of the cubic term, since its sign determines the super-critical (real part of $\mu + \nu + \xi > 0$, see (4.8)-(4.10)) or sub-critical (real part of $\mu + \nu + \xi < 0$) nature of the bifurcation. They are computed from the different modes $\hat{\mathbf{q}}_1$, $\tilde{\mathbf{q}}_1$, $\hat{\mathbf{q}}_{20}$ and $\hat{\mathbf{q}}_{22}$ (Eq. (4.2)-(4.5)). The modes are plotted in Figures 2.5 and 4.1. The coefficients, computed for $Re = 46.8$ ($\epsilon \approx 10^{-3}$), $M = 0.1$ and $\beta = 0$ with the same normalisation scheme as in Sipp and Lebedev [177], are the following:

$$\mu = 9.24 - 33.2i, \tag{4.28}$$
$$\nu = -0.31 - 0.87i, \tag{4.29}$$
$$\xi = 0.00032 - 0.00095i. \tag{4.30}$$

The bifurcation is then super-critical here, which means that the critical value would be sufficient to build a safety envelope as the non-linearity have no hysteresis effect in the vicinity of the criticality. We note that the coefficient ξ involving the third-order derivative term is negligible with respect to the two other coefficients μ and ν (ratio about 10^{-3} between ν and ξ). This stems from the fact that $M = 0.1$ is close to the incompressible regime, for which this constant is strictly zero. This is due to the quadratic nature of the incompressible Navier-Stokes equations, so that the third-order derivative of the residual is zero. However this contribution would not disappear for higher Mach numbers and would therefore be mandatory to assess the nature of a bifurcation in transonic and supersonic configurations. The μ and ν coefficients can be compared to the incompressible values $\mu_{\text{REF}} = 9.4 - 30i$ and $\nu_{\text{REF}} = -0.30 - 0.87i$ [177]. The discrepancy remains small (maximum 10% for $Im(\mu)$) but cannot be reduced by any grid refinement or domain enlargement. It rather appears linked to the behaviour of the compressible Navier-Stokes equations as the Mach number decreases. Indeed, compressibility has a strong impact on the global modes, which deviate from the incompressible solutions when the Mach number is above 0.1. Conversely, at Mach numbers lower than $M = 0.02$, the system of equations is not well-conditioned making the calculation of the eigenmodes inaccurate. This comes from the division by a quasi-zero Mach number in the perfect gas law (non-dimensional form of Eq. (1.14)).

4.2 Theory and implementation for non-linear input-output analysis

4.2.1 Non-linear input-output analysis

The non-linear input-output analysis is the extension of the resolvent, described in §2.1.8, to the non-linear framework. Instead of considering the forcing $\check{\mathbf{f}}$ and response $\check{\mathbf{q}}$ of the system as one mode at a single angular frequency ω and a single spanwise wavenumber β, they are both described as Fourier series truncated after N harmonics in time and M harmonics in z-direction:

$$\check{\mathbf{q}}(x,y,z,t) = \sum_{n=-N}^{N} \sum_{m=-M}^{M} \check{\mathbf{q}}_{n,m}(x,y) e^{i(n\omega t + m\beta z)}. \tag{4.31}$$

The variables $\check{\mathbf{q}}_{n,m}$ represents the n-th harmonic in time and the m-th harmonic in the spanwise direction associated to $e^{i(n\omega t+m\beta z)}$ in the Fourier decomposition. To get real variables, we have

$$\check{\mathbf{q}}_{-n,-m} = \check{\mathbf{q}}^*_{n,m}, \tag{4.32}$$

and the mean-flow $\check{\mathbf{q}}_{0,0} = \overline{\mathbf{q}}$ is real. The mean flow deviation represents the difference between the mean-flow $\overline{\mathbf{q}}$ and the base-flow $\mathbf{q_b}$.

4.2.1.1 Non-linear response

The non-linear discrete Navier-Stokes equations write

$$\frac{\partial \mathbf{q}}{\partial t} + \mathbf{R}(\mathbf{q}) = \mathbf{P}\mathbf{f}. \tag{4.33}$$

By injecting the ansatz for the forcing $\check{\mathbf{f}}$ and the response $\check{\mathbf{q}}$ given by Eq. (4.31) in Eq (4.33), the system for the (n, m) harmonic writes in frequency domain:

$$\frac{\partial \check{\mathbf{q}}_{n,m}}{\partial t} + \check{\mathbf{R}}_{n,m}(\mathbf{q}) = \mathbf{P}\check{\mathbf{f}}_{n,m}, \tag{4.34}$$

with $\check{\mathbf{R}}_{n,m}$ the discrete residual in frequency domain through the application of the Discrete Fourier Transform. Because of the non-linearity of the Navier-Stokes operator, $\check{\mathbf{R}}_{n,m}(\mathbf{q}) \neq \check{\mathbf{R}}(\check{\mathbf{q}}_{n,m})$. By splitting the residual $\mathbf{R}$ into a linear term $\mathbf{L}$ and a non-linear term $\mathbf{N}$, we get

$$\check{\mathbf{R}}_{n,m}(\mathbf{q}) = \check{\mathbf{L}}(\check{\mathbf{q}}_{n,m}) + \sum_{\substack{-N<a,b,c<N \\ -M<d,e,f<M \\ a+b+c=n \\ d+e+f=m}} \check{\mathbf{N}}(\check{\mathbf{q}}_{a,d}, \check{\mathbf{q}}_{b,e}, \check{\mathbf{q}}_{c,f}). \tag{4.35}$$

Eq. (4.35) highlights that solving Eq. (4.34) for each harmonics is expensive because of the large number of non-linear combinations. In the incompressible framework, the system written in frequency domain Eq. (4.34) which includes only quadratic non-linear interactions was solved for instance by Rigas et al. [155] with the Analytical Harmonic Balance Method (AHBM). In the conservative framework of the compressible Navier-Stokes, the triadic interactions add more contributions which prevent the use of a similar method for computation efficiency (Sierra-Ausin et al. [176] managed to employ AHBM for compressible flows but only in time, not in the spanwise dimension).

4.2.1.2 Space-Time Spectral Method (STSM)

In order to overcome the difficulties from the AHBM, the system defined by Eq. (4.33) is solved in a pseudo-spectral framework in the time domain instead of the frequency domain (Eq. (4.36)). The method is called pseudo-spectral as the continuous Fourier coefficients of the residual are approximated by their discrete Fourier coefficients. It relies on a collocation approach therefore Eq. (4.33) is not solved for the N frequencies but for the $2N + 1$ discrete collocation points which own the same level of information according to Nyquist-Shannon criteria. This method is either called Time-Spectral Method (TSM) [61] or High-Dimensional Harmonic Balance method (HDHB) [101]. As this collocation method is applied both for time and for spanwise dimensions, we call it Space-Time Spectral Method (STSM).

$$\begin{array}{ccccccc} z\backslash t & -N & \cdots & n & \cdots & N \\ -M & \ddots & \cdots & \cdots & \cdots & \ddots \\ \vdots & \vdots & \ddots & \ddots & \ddots & \vdots \\ m & \vdots & \ddots & \check{\mathbf{q}}_{n,m}e^{i(n\omega t+m\beta z)} & \ddots & \vdots \\ \vdots & \vdots & \ddots & \ddots & \ddots & \vdots \\ M & \ddots & \cdots & \cdots & \cdots & \ddots \end{array} \quad \Longrightarrow \quad \begin{array}{ccccccc} z\backslash t & 0 & \cdots & k & \cdots & 2N \\ 0 & \ddots & \cdots & \cdots & \cdots & \ddots \\ \vdots & \vdots & \ddots & \ddots & \ddots & \vdots \\ j & \vdots & \ddots & \mathbf{q}_{k,j} = \mathbf{q}(t = k\Delta t, z = j\Delta z) & \ddots & \vdots \\ \vdots & \vdots & \ddots & \ddots & \ddots & \vdots \\ 2M & \ddots & \cdots & \cdots & \cdots & \ddots \end{array} \tag{4.36}$$

First, let's recall the Discrete Fourier Transform (DFT) written $\mathbf{E}_t$ between the frequency-domain variables $\check{\mathbf{q}}_n$ and the time-domain variables $\mathbf{q}_k = (\mathbf{E}_t^{-1})_{kn}\check{\mathbf{q}}_n$ defined by Eq. (4.37) and its Inverse Discrete Fourier Transform (IDFT) by Eq. (4.38).

$$(\mathbf{E}_t)_{nk} = \frac{1}{2N+1} e^{-(i2\pi kn)/(2N+1)}\mathbf{I}, \tag{4.37}$$

$$(\mathbf{E}_t^{-1})_{kn} = e^{(i2\pi kn)/(2N+1)}\mathbf{I}, \tag{4.38}$$

with $n \in [-N, N]$ and $k \in [0, 2N]$ and $\mathbf{I}$ the identity matrix of the two-dimensional discretisation. The Discrete Fourier Transform is defined similarly for both the time-domain variables $\mathbf{q}_k$ ($\mathbf{E}_t$) and the spanwise wavenumber-domain variables $\mathbf{q}_j$ ($\mathbf{E}_z$).

Therefore, Eq. (4.33) is solved for each time collocation point k and spanwise collocation points j in Eq. (4.39).

$$\frac{\partial \mathbf{q}_{k,j}}{\partial t} + \mathbf{R}(\mathbf{q}_{k,j}) = \mathbf{P}\mathbf{f}_{k,j}, \tag{4.39}$$

The derivatives in the non-discretised directions i.e. the time derivative $\mathbf{D}_t$ and the spanwise first and second derivatives $\mathbf{D}_z$ and $\mathbf{D}_{z^2}$ operators are defined as:

$$\frac{\partial \mathbf{q}_k}{\partial t} = \sum_{l=0}^{2N} (\mathbf{D}_t)_{kl}\mathbf{q}_l \quad , \quad \frac{\partial \mathbf{q}_j}{\partial z} = \sum_{l=0}^{2M} (\mathbf{D}_z)_{jl}\mathbf{q}_l \quad , \quad \frac{\partial^2 \mathbf{q}_j}{\partial z^2} = \sum_{l=0}^{2M} (\mathbf{D}_{z^2})_{jl}\mathbf{q}_l. \tag{4.40}$$

They are computed through the application of the DFT, the complex derivative in frequency domain and the IDFT (see Eq. (4.41)). For instance,

$$\frac{\partial \mathbf{q}_k}{\partial t} = \sum_{l=0}^{2N} (\mathbf{D}_t)_{kl}\mathbf{q}_l = \sum_{n=-N}^{N} \sum_{l=0}^{2N} (\mathbf{E}_t^{-1})_{kn} (in\omega\mathbf{I})(\mathbf{E}_t)_{nl}\mathbf{q}_l. \tag{4.41}$$

Therefore the coefficients of $\mathbf{D}_t$ are given by Eq. (4.42).

$$(\mathbf{D}_t)_{kl} = \frac{1}{2N+1} \sum_{n=-N}^{N} (in\omega) e^{(i2\pi n(k-l))/(2N+1)}\mathbf{I} = \frac{-2\omega}{2N+1} \sum_{n=1}^{N} n \sin\left(\frac{2\pi n(k-l)}{2N+1}\right)\mathbf{I}. \tag{4.42}$$

The second derivative is then found by replacing $in\omega$ in Eq. (4.42) by $-n^2\omega^2$. The coefficients of the derivative matrices $\mathbf{D}$ can be computed and stored before any computation as they only depend on the truncation levels N or M. Therefore, not any Discrete Fourier Transformation is required to be performed during the computation of the Navier-Stokes equations. In expanded form, they write for each time k and spanwise j collocation point as

$$\begin{aligned}\mathbf{D}_t\mathbf{q}_{k,j} + \mathbf{R}_{2\mathrm{D}}(\mathbf{q}_{k,j}) + \mathbf{B}(\mathbf{q}_{k,j})\mathbf{D}_z\mathbf{q}_{k,j} + \mathbf{C}_1(\mathbf{q}_{k,j})\mathbf{D}_{z^2}\mathbf{q}_{k,j} + \frac{\partial \mathbf{C}_2}{\partial \mathbf{q}}(\mathbf{D}_z\mathbf{q}_{k,j})(\mathbf{D}_z\mathbf{q}_{k,j}) \\ + \mathbf{D}_1(\mathbf{q}_{k,j})\mathbf{D}_z\mathbf{q}_{k,j} \odot \mathbf{D}_2(\mathbf{q}_{k,j})\mathbf{D}_z\mathbf{q}_{k,j} = \mathbf{P}\mathbf{f}_{k,j}.\end{aligned} \tag{4.43}$$

4.2.1.3 Optimal forcing

The non-linear response $\mathbf{q}$ is computed for a given forcing $\mathbf{f}$ by Eq. (4.43). Therefore, following a variational approach, we can compute the optimal forcing $\mathbf{f}$ through an adjoint procedure as in Rigas et al. [155].

The cost function $J(\mathbf{q})$ is chosen to be the squared skin-friction of the mean flow deviation $(\overline{\mathbf{q}} - \mathbf{q_b})$ given by Eq. (4.44). Maximising $J(\mathbf{q})$ is equivalent to maximise the drag on the flat plate as $\Delta C_D = 2\sqrt{J(\mathbf{q})}/Re$ [155].

$$J(\mathbf{q}) = \left(\int_{y=0} \left(\mu_b \frac{\partial \overline{u}}{\partial y} + \overline{\mu} \frac{\partial u_b}{\partial y} - 2\mu_b \frac{\partial u_b}{\partial y} \right) dx \right)^2. \tag{4.44}$$

The constraints are the finite amplitude forcing ($\|\mathbf{f}\|_f^2 = A^2$) and the non-linear relation Eq. (4.33) describing the system. We write Eq. (4.33) as $\mathbf{R}_{\mathrm{tot}}(\mathbf{q}) = 0$ and its linearised operator

$\mathbf{A}_{\text{tot}} = \partial \mathbf{R}_{\text{tot}}/\partial \mathbf{q}$. The Lagrangian, which is a function of the forcing $\mathbf{f}$, the state $\mathbf{q}$ and the Lagrangian multipliers $\tilde{\mathbf{q}}$ and λ, writes

$$\mathcal{L}(\mathbf{f}, \mathbf{q}, \tilde{\mathbf{q}}, \lambda) = J(\mathbf{q}) - \langle \tilde{\mathbf{q}}, \mathbf{R}_{\text{tot}}(\mathbf{q}) \rangle - \langle \lambda, \mathbf{f}^* \mathbf{Q}_f \mathbf{f} - A^2 \rangle. \tag{4.45}$$

By zeroing the variations of $\mathcal{L}$ with the state $\mathbf{q}$, we get

$$\mathbf{A}_{\text{tot}}^* \tilde{\mathbf{q}} = \frac{dJ(\mathbf{q})}{d\mathbf{q}}, \tag{4.46}$$

and by zeroing the variations of $\mathcal{L}$ with the optimal forcing:

$$2\lambda \mathbf{f} = \mathbf{Q}_f^{-1} \mathbf{P}^* \tilde{\mathbf{q}}. \tag{4.47}$$

The most general approach to compute the optimal forcing $\mathbf{f}$ is a gradient-based algorithm. Writing the reduced adjoint $\hat{\mathbf{q}} = \mathbf{Q}_f^{-1} \mathbf{P}^* \tilde{\mathbf{q}}$, the steepest ascent [90] to find the optimal forcing is given by Eq. (4.48). The constraint $\|\check{\mathbf{f}}\|_f^2 = A^2$ gives Eq. (4.49) for λ.

$$\mathbf{f}_{n+1} = \mathbf{f}_n + A\alpha_n (\hat{\mathbf{q}}_n - 2\lambda_n \mathbf{f}_n), \tag{4.48}$$

$$\lambda_n = \frac{1 + \alpha_n \gamma_n \cos\theta_n - \sqrt{1 - \alpha_n^2 \gamma_n^2 \sin^2\theta_n}}{2A\alpha_n}, \tag{4.49}$$

with $\gamma_n^2 = \hat{\mathbf{q}}_n^* \mathbf{Q}_f \hat{\mathbf{q}}_n$, $\cos\theta_n = \mathbf{f}_n^* \mathbf{Q}_f \hat{\mathbf{q}}_n / (A\gamma_n))$, $\alpha_n = c/\gamma_n$ and c a user-input parameter between 0 and 1 to control the optimisation step length.

Eq. (4.47) shows that the forcing $\mathbf{f}$ must be parallel to the reduced adjoint $\hat{\mathbf{q}}$. Defining $\gamma^2 = \hat{\mathbf{q}}^* \mathbf{Q}_f \hat{\mathbf{q}}$, the convergence criteria for the optimisation can be written

$$\cos(\theta) = \frac{\mathbf{f}^* \mathbf{Q}_f \hat{\mathbf{q}}}{A\gamma} = 1. \tag{4.50}$$

4.2.1.4 Amplitude of the harmonic components

The definition of the amplitude for each harmonic components of the optimal forcing and response is derived. The general solution writes

$$\check{\mathbf{q}}(x, y, z, t) = \sum_{n=-N}^{N} \sum_{m=-M}^{M} \check{\mathbf{q}}_{n,m}(x, y) e^{i(n\omega t + m\beta z)}. \tag{4.51}$$

In the case of a z-symmetrical solution, Eq. (4.51) expands as

$$\begin{aligned} \check{\mathbf{q}} &= \mathbf{q_b} + (\check{\mathbf{q}}_{0,0} - \mathbf{q_b}) + \sum_{n=1}^{N} \left(\check{\mathbf{q}}_{n,0} e^{in\omega t} + c.c. \right) + \sum_{m=1}^{M} \left(\check{\mathbf{q}}_{0,m} e^{im\beta z} + c.c. \right) \\ &+ \sum_{n=1}^{N} \sum_{m=1}^{M} \left(\check{\mathbf{q}}_{n,m} e^{i(n\omega t + m\beta z)} + \check{\mathbf{q}}_{n,-m} e^{i(n\omega t - m\beta z)} + c.c. \right). \end{aligned} \tag{4.52}$$

Therefore, the amplitude of each harmonic component of the response is defined using Chu's energy norm $\mathbf{Q}_q$, multiplied by 2, along with the appropriate coefficient given by Eq. (4.52):

$$A_q(n, m) = \begin{cases} \sqrt{2(\check{\mathbf{q}}_{0,0} - \mathbf{q_b})^* \mathbf{Q}_q (\check{\mathbf{q}}_{0,0} - \mathbf{q_b})}, & \text{if } (n, m) = (0, 0), \\ \sqrt{4\check{\mathbf{q}}_{n,m}^* \mathbf{Q}_q \check{\mathbf{q}}_{n,m}}, & \text{if } (n, m) \in (1...N, 0) \cup (0, 1...M) \\ \sqrt{8\check{\mathbf{q}}_{n,m}^* \mathbf{Q}_q \check{\mathbf{q}}_{n,m}}, & \text{if } (n, m) \in (1...N, 1...M). \end{cases} \tag{4.53}$$

The total amplitude of the system is then defined as

$$A_q = \sqrt{\sum_{n\geq 0, m\geq 0} A_q(n,m)^2}. \tag{4.54}$$

Similarly, the amplitude of the harmonic components of the forcing is defined as in Eq. (4.53) with the L^2 norm $\mathbf{Q}_f$ and the total forcing amplitude A reads

$$A = \sqrt{\sum_{n>0, m>0} A_f(n,m)^2}. \tag{4.55}$$

4.2.2 Numerical methods

All the tools required to compute the base-flow and the input/output analysis are already implemented in BROADCAST. The Space-Time Spectral Method implementation is based on the in-house python module from Moulin [130].

The non-linear system Eq. (4.33) is solved by a Newton method with $\mathbf{q}^{i+1} = \mathbf{q}^i + \delta\mathbf{q}^i$ and iterative solutions of Eq. (4.56).

$$\mathbf{A}_{\mathrm{tot}}(\mathbf{q}^i)\,\delta\mathbf{q}^i = -\mathbf{R}_{\mathrm{tot}}(\mathbf{q}^i), \tag{4.56}$$

with $\mathbf{R}_{\mathrm{tot}}(\mathbf{q}^i) = \frac{\partial \mathbf{q}^i}{\partial t} + \mathbf{R}(\mathbf{q}^i) - \mathbf{Pf}$ and then $\mathbf{A}_{\mathrm{tot}}(\mathbf{q}^i) = \mathbf{I}\frac{\partial(\cdot)}{\partial t} + \mathbf{A}(\mathbf{q}^i)$. The Newton method to find $\mathbf{q}$ follows the same pseudo-transient continuation method [37] as for the base-flow (see §2.1.5).

However, the size of the operator $\mathbf{A}_{\mathrm{tot}}$, which is the size of the two-dimensional discretisation multiplied by the number of collocation points, prevents us to apply the same direct inversion strategy employed for the base-flow and linear analysis. An iterative technique (§4.2.2.1) is then performed which requires an appropriate preconditioning strategy (§4.2.2.2).

4.2.2.1 Linear algebra

The linear system defined by Eq. (4.56) where $\mathbf{A}_{\mathrm{tot}}$ is defined in Eq. (4.57)-(4.58) is solved iteratively by a GMRES algorithm. The matrix-vector product $\mathbf{A}_{\mathrm{tot}}(\mathbf{q})\,\delta\mathbf{q}$ writes

$$\mathbf{A}_{\mathrm{tot}}(\mathbf{q})\,\delta\mathbf{q} = \begin{pmatrix} \ddots & \ddots & \ddots \\ \ddots & (\mathbf{A}_{\mathrm{tot}})_{(k,j),(c,d)} & \ddots \\ \ddots & \ddots & \ddots \end{pmatrix} \begin{pmatrix} \vdots \\ \delta\mathbf{q}_{c,d} \\ \vdots \end{pmatrix}, \tag{4.57}$$

with for the time collocation point k and the space collocation point j,

$$(\mathbf{A}_{\mathrm{tot}})_{(k,j),(c,d)} = (\mathbf{D}_t)_{kc} + \mathbf{A}_{2\mathrm{D}}(\mathbf{q}_{k,j}) + \mathbf{A}_z^q(\mathbf{q}_{k,j}) + \mathbf{A}_z^z(\mathbf{q}_{k,j})(\mathbf{D}_z)_{jd} + \mathbf{A}_z^{z^2}(\mathbf{q}_{k,j})(\mathbf{D}_{z^2})_{jd}. \tag{4.58}$$

For GMRES computations, only the matrix-vector product given by the linearised or the adjoint discrete residuals from Algorithmic Differentiation are necessary. Therefore, we avoid the expensive construction of the operator $\mathbf{A}_{\mathrm{tot}}$. For sake of completeness, in this work, the matrices $\mathbf{A}_z$ have been explicitly built for adjoint computations as the adjoint equations for the spanwise contributions have not been derived.

The GMRES algorithm needs to be preconditioned to achieve convergence within a finite number of iterations. From Eq. (4.56), a right-preconditioner $\mathbf{P}^C$ is used so that

$$\mathbf{A}_{\mathrm{tot}}(\mathbf{q})\left(\mathbf{P}^C\right)^{-1}\mathbf{x} = -\mathbf{R}_{\mathrm{tot}}(\mathbf{q}), \tag{4.59}$$

with the solution $\delta\mathbf{q}$ retrieved from $\mathbf{x}$ through

$$\mathbf{P}^C\delta\mathbf{q} = \mathbf{x}. \tag{4.60}$$

4.2.2.2 Block-circulant preconditioner

The GMRES algorithm uses the block-circulant preconditioning designed by Moulin [130]. Indeed, the pattern of the block Jacobian $\mathbf{A}_{\text{tot}}$ is almost block-circulant. For instance, if we consider only TSM in time for one harmonic ($N = 1$), the Jacobian writes

$$\mathbf{D}_t + \mathbf{A}_{2\text{D}}(\mathbf{q}) = \begin{pmatrix} (\mathbf{D}_t)_{00} + \mathbf{A}_{2\text{D}}(\mathbf{q}_0) & (\mathbf{D}_t)_{01} & (\mathbf{D}_t)_{02} \\ (\mathbf{D}_t)_{10} & (\mathbf{D}_t)_{11} + \mathbf{A}_{2\text{D}}(\mathbf{q}_1) & (\mathbf{D}_t)_{12} \\ (\mathbf{D}_t)_{20} & (\mathbf{D}_t)_{21} & (\mathbf{D}_t)_{22} + \mathbf{A}_{2\text{D}}(\mathbf{q}_2) \end{pmatrix}, \tag{4.61}$$

where from its definition Eq. (4.42), the coefficient $(\mathbf{D}_t)_{kl}$ is defined as $(\mathbf{D}_t)_u$ with $u = k - l$ and gets the following properties: $(\mathbf{D}_t)_{-u} = -(\mathbf{D}_t)_u$ and $(\mathbf{D}_t)_{2N+1-u} = -(\mathbf{D}_t)_u$. This yields to

$$\mathbf{D}_t + \mathbf{A}_{2\text{D}}(\mathbf{q}) = \begin{pmatrix} \mathbf{A}_{2\text{D}}(\mathbf{q}_0) & (\mathbf{D}_t)_1 & -(\mathbf{D}_t)_1 \\ -(\mathbf{D}_t)_1 & \mathbf{A}_{2\text{D}}(\mathbf{q}_1) & (\mathbf{D}_t)_1 \\ (\mathbf{D}_t)_1 & -(\mathbf{D}_t)_1 & \mathbf{A}_{2\text{D}}(\mathbf{q}_2) \end{pmatrix}. \tag{4.62}$$

The block-circulant pattern arises if the diagonal terms, the two-dimensional Jacobian $\mathbf{A}_{2\text{D}}(\mathbf{q})$, are equal for every collocation point $\mathbf{q}_j$ (for STSM in spanwise direction, the off-diagonal terms $\mathbf{A}_z(\mathbf{q})$ should also be equal). Therefore, approximating the Jacobian $\mathbf{A}_{\text{tot}}(\mathbf{q})$ by its value around the mean-flow $\mathbf{A}_{\text{tot}}(\overline{\mathbf{q}}) = \mathbf{P}^C$ leads to a block-circulant matrix which can be turned into a complex block-diagonal matrix through DFT and Eq. (4.62) becomes

$$\mathbf{D}_t + \mathbf{A}_{2\text{D}}(\overline{\mathbf{q}}) = \mathbf{E}_t^{-1} \begin{pmatrix} \mathbf{A}_{2\text{D}}(\overline{\mathbf{q}}) - i\omega\mathbf{I} & 0 & 0 \\ 0 & \mathbf{A}_{2\text{D}}(\overline{\mathbf{q}}) & 0 \\ 0 & 0 & \mathbf{A}_{2\text{D}}(\overline{\mathbf{q}}) + i\omega\mathbf{I} \end{pmatrix} \mathbf{E}_t. \tag{4.63}$$

This preconditioner $\mathbf{P}^C$ is equivalent to a block-Jacobi preconditioner in the frequency domain, such as the one used by Rigas et al. [155] for the AHBM. Therefore, it is adapted for the STSM when the off-diagonal components are dominated by the diagonal ones i.e. when the flow does not deviate too much from its mean value [130]. It enables through the DFT both in time and spanwise directions to reduce the Jacobian to a complex block-diagonal matrix $\check{\mathbf{P}}^C$:

$$\mathbf{P}^C = \mathbf{E}_t^{-1}\mathbf{E}_z^{-1}\check{\mathbf{P}}^C\mathbf{E}_z\mathbf{E}_t, \tag{4.64}$$

$$\check{\mathbf{P}}^C = \begin{pmatrix} \check{\mathbf{P}}^C_{-N-M} & & & & \\ & \ddots & & & \\ & & \check{\mathbf{P}}^C_{kj} & & \\ & & & \ddots & \\ & & & & \check{\mathbf{P}}^C_{NM} \end{pmatrix}. \tag{4.65}$$

The complex block diagonal matrix component for the time collocation point k and the space collocation point j writes

$$\check{\mathbf{P}}^C_{kj} = \mathbf{A}_{2\text{D}}(\overline{\mathbf{q}}) + \mathbf{A}^q_z(\overline{\mathbf{q}}) - j^2\beta^2\mathbf{A}^{z^2}_z(\overline{\mathbf{q}}) + i\left(k\omega\mathbf{I} + j\beta\mathbf{A}^z_z(\overline{\mathbf{q}})\right). \tag{4.66}$$

The block-diagonal matrix $\check{\mathbf{P}}^C$ is then solved through a block LU-factorisation. In order to reduce the memory consumption, different levels of approximation for the block LU-factorisation are considered. Apart from the direct LU, nested GMRES preconditioned by an incomplete LU (ILU) is also tested as well as a Block Low-Rank (BLR) approximated LU factorisation [116] available in MUMPS [2] with a tolerance set at 10^{-4}. The LU-BLR factorisation is used in this work and compared with other preconditioning strategies in 4.3.3.1.

4.2.2.3 Parallel implementation

The subroutines of BROADCAST code to compute the residuals and extract the derivative operators run sequentially. The linear systems are then multi-threaded with OpenMP using PETSc [96]. Therefore, MPI parallelism is used for the parallel implementation of the STSM with each MPI process handling one time or spanwise collocation point associated with a round-robin strategy to minimise the memory used and the number of parallel communications [131]. The current implementation does not support the distribution of one collocation point on multiple nodes through MPI communicators limiting then the maximal number of degrees of freedom.

4.2.2.4 De-aliasing

Because the STSM method is a pseudo-spectral method (the discrete Fourier coefficients being assumed equal to the continuous one), aliasing appears on the solution due to the non-linearity of the residual. Therefore, according to Orszag's "two-thirds" rule (one-half rule here as the compressible equations are cubic [94]), twice more harmonics have to be computed and the top half of the harmonics are truncated. In practice, it consists in defining a truncation operator $\mathbf{T}$. It is defined similarly to the derivative operator in Eq. (4.41)-(4.42) replacing the complex derivative function in frequency domain ($in\omega$) by the truncation function $t(n)$ given by Eq. (4.67) which yields Eq. (4.68) for the truncation coefficients.

$$t(n) = \begin{cases} 1, & \text{if } |n| \leq N//2 \\ 0, & \text{otherwise} \end{cases} \tag{4.67}$$

$$(\mathbf{T}_t)_{kl} = \frac{1}{2N+1}\left[1 + 2\sum_{n=1}^{N//2} \cos\left(\frac{2\pi n(k-l)}{2N+1}\right)\right]\mathbf{I}. \tag{4.68}$$

The truncation operator $\mathbf{T}$ is then applied to the non-linear system given by Eq. (4.43) and to its linearised form used in the Newton method. For the current work, as the spanwise harmonics carry more energy than the time harmonics, only the truncation operator in spanwise dimension $\mathbf{T}_z$ is applied.

4.2.2.5 Algorithm for non-linear input-output

The whole algorithm for the non-linear input-output analysis is then the direct-adjoint loop algorithm 6. The user-input parameter c for the optimisation step is chosen equal to 0.6 as a good trade-off between robustness and rapid convergence for this configuration. The convergence criteria θ_c is equal to 1°, this value being sufficient to observe converged solutions for this configuration. Slightly higher values of θ_c ($1° < \theta_c < 3°$) predict similar optimal forcing shape but with oscillations.

Algorithme 6 Iterative method for non-linear input-output

Initialise with the linear forcing $\check{\mathbf{f}}$ and the state $\mathbf{q}^0 = \mathbf{q_b} + \check{\mathbf{q}}$.
Normalise $\mathbf{f}$ to the finite amplitude A.
while $\theta_n > \theta_c$ **do** ▷ Adjoint loop for forcing optimisation.
  while $\mathbf{R}_{\text{tot}}(\mathbf{q}^i)/\mathbf{R}_{\text{tot}}(\mathbf{q}^{i-1}) > 10^{-8}$ **do** ▷ Newton loop for non-linear response.
    Apply $\mathbf{T}_z$ to $\mathbf{R}_{\text{tot}}(\mathbf{q}^i)$
    if $i = 0$ **then** ▷ Performed only once to save time.
      Compute the LU-factorisation of the block circulant preconditioner $\check{\mathbf{P}}^C$.
    end if
    $\delta\mathbf{q}^i \leftarrow$Solve the linear system Eq. (4.56) multiplied by $\mathbf{T}_z$ with a preconditioned GMRES.
    Apply $\mathbf{T}_z$ to $\delta\mathbf{q}^i$
    $\mathbf{q}^{i+1} \leftarrow \mathbf{q}^i + \delta\mathbf{q}^i$
  end while
  Compute the cost function $J(\mathbf{q})$ with Eq. (4.44).
  $\tilde{\mathbf{q}} \leftarrow$Solve the linear adjoint problem Eq. (4.46) multiplied by $\mathbf{T}_z$ with the same preconditioned GMRES.
  Compute the angle θ_n with Eq. (4.50). ▷ Check convergence to the optimal forcing.
  Update $\lambda_n(\theta_n)$ and $\mathbf{f}(\lambda_n)$ with Eqs. (4.48)-(4.49). ▷ Gradient ascent of the forcing.
end while

4.3 Non-linear input-output analysis of boundary layer flow

In the following, the non-linear input-output analysis of a boundary layer over an adiabatic flat plate is performed first at low Mach number regime for validation and then at Mach number 4.5.

4.3.1 Low Mach number boundary layer

The finite amplitude forcing for the non-linear input-output analysis is applied only on momentum equations with the same domain restriction as for the resolvent analysis (case N01 in Table 2.3). Only oblique forcing at a fundamental frequency 1ω and a fundamental spanwise wavenumber 1β is considered. Furthermore, symmetric solution is assumed so that we can prescribe $\check{\mathbf{f}}_{1,1} = \check{\mathbf{f}}_{1,-1}$. Therefore, the forcing is searched as two identical oblique waves of opposite angle in the $x-z$ plane. The amplitude of the forcing A and the amplitude of the harmonic components of the response A_q are defined in 4.2.1.4.

Rigas et al. [155] showed that the most dangerous fundamental forcing in the non-linear framework was a pair of oblique TS waves whose frequency $F = 11.7 \times 10^{-5}$ and spanwise wavenumber $\beta = 33.4 \times 10^{-5}$ were close to the linear ones. Starting from the forcing predicted by the resolvent analysis at a small amplitude $A = 10^{-5}$ and the level of truncation of $N = 2$ in time and $M = 2$ in spanwise direction, the non-linear input-output analysis is then repeated with an increasing amplitude A by initialising the optimal forcing and the non-linear solution from the one obtained at the previous lower amplitude. Evolution of the drag increase ΔC_D with the forcing amplitude A is plotted in Figure 4.2a. It is noticed that above $A = 3\times10^{-5}$, the non-linear interactions are not fully captured with $M = 2$ harmonics. Increasing the spanwise level of truncation up to $M = 4$ allows to take into account the higher harmonics generated by the $(0\omega,2\beta)$ streaks. From Figure 4.2, the STSM developed in this work compares well with the incompressible AHBM from Rigas et al. [155]. In Figure 4.2b, the skin-friction of the mean-flow is plotted for both methods at two different forcing amplitudes departing from the laminar

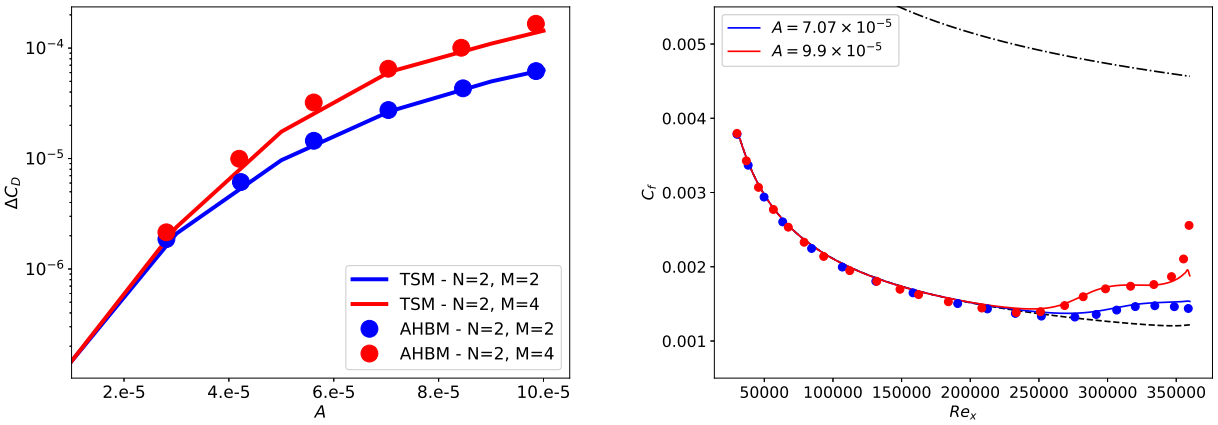

(a) **(b)**

Figure 4.2: Comparison of the drag increase and the mean-flow skin-friction coefficient at different forcing amplitude between the STSM at Mach number 0.1 (solid lines) and the incompressible AHBM from [155] (dots). (a) Drag increase ΔC_D with respect to the forcing amplitude A for $N = 2$ in time and two different levels of truncation in spanwise direction: $M = 2$ (blue) and $M = 4$ (red). (b) Mean-flow skin-friction coefficient C_f along the streamwise direction for $N = 2$ and $M = 4$ at two different forcing amplitudes: $A = 7.07 \times 10^{-5}$ (blue) and $A = 9.9 \times 10^{-5}$ (red). Black dashed line indicates the laminar skin-friction coefficient curve and dash-dotted line the turbulent curve.

flow. Except for the values close to the outlet, both methods converge to the same skin-friction coefficient. The discrepancies are explained by the different outlet boundary conditions applied between the present finite volume compressible framework and the finite element incompressible framework from Rigas et al. [155].

The STSM implementation being validated at low Mach number, the same boundary layer case is then explored at higher Mach number.

4.3.2 Hypersonic boundary layer

We consider the hypersonic boundary layer case (case N45 in Table 2.3). From the linear input-output analysis, we observe that the waves whose frequencies are around the first Mack mode ($F \sim 10 \times 10^{-5}$) would need four levels of non-linear interactions to reach the frequency where the second Mack mode is amplified ($F \sim 50 \times 10^{-5}$). Then, Rigas et al. [155] noticed on the low Mach number boundary layer that the non-linear interactions are stronger in the spanwise direction than in the time direction resulting that higher levels of truncation are necessary for M than N as shown in Figure 4.2a. From both observations above, it is expected that the second Mack mode will not be triggered by low frequency waves in the non-linear input-output analysis for this specific configuration. A non-linear input-output analysis restricted to two-dimensional disturbances is performed in appendix D where two second Mack modes interact together.

Therefore, the same constraints on the optimal forcing searched in the non-linear input-output analysis are prescribed as for low Mach number i.e. a pair of oblique waves. Forcing as well planar waves and streaks at respectively the fundamental frequency ω and spanwise wavenumber β did not affect the results, the optimal forcing mechanism remaining the oblique waves. It is called fundamental forcing. To compute the response, we initially select $N = 2$ time harmonics and $M = 4$ spanwise harmonics from the conclusions drawn from the low Mach number boundary layer and we look for the optimal (F,β) couple in the vicinity of the first

Mack mode. Rigas et al. [155] observed that asymmetric oblique waves promote transition faster in the incompressible boundary layer. Therefore, noise was added to the initial forcing to converge towards an asymmetric optimal forcing, however, for all cases considered, the optimal fundamental forcing includes only symmetric waves.

4.3.2.1 Fundamental forcing

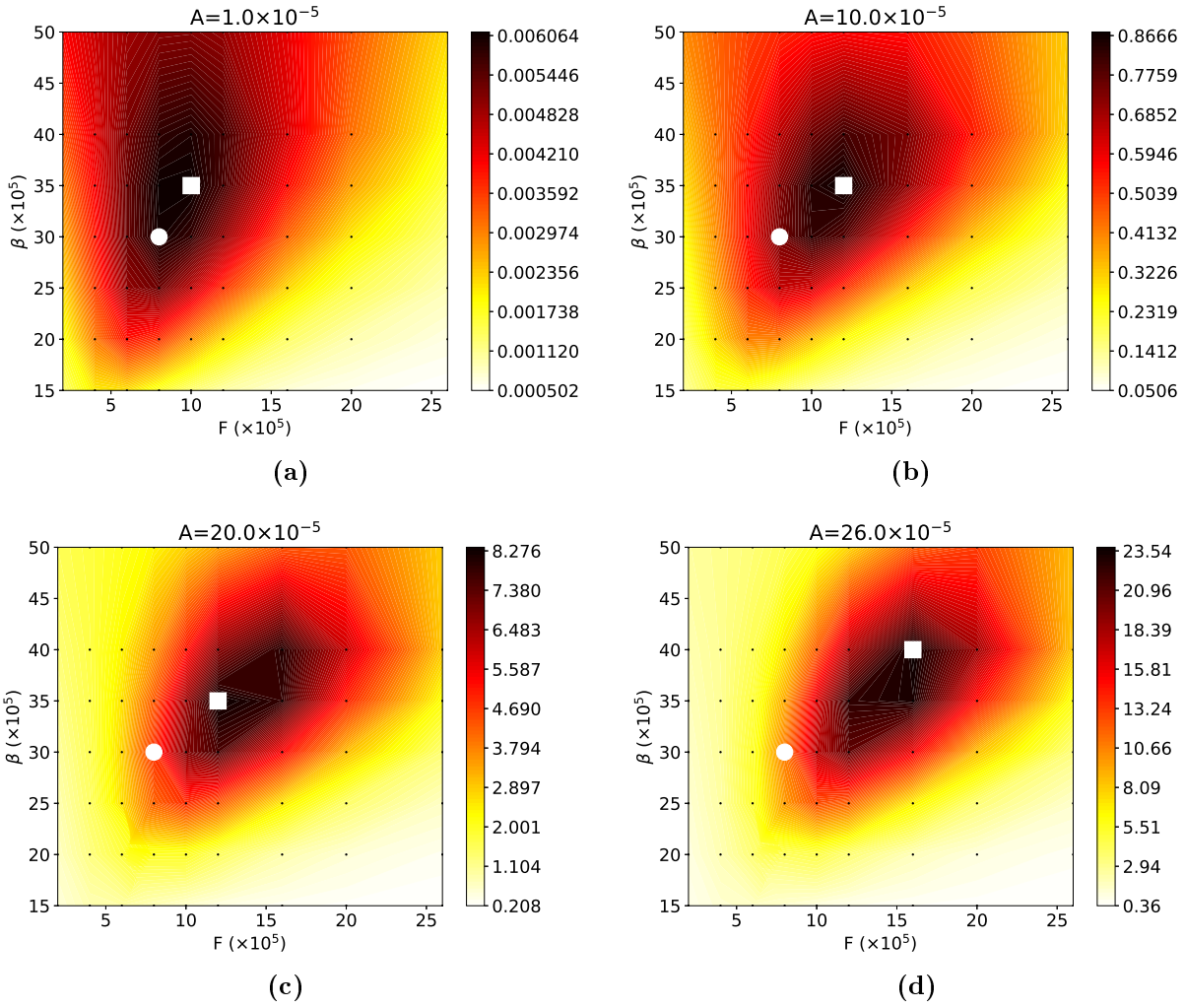

Figure 4.3: Square root of the cost function $\sqrt{J}$ with respect to the frequency F and the spanwise wavenumber β at Mach number 4.5 for $N = 2$ and $M = 4$ at different forcing amplitude A. White circle denotes the maximum location of the linear optimal gain μ (first Mack mode at $F = 8 \times 10^{-5}$ and $\beta = 30 \times 10^{-5}$) while white square denotes the maximum location of the cost function J from the non-linear input-output analysis. Small black dots indicate the grid points where the non-linear input-output analysis has been performed. (a) $A = 1 \times 10^{-5}$. (b) $A = 10 \times 10^{-5}$. (c) $A = 20 \times 10^{-5}$. (d) $A = 26 \times 10^{-5}$.

The cost function $\sqrt{J}$ proportional to the drag increase is plotted in the $F - \beta$ map for increasing forcing amplitudes A in Figure 4.3. Starting at low amplitude ($A = 10^{-5}$) where the frequency/spanwise wavenumber of the drag peak is close to the one predicted by the linear input-output analysis, larger amplitudes induce a shift of the peak value to higher frequency and spanwise wavenumber. The optimal couple ($F = 16 \times 10^{-5}$, $\beta = 40 \times 10^{-5}$) at the largest amplitude computed ($A = 26 \times 10^{-5}$) is substantially larger than the one from the resolvent analysis ($F = 8 \times 10^{-5}$, $\beta = 30 \times 10^{-5}$). For this optimal forcing, the mean-flow skin-friction

coefficient evolution along the streamwise direction is plotted in Figure 4.4. At this forcing amplitude, the skin-friction is between the laminar and turbulent skin-friction curves for zero pressure gradient flat plates. Keeping F and β constant, the forcing amplitude is then increased further to reach turbulence level. However, as we increase the forcing amplitude, the number of non-linear interactions is expected to increase as well. Therefore, $N = 2$ harmonics in time and $M = 4$ harmonics in spanwise direction are not sufficient to converge the non-linear response which is noticeable in Figure 4.4 where the solution at $A = 32\times10^{-5}$ yields different C_f predictions according to the level of truncation of N and M. By performing various simulations up to $N = 6$ and $M = 8$, it was found that $N = 4$ and $M = 6$ harmonics hold enough non-linear interactions to converge the non-linear solution at this forcing amplitude.

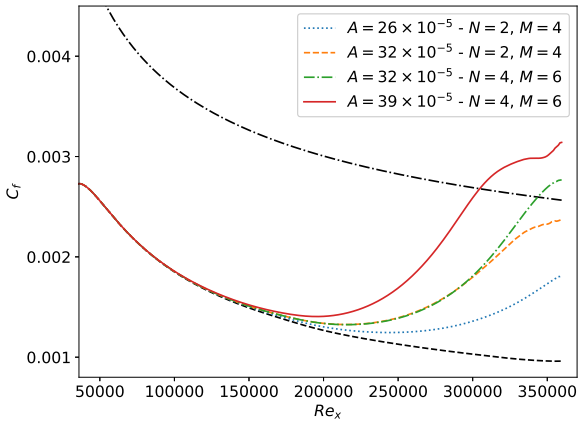

Figure 4.4: Mean-flow skin-friction coefficient C_f at Mach number 4.5 along the streamwise direction for $F = 16 \times 10^{-5}$ and $\beta = 40 \times 10^{-5}$ at different forcing amplitudes and levels of truncation in time and spanwise directions. Black dashed line indicates the laminar skin-friction coefficient curve and dash-dotted line the turbulent curve.

The distribution of the optimal forcing and non-linear response are then analysed. As for the linear input-output analysis (Figure 2.13b), the amplitude of the forcing (Figure 4.5a) and the response (Figure 4.5b) are computed for the forcing amplitude $A = 26 \times 10^{-5}$.

First, about the optimal forcing, both are very similar, the largest difference being that the oblique waves predicted by the STSM are more localised and slightly more upstream in comparison with the waves from the resolvent analysis (see appendix E.1 for a deeper comparison between both forcings). Secondly, about the non-linear response, the oblique first Mack mode forcing waves initially produce response through the linear mechanism $(1\omega,1\beta)$. Then, from $Re_x \sim 100000$, the non-linear interactions of both symmetric oblique waves generate streaks $(1\omega,1\beta) + (-1\omega,1\beta) \rightarrow (0\omega,2\beta)$ while their self-interactions produce mean-flow deviation $(1\omega,1\beta) + (-1\omega,-1\beta) \rightarrow (0\omega,0\beta)$. Notice that the harmonic component $(0\omega,0\beta)$ in Figure 4.5b represents the mean-flow deviation $\breve{\mathbf{q}}_{0,0} - \mathbf{q_b}$. Higher harmonics in time $(2\omega,...)$ are also produced and slowly grow in the downstream direction. As the linear amplification of the streaks is large (see Figure 2.15), they grow faster than the higher harmonics in time. From $Re_x \sim 150000$, they interact with the fundamental oblique waves $(0\omega,2\beta) + (1\omega,1\beta) \rightarrow (1\omega,3\beta)$ creating harmonic oblique response and from $Re_x \sim 200000$, they interact with themselves $(0\omega,2\beta) + (0\omega,2\beta) \rightarrow (0\omega,4\beta)$ to generate streaks of higher harmonic. All these harmonics transfer energy to the mean-flow resulting in a growing mean-flow deviation and an increased mean-flow skin-friction. The non-linear interactions at low Mach number (Figures 8b and 15b in Rigas et al. [155]) are quite different than those observed here at Mach number 4.5. For low Mach number, the linear amplification of the streaks are larger than the oblique

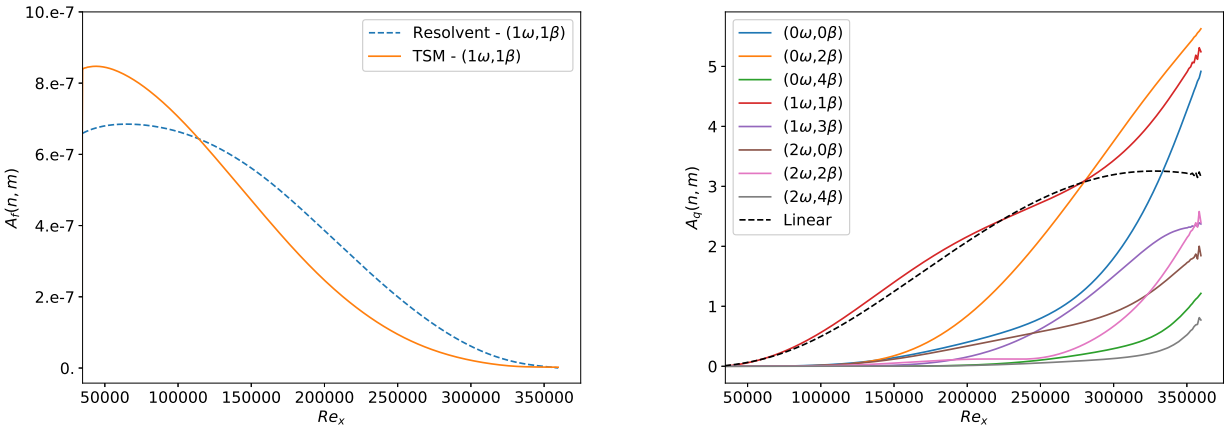

(a) **(b)**

Figure 4.5: Amplitude of the forcing and the response from the oblique forcing at $F = 16 \times 10^{-5}$, $\beta = 40 \times 10^{-5}$, $A = 26 \times 10^{-5}$, $N = 2$ and $M = 4$. (a) Amplitude of the optimal oblique forcing $A_f(1,1)$ given by the STSM (orange) compared with the linear forcing predicted by the resolvent analysis at the same (F, β) (blue). (b) Amplitude of the different harmonic components of the response $A_q(n,m)$ given by the STSM compared with the linear response predicted by the resolvent (dashed black line). Only the 8 harmonic components of largest amplitude are shown for clarity, they represent 99.96% of the total energy.

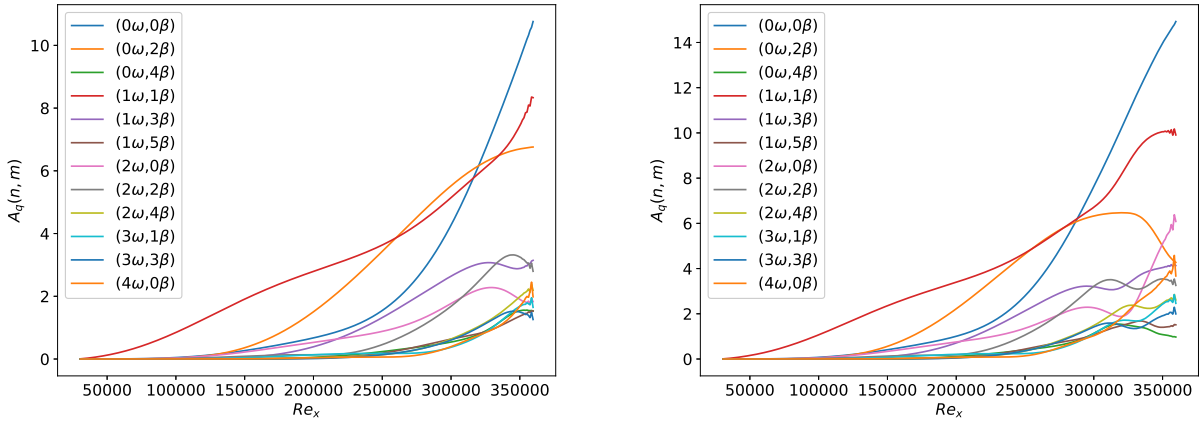

(a) **(b)**

Figure 4.6: Amplitude of the response from the oblique forcing at $F = 16 \times 10^{-5}$, $\beta = 40 \times 10^{-5}$, $N = 4$ and $M = 6$ at two different forcing amplitudes A. (a) $A = 32 \times 10^{-5}$. The 12 harmonic components of largest amplitude shown represent 99.4% of the total energy. (b) $A = 39 \times 10^{-5}$. The 12 harmonic components of largest amplitude shown represent 97.1% of the total energy.

waves, therefore, once produced by the interaction of the oblique waves, the streaks grow much faster yielding higher harmonics in spanwise dimension. They ultimately reach saturation and spread their energy to other harmonics components. At Mach number 4.5, the streaks are less amplified reaching similar level of energy than the oblique waves, producing therefore less harmonics in spanwise dimension. The linear and non-linear responses have been computed for various Mach numbers between 0.1 and 4.5 corroborating this trend (see appendix E.2). The effect of the compressibility on the optimal forcing is also explored in appendix E.2.3.

The response for larger forcing amplitudes, $A = 32 \times 10^{-5}$ (Figure 4.6a) and $A = 39 \times 10^{-5}$

(Figure 4.6b), show similar evolutions of the modes. The obliques waves and the streaks remain the dominant modes. Larger number of higher harmonics is generated from secondary interactions and the mean-flow deviation grows considerably.

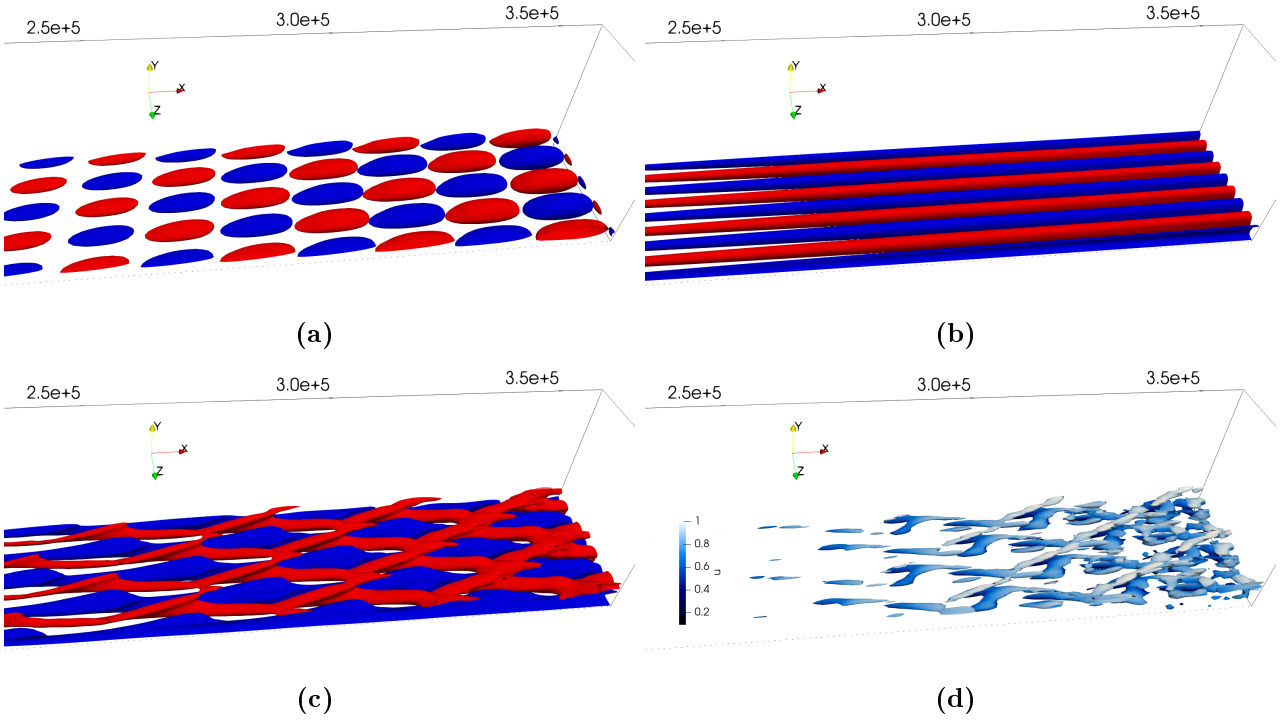

Figure 4.7: Isosurfaces of streamwise velocity fluctuations $u' = \pm 0.1$ of the response downstream $Re_x = 250000$ resulting from the oblique forcing at $F = 16 \times 10^{-5}$, $\beta = 40 \times 10^{-5}$, $A = 32 \times 10^{-5}$, $N = 4$ and $M = 6$. (a) Fundamental oblique harmonic $u'_{1,1}$ $(1\omega,1\beta)$. (b) Streak harmonic $u'_{0,2}$ $(0\omega,2\beta)$. (c) Instantaneous disturbance flow-field $u - u_b$ (sum of all harmonics). (d) Isosurfaces of Q-criterion at 1.5×10^{-9} coloured by streamwise velocity u.

Isosurfaces of the harmonic components and the full flow reconstruction are plotted in Figure 4.7 at the forcing amplitude $A = 32 \times 10^{-5}$ where the skin-friction overshoots the turbulent skin-friction. Initial stages of the laminar to turbulent transition are observed through staggered Λ-shaped vortices (Figure 4.7c) and other vortical structures in the downstream part of the domain highlighted by the Q-criterion (Figure 4.7d). Furthermore, one may observe that the disturbance flow-field $\mathbf{q} - \mathbf{q_b}$ (Figure 4.7c) results mainly of the combination of the oblique waves (Figure 4.7a) and the streaks (Figure 4.7b).

4.3.2.2 Superharmonic forcing

The optimal fundamental forcing is a pair of oblique waves. Nonetheless, in the previous section, it was highlighted that these waves generate streaks at twice spanwise wavenumber $(0\omega,2\beta)$. Therefore, a forcing which also triggers the higher harmonics would promote the response and increase the skin-friction. Studying the case at $A = 26 \times 10^{-5}$ with the levels of truncation $N = 2$ and $M = 4$, we let the steepest ascent optimisation algorithm explore forcing on higher harmonic components. We look for the so-called optimal superharmonic forcing.

Three different superharmonic forcings are compared to the fundamental one: fundamental oblique forcing with streaks $(0\omega,2\beta)$, forcing on all modes up to $N = 2$ and $M = 2$ and forcing on all modes up to $N = 2$ and $M = 4$. Evolution of the skin-friction coefficient is plotted in Figure 4.8 for the different superharmonic forcings. All these forcings promote faster transition as they amplify the higher harmonics modes before their generation by the non-linear interactions

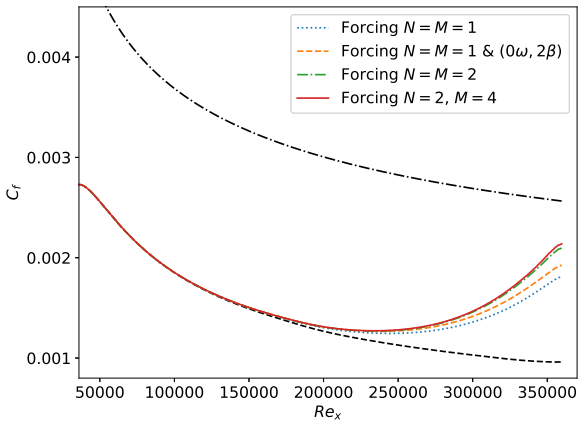

Figure 4.8: Mean-flow skin-friction coefficient C_f along the streamwise direction for $F = 16 \times 10^{-5}$, $\beta = 40 \times 10^{-5}$, $A = 26 \times 10^{-5}$, $N = 2$, $M = 4$ and different type of forcings: fundamental ($N = M = 1$), fundamental & streaks (0ω,2β), superharmonic at ($N = M = 2$) and superharmonic at ($N = 2$, $M = 4$). Black dashed line indicates the laminar skin-friction coefficient curve and dash-dotted line the turbulent curve.

of the oblique fundamental waves. While the streaks have the largest response in comparison with the other harmonics, see Figure 4.5b for instance, we notice that forcing only with oblique fundamental waves and the streaks is far from being optimal. Indeed, superharmonic forcing up to $N = 2$ and $M = 2$ increases further more the friction. This is confirmed by observing which harmonic components select the optimal superharmonic forcing (Figure 4.9a). Apart from the fundamental forcing (1ω,1β), from the largest to the lowest amplitude, forcing is applied to the streaks (0ω,2β), the secondary oblique waves (2ω,2β) at half the amplitude of the streaks, the planar waves (2ω,0β), the oblique waves (1ω,3β) and (2ω,1β). The two last harmonics do not contribute much as the skin-friction does not evolve much with the addition of the harmonic (1ω,3β). Therefore, in addition to the streaks, forcing the harmonics (2ω,2β) and (2ω,0β) promote transition. The comparison of the response between fundamental and superharmonic forcings (Figure 4.9b) evolves as expected with the higher harmonics growing earlier upstream when they are triggered by their corresponding forcings. All the harmonics have more energy even the fundamental oblique waves, which had initially less energy because of a lower forcing. The latter get additional energy, produced by the non-linear interactions of the other harmonics, from $Re_x \sim 200000$.

4.3.2.3 Link to weakly non-linear analysis

For low forcing amplitude A, the non-linear input-output analysis can be restricted to a weakly non-linear analysis [155]. Weakly non-linear analysis has been described for oscillator flows in §4.1.1 where we developed an amplitude equation (4.1) in the vicinity of a critical parameter: $\mathcal{A}(\epsilon)$. Here, for an amplifier flow, we aim at deriving an expression for the drag increase induced by the mean-flow deviation with respect to the forcing amplitude: $\sqrt{J}(A)$.

Let's assume a fundamental symmetric oblique forcing $\check{\mathbf{f}}_{1,1}$ which remains constant for every amplitude. At very low forcing amplitude A, the response $\check{\mathbf{q}}_{1,1}$ is proportional to the oblique forcing:

$$\check{\mathbf{q}}_{1,1} \propto A\check{\mathbf{f}}_{1,1}. \tag{4.69}$$

Then, the mean-flow deviation $\check{\mathbf{q}}_{0,0} - \mathbf{q_b}$ resulting from the non-linear interactions of $\check{\mathbf{q}}_{1,1}$ with

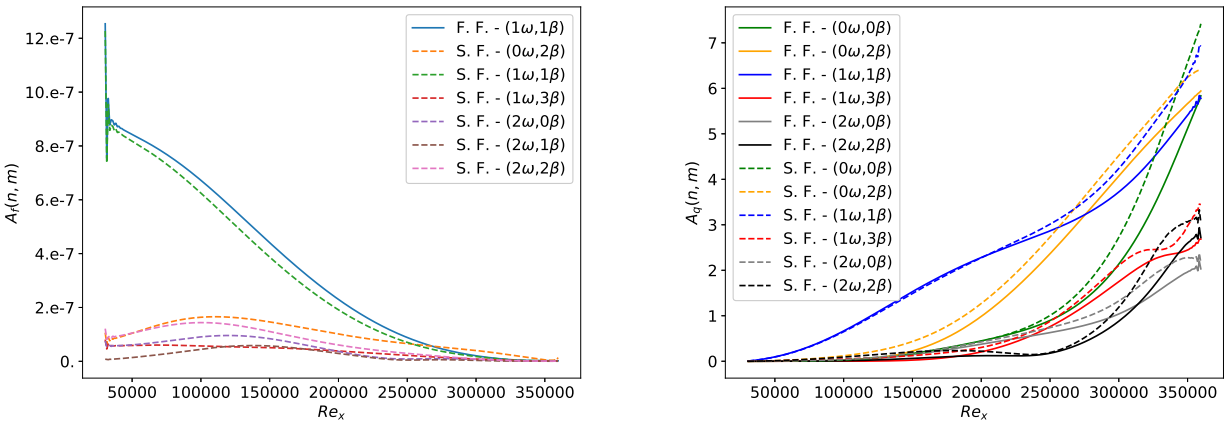

(a) **(b)**

Figure 4.9: Amplitude of the forcing and the response at $F = 16\times10^{-5}$, $\beta = 40\times10^{-5}$, $A = 26\times10^{-5}$, $N = 2$ and $M = 4$. Comparison between the fundamental forcing (F. F., solid lines) and the super-superharmonic forcing ($N = 2$, $M = 4$) (S. F., dashed lines). (a) Amplitude of the optimal forcing $A_f(n,m)$. Only the 6 harmonic components of largest amplitude of the super-superharmonic forcing are shown, they represent 99.9% of the total energy. (b) Amplitude of the different harmonic components of the response $A_q(n,m)$. Only the 6 harmonic components of largest amplitude are shown for clarity, they represent 99.4% of the total energy for fundamental forcing and 99.0% for superharmonic forcing.

$\check{\mathbf{q}}_{-1,-1}$ gives

$$\check{\mathbf{q}}_{0,0} - \mathbf{q_b} \propto (\check{\mathbf{q}}_{1,1} \times \check{\mathbf{q}}_{-1,-1}) \propto A^2(\check{\mathbf{f}}_{1,1} \times \check{\mathbf{f}}_{-1,-1}) \propto a_2 A^2. \tag{4.70}$$

Streaks are also generated from the non-linear interaction of $\check{\mathbf{q}}_{1,1}$ with $\check{\mathbf{q}}_{-1,1}$:

$$\check{\mathbf{q}}_{0,2} \propto (\check{\mathbf{q}}_{1,1} \times \check{\mathbf{q}}_{-1,1}) \propto a_3 A^2, \tag{4.71}$$

which will interact at higher amplitude with themselves to produce additional mean-flow deviation:

$$\check{\mathbf{q}}_{0,0} - \mathbf{q_b} \propto (\check{\mathbf{q}}_{1,1} \times \check{\mathbf{q}}_{-1,-1}) + (\check{\mathbf{q}}_{0,2} \times \check{\mathbf{q}}_{0,-2}) \propto a_2 A^2 + a_4 A^4. \tag{4.72}$$

Therefore, the square root of the cost function $\sqrt{J(\mathbf{q})}$ being almost a linear operator of the mean-flow deviation can be written as

$$\sqrt{J(\mathbf{q})} \propto a_2 A^2 + a_4 A^4 + a_6 A^6 + \cdots, \tag{4.73}$$

with a_2 the coefficient accounting for the non-linear interactions of $\check{\mathbf{q}}_{1,1}$ with $\check{\mathbf{q}}_{-1,-1}$, a_4 the interactions between $\check{\mathbf{q}}_{0,2}$ and $\check{\mathbf{q}}_{0,-2}$, $\check{\mathbf{q}}_{2,0}$ and $\check{\mathbf{q}}_{-2,0}$, $\check{\mathbf{q}}_{2,2}$ and $\check{\mathbf{q}}_{-2,-2}$, a_6 the interactions between $\check{\mathbf{q}}_{1,3}$ and $\check{\mathbf{q}}_{-1,-3}$,...

The analytical definitions of a_2, a_4,... are unknown, however, the validity of the polynomial expansion (4.73) can be assessed by comparing its evolution with respect to A with the evolution of the square root of the cost function computed with the non-linear input-output analysis. Comparison is shown in Figure 4.10a where the coefficients a_2, a_4 and a_6 have been computed through a least-square method using respectively only the first (at $A = 10^{-5}$), the two first (at $A = 10^{-5}$ and $A = 5\times10^{-5}$) and the three first (at $A = 10^{-5}$, $A = 5\times10^{-5}$ and $A = 10\times10^{-5}$) values of $\sqrt{J}$ given by the non-linear input-output analysis.

Three levels of polynomial approximations are assessed. The second order polynomial predicts well the evolution of $\sqrt{J}$ up to $A = 5\times10^{-5}$ but fails at higher amplitude where the streaks become large enough to induce mean-flow deviation. Then, the fourth order polynomial improves the prediction up to $A = 15\times10^{-5}$ where the $(1\omega, 3\beta)$ modes, generated by

the oblique modes and streaks, begin to provide additional skin-friction to the mean-flow. The sixth order polynomial approximation follows the good evolution up to $A = 28 \times 10^{-5}$. At this forcing amplitude, the skin-friction has deviated a lot from the laminar curve and is close to the turbulent level (see Figure 4.4) where the weakly non-linear analysis could not capture the dynamics. Higher order polynomial expressions do not improve the trend.

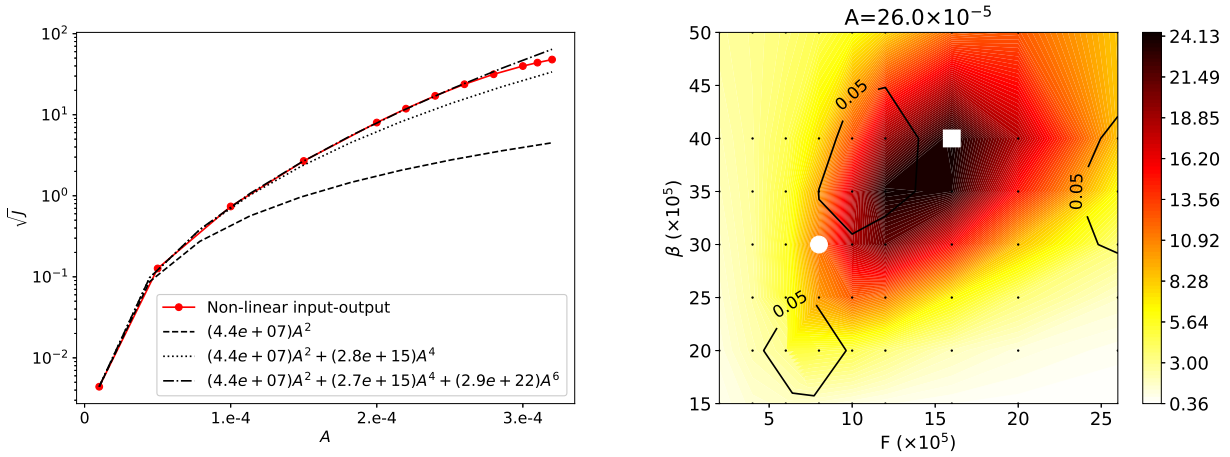

(a) **(b)**

Figure 4.10: (a) Square root of the cost function $\sqrt{J}$ with respect to the forcing amplitude A for the fundamental forcing case $F = 16 \times 10^{-5}$, $\beta = 40 \times 10^{-5}$, $N = 2$, $M = 4$. Comparison with the polynomial expressions from the weakly non-linear analysis. (b) Square root of the cost function $\sqrt{J}$ computed from the sixth order polynomial derived from the weakly non-linear analysis with respect to the frequency F and the spanwise wavenumber β at Mach number 4.5 for $N = 2$ and $M = 4$ at $A = 26 \times 10^{-5}$. Contour lines denotes the relative difference with the values from the non-linear input-output analysis (Figure 4.3d).

In this case, a sixth order polynomial whose coefficients have been computed from non-linear input-output analysis performed below $A = 10 \times 10^{-5}$ manages to predict the skin-friction evolution up to almost three times this forcing amplitude. Furthermore, we check the validity of such polynomial expansions at other frequencies and spanwise wavenumbers. The cost-function for all (F, β) at $A = 26 \times 10^{-5}$ (Figure 4.10b) is computed with the sixth order polynomial whose coefficients are computed from the cost-function at $A = 10^{-5}$ (Figure 4.3a), $A = 5 \times 10^{-5}$ and $A = 10 \times 10^{-5}$ (Figure 4.3b) at their respective (F, β). It predicts the good optimal frequency/spanwise wavenumber couple for the largest skin-friction and the cost function is similar to Figure 4.3d with a relative difference lower than 5% around the most amplified frequency/spanwise wavenumber. Therefore, for configurations where the optimal forcing remains similar at every amplitude, the combination of non-linear input-output analysis at low forcing amplitude, which converges quickly due to weak interactions, and the weakly non-linear analysis is a promising method to explore a larger parametric space at high forcing amplitude with a reduced computational cost.

4.3.2.4 Validation against DNS

The non-linear response obtained by the non-linear input-output analysis of the hypersonic boundary layer is further validated through Direct Numerical Simulation (DNS) computations made by Schioppa [164]. The DNS is performed with the in-house research solver FastS [139] already used for hypersonic transition analyses [103, 132]. For the set-up of the three-dimensional

DNS simulation, boundary conditions equivalent to those of the input-output analysis are applied. The useful DNS domain in the streamwise direction extends up to $Re_x = 10^6$, then a sponge layer consisting to a stretching of the mesh in the longitudinal direction is applied to avoid reflections. For the spanwise direction, the domain length corresponds to twice the wavelength of the fundamental mode (spanwise periodic boundary conditions). The mesh grid including $(N_x, N_y, N_z) = (1618, 160, 96)$ cells with $\max(\Delta x^+, \Delta y^+_{wall}, \Delta z^+) = (2, 0.3, 6)$ was fine enough to obtain converged results. The numerical scheme is a variant of a second-order upwind AUSM+(P) [97] associated with a fifth-order MUSCL reconstruction to limit the numerical dissipation. A similar shock-capture method [171] as for the two-dimensional discretisation (BROADCAST) is used (reduction of the reconstruction order based on the variables state for the shock-capture in FastS).

Injecting the optimal forcing predicted by the non-linear input-output analysis, STSM and DNS non-linear results for mean-flow skin-friction and amplitude of the different harmonics are compared in Figure 4.11. They show good agreement even for the harmonics generated after two and three levels of non-linear interactions, respectively the harmonics $(1\omega,3\beta)$ and $(2\omega,4\beta)$. Only small discrepancies are visible close to the outlet due to the presence of the boundary condition in the STSM at $Re_x = 3.6 \times 10^5$. Therefore, the STSM implementation is also validated for compressible flows.

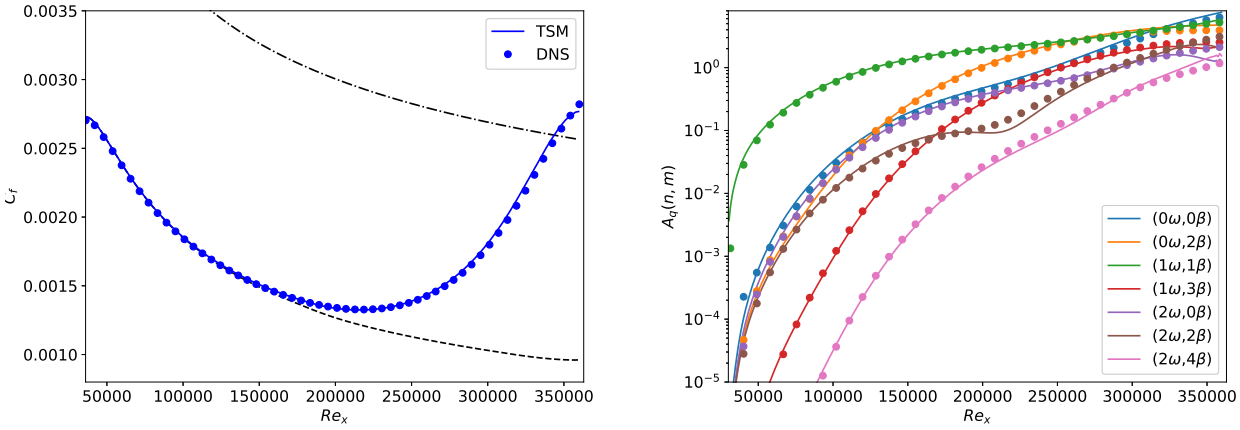

(a) **(b)**

Figure 4.11: Comparison between STSM (solid lines) and DNS (dots) non-linear responses with the optimal forcing obtained for $F = 16 \times 10^{-5}$, $\beta = 40 \times 10^{-5}$, $A = 32 \times 10^{-5}$, $N = 4$ and $M = 6$. (a) Mean-flow skin-friction coefficient C_f along the streamwise direction. Black dashed line indicates the laminar skin-friction coefficient curve and dash-dotted line the turbulent curve. (b) Amplitude of the different harmonic components of the response $A_q(n, m)$.

4.3.3 Computational performances

The computational performances of the non-linear input-output analysis through STSM are evaluated in the case where the laminar to turbulent transition occurs i.e. $F = 16 \times 10^{-5}$, $\beta = 40 \times 10^{-5}$, $A = 32 \times 10^{-5}$, $N = 4$ and $M = 6$ within ONERA HPC environment: Intel Xeon (Cascade Lake - 6240R, 2.4 GHz) with multi-threading on 6 cores. The performances of the preconditioning strategy and the scalability with the two-dimensional number of degrees of freedom of the STSM are studied. As the parallel implementation of the STSM relies on one MPI process per collocation point, scalability cannot be evaluated with respect to the

number of MPI cores for a given case. Moreover, the following results depend much on the case explored as, from Eq. (4.66), the preconditioner $\check{\mathbf{P}}^c$ explicitly depends on ω, β (high frequency/wavenumber and harmonic values reduce its sparsity) and the mean-flow $\overline{\mathbf{q}}$ (high mean-flow deviation deteriorates the approximation $\mathbf{P}^C = \mathbf{A}_{\text{tot}}(\overline{\mathbf{q}}) \approx \mathbf{A}_{\text{tot}}(\mathbf{q})$).

4.3.3.1 Preconditioning strategy

First, the preconditioning strategy performances are evaluated on the non-linear input-output for $N_x = 300$ points (mesh used for the present work). The LU factorisation of $\check{\mathbf{P}}^c$ is compared with the Block Low-Rank approximated LU factorisation (LU-BLR) [116] of $\check{\mathbf{P}}^c$ and factorisations applied on approximated block-circulant preconditioner $\check{\mathbf{P}}^c$ computed with lower order convective schemes reducing then the stencil and therefore the amount of off-diagonal components in the operator. Elapsed time, RAM consumed and number of GMRES iterations to converge the GMRES algorithm are displayed in Table 4.1.

Preconditioning strategy	Elapsed time	Elapsed time for LU	Total RAM	RAM for LU	GMRES iterations
LU on $\check{\mathbf{P}}^c$ at order 7	404	103	15.7	14.1	195
LU on $\check{\mathbf{P}}^c$ at order 5	320	81	12.2	10.9	168
LU on $\check{\mathbf{P}}^c$ at order 3	253	57	7.3	6.1	153
LU-BLR on $\check{\mathbf{P}}^c$ at order 7	409	86	10.1	8.5	202
LU-BLR on $\check{\mathbf{P}}^c$ at order 5	311	79	8.6	7.2	173
LU-BLR on $\check{\mathbf{P}}^c$ at order 3	255	58	6.2	5	154

Table 4.1: Elapsed time (seconds) to perform one Newton iteration (including the preconditioning) and RAM consumption per collocation point (Gigabytes) for different preconditioning strategies for the case $F = 16 \times 10^{-5}$, $\beta = 40 \times 10^{-5}$, $A = 32 \times 10^{-5}$, $N = 4$ and $M = 6$.

The LU-BLR considerably decreases the total RAM (10.1 Gb against 15.7 Gb per collocation point) by reducing the RAM of the LU factorisation. Furthermore, this approximated LU does not degrade much the preconditioner as the number of GMRES iterations to converge remains similar (202 against 195). Thanks to the time saved during the LU factorisation, it manages to reach a very similar elapsed time (409 s against 404 s). Then, about the lower order approximation strategy to build $\check{\mathbf{P}}^c$, the RAM decreases because of sparser preconditioner however, unexpectedly, the number of GMRES iterations decreases for a preconditioner more approximated with respect to the linear system. Both these factors strongly reduce the elapsed time. One possible clue to justify it may be that $\check{\mathbf{P}}^c$ is computed from $\mathbf{P}^C = \mathbf{A}_{\text{tot}}(\overline{\mathbf{q}})$ where the mean flow $\overline{\mathbf{q}}$ acts as a low-pass filter.

To further evaluate the approximation of $\check{\mathbf{P}}^c$ built with a lower order convective scheme, the case studied in this work is also compared to a case with 2 harmonics in time for the TSM (no spectral derivatives in the spanwise direction) at low forcing amplitude. The comparison of the computational performances between both cases highlights two opposite behaviours (Table 4.2). The large system case converges quicker with the low order preconditioner while the small system converges slower, both requiring less memory. A third preconditioning strategy is also studied with an inner GMRES (nested GMRES), with relative tolerance of 10^{-4}, preconditioned by an ILU(2). Parametric studies on the level of sparsity for the ILU and the tolerance of the inner GMRES were performed and only the best result in term of RAM consumption is shown. However, the nested GMRES strategy is not optimal for this case as for the same RAM used as the low order preconditioner, it is slower by almost a factor five.

Case	Preconditioning strategy	Elapsed time	Total RAM	GMRES iterations
225000 dof × 225 collocation points	LU on $\check{\mathbf{P}}^c$ at order 7	404	15.7	195
	LU on $\check{\mathbf{P}}^c$ at order 5	320	12.2	168
150000 dof × 5 collocation points	LU on $\check{\mathbf{P}}^c$ at order 7	187	8.5	4
	LU on $\check{\mathbf{P}}^c$ at order 5	201	5.9	70
	inner GMRES preconditioned with ILU(2)	920	5.9	6

Table 4.2: Elapsed time (seconds) to perform a Newton iteration (including the preconditioning) and RAM consumption per collocation point (Gigabytes) for different preconditioning strategies. The case studied in this work (225000 degrees of freedom multiplied by 225 collocation points) i.e. the case where laminar to turbulent transition occurs is compared with a case with a coarser mesh and only 5 collocation points at a lower forcing amplitude including less non-linear interactions.

Therefore, as the computations carried out on a different case (including less non-linear interactions) yielded opposite results, we adopt a conservative approach by using LU-BLR without low-order approximation.

4.3.3.2 Memory and time performances

Then, the memory and time scalability performance of the STSM algorithm with respect to the number of degrees of freedom of the two-dimensional discretisation are assessed.

As an overview, for the case considered, the system solves $(2N+1) \times (4M+1) = 225$ collocation points. For the mesh with $N_x = 300$ i.e. $n_{dof} = 225000$ degrees of freedom, the elapsed time to compute one GMRES iteration is around 1.6 seconds. With the GMRES relative tolerance set to 10^{-6} and BLR approximation for LU factorisation set to 10^{-4}, less than 250 GMRES iterations are required to converge the linear system and 14 Newton iterations to converge the non-linear solution. This represents a total elapsed time (without the optimisation of the forcing) on 1350 cores of about 1 hour and 35 minutes. Total RAM consumed is 3.5 Tb. However, these figures are valid for a specific configuration. As pointed out in Table 4.3, the number of GMRES iterations, as well as Newton iterations, strongly increases with the forcing amplitude when stronger non-linear interactions arise, increasing the total time and slightly the RAM consumption.

Forcing amplitude A	Number of Newton iterations	Number of GMRES iterations per Newton ite.	Elapsed Time (s)	Total RAM (Gb)
1×10^{-5}	8	13	239	1301
5×10^{-5}	8	17	264	1295
10×10^{-5}	9	18	298	1299
15×10^{-5}	9	22	335	1307
20×10^{-5}	11	32	520	1312
26×10^{-5}	11	82	1203	1343

Table 4.3: Number of Newton iterations, averaged number of GMRES iterations per Newton iteration to converge the non-linear solution, elapsed time (seconds) and total RAM consumption (Gigabytes) for different forcing amplitudes A with $n_{dof} = 225000$ degrees of freedom for the case $F = 16 \times 10^{-5}$, $\beta = 40 \times 10^{-5}$, $N = 2$ and $M = 4$ running on 510 cores.

Then, elapsed time (Figure 4.12a) and RAM consumption (Figure 4.12b) are evaluated with respect to the number of degrees of freedom for the construction and LU factorisation of

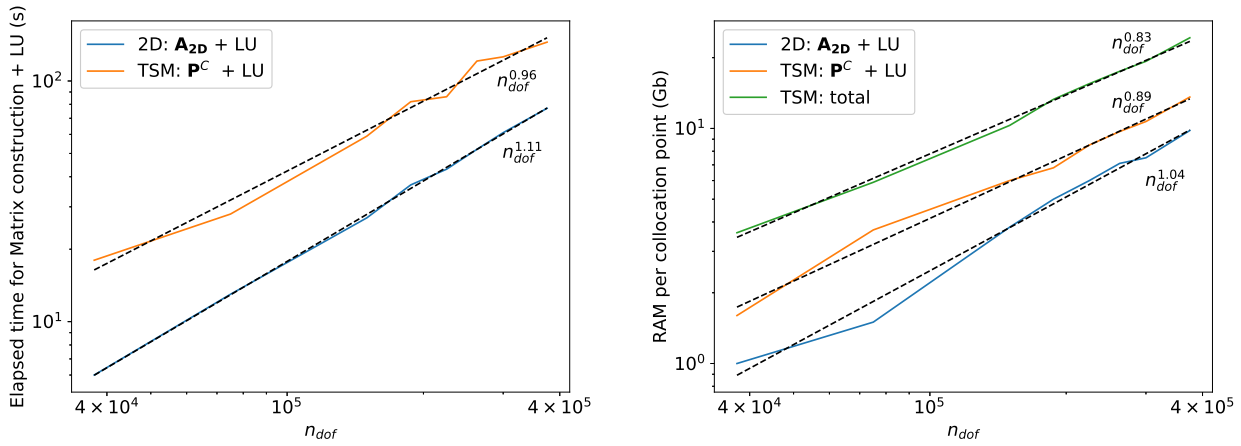

Figure 4.12: Elapsed time and RAM consumption per collocation point for the case $F = 16 \times 10^{-5}$, $\beta = 40 \times 10^{-5}$, $A = 32 \times 10^{-5}$, $N = 4$ and $M = 6$. (a) Elapsed time (seconds). (b) RAM consumption per collocation point (Gigabytes). Comparison between the matrix construction and the LU-BLR factorisation of the two-dimensional Jacobian $\mathbf{A}_{2\mathrm{D}}$ and the block-circulant preconditioner $\check{\mathbf{P}}^C$. Total RAM used for STSM computation (construction and LU-factorisation of $\check{\mathbf{P}}^C$ + construction of $\mathbf{A}_z$ for adjoint + Krylov subspace for GMRES) is also displayed.

the operator. The block-circulant preconditioner $\check{\mathbf{P}}^C$ scales similarly to the two-dimensional Jacobian $\mathbf{A}_{2\mathrm{D}}$ both for time and memory. The block-circulant preconditioner $\check{\mathbf{P}}^C$ requires larger memory and time for the construction of the operator and its LU-BLR factorisation because of the additional spanwise contributions $\mathbf{A}_z$ (Eq. (4.66)) which append non-zero components to the two-dimensional operator (see Table 2.2 of the spanwise contributions).

To compute the total memory to perform the non-linear input-output analysis through STSM, the memory required for the preconditioner, for the Krylov subspaces of the GMRES algorithm and for the construction of $\mathbf{A}_z$ for the adjoint product are summed. This yields a similar scalability and the full algorithm consumes about three times more memory per collocation point than the two-dimensional code BROADCAST in this configuration.

Eventually, a convergence analysis is performed with respect to the order of the numerical convective scheme. To assess that all harmonics are well solved, the total amplitude A_q of the fluctuations is computed following Eq. (4.54) for different refinements in the streamwise direction and scheme orders (see Table 4.4). With the seventh order scheme, convergence is obtained for around 29 cells per wavelength of the fundamental mode (harmonic $(1\omega,1\beta)$). Decreasing to the fifth order, 29 cells is enough to obtain similar results but convergence is reached at 43 cells per wavelength. For the third order scheme, it is necessary to considerably increase the number of cells per wavelength to at least 86 to reach similar total amplitude. Therefore, for converged results, it is beneficial to use a high order scheme (either 5^{th} or 7^{th} in this case) as even if the elapsed time for the LU-factorisation is similar to a low order scheme, their RAM consumption per collocation point is smaller (around 8 Gb against 10.7 Gb). Furthermore, the elapsed time per GMRES iteration, which is the predominant time constraint as around 200 GMRES iterations may be performed to solve one linear system at high forcing amplitudes, is much shorter (around 1.5 seconds against 4 seconds).

n_{dof}	N_c/ξ	Scheme order	Total amplitude A_q	RAM for LU	Elapsed time for LU	Elapsed time per GMRES iteration
150000	19	7	3745.1	6	59	1.4
225000	29	7	3749.8	8.5	86	1.6
150000	19	5	3716.4	5.2	43	1.0
225000	29	5	3740.6	7.4	66	1.5
337500	43	5	3749.9	9.4	101	2.3
225000	29	3	3521.4	4.5	33	1.2
450000	57	3	3698.0	7.8	62	2.6
675000	86	3	3717.0	10.7	85	4

Table 4.4: Convergence of the total amplitude A_q defined in Eq. (4.54) for different levels of refinement in the streamwise direction and numerical scheme orders for the case $F = 16 \times 10^{-5}$, $\beta = 40 \times 10^{-5}$, $A = 32 \times 10^{-5}$, $N = 4$ and $M = 6$. N_c/ξ is the number of cells per fundamental (first Mack mode) wavelength in the streamwise direction. RAM consumption per collocation point (Gigabytes) and elapsed time (seconds) to construct the matrix and perform the LU-BLR factorisation of the block-circulant preconditioner are indicated as well as the elapsed time (seconds) per GMRES iteration.

Chapter outcome summary:

The weakly non-linear analysis, developed in the discrete compressible framework, has been performed in the vicinity of the critical Reynolds number of the flow around a cylinder to show the supercritical nature of the bifurcation.
The linear resolvent has then been extended to a non-linear input-output analysis by taking into account the non-linear interactions of a finite number of time and spanwise harmonics. The worst-case disturbances have therefore been identified through a gradient-based algorithm. The compressible Navier-Stokes equations were written in a pseudo-spectral form through the Space-Time Spectral Method for both time and spanwise dimensions. Requiring de-aliasing technique, the large systems were solved iteratively using a block-circulant preconditioned GMRES. After validation at low Mach number, the transition of a boundary layer at $M_\infty = 4.5$ developing over an adiabatic flat plate has been studied. It results that the optimal fundamental forcing is a pair of symmetric oblique waves promoting the non-linear interactions of the first Mack mode with the streaks. Increasing the forcing amplitude, higher harmonics are generated until transition to turbulence is reached through a subharmonic varicose mode (staggered vortices).
Moreover, a weakly non-linear analysis which includes the third level of non-linear interactions (polynomial of order A^6) manages to substantially predict the skin-friction at a lower cost.

Chapter 5

Open-loop control of the non-linear solutions

Chapter foreword:

This chapter presents the open-loop control of the non-linear solutions derived in the previous chapter. The methodology relies on the same adjoint-based variational technique. To get an actuator closer to realistic configurations, the focus is thrown on mean-flow heat-flux control. A comparison is performed with the linear sensitivity derived in chapter 3 and the optimal heat-flux profiles to delay or promote the laminar to turbulent transition of the boundary layer at $M_\infty = 4.5$ are computed.

5.1 Open-loop control theory

In the previous chapter, the optimal forcing to generate the worst-case disturbances was searched through a Lagrangian approach. The same technique is here applied to find the optimal control vector to promote or mitigate the skin-friction induced by a fixed forcing (the optimal forcing calculated in §4.3.2).

The constraints are the finite amplitude control ($\|\mathbf{c}\|_c^2 = A_c^2$) and the non-linear relation Eq. (4.33) describing the system. The Lagrangian, which is a function of the control $\mathbf{c}$, the state $\mathbf{q}$ and the Lagrangian multipliers $\tilde{\mathbf{q}}$ and λ, writes

$$\mathcal{L}(\mathbf{c}, \mathbf{q}, \tilde{\mathbf{q}}, \lambda) = J(\mathbf{q}) - \langle \tilde{\mathbf{q}}, \mathbf{R}_{\text{tot}}(\mathbf{q}, \mathbf{c}) \rangle - \langle \lambda, \mathbf{c}^* \mathbf{Q}_c \mathbf{c} - A_c^2 \rangle. \tag{5.1}$$

By zeroing the variations of $\mathcal{L}$ with the state $\mathbf{q}$, we get

$$\mathbf{A}_{\text{tot}}^* \tilde{\mathbf{q}} = \frac{dJ(\mathbf{q})}{d\mathbf{q}}, \tag{5.2}$$

and by zeroing the variations of $\mathcal{L}$ with the optimal control:

$$2\lambda \mathbf{c} = -\mathbf{Q}_c^{-1} \frac{\partial \mathbf{R}_{\text{tot}}}{\partial \mathbf{c}}^* \tilde{\mathbf{q}}. \tag{5.3}$$

The most general approach to compute the optimal control $\mathbf{c}$ is a gradient-based algorithm. We define the reduced adjoint $\hat{\mathbf{q}} = -\mathbf{Q}_c^{-1}(\partial \mathbf{R}_{\text{tot}}/\partial \mathbf{c})^* \tilde{\mathbf{q}}$.

Then, whether the optimal control is searched for promoting transition or delaying it, either a steepest ascent or descent algorithm is performed. The steepest ascent is the same as for the optimal forcing which is recalled in Eq. (5.4). The constraint $\|\check{\mathbf{c}}\|_c^2 = A_c^2$ gives Eq. (5.5) for λ.

$$\mathbf{c}_{n+1} = \mathbf{c}_n + A_c \alpha_n (\hat{\mathbf{q}}_n - 2\lambda_n \mathbf{c}_n), \tag{5.4}$$

$$\lambda_n = \frac{1 + \alpha_n \gamma_n \cos\theta_n - \sqrt{1 - \alpha_n^2 \gamma_n^2 \sin^2\theta_n}}{2 A_c \alpha_n}, \tag{5.5}$$

with $\gamma_n^2 = \hat{\mathbf{q}}_n^* \mathbf{Q}_c \hat{\mathbf{q}}_n$, $\cos\theta_n = \mathbf{c}_n^* \mathbf{Q}_c \hat{\mathbf{q}}_n / (A_c \gamma_n))$, $\alpha_n = c/\gamma_n$ and c a user-input parameter between 0 and 1 to control the optimisation step length.

For the steepest descent i.e. to find the optimal control to delay transition, the equations become

$$\mathbf{c}_{n+1} = \mathbf{c}_n - A_c \alpha_n (\hat{\mathbf{q}}_n - 2\lambda_n \mathbf{c}_n), \tag{5.6}$$

$$\lambda_n = \frac{-1 + \alpha_n \gamma_n \cos\theta_n + \sqrt{1 - \alpha_n^2 \gamma_n^2 \sin^2\theta_n}}{2 A_c \alpha_n}, \tag{5.7}$$

5.2 Mean-flow heat-flux control of the hypersonic boundary layer

Following the conclusions from chapter 3 on the linear sensitivity to wall boundary control, we consider a single type of control: the heat-flux control $\mathbf{c} = \boldsymbol{\phi}_w$. Another possibility may have been blowing/suction control to generate streaks which stabilise the boundary layer [173]. We choose the L^2 norm for the control norm ($\mathbf{Q}_c$). Furthermore, for realistic configurations, the optimisation is restricted to mean-flow variations of heat-flux. However, conversely to the linear sensitivity analysis where the optimal heat-flux had to be homogeneous in the spanwise direction, it is here periodic as it can include any m harmonic components (0ω,$m\beta$). However,

the spanwise wavenumber of the heat-flux given by β has to be the same as those of the forcing/response which implies that the heat-flux variations have the same periodicity. Moreover, they must be aligned (no phase shift possible in the current framework).

We look for the optimal heat-flux to delay transition in §5.2.1 and to promote it in §5.2.2. So far, we have always linked laminar to turbulent transition with skin-friction. That is why we selected the integral of mean-flow skin-friction as the cost function, however, for any other purposes than drag reduction, another appropriate cost function may have been the integral of the wall temperature, especially for hypersonic flows, e.g. to design a lighter thermal shield for reentry vehicles, which may have arisen different optimal mean-flow heat-flux. Jahanbakhshi and Zaki [77] computed the non-linearly most dangerous disturbances with an ensemble-variational technique (different methodology than the adjoint procedure applied in the previous chapter) and tested both cost functions (skin-friction and wall temperature) for the optimisation algorithm. For both cases, they obtained very similar results in term of optimal disturbances, therefore we have keep the same cost function based on the skin-friction. They also found the corresponding optimal heat-flux [78] to delay the transition induced by these disturbances.

The same approach is followed in the next sections. In the previous chapter, the optimal transition scenario for our $M_\infty = 4.5$ configuration has been highlighted. These disturbances are frozen and the optimal open-loop control is computed following §5.1. Then, it is possible to iterate i.e. repeat the non-linear input-output on this controlled mean-flow and compute a new optimal heat-flux. Similarly to the linear sensitivity in chapter 3, we focus on the understanding of the optimal mean-flow heat-flux rather than finding the optimal one for this specific configuration through many optimisation iterations by minmax algorithms such as the Gradient Descent-Ascent method (GDA) [203]. We only compute once again the non-linear input-output analysis to check that the optimal heat-flux which damps the most dangerous disturbances does not promote other disturbances.

5.2.1 Delay transition

We consider the forcing amplitude where the maximum of skin-friction is midway the laminar and turbulent curves at outlet i.e. $A = 26 \times 10^{-5}$ for $F = 16 \times 10^{-5}$, $\beta = 40 \times 10^{-5}$. Indeed, from the amplitude of the harmonics plotted at $A = 26 \times 10^{-5}$ (Figure 4.5b) and when the turbulent level is reached (Figure 4.6a), the non-linear interactions remain similar. This choice is made to limit the computational cost so that the non-linear system is resolved using only $N = 2$ harmonics in time and $M = 4$ harmonics in spanwise dimension.

For this frozen forcing, an optimal heat-flux is computed gradually from a low amplitude where the initial guess is the heat-flux given by the linear sensitivity analysis of the first Mack mode up to an amplitude of $A_c = 20$. This heat-flux amplitude is equivalent to $C'_\theta = 1.65 \times 10^{-2}$ with C'_θ defined in Eq. (3.38). Increasing to higher heat-flux amplitudes produces a strong mean-flow deviation which is not the aim of this analysis where we look for a "small" open-loop heat-flux mainly acting on the the linear growth and non-linear interactions of the disturbances.

The optimal mean-flow heat-flux with only the harmonic component $(0\omega,0\beta)$ i.e. homogeneous in the spanwise direction is plotted in Figures 5.1 and 5.2a. It is compared to the linear sensitivity of the first Mack mode rescaled to a similar magnitude. They both have similar variations along the streamwise direction with a heating peak close to the inlet and a cooling region. However, they differ towards the outlet (oscillations due to the outlet boundary condition exist in the non-linear framework). The heat-flux obtained by the non-linear input-output analysis predicts a stronger heating region than the cooling one in opposition with the result from the linear sensitivity analysis. Spatial LST computation has been performed on the local mode corresponding to the first Mack mode. It is found that the location of the maximum of

the amplification rate is close to the maximum of heat-flux and branch II corresponds to the location of the change from a positive (heating) to a negative (cooling) heat-flux.

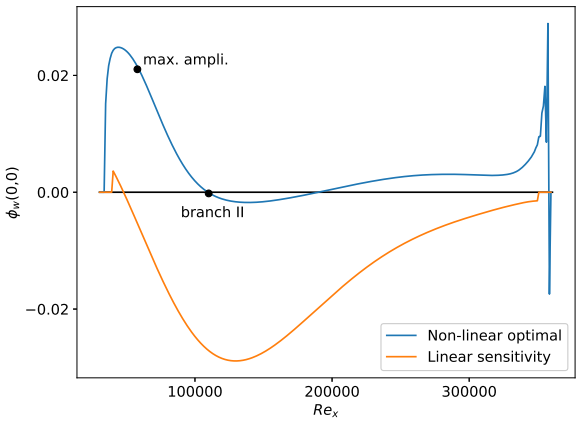

Figure 5.1: Optimal mean-flow heat-flux $\boldsymbol{\phi}_w$ at $C'_\theta = 1.65 \times 10^{-2}$ to delay the laminar to turbulent transition induced by the optimal fundamental forcing at $F = 16\times10^{-5}$, $\beta = 40\times10^{-5}$, $A = 26\times10^{-5}$, $N = 2$ and $M = 4$. Comparison with the linear sensitivity analysis for the first Mack mode at the same frequency and spanwise wavenumber rescaled to the same magnitude. Locations of branch II and maximal amplification rate ($\max(-\alpha_i)$) from the local stability analysis of the first Mack mode are also indicated.

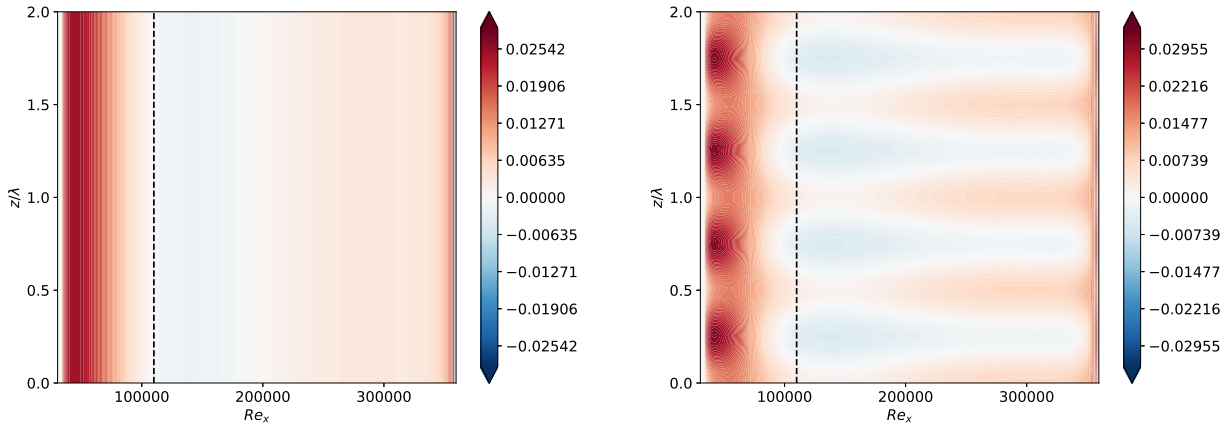

(a) **(b)**

Figure 5.2: Optimal mean-flow heat-flux $\boldsymbol{\phi}_w$ at $C'_\theta = 1.65 \times 10^{-2}$ to delay the laminar to turbulent transition induced by the optimal fundamental forcing at $F = 16\times10^{-5}$, $\beta = 40\times10^{-5}$, $A = 26\times10^{-5}$, $N = 2$ and $M = 4$. Dashed black line indicates the location of branch II. (a) Contours of mean-flow heat-flux on the $X - Z$ plane reconstructed from Figure 5.1. (b) Contours of mean-flow heat-flux on the $X - Z$ plane reconstructed with both the harmonic components $(0\omega,0\beta)$ and $(0\omega,2\beta)$.

By letting the algorithm optimise the heat-flux with other spanwise harmonic components $(0\omega,m\beta)$, a spanwise non-homogeneous heat-flux can be computed. Optimal heat-flux is given in Figure 5.2b. It only adds the harmonic $(0\omega,2\beta)$ to the mean-flow as no fluctuations exist for odd values of m and the mode $(0\omega,4\beta)$ is weak at this forcing amplitude. This heat-flux may then directly damp the amplification of the streaks $(0\omega,2\beta)$. The trend of the optimal heat-flux is relatively similar to the heat-flux from Jahanbakhshi and Zaki [78] computed for a

transition induced by the non-linear interactions of first and second Mack modes. They showed that alternation of almost spanwise homogeneous heating and cooling upstream, and spanwise periodic heat-flux patterns downstream, was optimal to delay the transition.

Then, for the spanwise homogeneous heat-flux control, we compute the skin-friction coefficient (Figure 5.3a) and amplitude of the response (Figure 5.3b) for two cases: the controlled flow with the frozen forcing and the flow with the new non-linear optimal forcing computed around the controlled mean-flow. About the skin-friction, the heat-flux reduces the skin-friction from $Re_x \sim 200000$ to the end of the domain (little overshoot and oscillations due to the outlet boundary condition). The new optimal forcing under a controlled mean-flow increases the skin-friction but still leads to smaller skin-friction levels than without control. By analysing the amplitude of the different modes, we notice that the heat-flux control, which is mainly located upstream $Re_x = 100000$, does not affect the fundamental oblique mode (1ω,1β) in this region. It only damps the amplification of this mode downstream. Similarly, for the streaks (0ω,2β), their apparition is not delayed but the heat-flux control reduces their growth downstream.

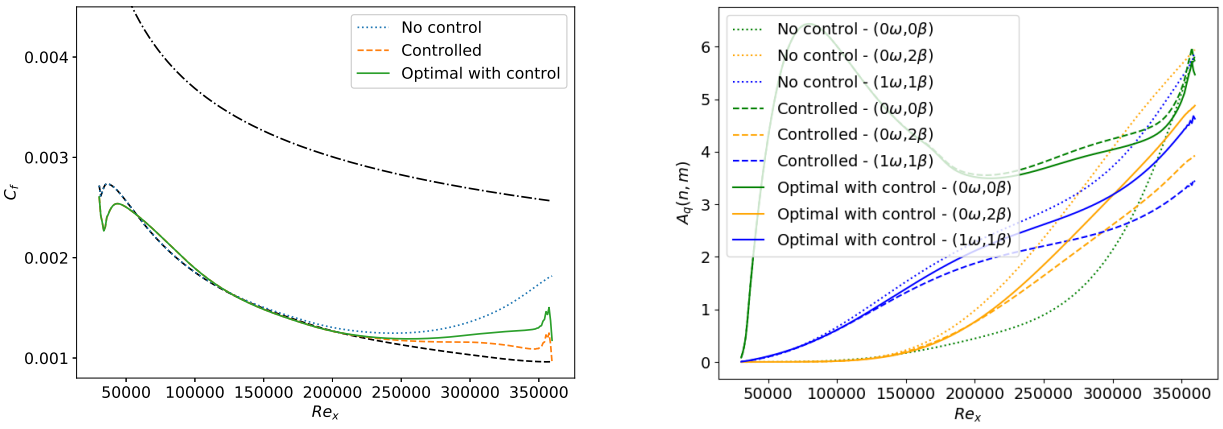

(a) **(b)**

Figure 5.3: Mean-flow skin-friction coefficient and amplitude of the response from the oblique forcing at $F = 16 \times 10^{-5}$, $\beta = 40 \times 10^{-5}$, $A = 26 \times 10^{-5}$, $N = 2$ and $M = 4$. Comparison without control (dotted lines), with control at $C'_\theta = 1.65 \times 10^{-2}$ with frozen optimal forcing (dashed lines) and with the new optimal forcing computed around the controlled mean-flow (solid lines). (a) Mean-flow skin-friction coefficient C_f along the streamwise direction. Black dashed line indicates the laminar skin-friction coefficient curve and dash-dotted line the turbulent curve. (b) Amplitude of the largest harmonic components of the response $A_q(n,m)$.

We have measured the efficiency of the mean-flow heat-flux control to decrease the skin-friction under the same forcing conditions i.e. for the same frequency F and spanwise wavenumber β. Keeping the spanwise wavenumber constant, we vary the frequency to check whether the heat-flux does not destabilise other modes. We may also compare the skin-friction given by both spanwise homogeneous and periodic heat-fluxes. In Figure 5.4a, with heat-flux control, the square root of the cost function $\sqrt{J}$ i.e. the integral of the skin-friction of the mean-flow deviation decreases for all frequencies except for the highest frequency computed. However, for high frequencies $F > 25 \times 10^{-5}$, skin-friction is much lower than at the optimal frequency $16 \times 10^{-5} < F < 20 \times 10^{-5}$. The spanwise periodic optimal heat-flux (Figure 5.2b) including the harmonic component (0ω,2β) only decreases further $\sqrt{J}$ by 3%. Therefore, a periodic heat-flux requiring a complex device with heating-cooling strips along the z-direction does not seem worthwhile to delay transition in this configuration.

To get further insight about the leverage of the heat-flux control on the delay of the transition, we define the transition location $Re_{x,t}$ as the location where the skin-friction coefficient is minimal:

$$C_f(Re_{x,t}) = \min(C_f(Re_x)). \tag{5.8}$$

Therefore, for a transition induced by a monotonic increase of C_f, a larger $Re_{x,t}$ represents a delayed transition onset while a constant $Re_{x,t}$ associated with a lower $\sqrt{J}$ means that the transition onset has not changed but the growth of skin-friction has been damped. From Figure 5.4b, the onset of transition is slightly shifted downstream for $16\times10^{-5} < F < 20\times10^{-5}$ but the reduction of the skin-friction of the mean-flow deviation mainly comes from its damped growth as shown in Figure 5.3a. At lower and larger frequencies, the transition onset is delayed.

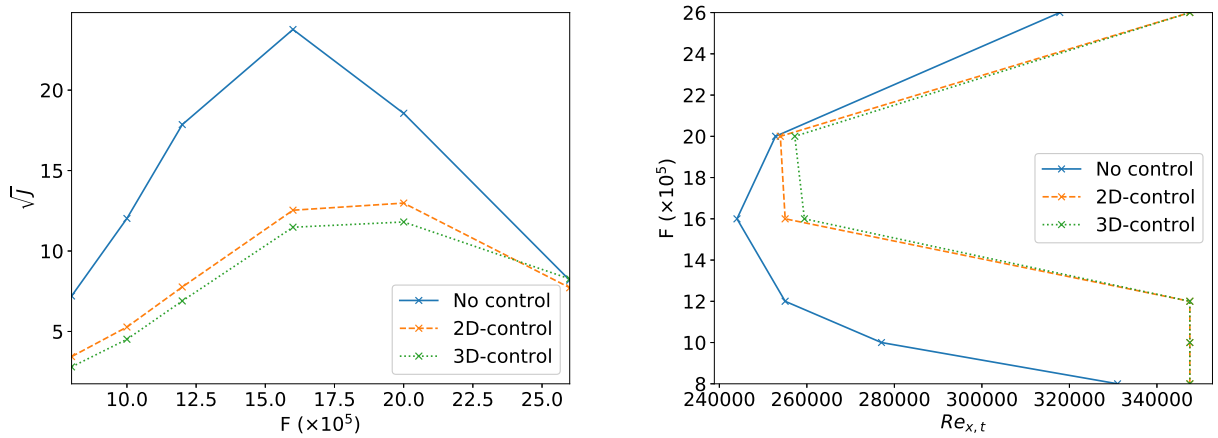

(a) **(b)**

Figure 5.4: Square root of the cost function $\sqrt{J}$ and transition location with respect to the frequency F at Mach number 4.5 for $N = 2$ and $M = 4$ at $A = 26 \times 10^{-5}$ without control (solid lines), with mean-flow heat-flux control at $C'_\theta = 1.65 \times 10^{-2}$ homogeneous in the spanwise direction from Figure 5.2a (dashed lines) and with $(0\omega,2\beta)$ component from Figure 5.2b (dotted lines). (a) Square root of the cost function $\sqrt{J}$. (b) Transition location $Re_{x,t}$.

Then, the spanwise homogeneous heat-flux is assessed for different spanwise wavenumbers. The skin-friction of the mean-flow deviation is plotted in Figure 5.5b and compared without control (Figure 5.5a). The heat-flux control has reduced the square root of the cost function $\sqrt{J}$ of the worst couple $F - \beta$ of disturbances by 37%. We notice that the control is more efficient at low frequencies which is expected as it only acts on the mean-flow, however, it was not anticipated that for a given frequency, the heat-flux control damps more the skin-friction for increasing spanwise wavenumbers. We eventually observe that high frequency fluctuations are promoted by the heat-flux control but remains smaller than the original worst disturbances.

We may measure the efficiency of the heat-flux control by computing the ratio of the flux of energy (power) saved i.e. the skin-friction saved multiplied by the free-stream velocity with respect to the heat-flux provided along the flat plate:

$$\eta_{NL} = \frac{U_\infty(\sqrt{J}(C'_\theta = 0) - \sqrt{J}(C'_\theta \neq 0))}{\int_{y=0} \lambda |\frac{\partial T}{\partial y}| \, dx}. \tag{5.9}$$

For spanwise homogeneous mean-flow heat-flux at $C'_\theta = 1.65 \times 10^{-2}$, the efficiency η_{NL} is 0.18 which means that it is required to provide about five times more heat power than what is saved in skin-friction. Therefore, this actuator does not appear much efficient, however, it should

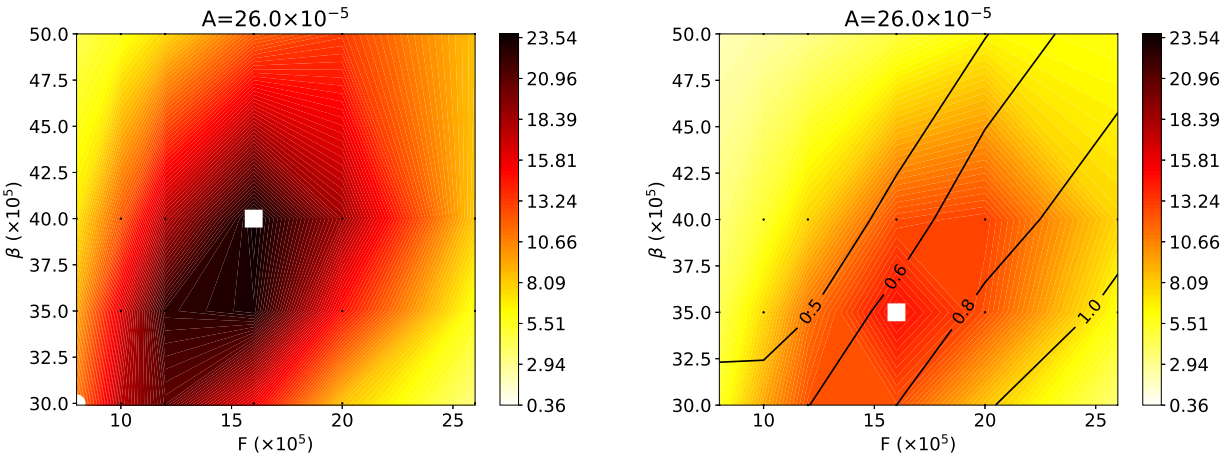

Figure 5.5: Square root of the cost function $\sqrt{J}$ with respect to the frequency F and the spanwise wavenumber β at Mach number 4.5 for $N = 2$ and $M = 4$ at $A = 26 \times 10^{-5}$. White square denotes the maximum location of the cost function J from the non-linear input-output analysis. Small black dots indicate the grid points where the non-linear input-output analysis has been performed. (a) No heat-flux control applied. (b) Mean-flow heat-flux control at $C'_\theta = 1.65 \times 10^{-2}$. Contour lines represent the ratio of the square root of the cost function $\sqrt{J}$ with over without control.

be pointed out that the heating, mainly applied upstream (almost no control downstream), damps the growth of the skin-friction, which implies that this computation repeated on a longer domain (until laminar to turbulent transition is reached) would have likely further increase the skin-friction saved without more heat-flux provided, improving such the efficiency η_{NL}.

To conclude, in order to delay transition, a spanwise homogeneous mean-flow heat-flux which solely targets the first Mack mode by heating upstream branch II of the local mode is almost as efficient as a spanwise periodic one. The optimal heat-flux computed for the most dangerous frequency effectively reduces the skin-friction induced by the transition for similar and lower frequencies.

5.2.2 Promote transition

The same analysis as in §5.2.1 is performed with a steepest ascent algorithm to find the optimal mean-flow heat-flux control to promote early transition. The same conditions are fixed for the prescribed forcing i.e. $A = 26 \times 10^{-5}$ for $F = 16 \times 10^{-5}$, $\beta = 40 \times 10^{-5}$ with $N = 2$ and $M = 4$. Similarly, the optimal heat-flux is computed gradually for increasing amplitude up to $C'_\theta = 1.65 \times 10^{-2}$ where increasing further the heat-flux amplitudes produces again too strong mean-flow deviation.

The optimal mean-flow heat-flux (Figure 5.6a) presents similar variations along the streamwise direction as the linear sensitivity and therefore an opposite behaviour than the optimal heat-flux to delay transition (Figure 5.2a). However, a few discrepancies are noticed. Branch II location refers now to the maximal heating region and a second region of cooling heat-flux has emerged in the downstream part of the flow. This second region may be justified as, for delaying transition, a small heat-flux control is applied upstream the development of the linear disturbances to damp their amplification while, for promoting transition, the optimal heat-flux should also sustain the developed disturbances downstream to support the non-linear interactions.

Then, it is expected that a spanwise periodic heat-flux which also triggers the streaks will

promote even faster transition. The harmonic component $(0\omega,2\beta)$, other components being negligible again, presents non-zero values for all streamwise positions with a strong periodicity roughly from the transition onset ($Re_x \sim 250000$) up to the end of the domain (Figure 5.6b). The reconstructed mean-flow heat-flux is shown in Figure 5.7. It includes spanwise uniform cooling upstream, a region of spanwise periodic medium heating around branch II location and eventually a region of spanwise periodic strong cooling from the transition onset. Notice that the heating and cooling periodic regions are staggered conversely to the optimal heat-flux to delay transition where they are aligned (see Figure 5.2b). No justification for this staggered heat-flux has yet been found.

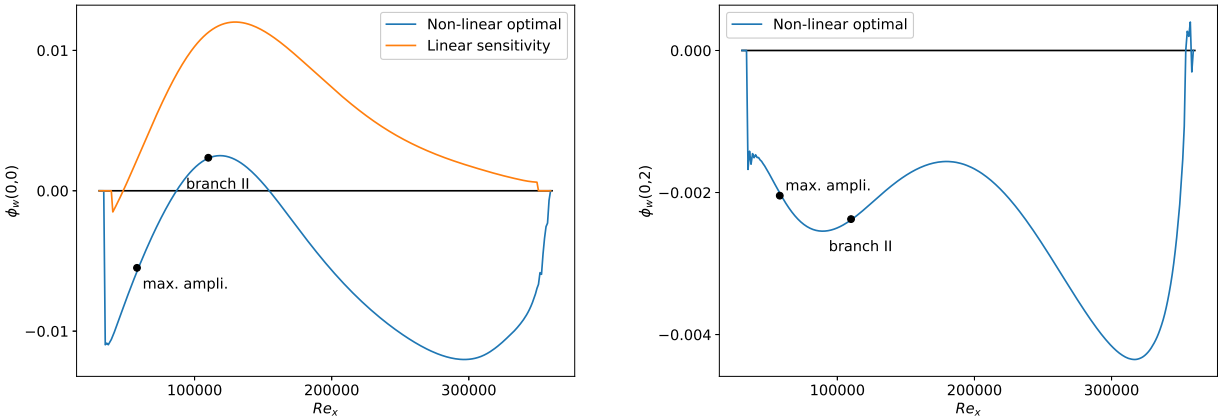

Figure 5.6: Optimal mean-flow heat-flux $\boldsymbol{\phi}_w$ at $C'_\theta = 1.65\times10^{-2}$ to promote the laminar to turbulent transition induced by the optimal fundamental forcing at $F = 16\times10^{-5}$, $\beta = 40\times10^{-5}$, $A = 26\times10^{-5}$, $N = 2$ and $M = 4$. Comparison with the linear sensitivity analysis for the first Mack mode at the same frequency and spanwise wavenumber rescaled to the same magnitude. Locations of branch II and maximal amplification rate ($\max(-\alpha_i)$) from the local stability analysis of the first Mack mode are also indicated. (a) $(0\omega,0\beta)$ harmonic component. (b) $(0\omega,2\beta)$ harmonic component.

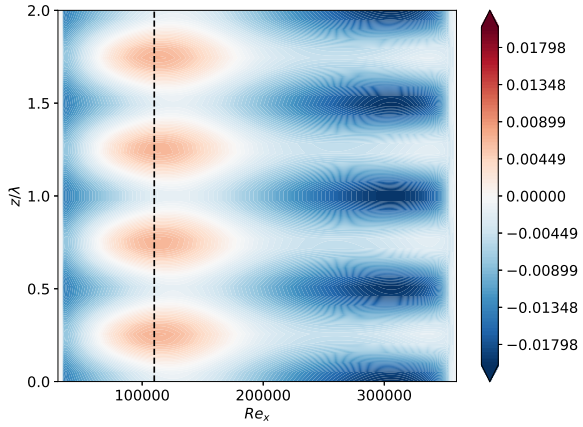

Figure 5.7: Contours of optimal mean-flow heat-flux $\boldsymbol{\phi}_w$ on the $X-Z$ plane reconstructed from Figure 5.6 at $C'_\theta = 1.65\times10^{-2}$ to promote the laminar to turbulent transition induced by the optimal fundamental forcing at $F = 16\times10^{-5}$, $\beta = 40\times10^{-5}$, $A = 26\times10^{-5}$, $N = 2$ and $M = 4$. Dashed black line indicates the location of branch II.

The skin-friction and response of the optimal spanwise homogeneous and periodic heat-fluxes are computed (Figure 5.8). Both heat-fluxes increase the skin-friction, the spanwise periodic increasing the integral of the skin-friction of the mean-flow deviation by further 23% for the same total heat-flux provided. About the response amplitude, the spanwise homogeneous heat-flux has little effect before transition onset but then amplifies the streaks $(0\omega,2\beta)$ in the cooling region downstream. The spanwise periodic heat-flux triggers the streaks upstream, where periodic heating is applied, and then recovers similar amplitude than with the homogeneous control.

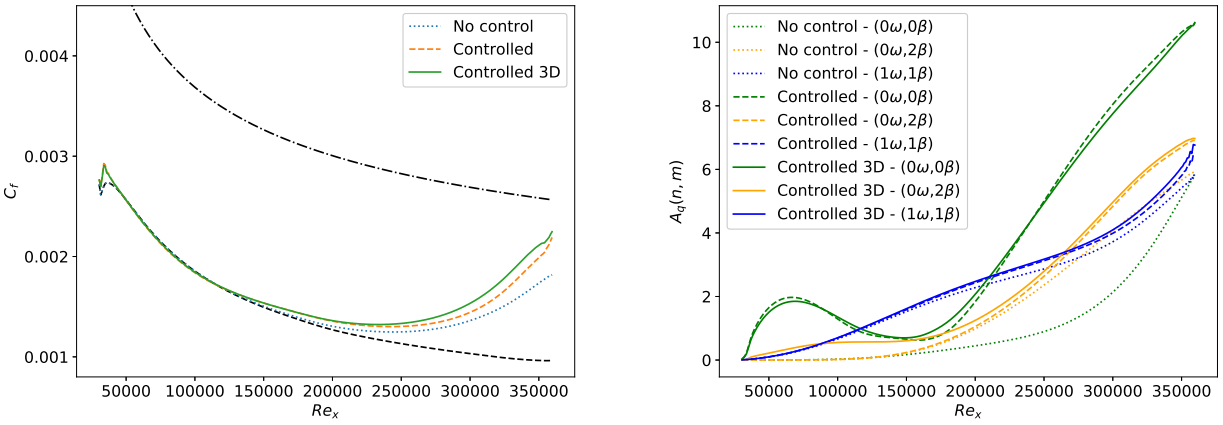

(a) **(b)**

Figure 5.8: Mean-flow skin-friction coefficient and amplitude of the response from the oblique forcing at $F = 16 \times 10^{-5}$, $\beta = 40 \times 10^{-5}$, $A = 26 \times 10^{-5}$, $N = 2$ and $M = 4$. Comparison without control (dotted lines), with mean-flow heat-flux control homogeneous in z-direction at $C'_\theta = 1.65 \times 10^{-2}$ with frozen optimal forcing (dashed lines) and with mean-flow heat-flux control with $(0\omega,2\beta)$ component (solid lines). (a) Mean-flow skin-friction coefficient C_f along the streamwise direction. Black dashed line indicates the laminar skin-friction coefficient curve and dash-dotted line the turbulent curve. (b) Amplitude of the largest harmonic components of the response $A_q(n,m)$.

Both optimal heat-fluxes are assessed for disturbances of different frequencies. For the designed frequency, they increase the square root of the cost function $\sqrt{J}$ by a ratio of 2.32 (spanwise homogeneous) and 2.55 (spanwise periodic) in Figure 5.9a. They also increase the skin-friction for all the frequencies computed. The origin of the additional skin-friction for the spanwise periodic heat-flux is explained by the transition location (Figure 5.9b). Indeed, while the spanwise homogeneous heat-flux slightly delays the transition, the periodic one moves the transition onset upstream. This is also observable in the skin-friction curve in Figure 5.8a where both controlled curves are only shifted in the streamwise direction but have a similar slope. These are the streaks generated upstream by the periodic heating which have promoted earlier transition. For low and high frequencies, the transition location is pushed downstream but larger skin-friction of mean-flow deviation is produced through a larger amplification of the fluctuations.

As for the delayed transition, the efficiency of the optimal control at $C'_\theta = 1.65 \times 10^{-2}$ may be assessed with η_{NL} (Eq. (5.9)). The efficiency η_{NL} is -0.65 for spanwise homogeneous heat-flux and -0.76 for the periodic control (efficient control for $\eta_{NL} < -1$). However, for this configuration, the efficiency is not much meaningful as the transition is not promoted to increase the drag but rather to change the flow topology towards the turbulent state to avoid flow separation for instance. An efficiency factor cannot be built upon that objective as the solution lies on a trade-off between fast transition and low energy control.

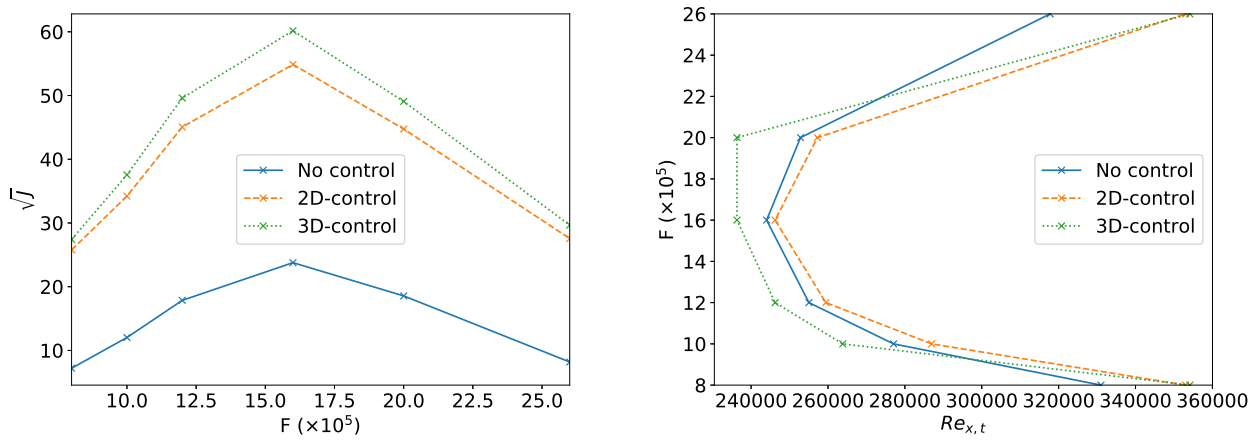

Figure 5.9: Square root of the cost function $\sqrt{J}$ and transition location with respect to the frequency F at Mach number 4.5 for $N = 2$ and $M = 4$ at $A = 26 \times 10^{-5}$ without control (solid lines), with heat-flux control at $C'_\theta = 1.65 \times 10^{-2}$ homogeneous in z-direction from Figure 5.6a (dashed lines) and with $(0\omega,2\beta)$ component from Figure 5.6b (dotted lines). (a) Square root of the cost function $\sqrt{J}$. (b) Transition location $Re_{x,t}$.

To conclude, these preliminary results on optimal heat-flux to delay or promote transition would require further investigations to explain their streamwise variations and design an optimal actuator. Furthermore, the open-loop control method presented above is not limited to wall heat-flux. Volume force control through plasma actuators might have been studied as well as optimal roughness [79] for realistic configurations. Eventually, the methodology framework may be improved in order to weakly part the spanwise periodicity of the disturbances with the periodicity of the parietal control (and their relative phase) to enlarge the optimisation space and find a better control.

Chapter outcome summary:

The optimal mean-flow heat-flux profiles to control laminar to turbulent transition have been derived through an adjoint-based variational technique for the $M_\infty = 4.5$ boundary layer. They predict similar variations along the streamwise direction than through linear sensitivity analysis.

To delay transition, under disturbances of medium amplitude, a spanwise-homogeneous mean-flow heat-flux which solely targets the first Mack mode by heating upstream branch II of the local mode is almost as efficient as a spanwise-periodic one. The optimal heat-flux computed for the most dangerous frequency effectively reduces the skin-friction induced by the transition for similar and lower frequencies by damping the amplification of the instabilities.

To promote transition, a spanwise-periodic mean-flow heat-flux with heating around the location of branch II and staggered cooling in the transitional region downstream is the most efficient control to increase the skin-friction by promoting the streaks. At similar frequencies where it has been computed, it acts on two fronts: it pushes the onset of transition upstream and strengthens the growth of the skin-friction coefficient. For other frequencies, it only affects the amplification of skin-friction.

Conclusions and outlook

Conclusions

The optimal non-linear solutions, or worst-case disturbances, developing in a hypersonic boundary layer have been identified and an optimal open-loop wall actuator to control them has been highlighted. These objectives were achieved through the development of numerical tools for compressible laminar flows and their application to the attached boundary layer at $M_\infty = 4.5$ over an adiabatic flat plate. The methodology of this work has initially addressed linear instabilities and their sensitivity and then been extended towards the computation of non-linear solutions.

In chapter 1, the key results from the literature on laminar to turbulent transition at supersonic regime have been recalled. Transition is generally the consequence of the amplification of linear instabilities (Mack modes) which trigger secondary mechanisms (three-dimensional vortices, streaks,...) that later break down to turbulent spots. In order to control the transition, the consensus has not been reached for the optimal location to apply an open-loop wall heating/cooling actuator despite many studies. Depending on the approximations assumed, many stability methods for fluid mechanics have been derived from linear (local, PSE, OWNS, non-modal, global, resolvent) to non-linear analysis by way of linear sensitivity and weakly non-linear analysis.

In chapter 2, the methods of the discrete global framework to solve the compressible Navier-Stokes equations have been implemented in the BROADCAST code: fixed-point, stability and resolvent analyses. They rely on a two-dimensional discretisation where the spanwise-periodic three-dimensional perturbations are solved with Fourier expansion to keep an affordable computational cost. The derivative operators are built with Algorithmic Differentiation for accuracy and straightforward evaluations of the linearised and adjoint operators. The high-order convective schemes implemented in BROADCAST enable to compute accurate resolvent gains at high frequencies at a low computational cost. Furthermore, this scheme may be used to Mach numbers as low as $M_\infty \approx 0.1$ to explore the incompressible regime both on Cartesian and curvilinear meshes. Eventually, these methods have been validated on the flow around a cylinder and then applied to the hypersonic boundary layer where the resolvent analysis identified the three main global mechanisms: the steady streaks, the first oblique Mack mode and the two-dimensional high-frequency second Mack mode.

In chapter 3, the linear sensitivity of the optimal gains i.e. the optimal location for small

amplitude open-loop control of the three main linear instabilities has been derived. Wall-based control was explored by computing the optimal location for steady wall blowing/suction or heating/cooling actuators to mitigate or strengthen the instabilities through an adjoint-based optimisation technique. For steady wall-blowing control, suction control is optimal to damp the second Mack mode if located upstream of the synchronisation point and conversely for blowing control. The application of the optimal wall suction and blowing control, computed for the second Mack mode, in the non-linear regime (finite amplitude control) yields a reduction of the optimal gain of the second Mack mode but shifts its peak to lower or higher frequencies, triggers a small decrease of the first Mack mode gains and lets the streaks unaffected. Therefore, only a local suction actuator would efficiently damp all instabilities. For heating/cooling control, the first Mack mode appears as the most sensitive instability. The first and second Mack modes have an opposite sensitivity with respect to wall temperature changes, however, wall heating located close to the leading edge damps both Mack modes. In the downstream region, a large cooling region damps the first Mack mode while only a local cooling strip located in the unstable region of mode S damps the second Mack mode but this is suboptimal in comparison with the leading edge region. The application of the optimal wall heating and cooling control, computed for the first Mack mode, at a non-linear regime yields a strong reduction of the first Mack mode gains but strongly amplifies the second Mack mode. The application of a single local steady heating strip close to the leading edge (and possibly a cooling strip downstream in the unstable region of mode S) manages to damp all the instabilities and might be considered as an actuator to delay transition towards turbulence for a various range of frequencies and spanwise wavenumbers.

In chapter 4, the weakly non-linear analysis near bifurcation for compressible oscillator flows and the extension of the linear resolvent to non-linear input-output analysis for compressible amplifier flows have been developed in the discrete framework. The latter takes into account the non-linear interactions of a finite number of time and spanwise harmonics. The worst-case disturbances have therefore been identified through a gradient-based algorithm. The compressible Navier-Stokes equations were written in a pseudo-spectral form through the Space-Time Spectral Method (STSM) for both time and spanwise dimensions. Requiring de-aliasing technique, the large systems were solved iteratively using a block-circulant preconditioned GMRES. After validation at low Mach number, the transition of a boundary layer at $M_\infty = 4.5$ developing over an adiabatic flat plate has been studied. It results that the optimal fundamental forcing is a pair of symmetric oblique waves promoting the non-linear interactions of the first Mack mode with the streaks. Increasing the forcing amplitude, higher harmonics are generated until transition to turbulence is reached through a subharmonic varicose mode (staggered vortices). Moreover, a weakly non-linear analysis which includes the third level of non-linear interactions (polynomial of order A^6) manages to substantially predict the skin-friction at a lower cost.

Finally, in chapter 5, the optimal mean-flow heat-flux profiles to control the laminar to turbulent transition induced by the optimal forcing previously derived has been computed through an adjoint-based variational technique. They predict similar variations along the streamwise direction than through linear sensitivity analysis. To delay transition, under disturbances of medium amplitude, a spanwise-homogeneous mean-flow heat-flux which solely targets the first Mack mode by heating upstream branch II of the local mode is almost as efficient as a spanwise-periodic one. The optimal heat-flux computed for the most dangerous frequency effectively reduces the skin-friction induced by the transition for similar and lower frequencies by damping the amplification of the instabilities. To promote transition, a spanwise-periodic mean-flow heat-flux with heating around the location of branch II and staggered cooling in the transitional region downstream is the most efficient control to increase the skin-friction by promoting the streaks. At similar frequencies where it has been computed, it acts on two fronts: it pushes

the onset of transition upstream and strengthens the growth of the skin-friction coefficient. For other frequencies, it only affects the amplification of skin-friction.

Outlook

The methods and tools developed in this work have been written within the discrete global framework in the aim of studying compressible flows around geometries without any parallel assumptions (but homogeneous in the spanwise direction). Therefore, their applications are not limited to the academic case of the boundary layer considered here. For instance, linear and non-linear analysis are (going to be) performed with BROADCAST on global and convective instabilities in a cone-cylinder-flare geometry including the receptivity with respect to nose bluntness, non-linear solutions in the shock-wave/boundary-layer interaction, closed-loop control optimisation in a compression ramp, reproduction of global instabilities developing in an experiment or the shape optimisation of a nozzle to obtain quiet flows.

As this work was the continuity of Bugeat [19], Mettot [123], Moulin [130], Rigas et al. [155] (among others), several suggestions are offered to continue further. Firstly, the numerical methods implemented may be improved to increase the time and memory efficiencies in order to tackle larger scale problems. Secondly, additional algorithms may be combined to extend the non-linear analysis. Lastly, some of these improvements would be useful to study more complex configurations.

Improvements of the numerical methods

About the numerical methods for the two-dimensional discretisation and the linear analysis, a few improvements may be performed to reduce time and memory consumptions. To reduce the time spent for the construction of the linearised operators, they might be built with a multi-colouring adapted to the stencil size [9] in order to perform less matrix-vector products. then, for solving linear systems, the current choice was to perform exact LU-factorisation but other options less memory consuming, but slower, would be the combination of iterative methods with appropriate preconditioning, such as GMRES preconditioned by ILU. Eventually, multi-block management would enable to solve high-dimensional problems by splitting efficiently the two-dimensional discretisation over multiple cores.

About the numerical methods for the non-linear input-output analysis, the main limitation was the memory as it is proportional to the number of collocation points. Therefore, the de-aliasing technique employed here which consisted in truncating half of the harmonics seems very expensive. However, de-aliasing through filtering as offered by LaBryer and Attar [94] was attempted in this work but did not show good de-aliased results in comparison with the truncation method, especially for the spanwise dimension. Nonetheless, such filtering approaches would require further investigations as any collocation point saved is a noteworthy memory gain.

Moreover, in the mathematical theory, the STSM only involves real numbers but an implementation with complex numbers has been performed in this work as the block-circulant preconditioner is complex because of the Discrete Fourier Transform. Therefore, to keep the same accuracy, the memory is twice larger when using complex numbers. An option to stay within a real number framework is to use the K formulation for the preconditioner in order to part its real and imaginary part efficiently [40, 52]. Indeed, splitting the full complex matrix as a real 2 by 2 block matrix is inefficient (more memory demanding than working in the complex framework) as the strong off-diagonal terms make the factorisation more expensive. The K formulation splits the real and imaginary parts for each cell i.e. at the level of the two-dimensional

discretisation such that the twice larger real matrix remains diagonal dominant (compactness of the pattern kept). The memory saved is difficult to predict as the factorisation of the preconditioner would be more expensive but each Krylov vector within the GMRES algorithm would consume half of the memory, therefore the K formulation may be interesting for non-linear systems with many harmonics where a large Krylov subspace was necessary to converge.

To reduce the time and memory within the optimisation loop of the forcing in the STSM, the analytical adjoint equations for the spanwise contributions might be derived. In the current implementation, the matrices $\mathbf{A}_z$ are explicitly built and trans-conjugated while AD may be used to compute directly the adjoint matrix-vector product, then saving time (no construction) and memory (no storage of the matrices). From the computations performed in this work, it would represent around 25% decrease of the total RAM.

Eventually, to further reduce the memory consumption, the size of the Krylov subspaces may be shrunk by using GMRES with deflated restarting [82, 128]. However, the optimal method remains a trade-off between memory and time depending on the size of the system to solve and the computational resources available.

Additional algorithms for non-linear analysis

Then, for a deeper analysis of the optimal non-linear solutions and to study further physical mechanisms, more complex algorithms may be developed.

At high forcing amplitude, the iterative methods hardly converged, therefore a better preconditioning may help. A first straightforward option is a block circulant preconditioner not based on the Jacobian matrices computed around the mean-flow but rather on the averaged Jacobian matrices. Moulin [130] highlighted that is is equivalent for incompressible flows (but not for compressible flows as the Jacobian is not linear with the state), however, computing an averaged Jacobian is more expensive within the current parallel implementation as large objects are distributed between the MPI processes. A second option is to apply the DFT on the exact Jacobian (not averaged, neither computed around the mean-flow) which will produce a matrix with diagonal terms composed of the averaged Jacobian and off-diagonal terms made of the Fourier coefficients of the Jacobian [130]. The current method is equivalent to a Block-Jacobi preconditioner as we keep only the diagonal terms. For a most accurate preconditioner, more expensive techniques such as Block Gauss-Seidel (applied in the AHBM framework by Sierra-Ausin et al. [176]) or BoomerAMG (algebraic multigrid) [184] methods could be implemented, however, they would all require an adaptation of the parallel implementation as the preconditioner would not be block-diagonal.

Then, for the optimisation of the forcing or the mean-flow control, various gradient-based algorithms may be used. Basic steepest descent and ascent methods were presented but non-linear conjugate gradient methods (Fletcher-Reeves and Polak-Ribière) were also attempted. An adaptive optimisation step length based on the previous steps was also implemented but none of these methods were robust and only marginally improved the convergence speed. Nonetheless, for the optimal control of the worst-case disturbances, a complete GDA (gradient descent-ascent) minmax algorithm [83] could be implemented to find the optimal robust control [203].

Finally, in order to study the secondary instabilities of globally unstable flows (oscillator flows), the STSM may be used by adding an equation (phase constraint) to find the unknown frequency of the instability, unlike the non-linear input-output analysis where the frequency and the spanwise wavenumber are prescribed. This self-excited harmonic method exists within the AHBM framework [176] and can be implemented in the TSM framework. To get an efficient preconditioner of the larger-size Jacobian, Moulin [130] offers to apply a Schur complement

method associated with the use of the block-circulant preconditioner.

Application cases

With improved numerical methods and new algorithms implemented, more complex applications cases may be studied through STSM.

In the direct continuation of this work, the hypersonic boundary layer could be studied not only for optimal fundamental (or superharmonic) forcings but for a set of frequencies / spanwise wavenumber (continuation of appendix D) to simulate for instance the non-linear interactions of first and second Mack modes on a longer flat plate [77] thanks to an improved preconditioner in order to handle more harmonics. Furthermore, a minmax algorithm would enable to fully optimise the mean-flow heat-flux. However, the most interesting control would be an optimal passive control through wall deformations, roughness [79] or the promising metamaterials [76].

BROADCAST and STSM codes are already respectively used to study more complex flows: the axi-symmetrical cone-cylinder-flare geometry [24] and the laminar oblique shock-wave/boundary-layer interaction. This last configuration may be studied as an amplifier flow [21] in the non-linear regime (continuation of Savarino et al. [163] at supersonic regime) or as an oscillator flow (low-frequency bubble unsteadiness [157]) through a self-excited STSM.

Finally, thanks to the implementation of turbulence models, arbitrary Lagrangian-Eulerian formulation and their adjoint derivatives, fluid-structure phenomena may be studied. For instance, the sensitivity of the worst-case disturbances to a compliant wall [104, 142] would help find the optimal material properties. Another example is the use of the self-excited STSM to study the origin of the mechanism which develops into limit cycle oscillations of the coupled problem compliant-wall/normal-shock at transonic regime [127].

Appendices

Appendix **A**

Wall boundary condition for blowing and heat-flux

The implementation of the boundary conditions in the code BROADCAST is described in further details in §2.1.3.4. They are enforced through the addition of ghost cells to prescribe characteristic-based conditions for permeable boundaries or mixed Dirichlet-Neumann conditions for solid boundaries. The wall boundary conditions with non-zero heat-flux and wall-normal velocity is derived below as they play a major role in the computation of the sensitivity in Chapter 3.

The boundary layer assumption is performed involving a zero pressure gradient in the wall-normal direction: $\partial p/\partial n = 0$ with n the wall-normal direction. From the derivative in the wall-normal direction of the perfect gas law (Eq. (1.14)), computed at the wall, one gets

$$\left.\frac{\partial p}{\partial n}\right|_w = \rho_w r \left.\frac{\partial T}{\partial n}\right|_w + r T_w \left.\frac{\partial \rho}{\partial n}\right|_w, \tag{A.1}$$

with the subscript $\cdot_w$ indicating the values at the wall. The temperature T_w is replaced by $p_w/(\rho_w r)$ from the perfect gas law. The pressure at the wall p_w is known from the value in the first cell as $\partial p/\partial n = 0$ and the temperature gradient writes as a heat flux $\phi = \lambda \partial T/\partial n$. Therefore, assuming a first order extrapolation for the density, Eq. (A.1) becomes a function of a single unknown, the wall density ρ_w:

$$-\frac{r}{2\lambda p_w}\phi_w \rho_w^2 + \rho_w - \rho_1 = 0, \tag{A.2}$$

with ρ_1 the density at the first cell centre. For an adiabatic wall condition $\phi_w = 0$, we get $\rho_w = \rho_1$, otherwise we obtain $\rho_w = (1-\sqrt{1-2r\phi_w\rho_1/(\lambda p_w)})/(r\phi_w/(\lambda p_w))$. However, the latter expression for ρ_w is not differentiable around $\phi_w = 0$. Then, in order to compute the Jacobian and Hessian of an adiabatic flow, which respectively involve the first and second derivative of the wall boundary conditions, the equation Eq. (A.2) is solved by a Newton method to compute ρ_w, this iterative method being then linearised by Algorithmic Differentiation to build the derivative operators. Eventually, all the conservative variables are prescribed at the wall: ρ_w, $(\rho u)_w = 0$ (no-slip), $(\rho v)_w = \rho_w \times v_w$ (with a non-zero v_w for a wall-normal blowing/suction condition) and $(\rho E)_w = p_w/(\gamma - 1) + 0.5\rho_w v_w^2$.

Appendix B

Norm matrices

The discrete inner product $\mathbf{Q}_f = \mathbf{Q}$ defined in Eq. (2.20) writes in matrix form:

$$\mathbf{Q} = \frac{1}{2}\, d\Omega \begin{pmatrix} 1 & 0 & 0 & 0 & 0 \\ 0 & 1 & 0 & 0 & 0 \\ 0 & 0 & 1 & 0 & 0 \\ 0 & 0 & 0 & 1 & 0 \\ 0 & 0 & 0 & 0 & 1 \end{pmatrix}, \tag{B.1}$$

with $d\Omega$ the cell volume.

The Chu's energy [35] may be expressed into different forms depending on the set of variables used. For the following fluctuations variables, velocity $\check{\mathbf{v}} = (\check{u}, \check{v}, \check{w})$, density $\check{\rho}$, pressure $\check{p}$, temperature $\check{T}$ and entropy $\check{s}$, Chu's energy writes for instance with dimensionless variables:

$$\begin{aligned} E_{\text{Chu}} = \check{\mathbf{q}}^* \mathbf{Q}_{\text{Chu}} \check{\mathbf{q}} &= \frac{1}{2}\int_\Omega \left(\overline{\rho}\, \|\check{\mathbf{v}}\|^2 + \frac{1}{\gamma}\frac{\check{p}^2}{\overline{p}} + \gamma(\gamma-1)M^4\, \overline{p}\, \check{s}^2 \right) d\Omega \\ &= \frac{1}{2}\int_\Omega \left(\overline{\rho}\, \|\check{\mathbf{v}}\|^2 + \frac{\overline{T}}{\overline{\rho}\gamma M^2}\, \check{\rho}^2 + \frac{\overline{\rho}}{(\gamma-1)\gamma M^2 \overline{T}}\, \check{T}^2 \right) d\Omega, \end{aligned} \tag{B.2}$$

with $\overline{q}$ indicating a base-flow variable.

As the Navier-Stokes equations are written in conservative form with the state vector $\mathbf{q} = (\rho, \rho\mathbf{v}, \rho E)$, the Chu's energy must be expressed with the conservative variables. For a spanwise homogeneous base-flow ($\overline{w} = 0$), the disturbance variables defined around the base-flow $\overline{\mathbf{q}}$ write

$$\check{u} = \frac{1}{\overline{\rho}}((\check{\rho u}) - \overline{u}\check{\rho}), \tag{B.3}$$

$$\check{T} = \frac{(\gamma-1)\gamma M^2}{\overline{\rho}} \left[\left(\frac{1}{2}(\overline{u}^2 + \overline{v}^2) - \overline{e} \right) \check{\rho} - \overline{u}(\check{\rho u}) - \overline{v}(\check{\rho v}) + (\check{\rho E}) \right], \tag{B.4}$$

with $\check{v}$ and $\check{w}$ defined similarly to $\check{u}$.

Following Bugeat et al. [20], two base-flow variables are introduced to simplify the notations:

$$a_1 = \frac{(\gamma-1)\gamma M^2 \overline{\rho}}{\overline{T}}, \tag{B.5}$$

$$a_2 = \frac{(\frac{1}{2}(\overline{u}^2 + \overline{v}^2) - \overline{e})}{\overline{\rho}}. \tag{B.6}$$

Therefore, Chu's energy matrix writes in conservative form:

$$\mathbf{Q}_{\mathrm{Chu}} = \frac{1}{2}\, d\Omega \begin{pmatrix} \frac{\overline{u}^2+\overline{v}^2}{\overline{\rho}} + \frac{\overline{T}}{\overline{\rho}\gamma M^2} + a_1 a_2^2 & -\frac{\overline{u}(1+a_1a_2)}{\overline{\rho}} & -\frac{\overline{v}(1+a_1a_2)}{\overline{\rho}} & 0 & \frac{a_1a_2}{\overline{\rho}} \\ -\frac{\overline{u}(1+a_1a_2)}{\overline{\rho}} & \frac{1}{\overline{\rho}} + \frac{\overline{u}^2 a_1}{\overline{\rho}^2} & \frac{\overline{u}\overline{v}a_1}{\overline{\rho}^2} & 0 & -\frac{\overline{u}a_1}{\overline{\rho}^2} \\ -\frac{\overline{v}(1+a_1a_2)}{\overline{\rho}} & \frac{\overline{u}\overline{v}a_1}{\overline{\rho}^2} & \frac{1}{\overline{\rho}} + \frac{\overline{v}^2 a_1}{\overline{\rho}^2} & 0 & -\frac{\overline{v}a_1}{\overline{\rho}^2} \\ 0 & 0 & 0 & \frac{1}{\overline{\rho}} & 0 \\ \frac{a_1a_2}{\overline{\rho}} & -\frac{\overline{u}a_1}{\overline{\rho}^2} & -\frac{\overline{v}a_1}{\overline{\rho}^2} & 0 & \frac{a_1}{\overline{\rho}^2} \end{pmatrix}. \tag{B.7}$$

Appendix C

Frequency dependence of linear sensitivity

To check how the gradients evolve with the instability frequency, 2D stability and sensitivity are repeated on a shorter domain which ends at $Re_{x,\text{out}} = 1 \times 10^6$ (half of the previous one). From Figure C.1a, the second Mack mode is maximal for larger frequencies ($F = 3 \times 10^{-4}$).

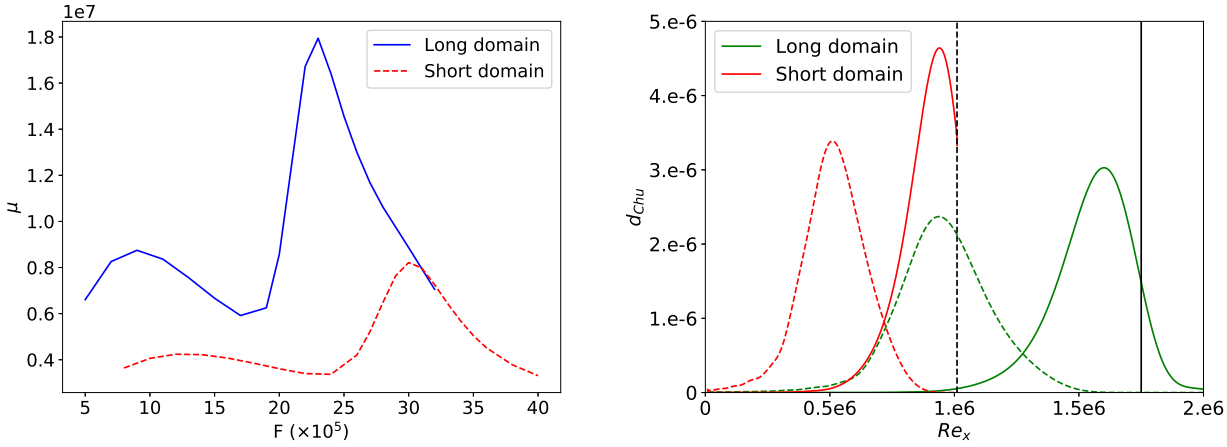

(a) **(b)**

Figure C.1: Resolvent analysis on short and long domains. (a) Two-dimensional optimal gain μ_0 with respect to the frequency F for short (red) and long (blue) domains. (b) Energy density d_{Chu} of the optimal forcing (dashed lines) and response (solid lines) of the second Mack mode for the short (red) and long (green) domains. Black vertical lines indicate the end of the optimisation domain for resolvent analysis for the short domain (dashed line) and for the long domain (solid line).

The gradients to steady wall control (Figure C.2) preserve a very similar trend in terms of variations along Re_x however their relative amplitude vary. Eventually, the gradient zones highlighted by local or global stability analyses remain similar on both domain length.

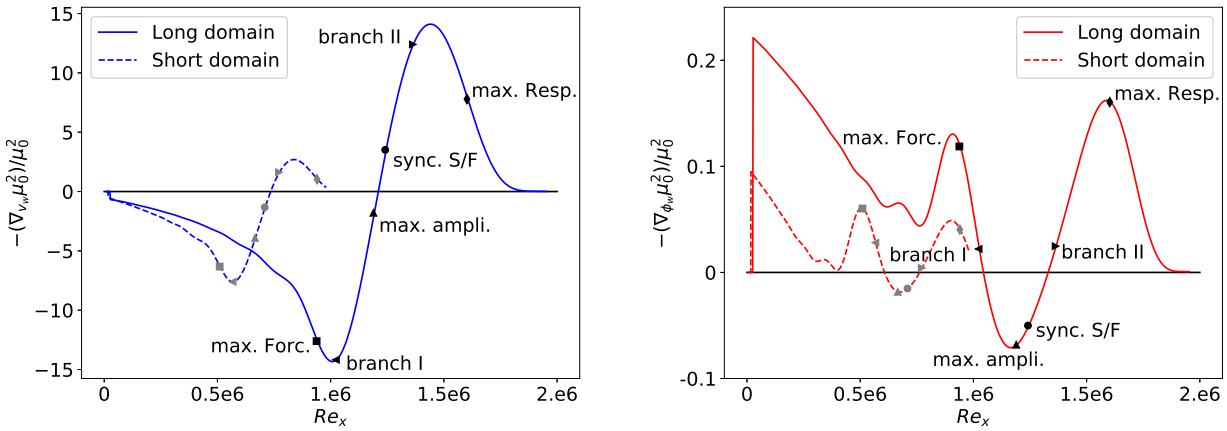

Figure C.2: Opposite of the sensitivity of the optimal gain for short (dashed lines) and long (solid lines) domains. (a) $-\nabla_{\mathbf{v}_w}\mu_0^2/\mu_0^2$ for short and long domains. (b) $-\nabla_{\phi_w}\mu_0^2/\mu_0^2$ for short and long domains.

Appendix D

Two-dimensional worst-case disturbances

The two-dimensional worst-case disturbances are searched with non-linear input-output analysis through TSM (only in time). No spanwise fluctuations are considered to mitigate the computational cost and overcome the convergence issue of a very large dynamical system.

The same hypersonic boundary layer case as in chapter 4 is considered. Unlike the fundamental (or superharmonic) forcing analysis performed in chapter 4, we look for an optimal forcing which may act on separate mechanisms. We therefore need a fine sampling, in order not to miss any localised amplification in frequency. Given the resources available, we choose $N = 15$ harmonics with the fundamental frequency $F = \Delta\omega = 4 \times 10^{-5}$ so the maximum frequency solved is $N \times \Delta\omega = 60 \times 10^{-5}$ which corresponds to a frequency slightly larger than the second Mack mode (see Figure 2.15a). Furthermore, because large forcing amplitude is considered to get sufficient non-linear interactions, de-aliasing by truncation is applied meaning that the TSM is performed on 61 time collocation points.

First, we recall in Figure D.1a the optimal gain obtained by linear resolvent analysis which predicts that the harmonic $n = 13$ ($F = 52 \times 10^{-5}$) associated with the second Mack mode is optimal. Therefore, it is expected that starting from any initial linear forcing, the non-linear input-output performed at low amplitude would converge to an optimal forcing at $n = 13$. This is the case up to $A = 10^{-3}$ as shown by the distribution of the forcing amplitude A_f among the different harmonics in Figure D.1b where almost only the harmonic $n = 13$ is forced. Then, by increasing the forcing amplitude at $A = 2 \times 10^{-3}$ (Figure D.1c) and $A = 3 \times 10^{-3}$ (Figure D.1d) and letting the adjoint TSM converge to a new optimal forcing (the objective function remaining the squared skin-friction of the mean-flow deviation), two other harmonics emerge in the forcing spectrum. The predominant forcing component becomes the harmonic $n = 15$ which represents as well the second Mack mode but at a larger frequency, therefore being amplified upstream the harmonic $n = 13$ where the boundary layer is thinner. Eventually, a low frequency harmonic component $n = 2$, which has the features of a two-dimensional first Mack mode, is also triggered at lower amplitude. It will be seen later that this mode likely helps the energy transfer between both second Mack modes.

The mean-flow skin-friction is plotted in Figure D.2a for increasing forcing amplitudes. At the lowest amplitude, the skin-friction has a single peak resulting from the amplification and decay of the second Mack mode ($n = 13$). At larger amplitudes, both peaks represent both second Mack modes ($n = 15$) upstream and ($n = 13$) downstream. Therefore, for this

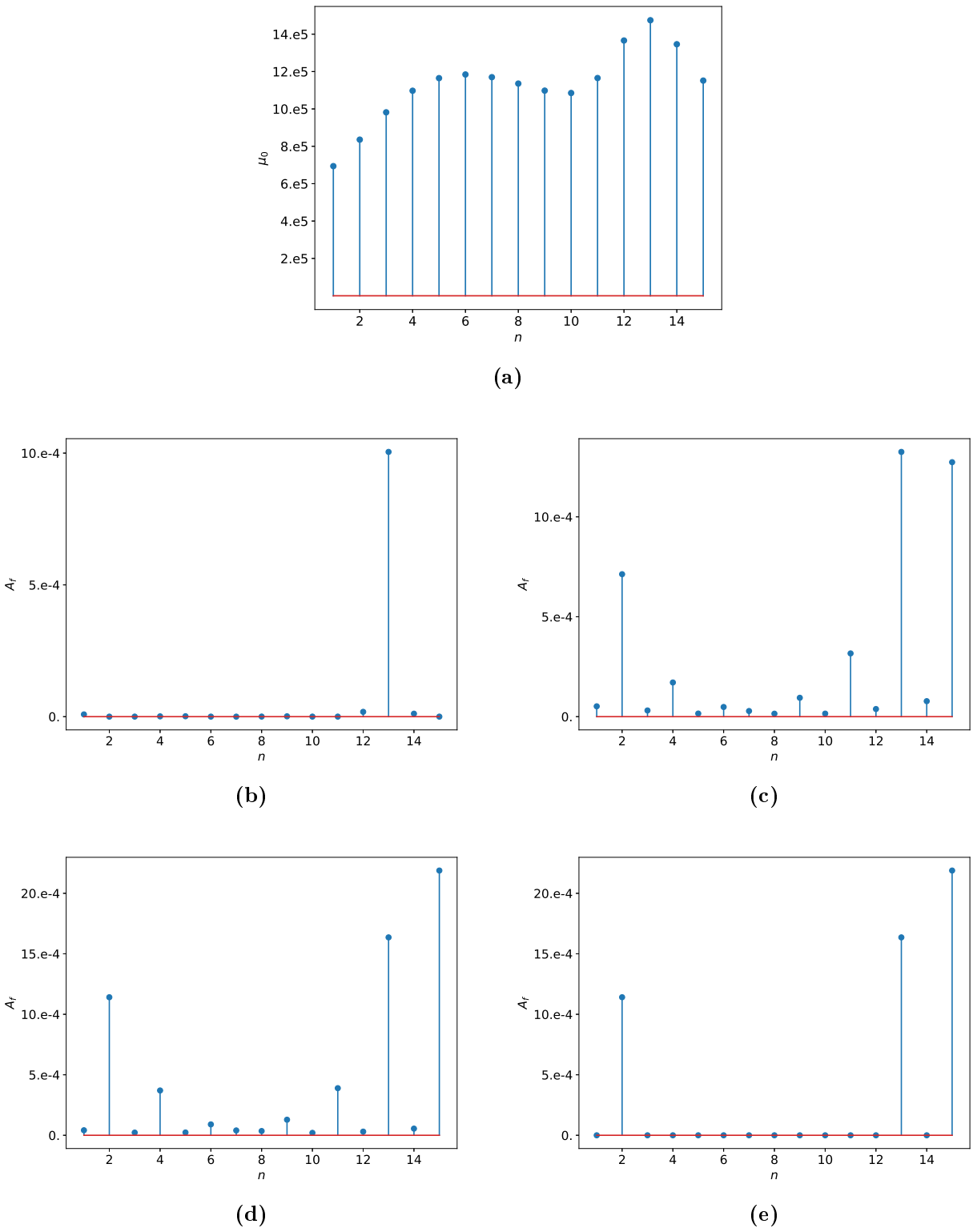

Figure D.1: (a) Optimal gain μ_0 with respect to the frequency harmonic component from linear resolvent analysis. (b) Forcing amplitude spectrum at $A = 10^{-3}$. (c) Forcing amplitude spectrum at $A = 2 \times 10^{-3}$. (d) Forcing amplitude spectrum at $A = 3 \times 10^{-3}$. (e) Forcing amplitude spectrum restricted to its three largest components ($A = 2.96 \times 10^{-3}$).

configuration, the optimal increase of the skin-friction consists of the successive amplification of two second Mack modes along the streamwise direction.

To understand the emergence of the three leading mechanisms, we restrict the forcing to its three most dominant components (Figure D.1e). Therefore, the forcing amplitude is now $A = 2.96 \times 10^{-3}$ with the following forcing energy distribution $A_f(n)^2/A^2$: 0.149 for $n = 2$, 0.305 for $n = 13$ and 0.546 for $n = 15$. The non-linear response produced by this three-component forcing only reduces by 3% the cost function in comparison with the optimal forcing.

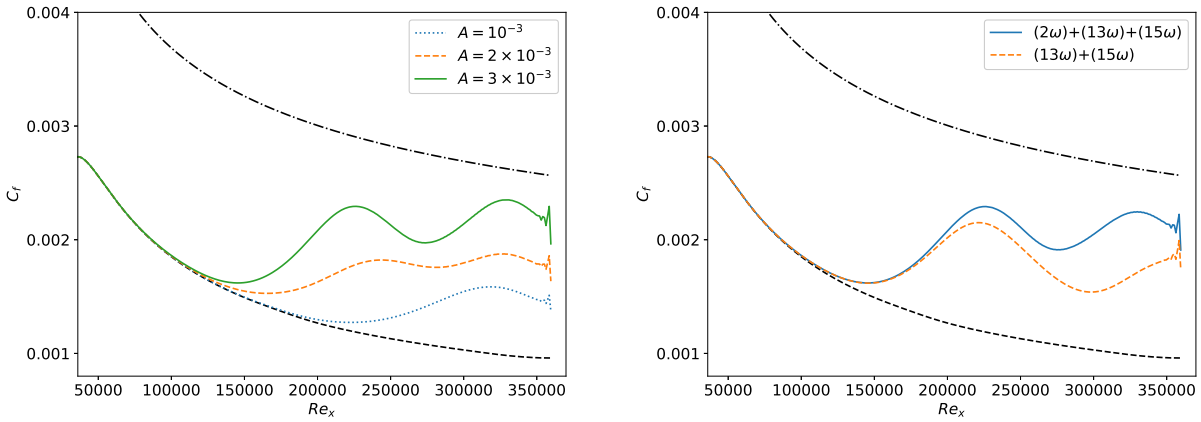

(a) **(b)**

Figure D.2: Mean-flow skin-friction coefficient C_f along the streamwise direction. Black dashed liner indicates the laminar skin-friction coefficient curve and dash-dotted line the turbulent curve. (a) Comparison for increasing amplitudes. (b) Comparison with and without the low-frequency ($n = 2$) harmonic component of the forcing.

The amplitude of the three-component forcing is plotted in Figure D.3a and compared with the resolvent forcing for each harmonic. We notice that while the linear forcings were mostly located upstream, acting on the same region, the optimal forcing isolates both second Mack modes ($n = 15$ upstream and $n = 13$ downstream) to cover a longer streamwise region and locates the low-frequency ($n = 2$) forcing between them. The amplitude of the response (Figure D.3b) shows the same evolution with maximal response of the harmonic $n = 15$ around $Re_x \sim 200000$, strong amplification of the harmonic $n = 2$ between $Re_x \sim 200000$ and $Re_x \sim 240000$, slightly downstream its forcing region, and maximal response of the harmonic $n = 13$ around $Re_x \sim 330000$. Other harmonics ($n = 4$ and $n = 11$) are generated by non-linear interactions involving in particular the harmonic $n = 2$.

As the low frequency ($n = 2$) component for forcing and response is small in comparison with the second Mack modes, investigating its impact on the response is of interest. Therefore, the $n = 2$ harmonic component is removed from the forcing and the non-linear response is computed again. The mean-flow skin-friction (Figure D.2b) keeps a similar trend but becomes lower than with the optimal forcing from $Re_x \sim 200000$ where the $n = 2$ harmonic response strongly increases in presence of forcing. By comparing the non-linear responses with and without the $n = 2$ harmonic forcing component in Figure D.3b, the $n = 2$ response is weaker, being only generated by the non-linear interactions of $n = 13$ and $n = 15$ harmonics without $n = 2$ forcing. However, one may notice that the harmonic $n = 15$ has more energy when the harmonic $n = 2$ is not forced than when it is. Conversely, the harmonic $n = 13$ gets more energy thanks to the non-linear interaction of $n = 15$ with the forced harmonic $n = 2$. Therefore, the $n = 2$ harmonic component forcing triggers larger $n = 2$ response in order to form a triad with $n = 13$ and $n = 15$ responses so that the latter conveys more energy to the former. The harmonic component $n = 2$ acts as a "transmitter" between both second Mack modes in order to sustain a larger mean-flow deviation along the stream.

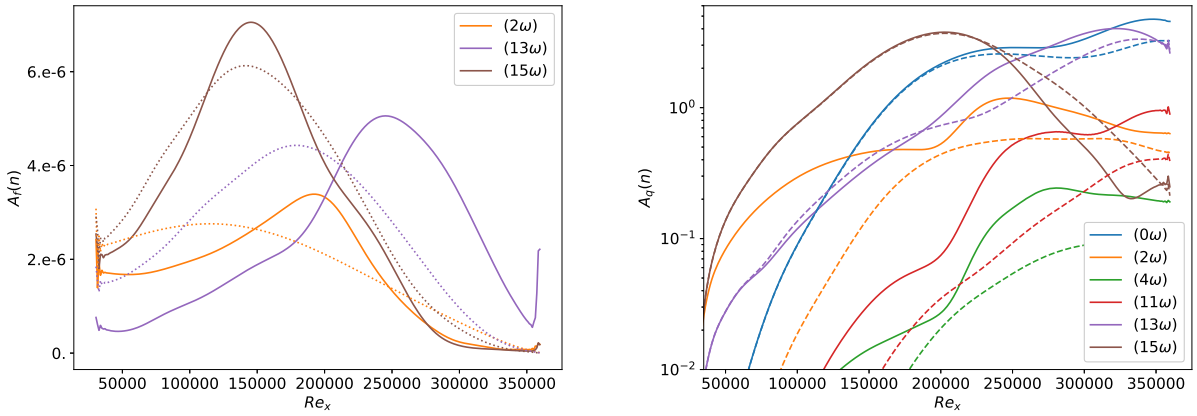

Figure D.3: (a) Amplitude of the optimal forcing $A_f(n)$ predicted by TSM (solid lines) and by resolvent (dotted lines) analyses for the three harmonic components: $n = 2$, $n = 13$ and $n = 15$. (b) Amplitude of the different harmonic components of the non-linear response $A_q(n)$ including low-frequency ($n = 2$) forcing (solid lines) and without (dashed lines). Only the 6 harmonic components of largest amplitude are shown for clarity, they represent 99.87% of the total energy.

The worst-case disturbances found by Jahanbakhshi and Zaki [77], where the forcing is only applied at the inlet, also included two second Mack modes but associated with an oblique first Mack mode. The latter three-dimensional mode is required to promote transition to turbulence, therefore a similar analysis for three-dimensional worst-case disturbances would be of interest to follow up this study.

Appendix **E**

Optimal non-linear solutions: optimal forcing analysis and compressibility effect

E.1 Optimal fundamental forcing analysis

The optimal forcing arisen by the non-linear input-output method is further studied in comparison with the optimal forcing predicted by the resolvent analysis. Indeed, we observe in Figure E.1a that both forcings applied at the same amplitude generate different non-linear response (weaker non-linear interactions producing weak mean-flow deviation). At this large amplitude, between both optimal forcings, the difference of the integral of the skin-friction of the mean-flow deviation is 24%. The optimisation criteria based on the alignment of the optimal forcing with the adjoint state is 22° for the resolvent forcing while it is less than 1° for the non-linear optimal forcing.

To understand the differences between both optimal forcings, we list the features of an optimal forcing. We consider a pair of symmetric fundamental forcing waves acting on the momentum equations. From spatial local stability theory, they can be written as $f(x,y,z,t) = f(y)e^{i(\alpha x+\omega t\pm\beta z)}$ and then have

- a wavelength or a streamwise wavenumber α_r,
- a spatial energy density A_f^2, which may be linked to $f(y)$ and the amplification rate α_i,
- an energy distribution between the momentum components $\|\mathbf{f}_x\|^2$, $\|\mathbf{f}_y\|^2$ and $\|\mathbf{f}_z\|^2$,
- a phase angle between the momentum components.

First, we compute the streamwise wavenumber α_r of both optimal forcings and compare them together in Figure E.1b. The streamwise wavenumber is computed through

$$\alpha_r = \mathrm{Im}\left(\frac{1}{\mathbf{f}}\frac{d\mathbf{f}}{dx}\right) \tag{E.1}$$

However, Eq. (E.1) produces high fluctuations of streamwise wavenumber along Re_x therefore Figure E.1b represents the polynomial expansion approximating the streamwise wavenumber

through a least-square method (low-pass filter). The streamwise wavenumber does not vary much along the streamwise direction (small frequency modulation) but the non-linear optimal forcing deviates more and more from the resolvent forcing along Re_x for all the momentum components.

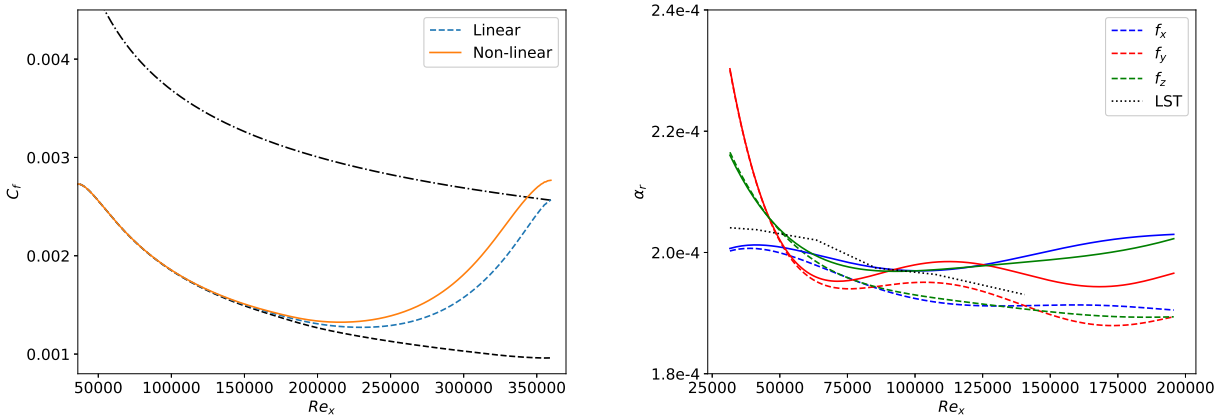

(a) **(b)**

Figure E.1: (a) Mean-flow skin-friction coefficient C_f along the streamwise direction for $F = 16 \times 10^{-5}$, $\beta = 40 \times 10^{-5}$, $A = 32 \times 10^{-5}$, $N = 4$, $M = 6$ for the optimal forcing predicted by non-linear input-output analysis (solid line) and linear input-output analysis (dashed line). Black dashed line indicates the laminar skin-friction coefficient curve and dash-dotted line the turbulent curve. (b) Streamwise wavenumber α_r normalised by unit Reynold number along the streamwise direction of the streamwise (blue), wall-normal (red) and spanwise (green) momentum components of the optimal non-linear (solid lines) and linear (dashed lines) forcings. The streamwise wavenumber predicted by LST analysis in black dotted line is slightly larger but follows the same evolution as the optimal linear forcing f_x.

Secondly, the spatial amplitude of both optimal forcings has already been plotted in Figure 4.5a. It was observed that the non-linear optimal forcing is more localised and located upstream the linear optimal forcing.

Thirdly, the energy distribution is shown in Table E.1. Linear and non-linear optimal forcings of the first Mack mode have similar energy distributions with a large spanwise momentum component $\mathbf{f}_z$, a streamwise component accounting for about a quarter of the total energy and a small wall-normal momentum component. At larger forcing amplitude, the energy of the spanwise momentum component slightly spreads into the other components.

Optimal forcing	$\|\mathbf{f}_x\|^2/A^2$	$\|\mathbf{f}_y\|^2/A^2$	$\|\mathbf{f}_z\|^2/A^2$
Linear	0.25	0.10	0.65
Non-linear: $A = 10^{-5}$	0.27	0.10	0.63
Non-linear: $A = 32 \times 10^{-5}$	0.29	0.11	0.60

Table E.1: Energy distribution between the momentum components of the optimal forcings.

Fourthly, the phase angle between the momentum components of the optimal forcings is evaluated. The phase angle does not change between the linear and non-linear optimal forcings. The streamwise momentum component has a phase of around $\pi/6$ with respect to the spanwise momentum component $\mathbf{f}_z$ while the wall-normal momentum component is almost in phase opposition (π) with respect to $\mathbf{f}_z$.

Having exposed the three different features (α_r, A_f and energy distribution between momentum components) of the optimal linear and non-linear forcings, we attempt to assess which of them produces the large deviation of the non-linear response between both forcings.

In order to quantify the effect of each feature, we compute the non-linear response of the optimal non-linear forcing whose only one feature is changed to match those of the resolvent forcing. First, about the energy distribution between the momentum components, as expected from the low differences observed in these quantities, imposing the energy distribution of the linear forcing decreases only by 0.1% the cost function. Secondly, prescribing the spatial energy density A_f^2 of the resolvent forcing to the non-linear forcing reduces the cost function by 2%. Therefore, the change of streamwise wavenumber seems to play the dominant role (the remaining 21.9%) in the difference between both optimal forcings. However, we did not prove it as we may have missed other features of the optimal forcing and the global framework applied here prevented us to compute an optimal forcing with a given streamwise wavenumber. Indeed, the streamwise wavenumber is not an input but computed from the spatial distribution of the two-dimensional forcing $f(x, y)$. A method to perform this test would consist in performing the non-linear input-output analysis on a forcing restricted to a spatial local definition $f(x, y) = f(y)e^{i\alpha x}$ where the optimisation space would be $f(y)$, α_i and α_r.

E.2 Compressibility effect

The non-linear input-output analysis has been performed at low Mach number ($M_\infty = 0.1$) and at hypersonic regime ($M_\infty = 4.5$). They present similar features with laminar to turbulent transition promoted by the non-linear interactions of the oblique waves and the streaks. However, as the differences between the linear and non-linear optimal forcings for the hypersonic boundary layer have been highlighted in the previous section, the same analysis is here repeated for lower Mach numbers. We study boundary layers in the same domain at $M_\infty = 0.1$ (incompressible regime), $M_\infty = 0.8$ (compressible and subsonic regime), $M_\infty = 1.2$ (supersonic regime) and $M_\infty = 2$. The linear input-output analysis is first performed to find the approximated optimal frequency and spanwise wavenumber of the oblique waves (§E.2.1). Then, optimal non-linear response (§E.2.2) and forcing (§E.2.3) are computed.

E.2.1 Linear input-output analysis

The resolvent analysis is performed at different Mach numbers M_∞ and the optimal gain is plotted in Figure E.2. Increasing the Mach number damps the optimal gain of the streaks and strengthen the optimal gain of the oblique waves (Tollmien-Schlichting waves at incompressible regime becoming first Mack mode waves at compressible regime). This different behaviour at various Mach numbers will impact the non-linear interactions of the streaks with the oblique waves (discussed in the next section). At Mach number 2, the optimal gain of the oblique waves overcomes those of the streaks. Furthermore, the spanwise wavenumber of the optimal streaks slightly decreases while it remains similar for the oblique modes for increasing Mach numbers. The frequency of the optimal oblique waves slightly decreases from $F = 10 \times 10^{-5}$ at $M_\infty = 0.1$ to $F = 6 \times 10^{-5}$ at $M_\infty = 2$.

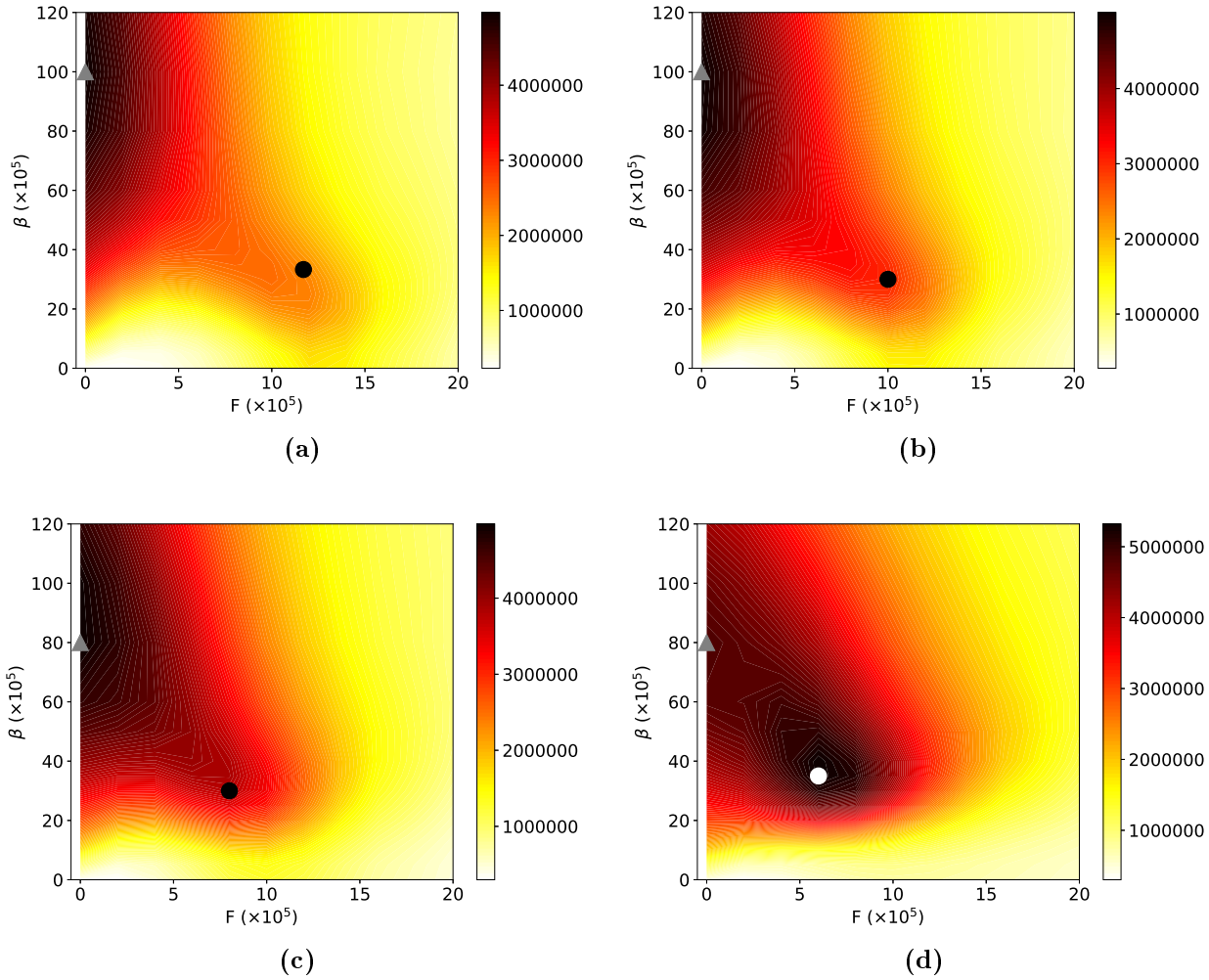

Figure E.2: Optimal gain μ_0 of the linear resolvent analysis at different Mach numbers with respect to the frequency F and the spanwise wavenumber β. Grey triangles denote the streaks and black or white circles indicate the oblique waves where the non-linear input-output analysis is later performed. (a) $M_\infty = 0.1$: streaks at $(F = 0, \beta = 100\times10^{-5})$ and oblique waves at $(F = 11.7\times10^{-5}, \beta = 33.4\times10^{-5})$. (b) $M_\infty = 0.8$: streaks at $(F = 0, \beta = 100\times10^{-5})$ and oblique waves at $(F = 10\times10^{-5}, \beta = 30\times10^{-5})$. (c) $M_\infty = 1.2$: streaks at $(F = 0, \beta = 80\times10^{-5})$ and oblique waves at $(F = 8\times10^{-5}, \beta = 30\times10^{-5})$. (d) $M_\infty = 2$: streaks at $(F = 0, \beta = 80\times10^{-5})$ and oblique waves at $(F = 6\times10^{-5}, \beta = 35\times10^{-5})$. Optimal gain at $M_\infty = 4.5$ plotted in Figure 2.15a.

E.2.2 Optimal non-linear response

We have noticed during the optimisation algorithm at different Mach numbers that the optimal forcing slowly updates with an increasing forcing amplitude. At Mach number 4.5, the optimal forcing was very similar between $A = 26\times10^{-5}$ (medium amplitude, Figure 4.4) and $A = 32\times10^{-5}$ (laminar to turbulent transition). Therefore, we assume that the optimal forcing at the amplitude where laminar to turbulent transition occurs has the same features as the optimal forcing at the medium forcing amplitudes computed in the cases below. For Mach number 0.1, we select the frequency-wavenumber $F-\beta$ couple where the non-linear input-output is maximal according to Rigas et al. [155]. For other Mach numbers, as a parametric analysis across $F-\beta$ has not been performed, we select the couple $F-\beta$ where the linear optimal gain is maximal. This should be relatively close to the region where the non-linear input-output analysis gives maximal skin-friction according to the results found by Rigas et al.

[155] and at Mach number 4.5 in §4.3.2.

The mean-flow skin-friction coefficient (Figure E.3) and the amplitude of the non-linear response (Figure E.4) produced by the optimal symmetric pair of oblique forcing is computed at different Mach numbers. The non-linear responses have been computed on a $N = 2$ and $M = 4$ spectral system at a forcing amplitude sufficient to deviate from the laminar solution but not too large so that the truncated system contains enough harmonics to represent the total energy of the solution (turbulent regime is not reached according to the Figure E.3). One may notice that, even if the skin-friction reached at the end of the domain is not equal for all Mach numbers, the higher the Mach number is, the larger the forcing amplitude is required to promote transition (compressibility stabilisation). Moreover, the shape of the skin-friction coefficient evolves with the Mach number. At low Mach numbers, it has a plateau, which shortens to becomes an inflection at larger Mach numbers, before a sudden rise towards the outlet. At $M_\infty = 2$ and $M_\infty = 4.5$, the increase along the streamwise direction is more monotonic.

This behaviour is also observed in the amplitude of the different harmonic components of the response (Figure E.4). At low Mach number, the streaks, as soon as they are generated by the oblique waves, predominates as predicted by their larger linear optimal gain (see §E.2.1). Increasing the Mach number, they have equivalent energy to the fundamental mode. The plateau observed in the skin-friction curve corresponds to the location where the oblique waves saturate and slightly decay (from $Re_x \sim 270000$ at $M_\infty = 0.1$) whereas the sudden rise is linked to the spreading of the streaks energy to the other harmonics (streaks breakdown from $Re_x \sim 330000$ at $M_\infty = 0.1$). At higher Mach numbers, the oblique mode saturates less and for even larger Mach numbers, the streaks do not decay at the outlet.

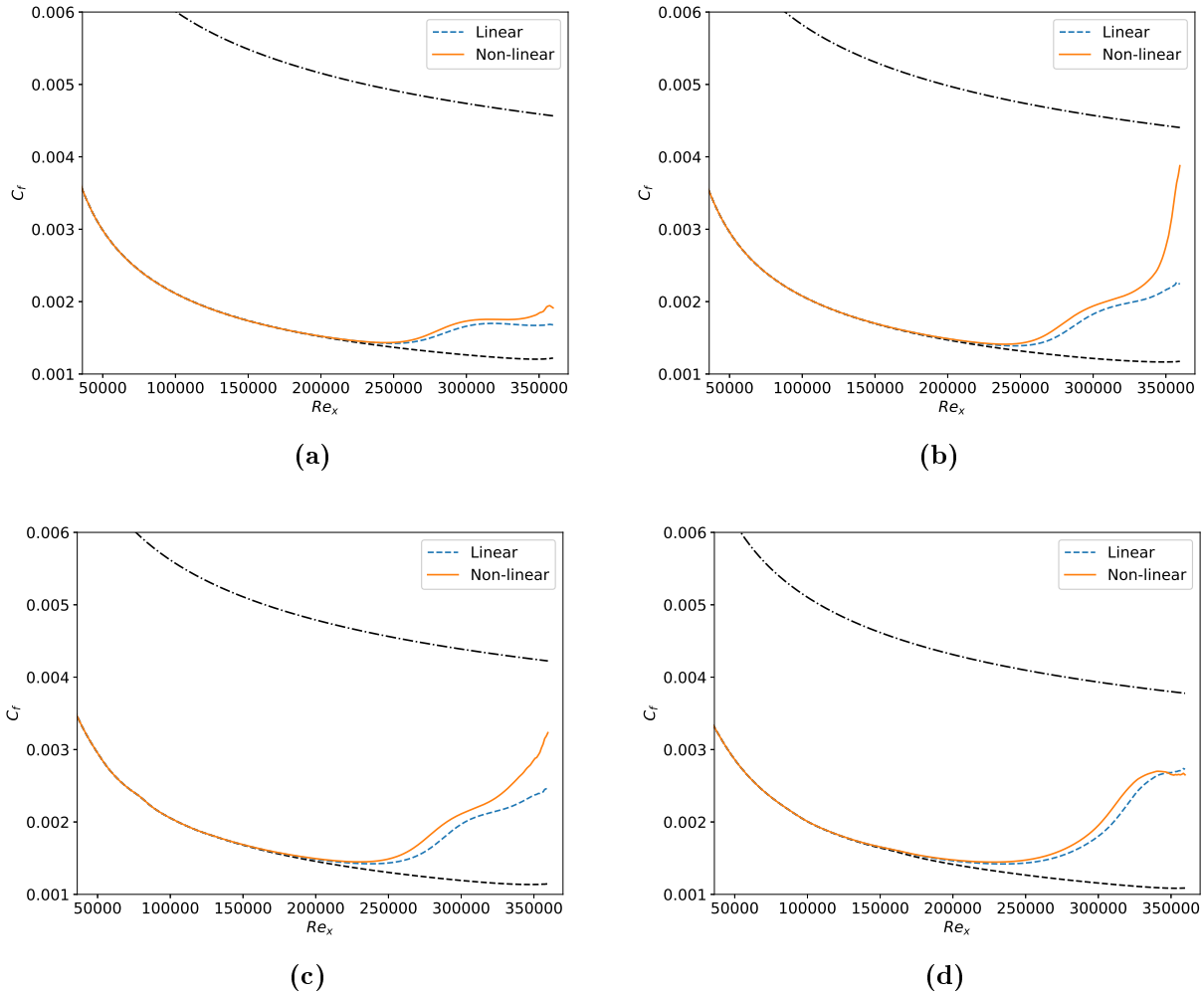

Figure E.3: Mean-flow skin-friction coefficient C_f along the streamwise direction for $N = 2$ and $M = 4$ for the optimal forcings predicted by non-linear input-output (solid line) and resolvent (dashed line) analysis for different Mach numbers. Black dashed line indicates the laminar skin-friction coefficient curve and dash-dotted line the turbulent curve. (a) $M_\infty = 0.1$: oblique waves at ($F = 11.7 \times 10^{-5}$, $\beta = 33.4 \times 10^{-5}$) at $A = 10 \times 10^{-5}$. (b) $M_\infty = 0.8$: oblique waves at ($F = 10 \times 10^{-5}$, $\beta = 30 \times 10^{-5}$) at $A = 13 \times 10^{-5}$. (c) $M_\infty = 1.2$: oblique waves at ($F = 8 \times 10^{-5}$, $\beta = 30 \times 10^{-5}$) at $A = 19 \times 10^{-5}$. (d) $M_\infty = 2$: oblique waves at ($F = 6 \times 10^{-5}$, $\beta = 35 \times 10^{-5}$) at $A = 26 \times 10^{-5}$. C_f at $M_\infty = 4.5$ plotted in Figure E.1a.

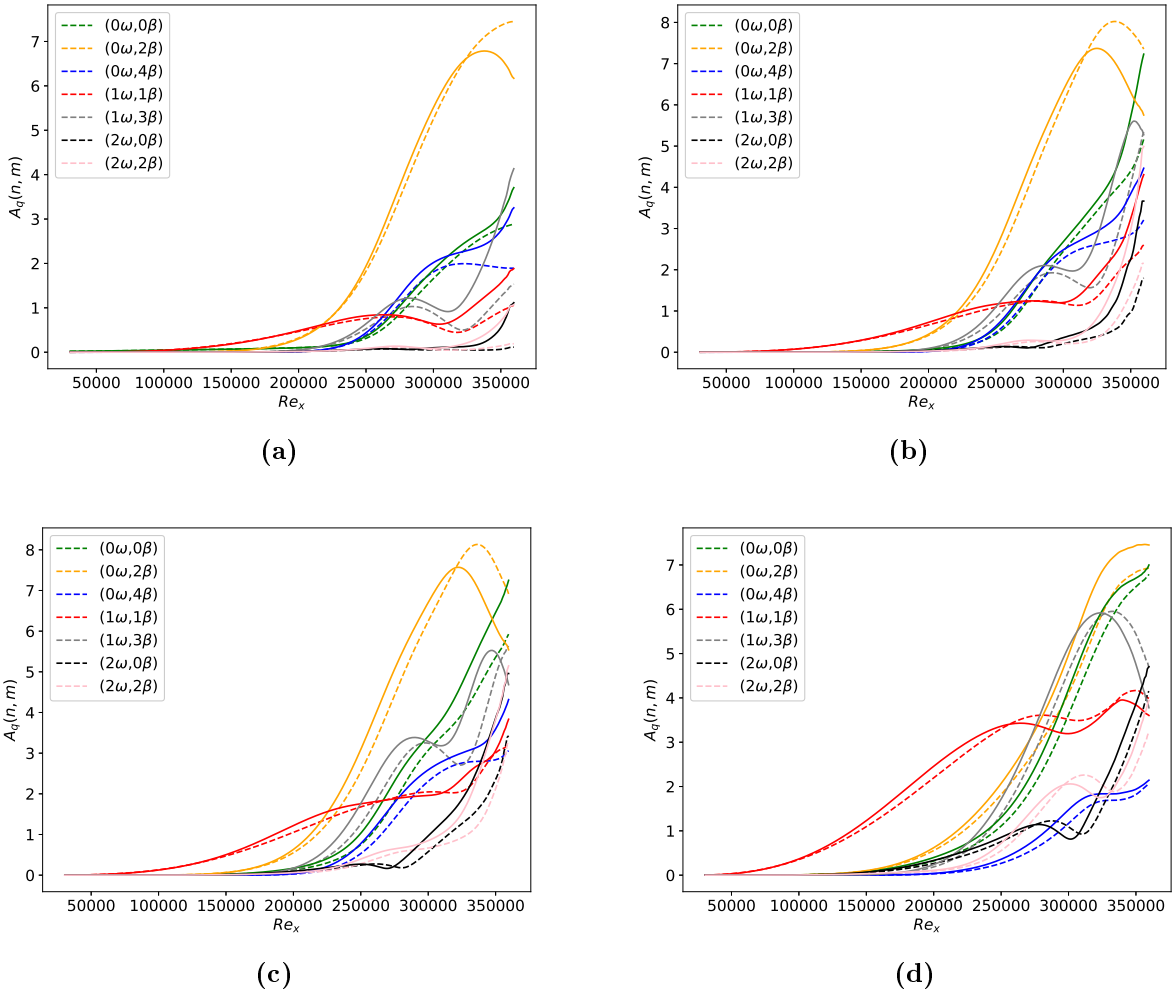

Figure E.4: Amplitude of the response from the non-linear optimal (solid lines) and resolvent (dashed lines) forcings for $N = 2$ and $M = 4$ at different Mach numbers. (a) $M_\infty = 0.1$: oblique waves at ($F = 11.7 \times 10^{-5}$, $\beta = 33.4 \times 10^{-5}$) at $A = 10 \times 10^{-5}$. The 8 harmonic components of largest amplitude shown represent 99.99% of the total energy. (b) $M_\infty = 0.8$: oblique waves at ($F = 10 \times 10^{-5}$, $\beta = 30 \times 10^{-5}$) at $A = 13 \times 10^{-5}$. The 8 harmonic components of largest amplitude shown represent 99.76% of the total energy. (c) $M_\infty = 1.2$: oblique waves at ($F = 8 \times 10^{-5}$, $\beta = 30 \times 10^{-5}$) at $A = 19 \times 10^{-5}$. The 8 harmonic components of largest amplitude shown represent 99.52% of the total energy. (d) $M_\infty = 2$: oblique waves at ($F = 6 \times 10^{-5}$, $\beta = 35 \times 10^{-5}$) at $A = 26 \times 10^{-5}$. The 8 harmonic components of largest amplitude shown represent 99.76% of the total energy. $A_q(n,m)$ at $M_\infty = 4.5$ plotted in Figure 4.5b.

E.2.3 Optimal forcing

The optimal pair of symmetric fundamental oblique forcing waves is analysed at different Mach numbers. The four main features of the optimal forcing have been listed in §E.1. It was found that at $M_\infty = 4.5$, the phase angle between the momentum components remains similar between the linear and non-linear optimal forcings. This conclusion holds at lower Mach number. Phase angles are given for information in Table E.2.

Mach number	Φ of $\mathbf{f}_x$ with respect to $\mathbf{f}_z$	Φ of $\mathbf{f}_y$ with respect to $\mathbf{f}_z$
0.1	0	π
0.8	0	π
1.2	0	π
2	$\pi/8$	π
4.5	$\pi/6$	π

Table E.2: Phase angle Φ of the momentum components with respect to the dominant spanwise momentum forcing component.

We consider first the energy distribution between the momentum components of the forcing. Results at different Mach numbers are given in Table E.3. Similarly to the hypersonic configuration, the spanwise momentum component is predominant over $\mathbf{f}_x$ and $\mathbf{f}_y$ and the optimal non-linear forcing spreads the energy of $\mathbf{f}_z$ to $\mathbf{f}_x$ at all Mach numbers considered. However, we notice that for lower Mach numbers, the streamwise and spanwise momentum components of the optimal forcing are of similar magnitude. Nonetheless, it was observed that the energy distribution also depends of the spanwise wavenumber β considered through $\mathbf{f}_z$. As different spanwise wavenumbers β were studied, it is difficult to compare accurately the energy distribution across the Mach numbers. To conclude, as the variations of energy distribution remain similar to the hypersonic configuration where it was highlighted that the effect on the skin-friction was negligible, we assume that it holds for all the Mach numbers considered.

Mach number	Optimal forcing	$\|\mathbf{f}_x\|^2/A^2$	$\|\mathbf{f}_y\|^2/A^2$	$\|\mathbf{f}_z\|^2/A^2$
0.1	Linear	0.42	0.02	0.56
	Non-linear	0.49	0.02	0.49
0.8	Linear	0.37	0.02	0.61
	Non-linear	0.42	0.02	0.56
1.2	Linear	0.25	0.03	0.72
	Non-linear	0.28	0.03	0.69
2	Linear	0.09	0.06	0.85
	Non-linear	0.11	0.07	0.82

Table E.3: Energy distribution between the momentum components of the optimal forcings. Results at Mach number 4.5 are given in Table E.1.

Therefore, we analyse the amplitude of both optimal forcings (Figure E.5). Similarly to the hypersonic case already explored, all the non-linear optimal forcings are more localised than their corresponding linear forcings. We also observe that for $M_\infty < 2$, a second peak appears downstream near $Re_x = 250000$. From Rigas et al. [155], this second region of forcing triggers streak oscillations in the streamwise direction leading to their breakdown. This is in agreement with the absence of streaks breakdown for $M_\infty > 2$ in Figure E.4. By comparing the linear and non-linear optimal forcings at the different Mach numbers, we notice that the non-linear forcing

whose main peak is located downstream the linear one at low Mach number gradually moves upstream for $M_\infty > 1.2$. An assumption may be that the convective amplification of the streaks being weaker for increasing Mach numbers, the non-linear optimal forcing generates the oblique modes more upstream in order to produce streaks earlier in the flow. In the hypersonic case where both amplitudes have a similar evolution along Re_x, the difference between the linear and non-linear amplitudes leads to only 2% variation of the skin-friction of the mean-flow deviation, however, as its trend is more different (second peak downstream) for lower Mach numbers, it may produce a larger effect on skin-friction. It is checked for the Mach number 0.1 configuration where the amplitude of the resolvent forcing is prescribed. This yields a 15% decrease of the skin-friction of the mean-flow deviation (out of 19% difference between both optimal forcings) mainly resulting from weaker streaks breakdown at the outlet (absence of the second peak of the forcing, see for instance Figure E.4a). Therefore, at low Mach number, it seems that the different amplitude plays the dominant role between linear and non-linear optimal forcings.

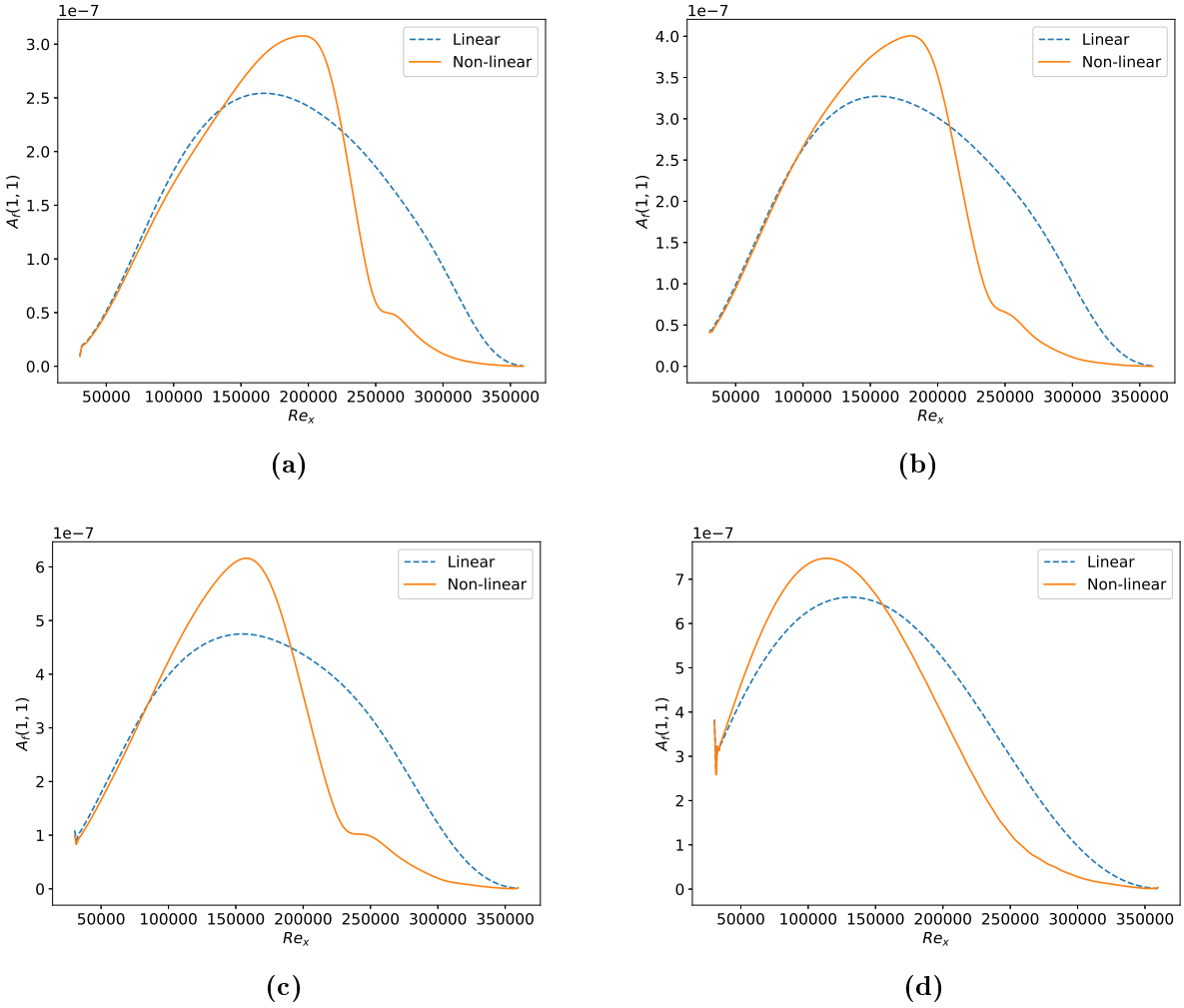

Figure E.5: Amplitude of the optimal oblique forcing $A_f(1,1)$ given by the TSM (orange) compared with the linear forcing predicted by the resolvent analysis at the same (F, β) (blue). (a) Mach number 0.1: oblique waves at $(F = 11.7 \times 10^{-5}, \beta = 33.4 \times 10^{-5})$ at $A = 10 \times 10^{-5}$. (b) Mach number 0.8: oblique waves at $(F = 10 \times 10^{-5}, \beta = 30 \times 10^{-5})$ at $A = 13 \times 10^{-5}$. (c) Mach number 1.2: oblique waves at $(F = 8 \times 10^{-5}, \beta = 30 \times 10^{-5})$ at $A = 19 \times 10^{-5}$. (d) Mach number 2: oblique waves at $(F = 6 \times 10^{-5}, \beta = 35 \times 10^{-5})$ at $A = 26 \times 10^{-5}$. $A_f(1,1)$ at Mach number 4.5 plotted in Figure 4.5a.

We finally compute the streamwise wavenumber of the optimal forcings at various Mach

numbers (Figure E.6). The evolution of the streamwise wavenumber along Re_x is similar for all Mach numbers. We notice that the amplitude of the variations of the streamwise wavenumber is larger for decreasing Mach numbers. Nonetheless, the main difference between linear and non-linear optimal forcings is a larger streamwise wavenumber downstream for high Mach numbers ($M_\infty > 2$).

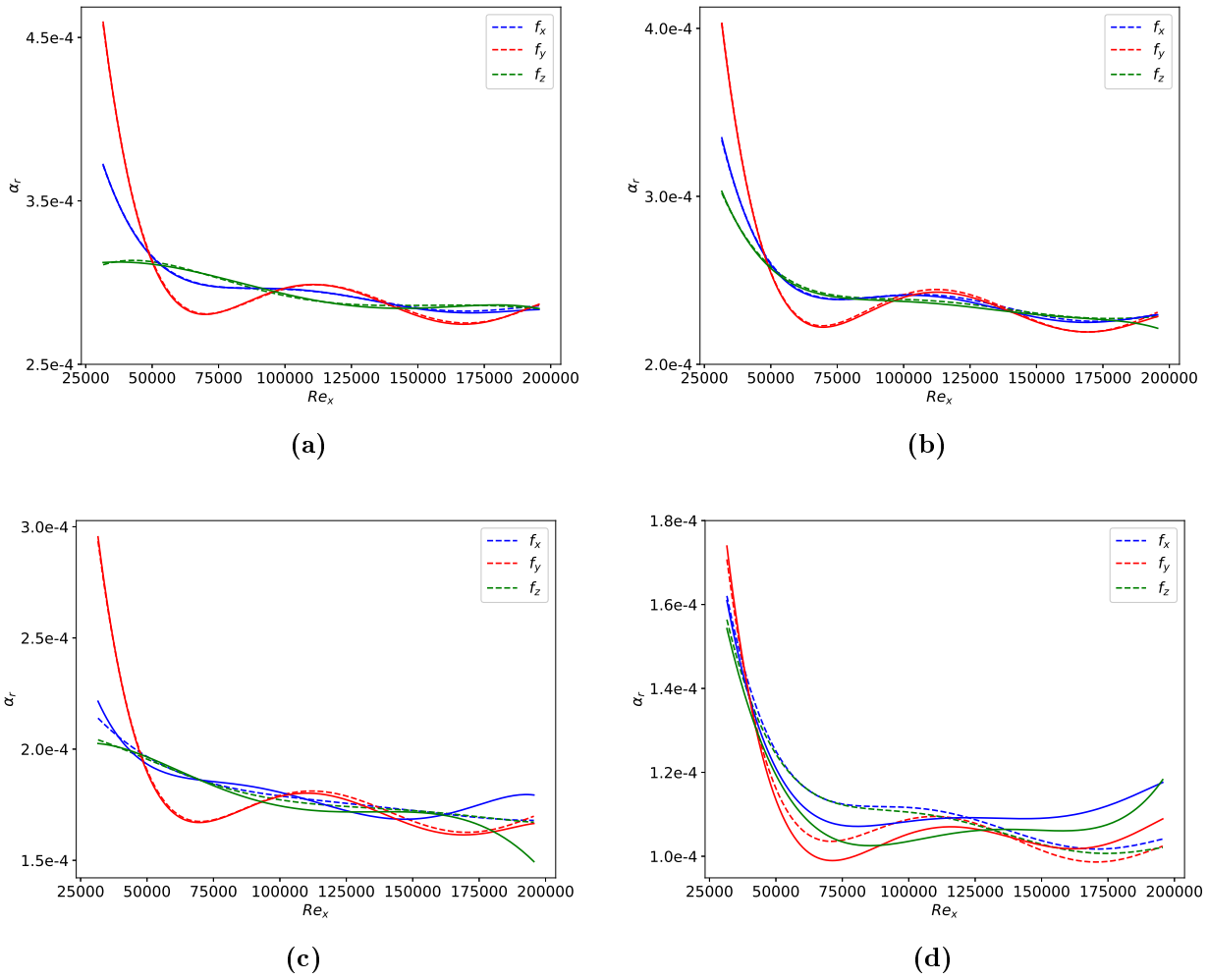

Figure E.6: Streamwise wavenumber α_r normalised by unit Reynold number along the streamwise direction of the streamwise (blue), wall-normal (red) and spanwise (green) momentum components of the optimal non-linear (solid lines) and linear (dashed lines) forcings. (a) Mach number 0.1: oblique waves at ($F = 11.7 \times 10^{-5}$, $\beta = 33.4 \times 10^{-5}$) at $A = 10 \times 10^{-5}$. (b) Mach number 0.8: oblique waves at ($F = 10 \times 10^{-5}$, $\beta = 30 \times 10^{-5}$) at $A = 13 \times 10^{-5}$. (c) Mach number 1.2: oblique waves at ($F = 8 \times 10^{-5}$, $\beta = 30 \times 10^{-5}$) at $A = 19 \times 10^{-5}$. (d) Mach number 2: oblique waves at ($F = 6 \times 10^{-5}$, $\beta = 35 \times 10^{-5}$) at $A = 26 \times 10^{-5}$. Streamwise wavenumber at Mach number 4.5 plotted in Figure E.1b.

To conclude, at low Mach numbers, the amplitude of the non-linear optimal forcing is more localised and located downstream with respect to the resolvent forcing. It has also a second lower peak downstream to generate the streaks breakdown. Increasing the Mach number leads to different non-linear forcing features with a forcing moving upstream and a larger streamwise wavenumber towards the outlet (no streaks breakdown). Therefore, the non-linear optimal forcing features depend much on the Mach number considered. However, it should be pointed out that we have only studied symmetric forcings but Rigas et al. [155] showed that asymmetric

forcing is optimal for this configuration at incompressible regime whereas we found in this work that the symmetric forcing is optimal at Mach number 4.5. Then, it exists an intermediate Mach number where the optimal asymmetric forcing (subharmonic sinuous breakdown [3]) becomes symmetric (subharmonic varicose breakdown). Further investigations would be necessary to explain the compressibility effect on the non-linear optimal forcing as the amplitude variations at low Mach numbers may justify the skin-friction differences produced by the non-linear and linear optimal forcings while the frequency modulation (streamwise wavenumber increase) at larger Mach numbers seems to be the main feature but was not measured.

References

[1] C. Airiau, A. Bottaro, S. Walther, and D. Legendre. A methodology for optimal laminar flow control: Application to the damping of Tollmien–Schlichting waves in a boundary layer. *Physics of Fluids*, 15(5):1131–1145, 2003. 13

[2] P. Amestoy, I. Duff, J.-Y. L'Excellent, and J. Koster. A fully asynchronous multifrontal solver using distributed dynamic scheduling. *SIAM Journal on Matrix Analysis and Applications*, 23(1):15–41, 2001. 31, 86

[3] P. Andersson, L. Brandt, A. Bottaro, and D. S. Henningson. On the breakdown of boundary layer streaks. *Journal of Fluid Mechanics*, 428:29–60, 2001. 10, 139

[4] P. Balakumar and P. Hall. Optimum suction distribution for transition control. *Theoretical and computational fluid dynamics*, 13(1):1–19, 1999. 12

[5] S. Balay, S. Abhyankar, M. Adams, J. Brown, P. Brune, K. Buschelman, L. Dalcin, A. Dener, V. Eijkhout, W. Gropp, et al. Petsc users manual. *ANL-95/11*, 2019. 23, 31

[6] A. Batista and J. Kuehl. Local wall temperature effects on the second-mode instability. *Journal of Spacecraft and Rockets*, 57(3):580–595, 2020. 12, 67

[7] G. Bégou. *Prévision de la transition laminaire-turbulent dans le code elsA par la méthode des paraboles*. PhD thesis, Toulouse, ISAE, 2018. 40

[8] S. Benbaba. *Analyse de stabilité globale pour un écoulement transsonique soumis au phénomène de tremblement de voilure*. PhD thesis, Palaiseau, Ecole polytechnique, 2011. 30

[9] S. Beneddine. *Characterization of unsteady flow behavior by linear stability analysis*. PhD thesis, Université Paris Saclay (COmUE), 2017. 115

[10] S. Berry, R. Nowak, and T. Horvath. Boundary layer control for hypersonic airbreathing vehicles. In *34th AIAA Fluid Dynamics Conference and Exhibit*, page 2246, 2004. 1

[11] A. Bhagatwala and S. K. Lele. A modified artificial viscosity approach for compressible turbulence simulations. *Journal of Computational Physics*, 14(228):4965–4969, 2009. 27

[12] H. M. Blackburn, D. Lee, T. Albrecht, and J. Singh. Semtex: A spectral element–Fourier solver for the incompressible Navier–Stokes equations in cylindrical or Cartesian coordinates. *Computer Physics Communications*, 245, Dec. 2019. ISSN 0010-4655. 23

[13] C. Bogey and C. Bailly. A family of low dispersive and low dissipative explicit schemes for flow and noise computations. *Journal of Computational physics*, 194(1):194–214, 2004. 28

[14] A. Bottaro, P. Corbett, and P. Luchini. The effect of base flow variation on flow stability. *Journal of Fluid Mechanics*, 476:293–302, 2003. 50

[15] E. Boujo. Second-order adjoint-based sensitivity for hydrodynamic stability and control. *Journal of Fluid Mechanics*, 920, 2021. 13

[16] L. Brandt. The lift-up effect: the linear mechanism behind transition and turbulence in shear flows. *European Journal of Mechanics-B/Fluids*, 47:80–96, 2014. 7

[17] L. Brandt, D. Sipp, J. Pralits, and O. Marquet. Effect of base-flow variation in noise amplifiers: the flat-plate boundary layer. *Journal of Fluid Mechanics*, 687:503–528, 2011. 13, 17, 51, 52, 55, 56, 57

[18] O. M. F. Browne, G. Rubio, E. Ferrer, and E. Valero. Sensitivity analysis to unsteady perturbations of complex flows: a discrete approach. *International Journal for Numerical Methods in Fluids*, 76(12):1088–1110, Dec. 2014. ISSN 02712091. 30

[19] B. Bugeat. *Stabilité et perturbations optimales globales d'écoulements compressibles pariétaux*. PhD thesis, Paris 6, 2017. 115

[20] B. Bugeat, J.-C. Chassaing, J.-C. Robinet, and P. Sagaut. 3D global optimal forcing and response of the supersonic boundary layer. *Journal of Computational Physics*, 398: 108888, 2019. 2, 10, 17, 23, 33, 34, 37, 41, 42, 43, 44, 121

[21] B. Bugeat, J.-C. Robinet, J.-C. Chassaing, and P. Sagaut. Low-frequency resolvent analysis of the laminar oblique shock wave/boundary layer interaction. *Journal of Fluid Mechanics*, 942:A43, 2022. 117

[22] K. M. Butler and B. F. Farrell. Three-dimensional optimal perturbations in viscous shear flow. *Physics of Fluids A: Fluid Dynamics*, 4(8):1637–1650, 1992. 7

[23] A. Buttari. *Scalability of parallel sparse direct solvers: methods, memory and performance*. PhD thesis, Toulouse INP, Sept. 2018. 23

[24] C. Caillaud, M. Lugrin, S. Esquieu, and C. Content. Global stability analysis of a hypersonic cone-cylinder-flare geometry. *arXiv preprint arXiv:2303.16325*, 2023. 117

[25] L. Cambier, S. Heib, and S. Plot. The Onera elsA CFD software: input from research and feedback from industry. *Mechanics & Industry*, 14(3):159–174, 2013. 18

[26] C. D. Cantwell, D. Moxey, A. Comerford, A. Bolis, G. Rocco, G. Mengaldo, D. De Grazia, S. Yakovlev, J. E. Lombard, D. Ekelschot, B. Jordi, H. Xu, Y. Mohamied, C. Eskilsson, B. Nelson, P. Vos, C. Biotto, R. M. Kirby, and S. J. Sherwin. Nektar++: An open-source spectral/hp element framework. *Computer Physics Communications*, 192:205–219, July 2015. ISSN 0010-4655. 23

[27] C. Canuto, M. Y. Hussaini, A. Quarteroni, A. Thomas Jr, et al. *Spectral methods in fluid dynamics*. Springer Science & Business Media, 2012. 18

[28] C.-L. Chang and M. R. Malik. Oblique-mode breakdown and secondary instability in supersonic boundary layers. *Journal of Fluid Mechanics*, 273:323–360, 1994. 10, 11

[29] C.-L. Chang, M. Malik, G. Erlebacher, and M. Hussaini. Compressible stability of growing boundary layers using parabolized stability equations. In *22nd Fluid Dynamics, Plasma Dynamics and Lasers Conference*, page 1636, 1991. 15

[30] X. Chanteux, G. Bégou, H. Deniau, and O. Vermeersch. Construction and application of transition prediction databased method for 2nd mode on sharp cone. In *AIAA AVIATION 2022 Forum*, page 3470, 2022. 45

[31] D. R. Chapman and M. W. Rubesin. Temperature and velocity profiles in the compressible laminar boundary layer with arbitrary distribution of surface temperature. *Journal of the Aeronautical Sciences*, 16(9):547–565, 1949. 40

[32] S. Cherubini. *Linear and non-linear global instability of attached and separated boundary-layer flows over a flat plate*. PhD thesis, Paris, ENSAM, 2010. 2, 18

[33] Y. Cho and A. Aessopos. Similarity transformation methods in the analysis of the two dimensional steady compressible laminar boundary layer. *Term paper*, 2, 2004. 40

[34] J.-M. Chomaz. Global instabilities in spatially developing flows: non-normality and nonlinearity. *Annu. Rev. Fluid Mech.*, 37:357–392, 2005. 17

[35] B.-T. Chu. On the energy transfer to small disturbances in fluid flow (part I). *Acta Mechanica*, 1(3):215–234, 1965. 33, 121

[36] P. Cinnella and C. Content. High-order implicit residual smoothing time scheme for direct and large eddy simulations of compressible flows. *Journal of Computational Physics*, 326: 1–29, 2016. 26, 28

[37] A. Crivellini and F. Bassi. An implicit matrix-free discontinuous galerkin solver for viscous and turbulent aerodynamic simulations. *Computers & fluids*, 50(1):81–93, 2011. 14, 29, 85

[38] J. Crouch, A. Garbaruk, and D. Magidov. Predicting the onset of flow unsteadiness based on global instability. *Journal of Computational Physics*, 224(2):924–940, 2007. 17

[39] L. Dalcin, R. Paz, P. Kler, and A. Cosimo. Parallel distributed computing using Python. *Advances in Water Resources*, 34(9):1124–1139, 2011. 31

[40] D. Day and M. A. Heroux. Solving complex-valued linear systems via equivalent real formulations. *SIAM Journal on Scientific Computing*, 23(2):480–498, 2001. 115

[41] M. F. De Pando, D. Sipp, and P. J. Schmid. Efficient evaluation of the direct and adjoint linearized dynamics from compressible flow solvers. *Journal of Computational Physics*, 231(23):7739–7755, 2012. 18

[42] N. De Tullio, P. Paredes, N. Sandham, and V. Theofilis. Laminar–turbulent transition induced by a discrete roughness element in a supersonic boundary layer. *Journal of Fluid Mechanics*, 735:613–646, 2013. 15

[43] A. Demetriades. Hypersonic viscous flow over a slender cone. III-Laminar instability and transition. In *7th Fluid and PlasmaDynamics Conference*, page 535, 1974. 10

[44] G. Dietz and S. Hein. Entropy-layer instabilities over a blunted flat plate in supersonic flow. *Physics of Fluids*, 11(1):7–9, 1999. 7

[45] P. Drazin. Kelvin–Helmholtz instability of finite amplitude. *Journal of Fluid Mechanics*, 42(2):321–335, 1970. 7

[46] Y.-M. Ducimetière, E. Boujo, and F. Gallaire. Weak nonlinearity for strong non-normality. *Journal of Fluid Mechanics*, 947:A43, 2022. 17

[47] F. Ducros, V. Ferrand, F. Nicoud, C. Weber, D. Darracq, C. Gacherieu, and T. Poinsot. Large-eddy simulation of the shock/turbulence interaction. *Journal of Computational Physics*, 152(2):517–549, 1999. 27

[48] D. Fabre, V. Citro, D. Ferreira Sabino, P. Bonnefis, J. Sierra, F. Giannetti, and M. Pigou. A practical review on linear and nonlinear global approaches to flow instabilities. *Applied Mechanics Reviews*, 70(6), 2018. 16, 17, 37, 38, 39

[49] A. Fedorov and A. Khokhlov. Receptivity of hypersonic boundary layer to wall disturbances. *Theoretical and Computational Fluid Dynamics*, 15(4):231–254, 2002. 12

[50] A. Fedorov and A. Tumin. High-speed boundary-layer instability: old terminology and a new framework. *AIAA journal*, 49(8):1647–1657, 2011. 10

[51] A. Fedorov, A. Ryzhov, V. Soudakov, and S. Utyuzhnikov. Numerical simulation of the effect of local volume energy supply on high-speed boundary layer stability. *Computers & Fluids*, 100:130–137, 2014. 12, 66

[52] V. Fer. *Scaling up of global stability tools in order tocharacterize phenomena specific to turbomachinery*. PhD thesis, HESAM Université, 2023. 115

[53] K. D. Fong, X. Wang, and X. Zhong. Numerical simulation of roughness effect on the stability of a hypersonic boundary layer. *Computers & Fluids*, 96:350–367, 2014. 12, 65

[54] A. Fosso, H. Deniau, F. Sicot, and P. Sagaut. Curvilinear finite-volume schemes using high-order compact interpolation. *Journal of Computational Physics*, 229(13):5090–5122, 2010. 37

[55] K. J. Franko and S. K. Lele. Breakdown mechanisms and heat transfer overshoot in hypersonic zero pressure gradient boundary layers. *Journal of Fluid Mechanics*, 730: 491–532, 2013. 10, 11

[56] R. A. Frantz, J.-C. Loiseau, and J.-C. Robinet. Krylov methods for large-scale dynamical systems: Application in fluid dynamics. *Applied Mechanics Reviews*, 75(3):030802, 2023. 18

[57] M. Gaster. On the effects of boundary-layer growth on flow stability. *Journal of Fluid Mechanics*, 66(3):465–480, 1974. 46

[58] J. George and R. Sujith. On Chu's disturbance energy. *Journal of Sound and Vibration*, 330(22):5280–5291, 2011. 33

[59] F. Giannetti and P. Luchini. Structural sensitivity of the first instability of the cylinder wake. *Journal of Fluid Mechanics*, 581:167–197, 2007. 1, 11, 17

[60] M. B. Giles and N. A. Pierce. Analytic adjoint solutions for the quasi-one-dimensional Euler equations. *Journal of Fluid Mechanics*, 426:327–345, 2001. 18

[61] A. Gopinath and A. Jameson. Time spectral method for periodic unsteady computations over two-and three-dimensional bodies. In *43rd AIAA aerospace sciences meeting and exhibit*, page 1220, 2005. 17, 82

[62] A. Griewank and A. Walther. *Evaluating derivatives: principles and techniques of algorithmic differentiation*. SIAM, 2008. 30

[63] M. D. Gunzburger, L. Hou, and T. P. Svobodny. Analysis and finite element approximation of optimal control problems for the stationary Navier-Stokes equations with distributed and Neumann controls. *Mathematics of Computation*, 57(195):123–151, 1991. 17

[64] P. Guo, Z. Gao, C. Jiang, and C.-H. Lee. Sensitivity analysis on supersonic-boundary-layer stability subject to perturbation of flow parameters. *Physics of Fluids*, 33(8):084111, 2021. 52, 57

[65] H. Görtler. Instabilität laminarer grenzschichten an konkaven wänden gegenüber gewissen dreidimensionalen störungen. *ZAMM-Journal of Applied Mathematics and Mechanics/Zeitschrift für Angewandte Mathematik und Mechanik*, 21(4):250–252, 1941. 7

[66] C. Hader and H. F. Fasel. Direct numerical simulations of hypersonic boundary-layer transition for a flared cone: Fundamental breakdown. *Journal of Fluid Mechanics*, 869: 341–384, 2019. 11

[67] A. Hanifi, P. Schmid, and D. Henningson. Transient growth in compressible boundary layer flow. *Physics of Fluids*, 8(3):826–837, 1996. 8, 16, 33

[68] L. Hascoet and V. Pascual. The Tapenade automatic differentiation tool: principles, model, and specification. *ACM Transactions on Mathematical Software (TOMS)*, 39(3): 1–43, 2013. 23, 30

[69] F. Hecht. New development in freefem++. *Journal of numerical mathematics*, 20(3-4): 251–266, 2012. 18, 38, 39

[70] T. Herbert. Secondary instability of boundary layers. *Annual review of fluid mechanics*, 20(1):487–526, 1988. 10

[71] T. Herbert. Parabolized stability equations. *Annual Review of Fluid Mechanics*, 29(1): 245–283, 1997. 15

[72] V. Hernández, J. Román, A. Tomás, and V. Vidal. Krylov-Schur methods in SLEPc. *Universitat Politecnica de Valencia, Tech. Rep. STR-7*, 2007. 32

[73] Z. Huang and X. Wu. The effect of local steady suction on the stability and transition of boundary layer on a flat plate. In *8th AIAA Flow Control Conference*, page 3471, 2016. 12

[74] P. Huerre and P. A. Monkewitz. Local and global instabilities in spatially developing flows. *Annual Review of Fluid Mechanics*, 22(1):473–537, 1990. 16, 32

[75] C. Jackson. A finite-element study of the onset of vortex shedding in flow past variously shaped bodies. *Journal of fluid Mechanics*, 182:23–45, 1987. 16

[76] A. Jafari, B. J. McKeon, and M. Arjomandi. Frequency-tuned surfaces for passive control of wall-bounded turbulent flow–a resolvent analysis study. *Journal of Fluid Mechanics*, 959:A26, 2023. 117

[77] R. Jahanbakhshi and T. A. Zaki. Nonlinearly most dangerous disturbance for high-speed boundary-layer transition. *Journal of Fluid Mechanics*, 876:87–121, 2019. 2, 11, 13, 104, 117, 128

[78] R. Jahanbakhshi and T. A. Zaki. Optimal heat flux for delaying transition to turbulence in a high-speed boundary layer. *Journal of Fluid Mechanics*, 916:A46, 2021. 13, 104, 105

[79] R. Jahanbakhshi and T. A. Zaki. Optimal two-dimensional roughness for transition delay in high-speed boundary layer. *arXiv preprint arXiv:2307.08817*, 2023. 111, 117

[80] A. Jameson and E. Turkel. Implicit schemes and LU decompositions. *Mathematics of Computation*, 37(156):385–397, 1981. 14

[81] A. Jameson, W. Schmidt, and E. Turkel. Numerical solutions of the Euler equations by finite volume methods using runge-kutta time stepping. *AIAA Paper 81-1259*, 1981. 27

[82] Y. Jang, L. Grigori, E. Martin, and C. Content. Randomized flexible gmres with deflated restarting. 2023. 116

[83] C. Jin, P. Netrapalli, and M. Jordan. What is local optimality in nonconvex-nonconcave minimax optimization? In *International conference on machine learning*, pages 4880–4889. PMLR, 2020. 116

[84] R. Joslin. Overview of laminar flow control. Technical Report TP-1998-20705, NASA, 1998. 1, 11

[85] R. Joslin, C. Streett, and C.-L. Chang. Spatial direct numerical simulation of boundary-layer transition mechanisms: Validation of PSE theory. *Theoretical and Computational Fluid Dynamics*, 4(6):271–288, 1993. 17

[86] Y. S. Kachanov, V. Kozlov, and V. Y. Levchenko. Nonlinear development of a wave in a boundary layer. *Fluid dynamics*, 12(3):383–390, 1977. 10

[87] O. Kamal, G. Rigas, M. T. Lakebrink, and T. Colonius. Application of the One-Way Navier-Stokes (OWNS) equations to hypersonic boundary layers. In *AIAA Aviation 2020 Forum*, page 2986, 2020. 16

[88] M. Karp and J. Cohen. On the secondary instabilities of transient growth in Couette flow. *Journal of Fluid Mechanics*, 813:528–557, 2017. 8

[89] A. Kazakov, M. Kogan, and V. Kuparev. Optimization of laminar-turbulent transition delay by means of local heating of the surface. *Fluid dynamics*, 30(4):563–570, 1995. 12

[90] R. Kerswell. Nonlinear nonmodal stability theory. *Annual Review of Fluid Mechanics*, 50:319–345, 2018. 84

[91] E. Kitzinger, T. Leclercq, O. Marquet, E. Piot, and D. Sipp. Attachment-line, cross-flow and Tollmien–Schlichting instabilities on swept ONERA-D and Joukowski airfoils. *Journal of Fluid Mechanics*, 957:A29, 2023. 7

[92] P. S. Klebanoff, K. Tidstrom, and L. Sargent. The three-dimensional nature of boundary-layer instability. *Journal of Fluid Mechanics*, 12(1):1–34, 1962. 10

[93] D. A. Knoll and D. E. Keyes. Jacobian-free Newton-Krylov methods: a survey of approaches and applications. *Journal of Computational Physics*, 193(2):357–397, 2004. 30

[94] A. LaBryer and P. Attar. High dimensional harmonic balance dealiasing techniques for a duffing oscillator. *Journal of Sound and Vibration*, 324(3-5):1016–1038, 2009. 87, 115

[95] A. C. Laible and H. F. Fasel. Continuously forced transient growth in oblique breakdown for supersonic boundary layers. *Journal of Fluid Mechanics*, 804:323–350, 2016. 10

[96] M. Lange, G. Gorman, M. Weiland, L. Mitchell, and J. Southern. Achieving Efficient Strong Scaling with PETSc Using Hybrid MPI/OpenMP Optimisation. In J. M. Kunkel, T. Ludwig, and H. W. Meuer, editors, *Supercomputing*, Lecture Notes in Computer Science, pages 97–108, Berlin, Heidelberg, 2013. Springer. ISBN 978-3-642-38750-0. 23, 87

[97] C. Laurent. *Étude d'écoulements transitionnels et hors équilibre par des approches DNS et RANS.* PhD thesis, Ecole nationale supérieure d'arts et métiers-ENSAM, 2012. 97

[98] A. Lerat and C. Corre. Approximations d'ordre élevé pour les écoulements compressibles. *Ecole de Printemps de Mécanique des Fluides Numérique, Fréjus*, 2003. 26

[99] A. Lerat and C. Corre. Higher order residual-based compact schemes on structured grids. *VKI LS 2006-1, von Karman Institute for Fluid Dynamics*, 2006. 27

[100] F. Li and M. R. Malik. On the nature of PSE approximation. *Theoretical and Computational Fluid Dynamics*, 8(4):253–273, 1996. 15

[101] L. Liu, J. P. Thomas, E. H. Dowell, P. Attar, and K. C. Hall. A comparison of classical and high dimensional harmonic balance approaches for a Duffing oscillator. *Journal of Computational Physics*, 215(1):298–320, 2006. 82

[102] A. Logg and G. N. Wells. Dolfin: Automated finite element computing. *ACM Transactions on Mathematical Software (TOMS)*, 37(2):1–28, 2010. 18

[103] M. Lugrin, S. Beneddine, C. Leclercq, E. Garnier, and R. Bur. Transition scenario in hypersonic axisymmetrical compression ramp flow. *Journal of Fluid Mechanics*, 907:A6, 2021. 96

[104] M. Luhar, A. S. Sharma, and B. McKeon. A framework for studying the effect of compliant surfaces on wall turbulence. *Journal of Fluid Mechanics*, 768:415–441, 2015. 117

[105] Y. Ma and X. Zhong. Receptivity of a supersonic boundary layer over a flat plate. part 1. wave structures and interactions. *Journal of Fluid Mechanics*, 488:31–78, 2003. 10, 15

[106] L. Mack. The inviscid stability of the compressible laminar boundary layer. *Space Programs Summary*, 37:23, 1963. 1, 2, 7, 8, 9, 15

[107] L. Mack. Boundary-layer stability theory. JPL Report 900-277 Rev. A. *Jet Propulsion Laboratory, Pasadena, USA*, 1969. 9

[108] L. Mack. Effect of cooling on boundary-layer stability at mach number 3. In *Instabilities and turbulence in engineering flows*, pages 175–188. Springer, 1993. 12, 15, 60, 61, 74

[109] M. Malik. Prediction and control of transition in supersonic and hypersonic boundary layers. *AIAA journal*, 27(11):1487–1493, 1989. 14

[110] M. Malik, F. Li, and C.-L. Chang. Crossflow disturbances in three-dimensional boundary layers: nonlinear development, wave interaction and secondary instability. *Journal of Fluid Mechanics*, 268:1–36, 1994. 17

[111] O. Marquet, D. Sipp, J.-M. Chomaz, and L. Jacquin. Amplifier and resonator dynamics of a low-Reynolds-number recirculation bubble in a global framework. *Journal of Fluid Mechanics*, 605:429–443, 2008. 38, 39

[112] O. Marquet, D. Sipp, and L. Jacquin. Sensitivity analysis and passive control of cylinder flow. *Journal of Fluid Mechanics*, 615:221–252, 2008. 17, 18, 51, 52

[113] A. Martínez-Cava. *Direct and adjoint methods for highly detached flows.* PhD thesis, Espacio, 2019. 51

[114] A. Martinez-Cava, M. Chávez-Modena, E. Valero, J. de Vicente, and E. Ferrer. Sensitivity gradients of surface geometry modifications based on stability analysis of compressible flows. *Physical Review Fluids*, 5(6):063902, June 2020. ISSN 2469-990X. 13, 17

[115] E. Martini, D. Rodríguez, A. Towne, and A. V. Cavalieri. Efficient computation of global resolvent modes. *Journal of Fluid Mechanics*, 919, 2021. 17, 34

[116] T. Mary. *Block Low-Rank multifrontal solvers: complexity, performance, and scalability.* PhD thesis, Université Paul Sabatier-Toulouse III, 2017. 86, 98

[117] J. Masad. Transition in flow over heat-transfer strips. *Physics of Fluids*, 7(9):2163–2174, 1995. 12

[118] J. Masad and R. Abid. On transition in supersonic and hypersonic boundary layers. *International journal of Engineering Science*, 33(13):1893–1919, 1995. 12, 15

[119] B. Maugars. *Méthodes de volumes finis d'ordre élevé en maillages non coïncidents pour les écoulements dans les turbomachines.* PhD thesis, Paris, ENSAM, 2016. 26

[120] B. Maugars, S. Bourasseau, C. Content, B. Michel, B. Berthoul, J. N. Ramirez, P. Raud, and L. Hascoët. Algorithmic Differentiation for an efficient CFD solver. In *ECCOMAS 2022 - 8th European Congress on Computational Methods in Applied Sciences and Engineering*, June 2022. 23

[121] C. S. Mayer, D. A. Von Terzi, and H. F. Fasel. Direct numerical simulation of complete transition to turbulence via oblique breakdown at mach 3. *Journal of Fluid Mechanics*, 674:5–42, 2011. 10

[122] P. Meliga, E. Boujo, G. Pujals, and F. Gallaire. Sensitivity of aerodynamic forces in laminar and turbulent flow past a square cylinder. *Physics of Fluids*, 26(10):104101, 2014. 17

[123] C. Mettot. *Linear stability, sensitivity, and passive control of turbulent flows using finite differences*. PhD thesis, Palaiseau, Ecole polytechnique, 2013. 17, 30, 115

[124] C. Mettot, F. Renac, and D. Sipp. Computation of eigenvalue sensitivity to base flow modifications in a discrete framework: Application to open-loop control. *Journal of Computational Physics*, 269:234–258, 2014. 17, 30, 50, 51, 52, 55

[125] R. W. Milling. Tollmien–Schlichting wave cancellation. *The Physics of Fluids*, 24(5): 979–981, 1981. 11

[126] F. Miró Miró and F. Pinna. Effect of uneven wall blowing on hypersonic boundary-layer stability and transition. *Physics of Fluids*, 30(8):084106, 2018. 65

[127] C. R. Moreno, M. Couliou, N. Fabbiane, O. Marquet, and R. Bur. Experimental characterization of synchronized interactions between a normal shock-wave and compliant wall. In *ERCOFTAC 2023*, 2023. 117

[128] R. B. Morgan. GMRES with deflated restarting. *SIAM Journal on Scientific Computing*, 24(1):20–37, 2002. 116

[129] M. Morkovin. Transition in open flow systems-a reassessment. *Bull. Am. Phys. Soc.*, 39: 1882, 1994. 1, 7, 8

[130] J. Moulin. *On the flutter bifurcation in laminar flows: linear and nonlinear modal methods*. PhD thesis, Institut Polytechnique de Paris, 2020. 17, 85, 86, 115, 116

[131] N. Mundis and D. Mavriplis. Toward an optimal solver for time-spectral fluid-dynamic and aeroelastic solutions on unstructured meshes. *Journal of Computational Physics*, 345: 132–161, 2017. 87

[132] P. Nibourel. *Robust reactive control of transition to turbulence of a supersonic boundary layer*. PhD thesis, Institut polytechnique de Paris, 2023. 96

[133] P. Nibourel, C. Leclercq, F. Demourant, E. Garnier, and D. Sipp. Reactive control of second mack mode in a supersonic boundary layer with free-stream velocity/density variations. *Journal of Fluid Mechanics*, 954:A20, 2023. 11, 45

[134] F. Oz, T. E. Goebel, J. S. Jewell, and K. Kara. Local wall cooling effects on hypersonic boundary-layer stability. *Journal of Spacecraft and Rockets*, 60(2):412–426, 2023. 12, 15

[135] S. Özgen and S. A. Kırcalı. Linear stability analysis in compressible, flat-plate boundary-layers. *Theoretical and Computational Fluid Dynamics*, 22(1):1–20, 2008. 41

[136] F. Palacios, J. Alonso, K. Duraisamy, M. Colonno, J. Hicken, A. Aranake, A. Campos, S. Copeland, T. Economon, A. Lonkar, T. Lukaczyk, and T. Taylor. Stanford University Unstructured (SU^2): An open-source integrated computational environment for multi-physics simulation and design. In *51st AIAA Aerospace Sciences Meeting including the New Horizons Forum and Aerospace Exposition*. American Institute of Aeronautics and Astronautics, 2013. 18, 23

[137] P. Paredes, M. M. Choudhari, F. Li, and C.-L. Chang. Optimal growth in hypersonic boundary layers. *AIAA Journal*, 54(10):3050–3061, 2016. 7

[138] J. Park and T. Zaki. Sensitivity of high-speed boundary-layer stability to base-flow distortion. *Journal of Fluid Mechanics*, 859:476–515, 2019. 57

[139] S. Péron, T. Renaud, I. Mary, C. Benoit, and M. Terracol. An immersed boundary method for preliminary design aerodynamic studies of complex configurations. In *23rd AIAA Computational Fluid Dynamics Conference*, page 3623, 2017. 96

[140] J. E. Peter and R. P. Dwight. Numerical sensitivity analysis for aerodynamic optimization: A survey of approaches. *Computers & Fluids*, 39(3):373–391, 2010. 18

[141] I. Petropoulos, M. Costes, and P. Cinnella. Development and analysis of high-order vorticity confinement schemes. *Computers & Fluids*, 156:602–620, Oct. 2017. ISSN 0045-7930. 27

[142] J.-L. Pfister. *Instabilities and optimization of elastic structures interacting with laminar flows*. PhD thesis, Université Paris Saclay, 2019. 117

[143] T. Poinsot and S. Lele. Boundary conditions for direct simulations of compressible viscous flows. *Journal of Computational Physics*, 101(1):104–129, 1992. 28, 37

[144] Y. Pomeau and P. Manneville. Intermittent transition to turbulence in dissipative dynamical systems. *Communications in Mathematical Physics*, 74:189–197, 1980. 7

[145] J. Pralits, C. Airiau, A. Hanifi, and D. Henningson. Sensitivity analysis using adjoint parabolized stability equations for compressible flows. *Flow, turbulence and combustion*, 65(3):321–346, 2000. 13

[146] J. Pralits, A. Hanifi, and D. Henningson. Adjoint-based optimization of steady suction for disturbance control in incompressible flows. *Journal of Fluid Mechanics*, 467:129–161, 2002. 13

[147] L. Rayleigh. On the stability, or instability, of certain fluid motions. *Proc. London Math. Soc.*, 9:57–70, 1880. 8

[148] H. Reed and A. Nayfeh. Numerical-perturbation technique for stability of flat-plate boundary layers with suction. *AIAA journal*, 24(2):208–214, 1986. 12

[149] H. L. Reed and W. S. Saric. Stability of three-dimensional boundary layers. *Annual Review of Fluid Mechanics*, 21(1):235–284, 1989. 7

[150] H. L. Reed, W. S. Saric, and D. Arnal. Linear stability theory applied to boundary layers. *Annual review of fluid mechanics*, 28(1):389–428, 1996. 15

[151] E. Reshotko. Transient growth: A factor in bypass transition. *Physics of Fluids*, 13(5): 1067–1075, 2001. 8

[152] G. Reynolds and W. Saric. Experiments on the stability of the flat-plate boundary layer with suction. *AIAA journal*, 24(2):202–207, 1986. 12

[153] O. Reynolds. XXIX. An experimental investigation of the circumstances which determine whether the motion of water shall be direct or sinuous, and of the law of resistance in parallel channels. *Philosophical Transactions of the Royal society of London*, (174):935–982, 1883. 7

[154] A. Rezgui, P. Cinnella, and A. Lerat. Third-order accurate finite volume schemes for Euler computations on curvilinear meshes. *Computers & fluids*, 30(7-8):875–901, 2001. 26, 37

[155] G. Rigas, D. Sipp, and T. Colonius. Nonlinear input/output analysis: application to boundary layer transition. *Journal of Fluid Mechanics*, 911, 2021. 2, 17, 46, 82, 83, 86, 88, 89, 90, 91, 94, 115, 132, 133, 136, 138

[156] U. Rist and H. Fasel. Direct numerical simulation of controlled transition in a flat-plate boundary layer. *Journal of Fluid Mechanics*, 298:211–248, 1995. 10

[157] J.-C. Robinet. Bifurcations in shock-wave/laminar-boundary-layer interaction: global instability approach. *Journal of Fluid Mechanics*, 579:85–112, 2007. 16, 117

[158] J. Roman, C. Campos, E. Romero, and A. Tomás. SLEPc users manual. *D. Sistemes Informàtics i Computació Universitat Politècnica de València, Valencia, Spain, Report No. DSIC-II/24/02*, 2015. 32

[159] J. Saint-James. *Prévision de la transition laminaire-turbulent dans le code elsA. Extension de la méthode des paraboles aux parois chauffées.* PhD thesis, Institut Supérieur de l'Aéronautique et de l'Espace (ISAE), 2020. 45

[160] N. Sandham, N. A. Adams, and L. Kleiser. Direct simulation of breakdown to turbulence following oblique instability waves in a supersonic boundary layer. *Applied scientific research*, 54:223–234, 1995. 10

[161] W. S. Saric, H. L. Reed, and E. J. Kerschen. Boundary-layer receptivity to freestream disturbances. *Annual review of fluid mechanics*, 34(1):291–319, 2002. 1

[162] F. Sartor, C. Mettot, R. Bur, and D. Sipp. Unsteadiness in transonic shock-wave/boundary-layer interactions: experimental investigation and global stability analysis. *Journal of Fluid Mechanics*, 781:550–577, 2015. 33

[163] F. Savarino, D. Sipp, and G. Rigas. Laminar-turbulent transition mechanisms of separated flows using the harmonic balance method. *Bulletin of the American Physical Society*, 2022. 117

[164] A. Schioppa. Optimal laminar-to-turbulence transition scenario in hypersonic boundary layer. Master's thesis, ISAE-SUPAERO/ONERA, 2023. 96

[165] H. Schlichting. Zur enstehung der turbulenz bei der plattenströmung. *Nachrichten von der Gesellschaft der Wissenschaften zu Göttingen, Mathematisch-Physikalische Klasse*, 1933:181–208, 1933. 7, 8

[166] P. J. Schmid. Nonmodal stability theory. *Annu. Rev. Fluid Mech.*, 39:129–162, 2007. 8, 16

[167] P. J. Schmid, D. S. Henningson, and D. Jankowski. Stability and transition in shear flows. applied mathematical sciences, vol. 142. *Appl. Mech. Rev.*, 55(3):B57–B59, 2002. 15

[168] S. P. Schneider. Hypersonic laminar–turbulent transition on circular cones and scramjet forebodies. *Progress in Aerospace Sciences*, 40(1-2):1–50, 2004. 1

[169] S. P. Schneider. Lecture notes in AAE624 laminar turbulent transition, January-April 2021. 2, 7

[170] A. Scholten, P. Paredes, M. M. Choudhari, F. Li, M. Carpenter, and M. Bailey. Nonlinear nonmodal analysis of hypersonic flow over blunt cones. In *AIAA AVIATION 2023 Forum*, page 3420, 2023. 17, 18

[171] L. Sciacovelli, D. Passiatore, P. Cinnella, and G. Pascazio. Assessment of a high-order shock-capturing central-difference scheme for hypersonic turbulent flow simulations. *Computers & Fluids*, 230:105134, 2021. 23, 27, 97

[172] B. Sharma and S. S. Girimaji. Effect of flow–thermodynamics interactions on the stability of compressible boundary layers: insights from Helmholtz decomposition. *Journal of Fluid Mechanics*, 962:A18, 2023. 10

[173] S. Sharma, M. S. Shadloo, A. Hadjadj, and M. J. Kloker. Control of oblique-type breakdown in a supersonic boundary layer employing streaks. *Journal of Fluid Mechanics*, 873: 1072–1089, 2019. 103

[174] Y. Shen, G. Zha, and X. Chen. High order conservative differencing for viscous terms and the application to vortex-induced vibration flows. *Journal of Computational Physics*, 228(22):8283–8300, 2009. 28

[175] A. Sidorenko, Y. Gromyko, D. Bountin, P. Polivanov, and A. Maslov. Effect of the local wall cooling/heating on the hypersonic boundary layer stability and transition. *Progress in Flight Physics–Volume 7*, 7:549–568, 2015. 12

[176] J. Sierra-Ausin, V. Citro, F. Giannetti, and D. Fabre. Efficient computation of time-periodic compressible flows with spectral techniques. *Computer Methods in Applied Mechanics and Engineering*, 393:114736, 2022. 17, 82, 116

[177] D. Sipp and A. Lebedev. Global stability of base and mean flows: a general approach and its applications to cylinder and open cavity flows. *Journal of Fluid Mechanics*, 593: 333–358, 2007. 17, 37, 39, 77, 78, 80, 81

[178] D. Sipp and O. Marquet. Characterization of noise amplifiers with global singular modes: the case of the leading-edge flat-plate boundary layer. *Theoretical and Computational Fluid Dynamics*, 27(5):617–635, 2013. 15, 16, 46

[179] D. Sipp, O. Marquet, P. Meliga, and A. Barbagallo. Dynamics and control of global instabilities in open-flows: a linearized approach. *Applied Mechanics Reviews*, 63(3), 2010. 50

[180] M. K. Sleeman, M. T. Lakebrink, and T. Colonius. Nonlinear stability of wall-bounded flows using the One-Way Navier-Stokes (OWNS) Equations. In *AIAA AVIATION 2023 Forum*, page 3273, 2023. 17

[181] V. Soudakov, A. Fedorov, and I. Egorov. Stability of high-speed boundary layer on a sharp cone with localized wall heating or cooling. *Progress in Flight Physics–Volume 7*, 7:569–584, 2015. 12

[182] G. Stuckert, N. Lin, and T. Herbert. Nonparallel effects in hypersonic boundary layer stability. In *33rd Aerospace Sciences Meeting and Exhibit*, page 776, 1995. 15

[183] W. Sutherland. LII. The viscosity of gases and molecular force. *The London, Edinburgh, and Dublin Philosophical Magazine and Journal of Science*, 36(223):507–531, 1893. 19

[184] Hypre. *hypre*: High Performance Preconditioners. 116

[185] O. Thomas, A. Lazarus, and C. Touzé. A harmonic-based method for computing the stability of periodic oscillations of non-linear structural systems. In *International Design Engineering Technical Conferences and Computers and Information in Engineering Conference*, volume 44137, pages 883–892, 2010. 18

[186] A. Towne and T. Colonius. One-way spatial integration of hyperbolic equations. *Journal of Computational Physics*, 300:844–861, 2015. 16

[187] A. Towne, G. Rigas, and T. Colonius. A critical assessment of the parabolized stability equations. *Theoretical and Computational Fluid Dynamics*, 33:359–382, 2019. 15

[188] A. Towne, G. Rigas, O. Kamal, E. Pickering, and T. Colonius. Efficient global resolvent analysis via the One-Way Navier–Stokes equations. *Journal of Fluid Mechanics*, 948:A9, 2022. 17

[189] L. N. Trefethen, A. E. Trefethen, S. C. Reddy, and T. A. Driscoll. Hydrodynamic stability without eigenvalues. *Science*, 261(5121):578–584, 1993. 16

[190] S. Unnikrishnan and D. V. Gaitonde. First-mode-induced nonlinear breakdown in a hypersonic boundary layer. *Computers & Fluids*, 191:104249, 2019. 10

[191] S. Unnikrishnan and D. V. Gaitonde. Linear, nonlinear and transitional regimes of second-mode instability. *Journal of Fluid Mechanics*, 905:A25, 2020. 11

[192] B. van Leer and H. Nishikawa. Towards the ultimate understanding of MUSCL: Pitfalls in achieving third-order accuracy. *Journal of Computational Physics*, 446, Dec. 2021. ISSN 0021-9991. 23, 26

[193] S. Walther, C. Airiau, and A. Bottaro. Optimal control of Tollmien–Schlichting waves in a developing boundary layer. *Physics of Fluids*, 13(7):2087–2096, 2001. 13

[194] X. Wang and X. Zhong. Effect of wall perturbations on the receptivity of a hypersonic boundary layer. *Physics of fluids*, 21(4):044101, 2009. 12

[195] X. Wang, X. Zhong, and Y. Ma. Response of a hypersonic boundary layer to wall blowing-suction. *AIAA journal*, 49(7):1336–1353, 2011. 12

[196] Y. Wang, E. Ferrer, A. Martínez-Cava, Y. Zheng, and E. Valero. Enhanced stability of flows through contraction channels: Combining shape optimization and linear stability analysis. *Physics of Fluids*, 31(7):074109, 2019. 13

[197] H. Werlé. Transition et décollement: visualisations au tunnel hydrodynamique de l'ONERA. 1980. 9

[198] F. M. White. *Viscous fluid flow*, volume 3. McGraw-Hill New York, 2006. 7

[199] S. Yoon and D. Kwak. Three-dimensional incompressible Navier-Stokes solver using lower-upper symmetric-Gauss-Seidel algorithm. *AIAA Journal*, 29(6):874–875, 1991. 28

[200] R. Zhao, C. Wen, X. Tian, T. Long, and W. Yuan. Numerical simulation of local wall heating and cooling effect on the stability of a hypersonic boundary layer. *International Journal of Heat and Mass Transfer*, 121:986–998, 2018. 12, 65, 67, 68

[201] T. Zhou, Z. Liu, Y. Lu, Y. Wang, and C. Yan. Direct numerical simulation of complete transition to turbulence via first-and second-mode oblique breakdown at a high-speed boundary layer. *Physics of Fluids*, 34(7), 2022. 10, 11

[202] D. Zingg, S. De Rango, M. Nemec, and T. Pulliam. Comparison of several spatial discretizations for the Navier–Stokes equations. *Journal of computational Physics*, 160(2): 683–704, 2000. 28

[203] S. Zuccher, P. Luchini, and A. Bottaro. Algebraic growth in a blasius boundary layer: optimal and robust control by mean suction in the nonlinear regime. *Journal of Fluid Mechanics*, 513:135–160, 2004. 13, 104, 116

Résumé en français

Une donnée essentielle pour la conception des véhicules hypersoniques est la nature de l'écoulement le long de sa surface, à savoir si la couche limite est laminaire ou turbulente. Tandis qu'un écoulement laminaire induit moins de flux de chaleur et de frottement, réduisant le poids de la protection thermique ainsi que la consommation de carburant, un écoulement turbulent est souhaitable afin d'éviter la séparation de couche limite provoquée par l'interaction avec les ondes de choc. La transition laminaire/turbulent est souvent produite par l'amplification de perturbations extérieures au sein de la couche limite. Par conséquent, l'identification et le contrôle en boucle ouverte des perturbations les plus défavorables, aussi nommées les solutions optimales non linéaires, sont l'objet de ce travail. Ces objectifs ont été atteints grâce au développement d'outils numériques pour les écoulements laminaires compressibles et à leur application à une couche limite à un nombre de Mach de 4,5 sur une plaque plane adiabatique. Les méthodes employées ont initialement permis d'étudier les instabilités linéaires et leur sensibilité puis ont été étendues au calcul de solutions non linéaires.

En premier lieu, les principaux résultats connus sur la transition laminaire/turbulent en régime supersonique ont été rappelés. La transition résulte généralement de l'amplification d'instabilités linéaires (les modes de Mack) qui déclenchent des mécanismes secondaires (vortex tridimensionnels, stries,...) qui se dissipent ensuite en zones turbulentes. Afin de contrôler la transition, aucun consensus n'a été atteint sur l'emplacement optimal pour appliquer un actionneur de chauffage/refroidissement pariétal en boucle ouverte malgré de nombreuses études. Selon les configurations étudiées et les hypothèses réalisées, de nombreuses méthodes d'analyse de stabilité appliquées à la mécanique des fluides ont été développées au cours du temps, de l'analyse linéaire (locale, PSE, OWNS, non modale, globale, résolvante) à celle non linéaire en passant par la sensibilité linéaire et les analyses faiblement non linéaires.

Dans le cadre de ce travail, les méthodes de stabilité globale pour résoudre les équations compressibles de Navier-Stokes ont été implémentées dans le formalisme mathématique discret dans le code BROADCAST : analyses de point fixe, de stabilité et de résolvante. Ces méthodes s'appuient sur une discrétisation bidimensionnelle où les perturbations périodiques selon la troisième direction spatiale (z) sont résolues par développement de Fourier afin de maintenir un coût de calcul abordable. Les opérateurs de dérivation sont construits par Dérivation Automatique pour une plus grande précision et un calcul immédiat des opérateurs linéarisés et adjoints. Les schémas numériques d'ordre élevé implémentés dans BROADCAST permettent de calculer précisément les gains optimaux de la résolvante à hautes fréquences pour un faible coût de calcul. De plus, ces schémas peuvent être utilisés à faible nombre de Mach ($M_\infty \approx 0,1$) pour

étudier le régime incompressible à la fois sur des maillages cartésiens et curvilignes. Enfin, ces méthodes ont été validées sur l'écoulement incompressible autour d'un cylindre puis appliquées à la couche limite hypersonique où l'analyse de résolvante a identifié les trois principaux mécanismes de stabilité globaux : les stries stationnaires, le premier mode de Mack oblique et le second mode de Mack (haute fréquence et bidimensionnel).

Ensuite, la sensibilité linéaire des gains optimaux de la résolvante, c'est-à-dire l'emplacement optimal pour le contrôle en boucle ouverte à faible amplitude des trois principales instabilités linéaires, a été calculée. Le contrôle pariétal a été étudié en calculant l'emplacement optimal des actionneurs de soufflage/aspiration ou de chauffage/refroidissement afin d'atténuer ou de renforcer les instabilités par une technique d'optimisation adjointe. Pour un contrôle par soufflage/aspiration, l'aspiration est optimale pour stabiliser le second mode de Mack si elle est située en amont du point de synchronisation et inversement pour un soufflage. L'application en régime non linéaire (amplitude finie) du contrôle optimal de soufflage/aspiration, calculé pour le second mode Mack, entraîne une réduction du gain optimal du second mode Mack mais déplace son pic vers des fréquences plus basses ou plus élevées, déclenche une légère diminution des gains du premier mode de Mack et laisse les stries inchangées. Par conséquent, seul un actionneur localisé d'aspiration amortirait efficacement toutes les instabilités. Pour un contrôle par chauffage/refroidissement, le premier mode de Mack est l'instabilité la plus sensible. Les premier et second modes de Mack ont une sensibilité opposée en ce qui concerne les variations de température pariétale, cependant, une source de chaleur située à proximité du bord d'attaque amortit les deux modes Mack en même temps. Dans la partie aval de l'écoulement, le premier mode de Mack est stabilisé par une longue zone de refroidissement tandis que seule une courte bande de refroidissement située dans la région instable du mode S permet d'amortir le second mode de Mack, mais cela est sous-optimal par rapport à la région du bord d'attaque. Ainsi, l'application du contrôle optimal par chauffage/refroidissement en régime non linéaire, calculé pour le premier mode Mack, entraine une forte réduction des gains du premier mode Mack mais amplifie fortement le second mode Mack. L'application d'une unique bande chauffante située proche du bord d'attaque (et éventuellement d'une bande de refroidissement en aval dans la région instable du mode S) parvient à amortir toutes les instabilités et pourrait être considérée comme un actionneur pour retarder la transition vers la turbulence pour plusieurs gammes de fréquences et nombres d'ondes.

L'analyse faiblement non linéaire au voisinage d'une bifurcation pour les écoulements compressibles oscillateurs et l'extension de la résolvante linéaire à l'analyse entrée-sortie non linéaire pour les écoulements compressibles amplificateurs de bruit ont été développées dans le formalisme mathématique discret. Cette dernière prend en compte les interactions non linéaires d'un nombre fini d'harmoniques temporelles et spatiales selon z. Les perturbations les plus défavorables ont été ensuite identifiées par descente de gradient. Les équations compressibles de Navier-Stokes ont été écrites sous une forme pseudo-spectrale grâce à la méthode STSM (Space-Time Spectral Method) pour le temps et selon z. Nécessitant une technique d'anti-repliement de spectre, ces systèmes de large dimension ont été résolus de manière itérative à l'aide d'un algorithme GMRES préconditionné par une méthode bloc-circulante. Après validation à faible nombre de Mach, la transition d'une couche limite hypersonique a été étudiée. Il en résulte que le forçage fondamental optimal est une paire d'ondes obliques symétriques favorisant les interactions non linéaires du premier mode de Mack avec les stries. En augmentant l'amplitude du forçage, des harmoniques plus élevées sont générées jusqu'à ce que la transition vers la turbulence soit atteinte via un mode variqueux sous-harmonique (vortex en quinconce). De plus, une analyse faiblement non linéaire qui inclut le troisième niveau d'interactions (polynôme d'ordre A^6) parvient à prédire substantiellement le frottement à moindre coût.

Enfin, les profils de flux thermique optimaux pour contrôler la transition laminaire/turbulent

induite par le forçage optimal précédemment révélé ont été calculés par méthode adjointe. Ils prédisent des variations similaires dans la direction de l'écoulement que celles obtenues grâce à une analyse de sensibilité linéaire. Pour retarder la transition, sous des perturbations d'amplitude moyenne, un flux thermique à flux d'intensité moyenne homogène selon z et qui cible uniquement le premier mode de Mack en chauffant en amont de la branche II du mode local est presque aussi efficace qu'un flux thermique périodique selon z de la même intensité. Le flux thermique optimal calculé pour la fréquence la plus dangereuse réduit efficacement le frottement induit par la transition pour des fréquences similaires et inférieures en amortissant l'amplification des instabilités. Pour favoriser la transition, un flux thermique périodique selon z avec chauffage autour de la branche II et un refroidissement décalé selon z, situé dans la région de transition en aval, constituent le contrôle le plus efficace pour augmenter le frottement en amplifiant les stries. Dans la même bande de fréquences dans laquelle il a été calculé, le contrôle agit sur deux aspects : il décale le début de la transition vers l'amont et renforce la croissance du coefficient de frottement. Pour les autres fréquences, il n'affecte que l'amplification du frottement.

ECOLE
DOCTORALE

Titre : Solutions optimales linéaires et non-linéaires dans une couche limite hypersonique : stabilité et contrôle en boucle ouverte.

Mots clés : Ecoulement hypersonique, Couche limite, Transition laminaire/turbulent, Stabilité, Optimisation adjointe.

Résumé : Une donnée essentielle pour la conception des véhicules hypersoniques est la nature de l'écoulement le long de sa surface, à savoir si la couche limite est laminaire ou turbulente. Tandis qu'un écoulement laminaire induit moins de flux de chaleur et de frottement, réduisant le poids de la protection thermique ainsi que la consommation de carburant, un écoulement turbulent est souhaitable afin d'éviter la séparation de couche limite provoquée par l'interaction avec les ondes de choc. La transition laminaire/turbulent est souvent produite par l'amplification de perturbations extérieures au sein de la couche limite. Par conséquent, l'identification et le contrôle des perturbations les plus défavorables sont l'objet de ce travail.
Nous avons développé des outils numériques dans le formalisme mathématique discret de stabilité globale pour identifier les instabilités linéaires, calculer leur sensibilité linéaire, les solutions optimales non linéaires ainsi que leur contrôle optimal en boucle ouverte. Les méthodes employées s'appuient sur la Dérivation Automatique de la discrétisation spatiale bidimensionnelle des équations régissant la dynamique des fluides. Afin de maintenir un coût de calcul abordable, les instabilités périodiques selon la troisième direction spatiale (z) sont étudiées par développement de Fourier. Les solutions non linéaires sont ensuite calculées sous forme pseudo-spectrale par Space-Time Spectral Method selon le temps et selon z. Les perturbations optimales sont enfin déduites par optimisation adjointe.
Nous avons appliqué ces outils à une couche limite attachée, à un nombre de Mach de 4,5, où le scénario de transition optimal repose sur l'interaction non linéaire du premier mode oblique de Mack. De plus, les actionneurs optimaux de flux thermique et de soufflage/aspiration pariétaux en boucle ouverte ont été calculés afin d'amortir la croissance linéaire des trois instabilités les plus prédominantes : les stries stationnaires, les premier et second modes de Mack. Enfin, les flux thermiques optimaux agissant sur le champ moyen pour retarder ou promouvoir le scénario de transition optimal ont été déterminés.

Title : Optimal linear and non-linear solutions in hypersonic boundary layers: stability and open-loop control.

Keywords : Hypersonic flow, Boundary layer, Laminar to turbulent transition, Stability, Adjoint optimisation.

Abstract : A key parameter for the design of hypersonic air-breathing vehicles is the flow state over its surface, whether the boundary layer is laminar or turbulent. While the former induces less heat-flux and skin-friction, reducing the weight of the thermal protection and the fuel consumption, the latter is desirable to avoid any flow separation induced by the interaction with the shock waves. Laminar to turbulent transition is often produced by the growth of free-stream disturbances within the boundary layer. Therefore, the identification and control of the worst-case disturbances are the aim of this work.
We have developed numerical tools in the discrete global framework to identify the linear instabilities, compute their linear sensitivity, derive the non-linear optimal solutions and their corresponding optimal open-loop control. The methods rely on the Algorithmic Differentiation of the two-dimensional spatial discretisation of the equations governing the fluid dynamics. To maintain an affordable computational cost, the spanwise periodic instabilities are studied by Fourier expansion. The non-linear solutions are then derived in a pseudo-spectral form by Space-Time Spectral Method for time and spanwise dimensions. The optimal disturbances are finally found by adjoint procedure.
We have applied this framework to a Mach 4.5 attached boundary layer where the first Mack mode oblique breakdown prevails as the optimal transition scenario. Moreover, the optimal open-loop wall heat-flux and blowing/suction actuators were derived to damp the linear amplification of the three most predominant instabilities: the stationary streaks, the first and second Mack modes. Eventually, the optimal mean-flow heat-fluxes to delay or promote the optimal transition scenario have been computed.

Institut Polytechnique de Paris
91120 Palaiseau, France